

**Force generation in dividing *E. coli* cells:
A handles-on approach using optical tweezers**

**Force generation in dividing E. coli cells:
A handles-on approach using optical tweezers**

PROEFSCHRIFT

TER VERKRIJGING VAN
DE GRAAD VAN DOCTOR
AAN DE UNIVERSITEIT LEIDEN,
OP GEZAG VAN DE RECTOR MAGNIFICUS
PROF.MR. P.F. VAN DER HEIJDEN,
VOLGENS BESLUIT VAN HET COLLEGE VOOR PROMOTIES
TE VERDEDIGEN OP DINSDAG 2 DECEMBER 2008
TE KLOKKE 11.15 UUR

DOOR

GERTJAN SEBASTIAAN VERHOEVEN

GEBOREN TE LEIDERDORP IN 1977

Promotiecommissie:

Promotor:	Prof. dr. M. Dogterom
Co-promotor:	Dr. T. den Blaauwen
Referent:	Prof. dr. A.J.M. Driessen (Universiteit Groningen)
Overige leden:	Prof. dr. J.P.M. Tommassen (Universiteit Utrecht)
	Dr. L.B. Oddershede (Niels Bohr Institute, Copenhagen)
	Prof. dr. H. Schiessel
	Prof. dr. T. Schmidt
	Prof. dr. J.M. van Ruitenbeek

Force generation in dividing E. coli cells:

A handles-on approach using optical tweezers

©2008 by Gertjan Sebastiaan Verhoeven. All rights reserved.

Nederlandse titel: Krachtgeneratie in delende *E. coli* cellen: handvatten voor een benadering met een optisch pincet

The work described in this thesis was performed at the FOM Institute for Atomic and Molecular Physics (AMOLF), Kruislaan 407, 1098 SJ Amsterdam as well as at the Swammerdam Institute for Life Sciences, University of Amsterdam, Kruislaan 316, 1098 SM Amsterdam. This work is financially supported by the "Nederlandse organisatie voor Wetenschappelijke Onderzoek (NWO)" as part of the "From Molecule to Cell" program.

ISBN 978-90-77209-28-8

A digital version of this thesis can be downloaded from <http://ub.leidenuniv.nl>. Printed copies can be obtained by addressing the library at the FOM institute for Atomic and Molecular Physics (AMOLF): library@amolf.nl; Kruislaan 407, 1092 SJ, Amsterdam, The Netherlands.

Printed in the Netherlands by Ponsen & Looijen BV graphical company, Wageningen.

Aan mijn ouders

This thesis is partly based on the following articles:

Gertjan S. Verhoeven, Svetlana Alexeeva, Marileen Dogterom and Tanneke den Blaauwen. Differential bacterial surface display of peptides by the transmembrane domain of OmpA, *to be resubmitted*

Gertjan S. Verhoeven, Marileen Dogterom and Tanneke den Blaauwen. Outer membrane assembly of N- and C-terminal fusions to the OmpA transmembrane domain, *to be submitted*

Gertjan S. Verhoeven, Tanneke den Blaauwen and Marileen Dogterom. Force-extension curves of DNA tethers attached to outer membrane protein OmpA in a living bacterium, *to be submitted*

Other articles:

Svetlana Alexeeva, Theodorus W.J. Gadella Jr, Gertjan S. Verhoeven, and Tanneke den Blaauwen. Spectral FRET with Background Unmixing Allows Determination of *E. coli* Protein Interactions at Native Expression Levels, *to be resubmitted*

Contents

Chapter 1: Introduction.....	11
<i>Measuring and exerting forces with optical tweezers.....</i>	<i>14</i>
<i>Force probe attachment to the site of division.....</i>	<i>16</i>
<i>Outline of this thesis.....</i>	<i>18</i>
Chapter 2: Force-induced cell shaping of bacteria?	19
<i>The PG cell wall.....</i>	<i>21</i>
<i>Turgor pressure.....</i>	<i>22</i>
<i>The cytoskeleton: FtsZ</i>	<i>23</i>
<i>The cytoskeleton: MreB</i>	<i>25</i>
<i>PBPs and PG hydrolases: making and breaking bonds in the sacculus</i>	<i>25</i>
<i>Cell division.....</i>	<i>26</i>
<i>Evidence for force-generation by the Z-ring.....</i>	<i>28</i>
<i>Modeling the Z-ring.....</i>	<i>29</i>
<i>Force-induced cell wall shaping.....</i>	<i>31</i>
Chapter 3: Differential bacterial surface display of peptides by the transmembrane domain of OmpA	35
ABSTRACT	35
INTRODUCTION.....	36
MATERIALS AND METHODS	38
RESULTS	42
<i>Design of loop insertions.....</i>	<i>42</i>
<i>Growth of cells expressing OmpA-177 loop insertion proteins</i>	<i>44</i>
<i>Expression of OmpA-177 loop insertion proteins</i>	<i>46</i>
<i>Role of the periplasmic domain.....</i>	<i>47</i>
<i>OM incorporation of truncate and full-length constructs</i>	<i>50</i>
<i>Surface display of loop insertions: fluorescent labeling of cells</i>	<i>52</i>
DISCUSSION.....	55

Contents

<i>Reduced protein levels of FLAG or myc loop insertions in OmpA</i>	55
<i>Overexpression of engineered OmpA variants in LMC500 versus MC1061</i>	56
<i>“Aberrant” heat-modifiability versus normal heat-modifiability</i>	57
<i>Summary</i>	57
SUPPLEMENTARY MATERIALS AND METHODS	62
Chapter 4: Domain fusions to the C-terminus of cell division protein FtsQ	65
ABSTRACT	65
INTRODUCTION	66
RESULTS	70
<i>Detection of fusion proteins on immunoblot</i>	70
<i>Localization and complementation of GFP-FtsQ and GFP-FtsQ-HSV</i>	72
<i>Localization of GFP-FtsQ-AcrA-X fusions in the presence of wild-type FtsQ</i>	76
<i>Localization of GFP-FtsQ-AcrA-X fusions in the presence of FtsQ(E125K)</i>	78
<i>Extending GFP-FtsQ with a myc linker and the ALBP domain</i>	80
DISCUSSION.....	82
<i>FtsQ as part of the divisome appears dynamic</i>	82
<i>Why are GFP-FtsQ-AcrA-X fusions excluded from mid-cell?</i>	83
<i>Recommendations for future work on GFP-FtsQ-myc-ALBP</i>	85
MATERIALS AND METHODS	87
Chapter 5: Outer membrane assembly of N- and C-terminal fusions to the OmpA transmembrane domain	93
ABSTRACT	93
INTRODUCTION	94
RESULTS	98
<i>A C-terminal Pal fusion to the OmpA TM domain</i>	98
<i>(OmpA-177)-Pal in wild-type cells is excluded from mid-cell</i>	100
<i>Localization of (OmpA-177)-Pal in ΔPal cells</i>	102
<i>A C-terminal mCherry fusion to the OmpA TM domain</i>	103
<i>An N-terminal mCherry fusion to the OmpA TM domain</i>	106
<i>An N-terminal ALBP₂ fusion to the OmpA TM domain</i>	110
<i>An N-terminal Pal-mCherry fusion to the OmpA TM domain</i>	111

Contents

<i>An N-terminal^TAmiC fusion to the OmpA TM domain</i>	115
DISCUSSION.....	116
<i>OMP domain organization</i>	116
<i>Toxicity of fusions</i>	117
<i>Mid-cell exclusion of (OmpA-177)-Pal</i>	118
<i>Why the N-terminal Pal and ^TAmiC fusions to the OmpA TM domain are degraded: incompatibility with Lol and Tat systems respectively?</i>	119
<i>On export to the periplasm of heterologous proteins</i>	120
MATERIALS AND METHODS	122
Chapter 6: A counter-propagating optical tweezers setup with independent dual position detection	131
ABSTRACT	131
INTRODUCTION	132
DETAILED EXPERIMENTAL SETUP AND CALIBRATION METHOD	135
<i>Optical tweezers setup</i>	135
<i>Calibrating the optical trap</i>	138
RESULTS	139
<i>Optical trapping at controlled temperatures</i>	139
<i>Water objectives</i>	140
<i>The roll-off frequency increases linearly with laser power</i>	142
<i>DNA tether formation between beads in time-shared traps</i>	143
<i>Effect of laser irradiation on single growing cells</i>	145
<i>Summary</i>	147
Chapter 7: Force-extension curves of DNA tethers attached to outer membrane protein OmpA in a living bacterium	149
ABSTRACT	149
INTRODUCTION	150
RESULTS	154
<i>DNA tethers to an immobilized bead</i>	154
<i>Axial dependence of the trap stiffness and trap center</i>	159
<i>Bacterial tethers to the OmpA β-barrel</i>	165

Contents

<i>What is the proper level of accuracy when analyzing bacterial tethers?</i>	170
<i>Bacterial F-x curves</i>	171
<i>Bacterial tethers to full-length OmpA</i>	175
<i>Analysis of the measured unbinding forces at two pulling speeds</i>	178
DISCUSSION	180
<i>OmpA-177 versus full-length OmpA</i>	180
<i>Correcting for axial displacements</i>	182
<i>Which unbinding force have we measured?</i>	183
MATERIALS AND METHODS	185
Chapter 8: Final Considerations and Recommendations	191
<i>Mobility of β-barrels in the OM</i>	192
<i>Restraining a β-barrel to mid-cell</i>	194
<i>Alternative approach: PG cell wall-less E. coli ("L-forms")</i>	196
<i>Experimental geometry: assembly of the construct in the trap</i>	197
<i>Effect of laser light on bacterial growth</i>	199
<i>Alternative geometries: surface and dumbbell approach</i>	200
<i>Increasing the strength of the protein-DNA connection</i>	203
<i>Effect of forces on a growing bacterium</i>	204
<i>Concluding remarks</i>	205
Bibliography	207
Summary	229
Samenvatting	233
Dankwoord	239
Curriculum Vitae	240

I

Chapter 1: Introduction

This thesis is devoted to the development of a novel experimental approach to the study of cell division in bacteria. For this we use the model bacterium *Escherichia coli*. *E. coli* is a rod-shaped bacterium that lives in the intestines of warm-blooded animals, as well as in many labs around the world. At first sight, it has a not-so-exciting life: it grows by increasing its length, duplicating its DNA and dividing in the middle of the cell by splitting itself in two. However, to actually live this not-so-exciting life is a formidable task for such a small cell, which can duplicate itself within 20 minutes when growth conditions are optimal.

Several complex processes take place within a bacterium; examples are motility, chemotaxis, DNA replication and segregation, transport processes etc. Over the past decades, a lot of the components (genes, proteins, interactions) of these processes have been discovered and characterized. More recently, our knowledge has become sufficiently detailed to start answering questions related to the mechanisms behind the observed phenomena. Advances are both on the biochemical connectivity of the proteins (wiring of the network), as well as on molecular mechanisms that drive or regulate these processes in space and time. Protein complexes that were once thought to consist of static components are now found to consist of highly dynamic subunits.

Cell division is one of the fundamental requirements of all life. It is textbook knowledge that an animal cell divides because a contractile ring of actin filaments and myosin II motor proteins contracts the cytoplasmic membrane (“the purse-string” model (Schroeder 1970; Schroeder 1972)). Since animal cells are often thought of as more complex than their prokaryotic counterparts, it might appear surprising that the simple binary fission of a bacterium is still poorly understood. A cell-walled bacterium such as *E. coli* has a three-layered cell envelope, consisting of a cytoplasmic membrane, a thin peptidoglycan (PG) cell wall and an outer membrane (depicted in **Figure 1.1**). It divides by a simultaneous inward growth (“invagination”) of all three layers. A simple question such as what drives the growth inwards during division has no satisfying answer. Instead, as in most fields in cell biology at the moment, the list of proteins involved is increasing every month (Errington et al. 2003; Weiss 2004; Goehring and Beckwith 2005; Vicente et al. 2006).

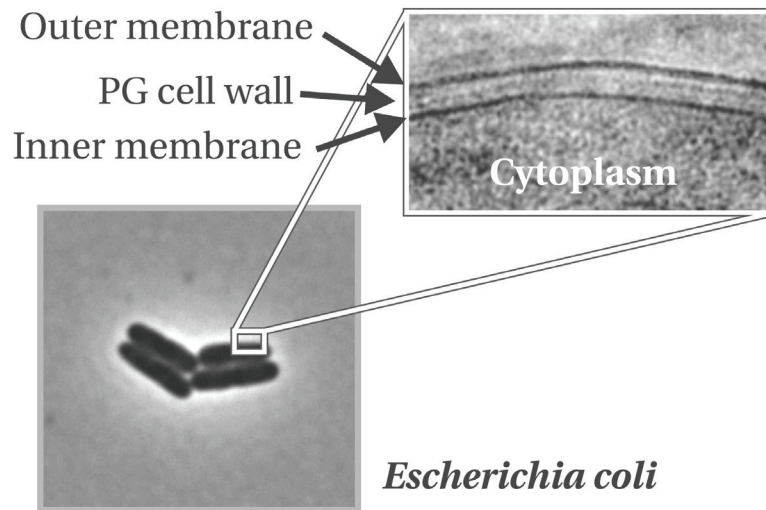


Figure 1.1: *Escherichia coli*. A growing micro-colony of *Escherichia coli* cells imaged with a phase-contrast microscope. After zooming in on the cell envelope (inset), a Cryo EM picture shows the crowded (electron dense) cytoplasm, surround by three layers: the cytoplasmic membrane, the peptidoglycan (PG) cell wall and the outer membrane. The compartment delineated by the inner and outer membrane (containing the PG cell wall) is called the periplasm. (Cryo EM picture reproduced from (Matias et al. 2003))

However, upon closer inspection of the animal cytokinesis field, both fields appear to be in a quite similar stage: It too, is faced with long “parts lists”, together with rudimentary models that basically cover the entire imaginable spectrum (Eggert et al. 2006). After discussing the textbook “purse-string” model and two other models, the authors conclude with the following remark: “*In our view, the mechanics of cytoskeletal force production in cytokinesis is still an open question*” (Eggert et al. 2006).

Until the early to mid 1990’s, bacteria were viewed as “bags of enzymes” that function as a result of simple physical principles such as tension, pressure and macromolecular crowding (Koch 1988). This made them distinct from eukaryotic cells, where observed phenomena were already being interpreted within a context of cytoskeletal elements such as microtubules and actin filaments, which together with motor proteins such as kinesin and myosin are responsible for mayor cellular events such as chromosome segregation

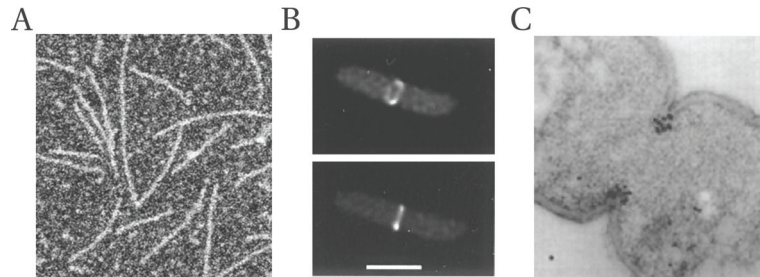


Figure 1.2: The Z-ring. (A) FtsZ polymerizes *in vitro* into protofilaments. (Reproduced from (Romberg et al. 2001)). Thickness of a protofilament is ~5 nm. (B) FtsZ forms a ring at mid-cell *in vivo* (Z-ring). Deconvoluted fluorescence microscopy images of cells expressing FtsZ-GFP. Bar indicates 1 μm (reproduced from (Ma et al. 1996)) (C) Division in *Escherichia coli* occurs through the simultaneous invagination of the three layers that constitute the cell envelope: Inner membrane, PG cell wall and outer membrane. Shown is an EM picture of a dividing *Escherichia coli* bacterium. The black dots are anti-FtsZ gold nanoparticles. (Reproduced from (Bi and Lutkenhaus 1991))

and cell division (Alberts 2002).

Recent years have seen these distinctions to fade, as more and more cytoskeletal elements are being discovered in bacteria (Cabeen and Jacobs-Wagner 2005). Of these, the actin homologue MreB and the tubulin homologue FtsZ have made the biggest impact on the field. MreB is found to polymerize into helical cables throughout the cell underneath the cytoplasmic membrane and is important for its rod-like shape (Jones et al. 2001). FtsZ polymerizes into filaments (**Figure 1.2A**) that form a ring in the middle of the cell (**Figure 1.2B,C**) and is required for formation of new spherical caps during division (Bi and Lutkenhaus 1991).

These new findings suggest that cytoskeletal elements “shape” the cell. Evidence is accumulating that FtsZ forms a force-generating contractile ring which directs cell wall growth inwards during division (Osawa et al. 2008). Likewise, the prevailing view of cylindrical cell wall growth is now based on cell wall synthesizing machinery that is guided along dynamic helical MreB tracks (den Blaauwen et al. 2008). It is possible that the maintenance of the rod-shape also requires inward forces to counter the turgor pressure and membrane tension (see also **Chapter 2**).

However, although appealing and likely, direct experimental evidence for a force-

induced cell shaping during growth and division is lacking. In this thesis, we describe the first steps towards a novel approach to study the role of forces generated by cytoskeletal elements inside living bacterial cells. The approach is based on the creation of artificial anchoring points on the cell surface at the site of division. This allows the attachment of sensitive force probes (optically trapped beads) that can locally exert and measure force simultaneously (**Figure 1.4A**). As optical tweezers allow easy manipulation of multiple trapped beads in a liquid environment, together with light microscopy, this approach has the potential of measuring the effect of external forces on the division process of a single cell.

Since to date in bacteria, no (protein) markers have been found that are localized at the site of division which are accessible from the exterior, such a protein has to be created first. A daunting task already by itself, ill-characterized bacteria, or ones that do not have the proper genetic tools available cannot be used. This leaves the main bacterial model organisms *E. coli* and *B. subtilis*. We chose *E. coli* because *B. subtilis* has a thick ~20 nm cell wall, and forms a proper cell wall septum (a double layered separation plate in the middle of the cell), which is only cleaved after its formation is complete (Fukushima et al. 2006). This means that the presumed force-generating process, the Z-ring contraction during septum formation, is shielded by a thick cell wall from the outside world.

In contrast, the cell envelope of *E. coli* consists of a cytoplasmic membrane, surrounded by a thin ~5 nm thick PG cell wall, in turn surrounded by the outer membrane (Matias et al. 2003) (**Figure 1.1**). The cellular compartment formed between the inner and outer membranes is called the periplasm (solvent accessible width ~15-20 nm (Matias et al. 2003)). Since in *Escherichia coli* the envelope layers invaginate simultaneously (**Figure 1.2C**), and the FtsZ ring is expected to exert small forces on the growing cell wall, this makes it conceivable that small forces (below 100 pN) exerted on the cell wall via an artificial construct in the OM can influence constriction.

Measuring and exerting forces with optical tweezers

Optical tweezers are capable of exerting and measuring forces typically in the range of ~0.1-100 pN (Moffitt et al. 2008). The use of high refractive index particles holds a promise to further increase the maximum force (van der Horst et al. 2008). These forces are typically those encountered inside living cells. As such, the technique is used extensively to study biological processes such as protein folding and force generation by molecular

motors and biopolymers (Visscher et al. 1999; Kerssemakers et al. 2003). This is accomplished by optical trapping of a micron-sized, spherical, transparent particle (a “bead”) in a highly focused laser beam. Physically, this is possible because light carries momentum \vec{p} with magnitude $p = E/c$ (with E the energy of the photons and c the speed of light) and direction \vec{k} (wave vector). When photons change direction due to refraction by the particle, this momentum vector is changed, implying that a force has been exerted on the light wave ($\vec{F} = \frac{d\vec{p}}{dt}$) (Newton’s second law). Since the particle has exerted a force on the light wave, it follows that (from Newton’s third law) that the light exerts an equal but opposite force on the particle (Svoboda and Block 1994).

Neglecting absorption, the forces exerted on the particle are caused by refraction and reflection of light. Typically, these forces are split into the gradient force that is directed in the direction of the light gradient (i.e. the laser focus) and the scattering force, that is directed along the optical axis and pushes the particle out of the focus. In 1986, it was demonstrated by Arthur Ashkin that these forces can compensate each other and stable three-dimensional (3D) trapping of micron-sized particles is possible (Ashkin et al. 1986).

How this is possible can be understood from a simplified ray-optics picture (Svoboda and Block 1994). In **Figure 1.3A**, the brighter ray 2 causes a larger reaction force than ray 1, and thus the resultant force points in the direction of increasing light intensity, i.e. towards the focus. The scattering force is along the optical axis, in the direction of the light, and pushes the particle out of the focus. In **Figure 1.3B**, it is shown that just below the focus, highly divergent rays can enter the particle to become less divergent. This creates a restoring force towards the focus. At the location where the scattering force balances this restoring gradient force stable 3D trapping occurs.

When an external force F pulls the trapped particle out of the trap, it responds (for small displacements x) as if it is attached to a harmonic spring, $F = kx$. When the spring constant k , also called the trap stiffness, is known, measuring the displacement of the particle becomes equivalent to measuring the force on it. The bead has become a sensitive force probe. Measuring the Brownian motion of the particle in the trap allows the determination of the trap stiffness (see also **Chapter 6**) (Visscher et al. 1996).

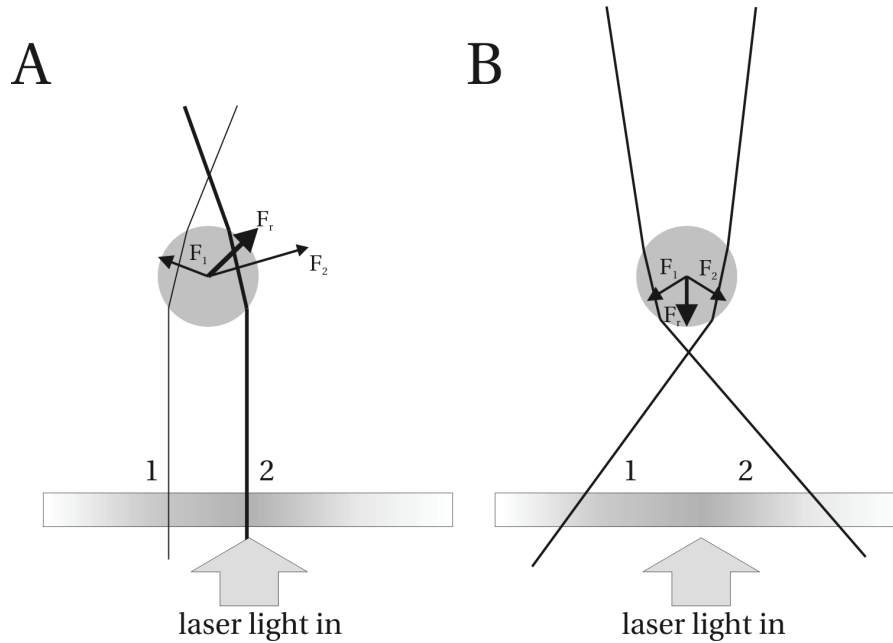


Figure 1.3: Stable 3D optical trapping of a transparent particle (“bead”). Individual light rays are drawn, the intensity gradient is indicated in the gray bar. (A) The bead is attracted to the region of highest laser intensity. (B) “Behind” the focus, stable 3D trapping can occur.

Force probe attachment to the site of division

For the study of FtsZ force generation, ideally one wants to measure and exert forces on the same entity on which FtsZ supposedly acts, i.e. the cytoplasmic membrane. As it is not possible to “strip” a bacterium of its OM and PG cell wall without losing its ability to divide, a molecular spacer construct that bridges the periplasm is required. In doing so, we assume that the multitude of molecular bonds that link the three layers together will efficiently transduce the force between Z-ring and trapped bead “handle”.

To create an anchoring point on the cell surface, we chose to genetically insert an antigenic peptide (epitope) into the surface-exposed loops of the highly abundant OM β -barrel protein OmpA (Freudl 1989). As the inward growth during division of the bacterium is relatively sharp, the bead handle cannot be directly attached to the division site, and a spacer is needed. We use dsDNA, as its force-extension behavior is well known (Smith et al. 1996), and its ends can easily be functionalized for attachment to either a bead, or to a

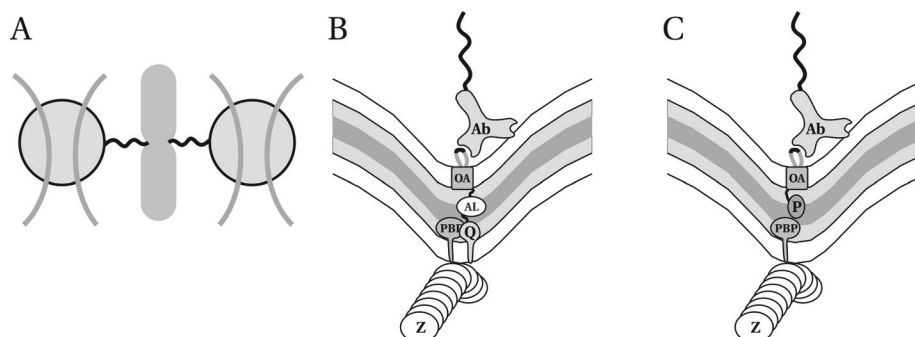


Figure 1.4: A molecular construct to bridge the periplasm. (A) Proposed experimental geometry. A bacterium is tethered via dsDNA to optically trapped beads. (B) Molecular construct based on mid-cell affinity protein FtsQ. (C) Molecular construct based on mid-cell affinity protein Pal. (B,C) Protein abbreviations: Z-ring (Z), the PG synthesizing complexes (PBP), FtsQ (Q), ALBP (AL), OmpA β -barrel (OA), Antibody (Ab), Pal (P).

protein such as an antibody or streptavidin (Cecconi et al. 2008).

Protein domain fusions to OmpA are employed to localize the OmpA β -barrel to mid-cell (**Figure 1.4B,C**). By fusing the OmpA domain to a protein domain that has mid-cell affinity (either for another mid-cell localized protein, or for a particular substrate present at mid-cell), we aim to localize the OmpA protein to mid-cell.

The location of the native cellular compartment of the mid-cell affinity domain determines the length and complexity of the resulting fusion protein. When this research was initiated (2002), no periplasmic or outer membrane mid-cell affinity domains had been discovered yet. Therefore, the inner membrane cell division protein FtsQ (van den Ent et al. 2008) was chosen as mid-cell localizing domain, fused via a spacer domain (in **Figure 1.4B** indicated with the ALBP sugar binding protein domain) to bridge the periplasm to the OmpA β -barrel.

With the discovery of the Pal protein at mid-cell (Gerding et al. 2007), an OM lipoprotein that has mid-cell affinity and binds PG became available, and a much simpler construct became possible (**Figure 1.4C**), as the Pal domain can be directly linked to the OmpA β -barrel.

Outline of this thesis

Since the force-induced cell shaping idea is relatively new, in **Chapter 2**, we will review the experimental evidence on which it is based, and the various mechanisms proposed that shape cell-walled organisms.

The remaining part of this thesis is divided in two parts. The first part deals with our quest for a fusion protein that is accessible on the cell surface and localizes predominantly to the division site: In **Chapter 3**, we describe the construction and characterization of engineered OmpA proteins with various epitopes. The OmpA variants were specifically tested for efficient membrane insertion *in vivo*. An epitope insertion fusion was found that inserted as efficient as wild-type OmpA. In **Chapter 4**, the construction of fusion proteins based on mid-cell localization domain FtsQ are described, and characterized for their ability to localize to mid-cell. After the discovery of a mid-cell localizing domain (Pal) that is tethered to the OM at its periplasmic side, as well as a fluorescent protein (mCherry) that fluoresces in the periplasm, we fused these domains to the OmpA β -barrel and characterized the resulting fusions for their ability to localize to mid-cell and/or to insert in the OM (**Chapter 5**).

The second part deals with the experimental setup (**Chapter 6**) used for the optical tweezers experiments described in **Chapter 7**. In these experiments, cells are immobilized on a surface, and DNA-coated beads are attached specifically to the engineered OmpA anchoring point on the cell surface. Force-extension curves of DNA tethers to the OmpA β -barrel are compared to the full-length OmpA that contains a cell wall binding domain. The data contain evidence for an increased probability of membrane tube formation when OmpA is not attached to the PG cell wall. The thesis concludes with a chapter that summarizes how far we have come, discusses alternative approaches, and provides recommendations for further experiments (**Chapter 8**).

II

Chapter 2: Force-induced cell shaping of bacteria?

In this chapter we will provide background information on the mechanisms of growth and division in rod-shaped Gram-negative bacteria, in particular the bacterium *E. coli*. For these processes, a possible role of (cytoskeletal) forces is discussed.

The instantaneous shape of cell-walled bacteria is determined by its peptidoglycan (PG) cell wall. This is illustrated in **Figure 2.1**, where EM pictures of three isolated cell walls (also termed “sacculi”) are shown. In all three cases, the shape of the cell wall was found to be identical to the shape of the bacterial cells they were isolated from. That it is the only determinant of cell shape in bacteria can be easily demonstrated by enzymatic degradation of the cell wall (e.g. by the PG hydrolase lysozyme), after which cells become spherical (termed “spheroplasts”) (Zinder and Arndt 1956; Malamy and Horecker 1964; Neu and Heppel 1964).

The sacculus of the dividing cell (**Figure 2.1B**) also makes it clear that division in bacteria is somewhat different from mammalian cells, as during division not only the cytoplasmic membrane needs to be constricted, but also cell wall synthesis needs to take place to form the new cell poles. Thus, to understand bacterial cell division, understanding cell wall growth is essential.

A key experiment was performed in 1971 (Schwarz and Leutgeb 1971): An *E. coli* mutant strain was used that requires an externally added particular precursor for PG cell wall growth, in the absence of which PG hydrolases break down the cell wall. As mentioned above, this results in the formation of spheroplasts. After re-addition of the precursor, the cells started to build a new cell wall, which (after isolation) was found to be spherical! (**Figure 2.1C**) Thus, not only does the wall shape the cell, but apparently the cell can also shape the wall. This suggests that the shape-information is not encoded in the molecular structure of PG. Instead, cell wall deposition appears determined by the location of the PBPs (penicillin-binding proteins, named after their penicillin binding property), the enzymes that synthesize new cell wall, and are typically anchored in the cytoplasmic membrane (Note that although in this thesis, we refer to PBPs when we mean PG synthesizing enzymes, actually some PBPs are PG hydrolases).

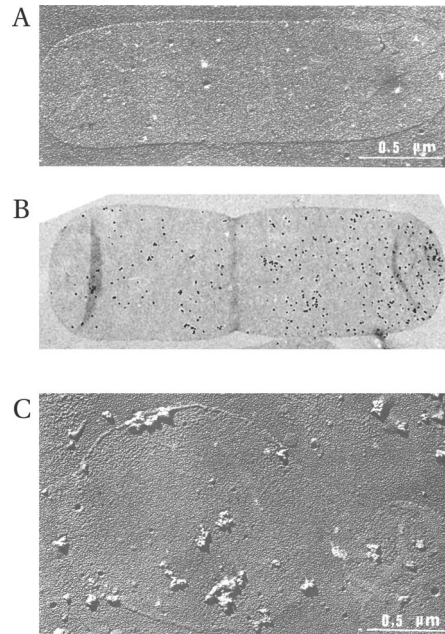


Figure 2.1: Isolated *Escherichia coli* cell walls (sacculi): PG Cell walls have the same shape as the cells from which they are isolated. (A) Isolated rod-shaped PG sacculus imaged by electron microscopy (Schwarz and Leutgeb 1971) (B) Isolated PG sacculus of a dividing bacterium (de Pedro et al. 1997). (C) Isolated PG sacculus of a spheroplast cell allowed to rebuild its cell wall (Schwarz and Leutgeb 1971).

As already mentioned in the introduction (**Chapter 1**), the discovery of cytoskeletal homologues of tubulin and actin in bacteria (FtsZ and MreB, respectively) has had a major impact on bacterial cell biology. In this chapter we discuss experimental evidence that suggest an active force-generating *modus operandi* of the Z-ring. Interpreted as a force-induced formation of the new cell poles, bacterial cell division can be seen as one aspect of bacterial morphogenesis, i.e. the processes that underlie the creation and maintenance of bacterial shape.

There are various factors that play a role in shaping of the cell wall. The main factors are the cellular turgor pressure, due to the osmotic difference inside and outside the cell, the cytoskeleton, built from protofilaments of MreB (actin) and FtsZ (tubulin), and the enzymes that make (PBPs) and break (hydrolases) covalent bonds in the cell wall. How

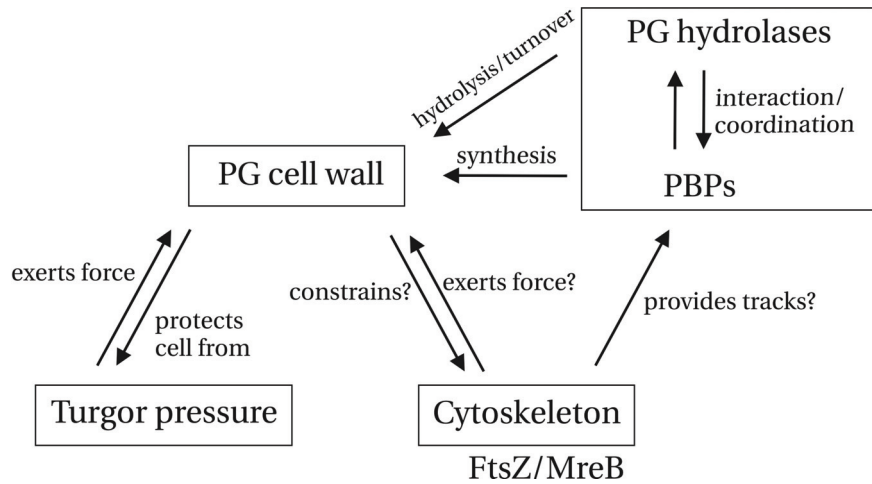


Figure 2.2: Schematic indicating the interplay between various factors that are thought to shape the bacterial cell wall. See text for details.

these factors (potentially) affect the (shape of the) cell wall is depicted schematically in **Figure 2.2**. In this chapter, we will review what is known about these factors, limiting ourselves to information relevant for a coarse mechanistic understanding of morphogenesis. We start with a brief description of what is known about the structure and properties of the cell wall itself.

The PG cell wall

The peptidoglycan (PG) cell wall (or “sacculus”) is a covalent macromolecule in the shape of the bacterium from which it originates (**Figure 2.1**). In *E. coli*, the PG cell wall has a thickness of 3-8 nm (Matias et al. 2003). It consists of approximately a monolayer (Wientjes et al. 1991) of stiff glycan chains cross-linked via flexible peptide cross-bridges. Its 3D structure has been elusive for many years, and various models have been proposed (Vollmer et al. 2008).

Light scattering experiments on isolated sacculi have shown that it is flexible, with a capacity to expand over 300% (Koch and Woeste 1992). This flexibility is mainly ascribed to flexibility in the peptide cross-bridges (Boulbitch 2000; Boulbitch et al. 2000). The elastic properties (the tendency to deform reversibly) of a material are defined through its elastic moduli λ_{ij} . When stress (force per area; unit pressure) is applied, a certain amount of strain

(length change/length) will occur in the material. The Young's modulus λ_{22} (a material property) is the proportionality factor. For sufficiently small deformations, the response is linear.

$$\frac{F}{A} = \lambda_{22} \frac{\Delta l}{l}$$

For cell-walled bacteria and yeasts, the Young's modulus has been determined using various techniques, and typically values around 10^7 - 10^8 Pa are found (Thwaites and Mendelson 1985; Mendelson and Thwaites 1989; Thwaites and Mendelson 1989; Yao et al. 1999; Arnoldi et al. 2000; Mendelson et al. 2000; Smith et al. 2000). This allows one to calculate e.g. the force required to increase the length of a bacterium by 10% through pulling at its ends. Assuming a cylindrical bacterium with radius 500 nm and PG thickness of 5 nm, and assuming $\lambda_{22} = 10^7$ Pa, one finds that 15 nN of force needs to be applied. As such a force is way outside the range what is typically generated inside cells (~pN range), division by a direct elastic deformation of the PG cell wall to "pinch" a static non-growing cell into two daughter cells is unlikely to take place.

Since in **Chapter 3**, molecular constructs are created that need to go through the PG cell wall, information about the permeability of the cell wall is important. Fluorescently labeled dextrans were used to estimate the pore size in isolated sacculi. It was found that the mean radius of the (unstretched) pores was ~2 nm (Demchick and Koch 1996). After stretching of the wall due to the intra-cellular turgor pressure (see below), possibly globular proteins up to ~50 kDa can pass through the PG pores. A sub-set of cellular protein content <100 kDa is released when cells are osmotically "shocked". The authors suggested that the pores in the PG cell wall acts as a molecular sieve (Vazquez-Laslop et al. 2001). The cell envelope contains several huge protein complexes that bridge the periplasm, such as the flagellar motor. For several such complexes it appears that dedicated PG hydrolases enlarge the PG locally for the complex to fit in (for references see (Vollmer et al. 2008)). An older but more comprehensive review regarding issues with PG permeability pertaining to large protein complexes also exists (Dijkstra and Keck 1996).

Turgor pressure

Osmotic pressure is the hydrostatic pressure that is produced by the difference in concentrations of solutes on both sides of a semi-permeable membrane, such as a lipid bilayer, or the Gram-negative cell envelope (see also below). Since not all particles

contribute to osmosis, the osmole unit is used to count the number of particles that contribute. The osmolality difference between inside and outside the cell causes a turgor pressure (force/area) on the cell envelope:

$$\Delta\Pi = RT(Osm_{cyto} - Osm_{ext})$$

This exerts a force on the PG cell wall, which is thought to be important for wall growth. For gram-negative bacteria, the turgor pressure is reported to range from 1-5 atm (Koch and Pinette 1987) ($1 \text{ atm} = 10^5 \text{ Pa} = 10^5 \text{ N/m}^2 = 100 \text{ pN}/\mu\text{m}^2$). In addition, the turgor pressure depends on the osmolality of the growth medium (Cayley et al. 2000).

As briefly explained in the previous chapter, Gram-negative bacteria have an additional compartment surrounding the cytoplasm called the periplasm. The osmotic pressure in the periplasm has long been assumed to be lower than that of the cytoplasm, resulting in a force exerted outwards on the cytoplasmic membrane (Koch 1998). This was thought to compress the contents of the periplasm, explaining the concentrated periplasm (observed in EM pictures of freeze-substituted bacteria) that led to the periplasmic gel concept: The periplasm was proposed to consist of a compressed, gel-like, viscous, protein-dense matrix that reduced diffusion coefficients two orders of magnitude compared to the cytoplasm (Hobot et al. 1984; Brass et al. 1986; Koch 1998).

Recently, both the osmotic pressure difference over the cytoplasmic membrane, as well as the periplasmic gel concept, has been challenged by new experimental evidence. Cryo-transmission electron microscopy of frozen-hydrated sectioned cells shows that the periplasm is relatively empty compared to the cytoplasm (Matias et al. 2003). The authors suggest that the cytoplasmic membrane has some capacity to float freely in the periplasm. In addition, new, more direct measurements of diffusion coefficients (using GFP) in the periplasm gave values similar to that of the cytoplasm (Mullineaux et al. 2006). Finally, from cytoplasmic and total cell volume measurements it was recently concluded that the cytoplasm and periplasm are iso-osmotic (Cayley et al. 2000). It follows that the turgor pressure is exerted on the outer membrane (this would “explain” the high amount of covalent lipoprotein trimers tethering the OM to the PG cell wall).

The cytoskeleton: FtsZ

FtsZ is a prokaryotic tubulin-homologue (Erickson 1995) which polymerizes into protofilaments (Mukherjee and Lutkenhaus 1994) in a GTP-dependent manner

(RayChaudhuri and Park 1992). Depending on the conditions, FtsZ can polymerize in a wide variety of higher order shapes: straight protofilaments, tubules, double-stranded filaments and curved and/or circular shapes have been reported (see (Horger et al. 2008) for references). Experimental evidence indicates that GDP in between two monomers inside a protofilament can be exchanged with GTP (see (Mingorance et al. 2005) for references). The details of GTP hydrolysis, such as the effect of nucleotide phosphorylation state on the monomer-monomer bond strength and angle (and thus intrinsic curvature) are not fully understood yet. Phosphate release after GTP hydrolysis could cause a conformational change to a more curved shape (Erickson 1997; Lu et al. 2000). It is hypothesized that this can generate force (Lu et al. 2000). However, AFM images of FtsZ in the presence of GTP or in the presence of GDP with aluminum fluoride (an analog of the γ -phosphate of GTP) were observed to be structurally similar (Mingorance et al. 2005).

In vivo, FtsZ filaments localize to mid-cell in a ring, termed the Z-ring (Ma et al. 1996). In EM pictures, it can be seen that FtsZ localizes underneath the leading edge of a constricting cytoplasmic membrane (Bi and Lutkenhaus 1991). Recently, FtsZ from *E. coli* was expressed in fission yeast and found to form rings, suggesting that a cylindrical geometry is enough to cause the helical filaments to condense into a ring (Srinivasan et al. 2008). Z-spirals that condensed into constricting rings were also observed when YFP-tagged FtsZ fused to an amphipathic membrane binding α -helix (originating from the MinD protein), was present in tubular vesicles (Osawa et al. 2008).

Cryo EM images (Li et al. 2007) of *Caulobacter* indicate that the FtsZ ring consists of a few separate, arc-like protofilaments. This does not match with the continuous FtsZ spirals in *E. coli* observed with fluorescence microscopy *in vivo* (Thanedar and Margolin 2004). Furthermore, experiments also show that lateral interactions are important for Z-ring formation (Lan et al. 2008). The location of the Z-ring determines the site of constriction. Interestingly, *in vivo*, an FtsZ mutant that does not condense into a ring but remains spiral also forms spiral invaginations (Addinall and Lutkenhaus 1996). In spherical cells, FtsZ formed arcs that locally constricted the cells. This suggests that complete circumference of the Z-ring is not required for constriction (Addinall and Lutkenhaus 1996). FRAP experiments on GFP-tagged FtsZ have shown that the FtsZ ring is highly dynamic, with a recovery on a second time-scale (Stricker et al. 2002). This is consistent with continuous polymerization and depolymerization. An FtsZ mutant with a 100-fold reduction in

GTPase activity forms stable polymers and surprisingly, supports *in vivo* constriction (Mukherjee et al. 2001). If this is true, then the GTPase activity is not important for its function.

The cytoskeleton: MreB

The actin-homologue MreB forms helical cables in the cytoplasm, just below the cytoplasmic membrane (Jones et al. 2001). MreB cables are dynamic structures as well: it was found that *in vivo*, MreB filaments are ~400 nm in length and exhibit treadmilling, in which monomers are assembled on one end, and depolymerize on the other end (Kim et al. 2006). In the absence of MreB, cell width increases and the cells become more round (Wachi and Matsushashi 1989). Thus, it was concluded that MreB is responsible for the maintenance of constant cell width during growth. Consistent with this idea is the absence of MreB-like genes from *cocci* species (round). However, MreB is also present in cell wall-less species such as *Spiroplasma* (Cabeen and Jacobs-Wagner 2005).

The prevalent view is that treadmilling MreB helical tracks in the cytoplasm guide the PG synthesizing complexes (PBPs) and cause disperse helical insertion of new cell wall material during cell elongation (den Blaauwen et al. 2008). However, in the absence of MreB or Mbl, localization patterns of nascent PG (fluorescently stained) or some PBPs (typically a single bacterial species has ~5-10 different PBPs) are unaltered (Scheffers et al. 2004). Localization by substrate recognition was subsequently proposed to explain the observed PBP localization patterns (Scheffers and Pinho 2005). For a more extensive discussion of this subject see a recent review (Cabeen and Jacobs-Wagner 2007).

PBPs and PG hydrolases: making and breaking bonds in the sacculus

After division of a rod-shaped bacterium such as *E. coli*, first an elongation phase takes place before the next round of division is initiated. This elongation phase was found to consist of two sequential sub-phases: (i) only “diffusive” elongation along the cylindrical sidewalls, followed by (ii) a phase in which, on top of the diffusive elongation, also FtsZ-dependent zonal elongation at mid-cell takes place (de Pedro et al. 1997).

“Diffusive” elongation occurs through insertion of new PG everywhere along the cylindrical part of the cell. As already mentioned, PBPs (penicillin-binding proteins) are the cell’s workers that perform the enzymatic reactions required to synthesize new PG cell

wall, and to maintain the existing cell wall (den Blaauwen et al. 2008). In *E. coli*, as many as 12 different PBPs exist. When 8 of the 12 PBPs were deleted, cells were still viable (Denome et al. 1999). This indicates a very robust wall deposition mechanism.

The new cell wall material (“precursor”) is synthesized in the cytoplasm in a set of sequential enzymatic steps, is then attached to the membrane (“Lipid II”) and translocated to the periplasmic side (by a “flippase” membrane protein (Ruiz 2008)). In the periplasm, PBP’s incorporate the new material into the pre-existing cell wall.

Per cell cycle, 50% of the PG is turned over (Park 1993; Park 1995). As the PG is a covalent structure, and in *E. coli* only a monolayer thick, new PG precursor insertion is thought to require the breaking of bonds. Enzymes that break the covalent bonds in the PG cell wall are called PG hydrolases. However, multiple deletions of PG hydrolases, e.g. all (six) known lytic transglycosylases or all (three) known amidases are viable, and only cell separation appears affected, causing chain formation (Heidrich et al. 2002). Apparently also among the PG hydrolases a large redundancy exists, and the degradation of a cross-linked structure might be performed either by breaking peptide bonds or glycan bonds.

It is tempting to speculate that wall growth in *E. coli* occurs in a similar manner as in *B. subtilis*, i.e. in an inside-to-outside manner, with deposition on the IM side of the PG cell wall, and degradation by PG hydrolases (tethered to the OM) at the OM side of the wall. However, such a discussion is beyond the purpose of this chapter.

Cell division

Here, we discuss the details of the division process in *E. coli*. As mentioned in the introduction (**Chapter 1**), the envelope consists of a thin PG cell wall sandwiched in between two lipid membranes. The inner cytoplasmic membrane surrounds the cytoplasm; the outer membrane is overlaid on the PG cell wall and forms the bacterial cell surface. The outer membrane is an asymmetric bilayer, with the inner leaflet containing lipids and the outer leaflet containing lipopolysaccharide (LPS), a compound with extended sugar chains that are exposed on the cell surface.

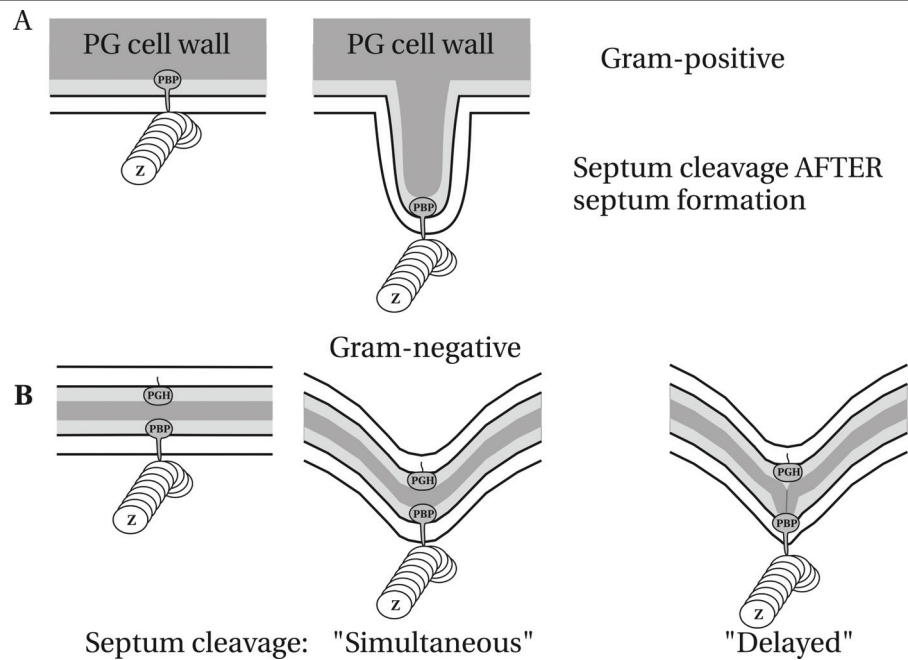


Figure 2.3: Models of cell division in Gram-positive and Gram-negative bacteria. (A) In Gram-positive bacteria, such as *Bacillus subtilis*, a ~20 nm thick cell wall is synthesized (by PBPs) inwards-to-outwards during cylindrical elongation of the cell. During division, wall growth is directed inwards, presumably by a force-generating Z-ring. After completion of the septal plate, PG hydrolases (PGH) subsequently split the septum through the cleavage of molecular bonds. This allows the daughter cells to separate. (B) In Gram-negative bacteria, such as *Escherichia coli*, a ~5 nm thick cell wall is synthesized by the PBPs during cylindrical elongation of the cell. During division, wall growth is directed inwards, presumably by a force-generating Z-ring. Almost simultaneously, PG hydrolases (PGH) cleave the septum. This causes the typical V-shaped septum observed in EM pictures ("simultaneous"). When several PG hydrolases are deleted, cleavage is delayed, and a septum forms that is visible in EM pictures ("delayed").

Rod-shaped bacteria grow by elongation at approximately constant width, and then switch to a "division" mode at mid-cell. In Gram-positive bacteria such as *B. subtilis*, a thick septum (septal plate) is deposited while the Z-ring constricts inwards. Only after the septum is complete do the PG hydrolases cleave the septum to separate the daughter cells (Figure 2.3A).

In contrast, in Gram negative bacteria, all three layers of the cell envelope appear to invaginate simultaneously (Figure 2.3B, "simultaneous"), as judged from EM pictures (Bi

and Lutkenhaus 1991). During division, cell wall addition occurs with a progressively decreasing diameter. This results in the formation of two new polar cell caps, which are approximately hemi-spherically shaped (Reshes et al. 2008). Nevertheless, already in the 1970s experiments indicated that Gram-negative bacteria also form a septum during division (Burdett and Murray 1974). Final proof came when strains lacking particular PG hydrolases were shown to form un-cleaved septa (Heidrich et al. 2001; Holtje and Heidrich 2001; Heidrich et al. 2002) (**Figure 2.3B “delayed”**). The currently held view is that wild-type *E. coli* does form a septum, but cleavage occurs “almost” simultaneously with cell division, resulting in a V-shaped constriction instead of the Gram-positive septal plate. Recent results suggest that the septum consists of 3 or 4 PG monolayers instead of two (assuming a monolayer thickness for the cylindrical cell wall), of which one or 2 layers are degraded as constriction proceeds (Uehara and Park 2008).

What is known about the steps that finally lead to the formation of two daughter cells can be summarized as follows: During septum formation, addition of new PG is thought to occur specifically at the leading edge (Wientjes and Nanninga 1989). On the OM side of the PG layer, PG hydrolases start to cleave the double-layered PG wall, and the layers will separate. Then proteins that tether the OM to the PG move in and make sure that the OM follows the invaginating PG. In highly constricted *Caulobacter* cells (Judd et al. 2005), cryo-EM images show that the distance between IM and OM increased during (late) constriction, from 30 nm to ~ 60 nm. Although the PG layer could not be imaged, it is possible that the septal splitting at the late stage starts to “lag” behind with constriction. At the final stages, the inner membranes fuse, the PG septum closes, and the OM connection is severed (Judd et al. 2005).

Evidence for force-generation by the Z-ring

In biology, non-motor protein elements exist that can generate force by polymerization. An example of a polymerizing structure that can generate forces is a microtubule, which can generate up to several pN of force (Dogterom and Yurke 1997; Janson and Dogterom 2004). Working together, molecular motors such as kinesins that individually can only generate 4-6 pN can pull tubes out of vesicles, which required forces >18 pN (Koster et al. 2003). Not only polymerization, but also depolymerization of microtubules can produce force (Grishchuk et al. 2005). A collection of small (de)polymerizing FtsZ filaments might locally generate similar amounts of force along a concentric circle.

Thus, as soon as was found that FtsZ polymerized into higher order structures (Bramhill and Thompson 1994), models for “active” constriction were proposed (Bramhill 1997). However, since in bacteria, constriction of the cytoplasmic membrane and PG septum formation occur simultaneously, it is difficult to separate cause and effect. For example, one could argue that the observed cell envelope constriction can also be caused by an inward “pushing” of the newly synthesized PG, followed by a dynamic remodeling (decrease in diameter) of the Z-ring. The Z-ring’s function would then be limited to the mid-cell localization of the PG synthesizing complexes (“scaffold function”).

More and more evidence accumulates that the Z-ring actively constricts the cytoplasmic membrane, and that it can do so without simultaneous PG septum formation. For example, FtsZ is highly conserved within the bacterial kingdom, and even bacteria that have no cell wall, such as the *Mycoplasma* species, contain FtsZ (Wang and Lutkenhaus 1996). Furthermore, it has been shown that in a mutant deficient in cell separation (Δ AmiABC), the PG inward growth was stalled, but that in some cells, the cytoplasmic membrane could still be constricted, presumably by the Z-ring (Heidrich et al. 2002) (see **Figure 2.4**). Thus, inward growth of PG is not a prerequisite of Z-ring constriction. Additional evidence that neighboring cells are compartmentalized in these mutant cells with stalled inward PG growth was reported recently using Fluorescence Loss In Photobleaching (FLIP) techniques on cytoplasmic GFP in the chained Δ AmiABC cells (Priyadarshini et al. 2007). Also in *B. subtilis* cytoplasmic membrane invagination could be separated from PG septum formation in a PBP2B (PBP3 in *E. coli*) mutant (Daniel et al. 2000). Recently, it was demonstrated that when FtsZ was mixed with lipids, Z-rings inside tubular vesicles formed, and dependent on GTP hydrolysis, constriction occurred (Osawa et al. 2008). Together, these data suggests that FtsZ by itself can generate a constrictive force.

Modeling the Z-ring

Models can focus on two different aspects of Z-ring mediated division: the actual force-generating mechanism of the Z-ring itself, or the ability of a force-generating Z-ring to drive wall synthesis inwards to form the new polar caps.

For models in the first category several experimental observations need to be taken into account. These are: the (perceived) absence of motor proteins such as myosin or kinesin in bacteria, the dynamic polymerization and depolymerization of the ring, and the

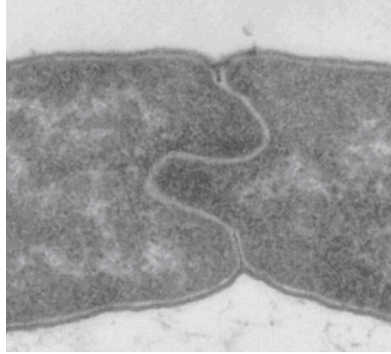


Figure 2.4: Z-ring constriction and septum formation can be uncoupled. EM picture of an *E. coli* mutant from which seven different PG cell wall hydrolases (three amidases, three endopeptidases and one lytic transglycosylase) have been deleted (Heidrich et al. 2002). Incomplete septa are visible that have remained uncleaved for the greater part. Nevertheless, here the cytoplasmic membrane has clearly constricted and even fused. This suggests that the Z-ring can generate force by itself.

ability of Z-arcs to locally constrict. Recently, such a model was formulated (Ghosh and Sain 2008): it assumes that GTP-FtsZ protofilaments prefer to be straight, and GDP-FtsZ protofilaments to have an intrinsic curvature. The authors estimated that the ring could generate a radial contractile force of the order of 0.5 pN/nm. Another model was recently reported (Horger et al. 2008): The model emphasized lateral interactions, in which energetically favored fitting of parallel filaments produces an inward force.

In the second category, also two models have been reported. As discussed earlier, in Gram-negative cells such as *E. coli* and *Caulobacter*, Z-ring constriction and PG growth occur at similar timescales. Therefore, both models combine small constriction forces with PG growth, and show that division can be accomplished this way (Fero et al, Biophysical Society Meeting 2006) (Lan et al. 2007). Fero *et al.* assume a small constant contractile “pressure” (force/area) that induces a deflection on the PG, which combined with the sequential additional of rings of new PG material results in division shapes similar to those observed for *Caulobacter* using Cryo-electron Tomography (Judd et al. 2005). A more comprehensive and detailed model was presented by (Lan et al. 2007). In this work, turgor pressure, as well the elasticity of the cell wall is taken into account. The idea is that the Z-ring slightly changes the wall radius and in doing so establishes the direction in which the new wall is added. To explain how a Z-ring that generates only ~8 pN of force can constrict

the cell, the authors propose that over time, the wall is remodeled by the PBPs (“turnover”) to remove the elastic stresses. This is similar to the concept of “morpho-elastic” materials used to theoretically describe the alteration of equilibrium shapes of plant tendrils and bacterial filaments under externally imposed stresses (Goldstein and Goriely 2006).

Force-induced cell wall shaping

From the experimental results and models on FtsZ, a picture emerges in which the Z-ring generate constrictive force to control the cell shape, in this case the shape of the new cell poles. As no significant differences can be detected in the PG building blocks present in dividing and non-dividing cells using HPLC (de Jonge et al. 1989), this argues for a physical mechanism that controls new cell wall deposition and thus shape.

In a second key experiment, it was found that when cells were restricted in agarose chambers (created by a PDMS mold) and filamentation was induced, cells formed straight filaments until a barrier was hit, after which they slowly adopted the shape of the chamber. After release from the chambers, helical, spiral and zig-zag shaped bacteria were obtained (Takeuchi et al. 2005) (**Figure 2.5**). Astonishingly, the change in shape was not elastic but plastic! This provides indirect evidence that external forces can influence the shape of the cell wall, which is (re-) modeled such that stresses are minimized. Furthermore, the remodeling occurred dispersed throughout the filament, indicating forces are felt throughout the cell, and can affect growth locally.

Shape changes upon growth during confinement have also been observed for fission yeast, which is also rod-shaped with a rigid glycan-based cell wall (Terenna et al, ASCB Meeting 2007). However, whether the shape changes are elastic or plastic is not known yet. It might well be possible that in *E. coli* and fission yeast similar mechanisms work to accomplish cell division. Fission yeast contains an acto-myosin ring that is thought to generate force to “guide” the septation process, and is tightly coupled to septum formation that occurs simultaneously (Vjestica et al. 2008).

The experiment mentioned in the introduction in which cells had rebuild spherical cell walls, actually restored their rod-shape after continuation of growth. If a proper cylindrical cell shape is required as template to maintain this shape, this observation is difficult to explain. Instead, it points to a local mechanism that can restore severely distorted cell shapes. As the turgor pressure is equal in all directions, and PBPs themselves appear “dumb” and just synthesize cell wall where they happen to sit, it is expected that

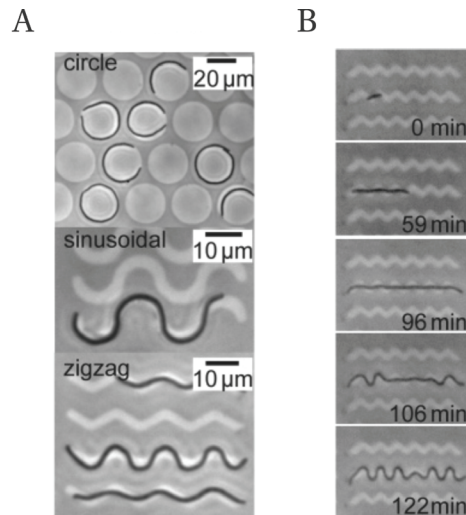


Figure 2.5: External forces can shape a growing bacterium. (A) After constraining *E. coli* cells to micron-sized chambers and inducing filamentation, the growing filaments would adopt the shape of their confining geometry. Releasing the cells from the chambers showed that the cells were not bent elastically, but that the new shape was encoded in their cell walls. (B) Time sequence of a single filament. Only when the filament is constrained end-to-end does the filament shape start to adopt the shape of the chamber. Images reproduced from (Takeuchi et al. 2005).

the default shape is a round cell wall. What brings back and maintains the rod-shape? Or: what generates the forces to maintain the rod-shape? Just as the Z-ring provides the force to direct growth inwards, we can hypothesize that MreB helices provides the inward force to maintain the rod-shape. Local force might be exerted on the growing cell wall that favors a gradual change of cell shape back to rod-shape. Perhaps mechanical forces of MreB exerted on the IM would be responsible for the gradual conversion back to rod-shape. Interestingly, a similar slow process back to rod-shape is observed after MreB is re-expressed in spherical cells depleted from MreB (T. den Blaauwen, unpublished observations).

A recent theoretical study has focused on the polymerization of polymers on curved membranes, with the observed behavior of FtsZ and MreB polymers in mind (Andrews and Arkin 2007). If e.g. MreB binds strongly with one face to the membrane, it can in polymerized form impose its preferred radius on to the membrane, and as such, generate inward force. It will be interesting to polymerize MreB inside model membranes and see

whether cylinders are formed, and which helical period and radius those helices have.

As indicated in **Figure 2.2**, there are at least two ways imaginable in which forces can influence cell wall growth. The forces can displace/relocate the PBPs in the cytoplasmic membrane, in this way controlling the location/direction where new cell wall is deposited (e.g. inwards during division). Alternatively, (small) forces are exerted directly on the PG cell wall, locally creating (small) displacements. Subsequent PG turnover and remodeling then could make these displacements permanent (“morpho-elasticity” (Goldstein and Goriely 2006)).

The experiments that are aimed at in this thesis might be used to distinguish between these alternatives. If the shape is regulated internally by modulating the distance of the (inner membrane) PBP's to the PG cell wall, then we expect that higher forces are needed to influence wall growth when exerting them from the outside. This is because the external force needs to displace the cell wall, whereas the internal force (such as the Z-ring) needs only to displace the cytoplasmic membrane. The latter is expected to require much smaller forces than the former. However, if small displacements are made in the cell wall that are subsequently remodeled to become permanent, then it does not matter if force is exerted on the outside or on the inside.

III

Chapter 3: Differential bacterial surface display of peptides by the transmembrane domain of OmpA

Abstract

We have displayed the highly charged and hydrophilic 3xFLAG and 2xmyc epitopes on the surface of *Escherichia coli* by inserting them in surface exposed loops of the transmembrane (TM) domain of OmpA. These OmpA TM domain variants were examined for their stability and membrane incorporation in vivo. We show that these constructs are incorporated in the outer membrane (OM), and that intact cells can be fluorescently labelled with antibodies against the epitope insertions. However, all suffer from degradation and are present in the cell at approximately 10% of the TM domain concentration without epitope tag inserted. As wild-type OmpA contains an additional C-terminal periplasmic domain, we investigated if addition of this domain would have a beneficial effect on the protein levels of the 3xFLAG variants. Our data demonstrate that this is not the case. In contrast, insertion of a neutrally charged SA-1 peptide in the TM domain of OmpA does not affect protein levels at all. These results suggest an incompatibility of the widely used negatively charged 3xFLAG and 2xmyc epitopes with the biogenesis pathway of OmpA that could have implications for the random selection of peptides displayed on the Gram-negative cell surface.

Introduction

Integral outer membrane proteins (OMPs) are a class of proteins that are embedded in the bacterial outer membrane (OM) as β -barrels. Among these, Outer membrane protein A (OmpA) is a very abundant (typically about 10^5 copies/cell (Koebnik et al. 2000)) and widely studied OMP, and considered a model system for outer membrane insertion (Koebnik 1999; Kleinschmidt 2006). OmpA has four surface exposed loops. In the field of molecular recognition, the OmpA protein has been used as a bacterial surface display system, where combinatorial peptide libraries are displayed on the cell surface via one of its surface exposed loops (Bessette et al. 2004). This allowed high-throughput screening for peptides that bind with high affinity to a desired target. In this way, the authors identified inserted peptides that bind streptavidin with high affinity. Their highest affinity peptide (SA-1) had an equilibrium dissociation constant in the low nanomolar range.

The full-length, processed OmpA protein (325 residues) consists of two domains, a N-terminal transmembrane (TM) domain of 170 residues, connected via a short 19-residue Ala-Pro rich hinge region to a C-terminal periplasmic domain of 136 residues (Chen et al. 1980). The periplasmic domain plays an important structural role in the periplasm, tethering the OM to the peptidoglycan layer (a function shared with Braun's lipoprotein Lpp, and the lipoprotein Pal (for references consult (den Blaauwen et al. 2008))). For a comprehensive review on OmpA structure and function see (Smith et al. 2007).

In vivo, genetically truncated OmpA-171 consisting of only the TM domain assembles into the outer membrane as efficiently as the full-length protein. This has been shown using protease digestion combined with heat-modifiability experiments (Ried et al. 1994). In these experiments, the authors made use of the fact that when isolated cell membranes are treated with proteases (such as trypsin or proteinase K), the periplasmic domain of OmpA is digested, but its TM domain is protected by the outer membrane (Chen et al. 1980).

Our goal was to create an anchoring point on the bacterial cell surface that could act as a handle in biophysical force experiments. Therefore, we have inserted the epitope tags 3xFLAG and 2xmyc into loop 2 and 3 of the transmembrane domain of OmpA, and studied their stability and outer membrane incorporation in vivo. As the cell wall anchoring by the periplasmic domain was unwanted in these experiments, the TM domain of OmpA was

initially used instead of the full-length protein.

We show that these engineered OmpA TM domain variants can be incorporated into the OM, but suffer from degradation, and are present at reduced levels (approximately 10% compared to the TM domain level without epitope insertion). This was unexpected, since it has been shown that similar-sized insertions in loop 2 or 4 did not reduce protein levels at all (Freudl 1989). Since to our knowledge, all *in vivo* loop insertions to date have been made in full-length OmpA, we investigated a possible stabilizing role of the periplasmic domain. Our data demonstrate that the periplasmic domain did not stabilize the 3xFLAG insertion variants. These results suggest an incompatibility of 3xFLAG and 2xmyc tags with the biogenesis pathway of OmpA. The reason for the inefficient display of the 3xFLAG and 2xmyc peptides may be their strong (negative) charges. Using the neutrally charged peptide tag SA-1 we show that it is possible to insert a peptide in the TM domain of OmpA that is expressed at similar protein levels as the TM domain without insertion. Apparently OmpA does not display all small peptides equally efficient, which can have consequences for applications in which OmpA is used as a carrier of randomly generated peptide libraries. Certain peptides would be inefficiently displayed, leading to a bias during the selection process (Lee et al. 2003). Whether these results are specific for OmpA or reflect a more general constraint on surface-exposed loops remains to be established. These results could also be of interest for biotechnological applications based on antigen-displaying *E. coli* cells, e.g. to capture and isolate antibody-displaying phage (Benhar 2001).

Materials and Methods

Bacterial strains and growth conditions

E. coli strains (**Table 1**) were grown at 37°C in TY medium containing 1% Bacto trypton, 0.5% Bacto yeast extract, 0.5% NaCl and 3 mM NaOH. Expression of the constructs was induced by adding up to 1 mM IPTG or 0.02 % L-arabinose, depending on the plasmid vector. Antibiotics were ampicillin (100 µg/ml) or Chloramphenicol (25 µg/ml). LMC500 (MC4100 *lysA*) was made chemically competent using the calcium chloride method. MC1061 and its derivative MC1061 ΔOmpA were transformed using electroporation.

Constructs

All DNA manipulation, analysis and bacterial transformations were performed according to standard protocols (Sambrook et al., 1989). All PCR fragments were sequenced, either at Baseclear (Leiden) or at the AMC DNA sequencing facility (Amsterdam Medical Centre). Primers were ordered from MWG or Biolegio, and Advantage DNA polymerase (Clontech) or *pfuTurbo* DNA polymerase (Stratagene) was used for the PCR reactions. The cloning steps performed to obtain the plasmids are described in the Supplementary Materials and Methods.

Preparation of cell lysates

Fresh overnight cultures grown at 37°C were diluted 1000x into 50-100 ml fresh TY medium and cultured at 37°C. Growth was monitored by measurement of the optical density at 600 nm with a spectrophotometer (Perkin-Elmers). IPTG was added at around an OD₆₀₀ of 0.1, and when the cells reached an OD₆₀₀ of 1.0, they were transferred to a 50 ml Falcon tube and put on ice. The cells were then collected by centrifugation for 15 min at 4000 rpm in a tabletop centrifuge at 4°C (Eppendorf). The supernatant was carefully removed, and the cells were resuspended in ice-cold sonication buffer (10 mM Tris-HCl buffer, pH 7.9, supplemented with 1 mM EDTA and 1 tablet of Roche Protease Inhibitor Cocktail), at a concentration corresponding to an OD₆₀₀ of 250. This cell suspension was transferred to a 2 ml Eppendorf tube, and sonicated on ice with a tip sonicator (Branson) in 4-5 10-second bursts with 10 second cooling in between each burst. Debris and intact cells were pelleted in a 4°C cooled centrifuge at 2700 x g for 2 min. The supernatant was

transferred to a 1.5 ml Eppendorf tube and frozen at -20°C as total cell lysate.

Fractionation of cell lysates

After thawing, the cell lysate was diluted to 4 ml (corresponding to an OD600 of 12.5), and 100 µl of this was saved as “total cell lysate”. The samples were pelleted at 45000 rpm (corresponding to 200.000 x g) for 45 min in an ultracentrifuge (Beckman-Coulter). After centrifugation, 500 µl was saved as “supernatant”. The membrane pellet was resuspended in 100 µl sonication buffer and frozen at -20°C.

SDS-PAGE and Western blotting

For SDS-PAGE, samples were mixed with sample buffer (end concentration: 62.5 mM Tris pH 6.8, 2% SDS, 10% glycerol, 2% 2-mercaptoethanol) and either heated to 99°C for 5 min or heated to 50°C for 15 min and electrophoresed on 15% polyacrylamide slabs. Anti-FLAG and anti-myc monoclonal antibodies used for the immunoblots were obtained from Sigma and Roche, respectively. The polyclonal anti-OmpA antibody was a kind gift from A. Driessen (University of Groningen, Netherlands). The bands were detected using the ECL+ chemiluminescence kit (Amersham) and scanning with a STORM 860 fluorescence imager. Densitometry was performed using ImageJ (<http://rsb.info.nih.gov/ij/>). The mean pixel value of a rectangular region was calculated close but outside a band of interest to calculate the mean background pixel value. The same selection rectangle was positioned to include the band of interest, and again a mean pixel value is calculated. Subtraction then gives a band intensity value. All band comparisons were performed using the same selection rectangle.

Fluorescent labeling of fixed cells

Cells were fixed in 2.8% formaldehyde (FA) and 0.04% glutaraldehyde (GA) in growth medium for 15 min at room temperature, then washed and resuspended in PBS (140 mM NaCl, 27 mM KCl, 10 mM Na₂HPO₄·2H₂O, 2 mM KH₂PO₄ pH 7.2). Cell concentration was adjusted to an OD600 of 0.6 and samples were incubated in 75 µl PBS containing 30 mg/ml BSA to block non-specific sites on the cell surface for 30 min at 37°C. Then antibodies were added, either anti-FLAG (M2, Sigma) or anti-myc (9E10, Roche) at an end concentration of 20 µg/ml, and samples were incubated at 37°C for 30 min. The cells were washed 3 times with 2 volumes of PBS containing 30 mg/ml BSA, and then incubated in 1 volume with

Donkey-anti-Mouse-Cy3 conjugate (Jackson ImmunoResearch) at 10 $\mu\text{g/ml}$ end concentration for 30 min at 37°C, washed 3 times with 2 volumes PBS and imaged.

Fluorescent labeling of living cells

Cells were put on ice, and an amount of cells equivalent to 1 ml OD600 of 0.3 (around $2 \cdot 10^8$ cells) was taken for labeling. Cells were collected in all cases by centrifugation at $20.000 \times g$ for 5 min at 4°C. The pellet was resuspended in 75 μl PBS at room temperature (RT) with 0.1% BSA. The cells are left at RT for 10 min to block aspecific sites on the cell surface. Then either biotinylated anti-FLAG (Sigma) was added (50 $\mu\text{g/ml}$) (FLAG constructs), or streptavidin-Alexa 488 (Molecular Probes) was added directly (40 $\mu\text{g/ml}$) (SA-1 constructs). Cells were incubated at RT for 30 min. The cells were spun down and washed twice with 0.5 ml PBS, and resuspended in 150 μl PBS. For the cells labeled with biotinylated FLAG, streptavidin-Alexa 546 (Molecular Probes) was added (5 $\mu\text{g/ml}$), and samples were incubated for 30 min at RT. Then, PBS (0.85 ml) was added and the cells were pelleted. After a second wash with 0.5 ml PBS, the cells were fixed in 1 ml PBS with 2.8% formaldehyde and 0.042% glutaraldehyde, washed in 1 volume of PBS and resuspended in 0.1 volume PBS. The cells were either imaged directly or stored at 4°C over night before imaging.

Fluorescence Microscopy

Cells were immobilized on 1% agarose in water slabs-coated object glasses as described by (Koppelman et al. 2004) and photographed with a CoolSnap *fx* (Photometrics) CCD camera mounted on an Olympus BX-60 fluorescence microscope through a UPLANFL 100x/1.3 oil objective (Japan). Images were taken using the public domain program Object-Image2.19 by Norbert Vischer (University of Amsterdam, <http://simon.bio.uva.nl/object-image.html>), which is based on NIH Image by Wayne Rasband. In all experiments the cells were first photographed in the phase contrast mode. Then a fluorescence image was taken using either a green excitation/red emission (U-MNG, ex. 530–550 nm), or a blue excitation/green emission filter cube (U-MNB or EGFP, ex. 470–490 nm).

Differential surface display of peptides

Strains	Genotype	Reference
LMC500 (MC4100 <i>lysA</i>)	<i>F⁻, araD139, Δ(argF-lac)U169, deoC1, flbB5301, ptsF25, rbsR, relA1, rpsL150, lysA1</i>	(Taschner et al. 1988)
MC1061	<i>F⁻, araD139, Δ(ara-leu)7696, ΔlacX74, galU, galK, hsdR2 (r_k- m_{k+}), mcrA0, mcrB1, rpsL, spoT1</i>	(Casadaban and Cohen 1980)
MC1061 Δ OmpA	MC1061 Δ OmpA	(Besette et al. 2004)
DH5 α	<i>F⁻, endA1, hsdR17(r_k- m_{k+}), supE44, thi-1, recA1, gyrA, relA1, Δ(lacZYA-argF)U169, deoR, Φ80 lacZΔM15</i>	Lab collection
DH5 α -Z1	DH5 α <i>LacI_q⁺ TetR⁺</i>	(Lutz and Bujard 1997)
Plasmids	Proteins expressed	Reference
pMD005	pTHV037 OmpA-177	This work
pGV1	pTHV037 OmpA-177 2xmyc in Loop 2	This work
pGV2	pTHV037 OmpA-177 3xFLAG in Loop 2	This work
pGV3	pTHV037 OmpA-177 2xmyc in Loop 3	This work
pGV4	pTHV037 OmpA-177 3xFLAG in Loop 3	This work
pGI9	pTHV037 OmpA-LEDPPAEF	This work
pGI6	pTHV037 OmpA-LEDPPAEF containing 3xFLAG in Loop 3	This work
pB33OmpA14-SA1	pBAD33 OmpA SA-1 in Loop 1	(Besette et al. 2004)
pGV28	pTHV037 OmpA-177-SS SA-1 in Loop 1	This work
pGV32	pTHV037 OmpA-LEDPPAEF 3xFLAG in Loop 2	This work
pGV33	pTHV037 OmpA-LEDPPAEF SA-1 in Loop 1 OmpA-177	This work
pTHV037	pTRC99A with a weakened IPTG inducible promoter	(Den Blaauwen et al. 2003)

Table I. All strains and plasmids used for this study.

Results

Design of loop insertions

A topology model of the transmembrane domain of OmpA is shown in **Figure 3.1**. For locations in loop 2 and loop 4 (after Y63, G70 and I153 respectively), it has been shown that small (up to 21 residue) peptides can be inserted without any reduction in protein levels (Cole et al. 1983; Freudl 1989) and membrane incorporation (after G70 and I153, (Freudl 1989)). For loop 2, reported inserted peptides are listed in **Table II**. Initially, we used only the OmpA TM domain, but later also the periplasmic domain was added. 3xFLAG and 2xmyc peptides were chosen as epitope tags (**Table II**). We will refer to them as FLAG and myc from now on. High-affinity monoclonal antibodies are commercially available for these epitopes. SWISS-Model (Guex and Peitsch 1997) was used to predict OmpA folding after peptide insertion. First, a continuous model was generated of the first 176 residues, based on the published crystal structures of OmpA-171 (**Figure 3.S1A**). Then, models were generated of loop insertions after different residues in the protein, and the resulting (static) loop conformations were examined for their propensity to extend away from the

Name	Target	Loop	AA	Sequence	-/+ Charge	Reference
8 AA	pronase	L2	8	NWLGRMPY	0/1	(Cole et al. 1983)
21 AA	proteinase K	L2	21	AGMQAYRIRA RYPGILFSRPA	0/4	(Freudl 1989)
3xFLAG	mAb M2	L2/3	22	DYKDHDG-DYKDHDH- DYKDDDDK	-11/4	This study
2xmyc	mAb 9E10	L2/3	20	EQKLISEEDL EQKLISEEDL	-8/2	This study
SA-1	Streptavidin	L1	15	RLEICQNVCYYLGTL	-1/1	(Bessette et al. 2004)

Table II. OmpA peptide insertions in loop 2 as reported in literature, and the insertions that are described in this study.

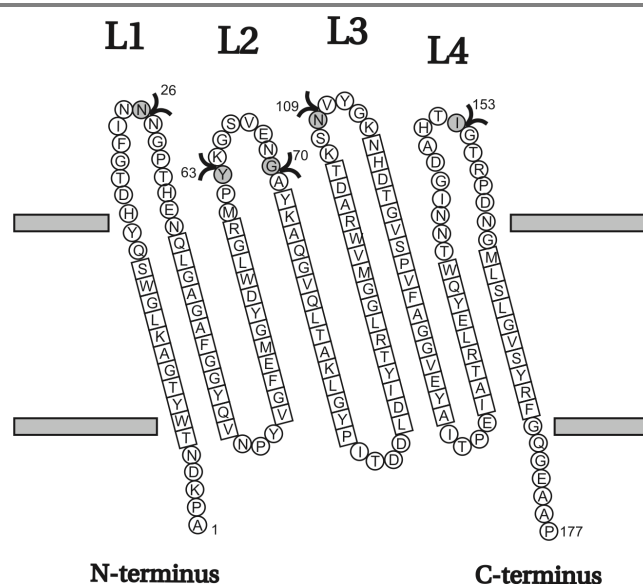


Figure 3.1. Topology model of the TM domain of OmpA (OmpA-177) (adapted from (Pautsch and Schulz 1998)). Black arrowheads indicate positions where peptides have been inserted: after N26 (Bessette et al. 2004) and this study, Y63 (Cole et al. 1983), G70 (Freudl 1989) and this study, N109 this study, and I153 (Freudl et al. 1986; Freudl 1989). Residues present in beta-strands are indicated with squares. Other residues are presented as circles.

membrane normal axis. Models were generated of insertions in loop 2, 3 and 4. Finally, loop 3 was chosen, since the computer-generated model of an inserted FLAG peptide after N109 predicted the largest distance away from the surface (**Figure 3.S1C**).

To be able to compare the performance of our constructs with results reported in literature, we also constructed loop 2 insertions with the FLAG and myc epitopes. For loop 2, insertions after G65, G70, Y72 and Q75 were modeled. In the end G70 was chosen, because (a) as mentioned, it was shown that at this location, a 21-residue peptide could be inserted without any negative effects on membrane insertion (Freudl 1989), and (b) modeling with SWISS-Model of these four locations predicted that at G70, the loop would be extended away from the surface more than at the other three positions in loop 2 (**Figure 3.S1B**).

During the course of this work, a loop 1 peptide insertion in full-length OmpA was described in the literature (Bessette et al. 2004). The position of the insertion is indicated

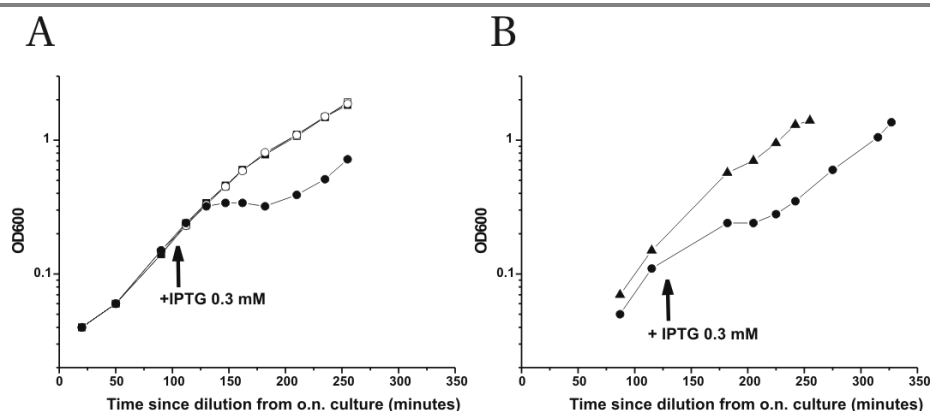


Figure 3.2. A FLAG insert in loop 2, but not in loop 3, causes a lag phase upon overexpression in LMC500. Shown are growth curves of OmpA-177 variants with and without induction with IPTG. Cultures grown over night at 37°C were diluted 500 times in fresh TY medium. At an OD₆₀₀ of 0.2, IPTG was added to a final concentration of 0.3 mM when indicated. A) Open squares represent control cells harboring an empty plasmid (THV037). Filled squares: same as open squares but now with IPTG added. Open circles represent cells that express OmpA-177 with a FLAG insertion in loop 2. Filled circles: same as open circles but now with IPTG added. B) Filled circles represent cells that express OmpA-177 with a FLAG insertion in loop 2 with IPTG added. Filled triangles represent cells that express OmpA-177 with a FLAG insertion in loop 3 and IPTG added.

in **Figure 3.1** (after N26). As mentioned in the introduction, the SA-1 peptide tag (listed in **Table I**) binds streptavidin directly with high affinity. Since this peptide was neutrally charged and could be conveniently labeled with fluorescent streptavidin, we decided to compare this loop insertion variant with our constructs. Therefore, it was cloned into our expression vector, both as a truncated TM domain and as a full-length protein, and assayed in the same way as the FLAG/myc insertions.

Growth of cells expressing OmpA-177 loop insertion proteins

The constructs were tested for expression in LMC500 (MC4100 *lysA*), a well characterized wild type strain (Taschner et al. 1988; Peters et al. 2003), MC1061 Δ OmpA (Bessette et al. 2004), an OmpA knockout strain, and in its parental strain MC1061 (Casadaban and Cohen 1980). To test to what extent the proteins could be expressed without affecting the growth rate, the growth was followed by measuring the optical density before and after addition of

the inducer IPTG. Growth curves from a typical experiment are shown in **Figure 3.2A**. In this experiment, cells carrying an empty vector were compared with cells expressing an OmpA-177 protein with a FLAG insertion in loop 2. Without IPTG induction, all growth curves appear identical. Approximately 15 minutes after addition of IPTG however, the OmpA-177 protein with a FLAG insertion in loop 2 shows a lag phase where growth stops for approximately 30 min, after which growth continues normally. Addition of IPTG did not affect the growth rate of the control cells carrying an empty vector. In **Figure 3.2B**, growth curves from a second experiment are shown where induction of two TM domain variants, a FLAG insertion either in loop 2 or loop 3, are compared. For the loop 3 insertion, after induction with IPTG no lag phase is observed and the growth curve is similar to the growth curve of uninduced cells (**Figure 3.2A**).

The induction experiment was performed for all the OmpA TM domain variants and the results are listed in **Table III**. It can be concluded that in strain LMC500, induction of the loop 2 (FLAG/myc), and to a lesser extent, the loop 1 (SA-1), but not the loop 3 (FLAG/myc) insertions caused a lag phase of 30-60 min after which growth continued normally. Surprisingly, this lag phase was absent both in MC1061 and in MC1061ΔOmpA. Induction with 0.3 mM IPTG of the loop 2 (FLAG), or loop 1 (SA-1) in these strains had no effect on the growth rate at all. Because in LMC500 and MC1061, similar expression levels were detected on immunoblots, it appears that strain MC1061 and its derivative

Construct	Peptide	Location	Growth after induction	Mass on PAGE/blot (kDa)
MD005	none	NA	++	19
GV2	3xFLAG	loop 2	--	25
GV4	3xFLAG	loop 3	+	25 and 27
GV1	2xmyc	loop 2	--	25
GV3	2xmyc	loop 3	+	25 and 27
GV28	SA-1	loop 1	-	21

Table III Growth and molecular mass as detected on immunoblot after induction with 0.3 mM IPTG of LMC500 expressing OmpA proteins with loop insertions. "Growth after induction" indicates the presence and extent of a lag phase after adding inducer (++ no lag phase, -- strong lag phase).

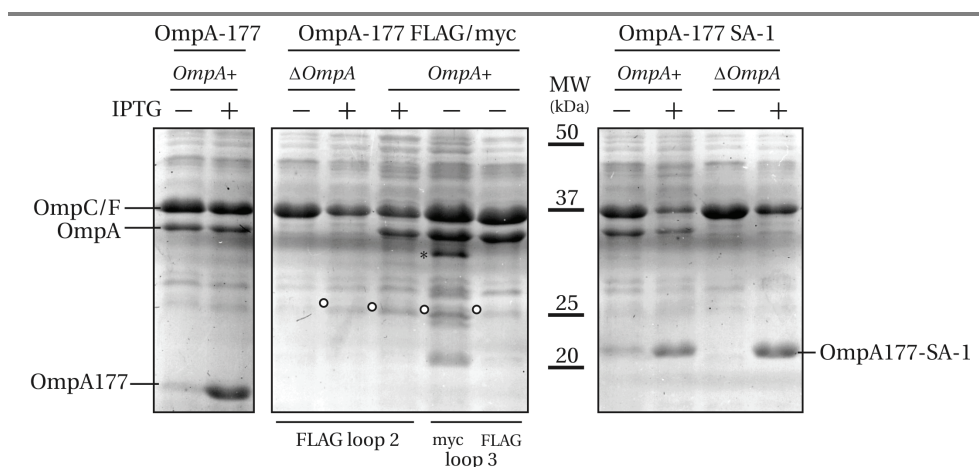


Figure 3.3. OmpA-177 TM domain variants containing FLAG or myc, but not SA-1 are present at reduced levels. Shown is a Coomassie stained 15% SDS-PAGE containing membrane fractions. Fractions corresponding to 1 ml OD₆₀₀ of 0.625 cells were loaded. IPTG was either absent (-), or added during exponential growth at an end concentration of 0.3 mM (+). Membrane fractions were isolated both from LMC500 (OmpA+) and MC1061 Δ OmpA. Open circles indicate the expected position of the FLAG and myc variants as determined from immunoblotting (e.g. Fig. S3). The asterisk indicates an unknown band that did not react with anti-myc on immunoblot. The positions of the OmpC/OmpF band, as well as the endogenous OmpA band are indicated.

MC1061 Δ OmpA are more able to cope with the perturbation caused by the induction (see also discussion).

Expression of OmpA-177 loop insertion proteins

Samples, harvested at the end of the induction experiment described above were analyzed by SDS-PAGE and immunoblotting. For the FLAG and myc constructs, a blot is shown in **Figure 3.S2**. Based on the immunoblots it was clear that all four variants were expressed, no degradation bands were observed, and all ran at a similar height that was retarded with respect to their calculated molecular weight (approx. 3-4 kDa). This was also observed for full-length constructs that carried a FLAG insertion (see below). The reduced mobility on gel was attributed to the high amount of negative charge in the FLAG and myc peptides. Unexpectedly, unprocessed (precursor) proOmpA-177 was also detected in uninduced samples as well as in induced samples expressing either FLAG or myc in loop 3 (see also **Figure 3.S3**). The difference in expression levels between induced and uninduced samples was a factor 2-5 fold (all protein levels were determined from immunoblot by densitometry

using ImageJ, data not shown). Without induction, for FLAG as well as myc, about 25% of the loop 3 constructs detected were not processed.

Induced OmpA-177 without loop insertion was directly visible on a Coomassie Brilliant Blue (Coomassie) stained SDS-PAGE (see Figure 3) and could be detected on immunoblot using a polyclonal antibody against OmpA, but the band was very weak compared to endogenous (full-length) OmpA (data not shown). From this, we conclude that this polyclonal antibody primarily recognizes the periplasmic domain of OmpA. Also, an attempt was made to detect the streptavidin binding peptide SA-1 construct on blot using a Streptavidin-HRP conjugate, but only the endogenous cytoplasmic biotinylated biotin carrier protein BCCP was detected (data not shown). Apparently, streptavidin does not bind sufficiently strong to the denatured conformation of SA-1.

To be able to directly compare the amounts of protein in the membrane, membrane fractions were isolated of cells expressing the various OmpA TM domain variants (**Figure 3.3**). Induction of both OmpA-177 and OmpA-177 SA-1 constructs resulted in strong bands at roughly their expected height (calculated MW of OmpA-177 is 19.3 kDa and of OmpA-177 SA-1 is 21.1 kDa). Surprisingly, no bands could be identified that corresponded to the FLAG or myc constructs.

To determine how much of the expressed construct is present in the envelope fractions put on gel, we compared soluble (S) to membrane (M) fractions. Although not visible on a Coomassie stained gel, immunoblots of the fractions showed that the FLAG and myc constructs were present, and fractionated predominantly to the membrane fraction (**Figure 3.S3**). We conclude that these constructs are present in the cell at greatly reduced amounts (less than 10% as judged from the Coomassie stained gel) compared to wild type OmpA-177 or the OmpA-177-SA1. This could either be due to a reduced synthesis rate (not expected for FLAG and myc tags), due an increased degradation rate (see also below) or both.

Role of the periplasmic domain

To our knowledge, all OmpA loop insertions reported in the literature have been made in full-length OmpA. To establish whether the periplasmic domain might play a role in preventing a reduction in protein levels after FLAG or myc insertion in the transmembrane domain, full-length constructs were made for the FLAG epitope in loop 2 and 3, and the SA-1 insertion in loop 1. These constructs were transformed to LMC500 and MC1061

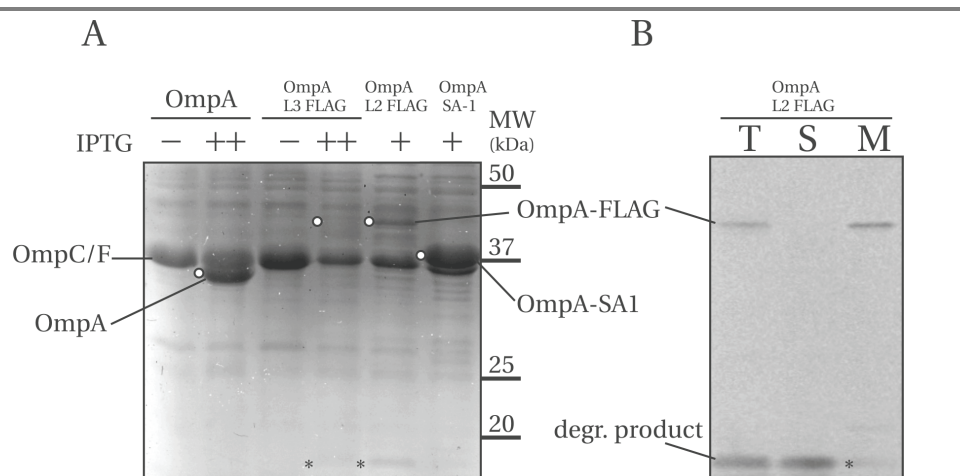


Figure. 3.4. The periplasmic domain does not stabilize the TM domain and FLAG constructs are degraded. Left panel: Coomassie stained 15% SDS-PAGE. Membrane fractions corresponding to 1 ml OD₆₀₀ of 0.625 cells were loaded. IPTG was either absent (-), or added during exponential growth at an end concentration of 0.3 mM (+), or 1 mM (++). Envelopes were isolated from MC1061ΔOmpA. Open circles indicate the position of the expressed constructs. The position of the OmpC/F band is indicated. The asterisks indicate a degradation band that reacted with anti-OmpA. Right panel: full-length OmpA with a loop 2 FLAG insertion induced with 0.3 mM IPTG, fractionated in total, soluble and membrane fraction. The immunoblot was probed with anti-OmpA (1:10000). The large degradation band at around 17 kDa is clearly visible, and was almost completely soluble. The strain was MC1061ΔOmpA.

ΔOmpA and were subjected to the same induction experiment as for the OmpA TM domain variants. Without induction, all full-length constructs grew normally in both genetic backgrounds. After induction, the growth rate remained unaffected for all full-length OmpA loop insertion constructs in the MC1061 ΔOmpA background whereas expression in LMC500 resulted in growth curves similar to those obtained for the OmpA-177 constructs (only tested for the loop 3 FLAG insertion).

The full-length constructs were detected both on Coomassie stained gel (**Figure 3.4A**) as well as on immunoblot using a polyclonal antibody that recognizes the periplasmic domain of OmpA (**Figure 3.4B, Figure 3.S4**). As with the FLAG OmpA-177 proteins, full-length OmpA FLAG constructs had a higher apparent molecular weight than calculated. Comparing soluble to membrane fractions using immunoblots yielded similar results as for the OmpA-177 variants, with the majority of each construct fractionating to the membrane fraction, except loop 3, which was divided over the soluble and membrane

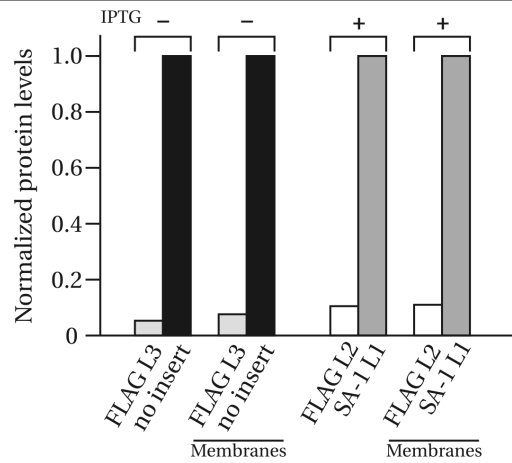


Figure 3.5. FLAG insertions, either in Loop 2 or 3, are present at approx. 5-10% relative to either the full-length OmpA without insertion or the full-length OmpA with a SA-1 insertion in Loop 1. The levels were quantified from immunoblots by densitometry using ImageJ and are normalized relative to the stronger band. Both total cell lysates and membrane fraction were quantified. For 3xFLAG in Loop 3, compared with full-length OmpA without insertion, no IPTG was added. For 3xFLAG in Loop 2, compared with SA-1 in Loop 1, constructs were induced with 0.3 mM IPTG.

fraction (**Figure 3.S4**).

Again, the FLAG constructs appear greatly reduced compared to both the OmpA without insertion and the OmpA with an SA-1 insertion, all expressed from plasmid. The intensities of the anti-OmpA bands from **Figure S4** were quantified using ImageJ and plotted as bar graphs in **Figure 3.5**. Together with **Figure 3.4A**, it can be concluded that full-length OmpA constructs with FLAG insertions either in loop 2 or loop 3, are present at approximately 5-10% compared to full-length OmpA without insertion or the full-length OmpA carrying a SA-1 insertion, respectively.

Apart from intact construct, the immunoblots probed with anti-OmpA antibody revealed a strong band around 17 kDa (the expected size of the periplasmic domain) that fractionates to the soluble fraction (**Figure 3.4B**). This band was absent from samples containing induced full-length OmpA without insertion and weakly detected in induced full-length OmpA with the SA-1 insertion (data not shown). From this we conclude that the degradation band is specific and that it is related to the reduced protein levels of the FLAG constructs. In addition, the FLAG constructs were detected using anti-FLAG antibody (**Figure S4** and not shown). The 17 kDa degradation band did not react with anti-FLAG (the

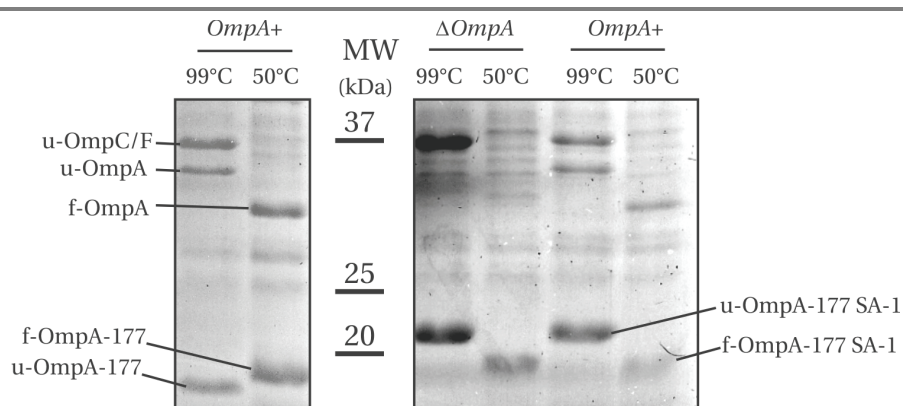


Figure 3.6. The OmpA TM domain constructs OmpA-177 and OmpA-177 SA-1 are fully heat modifiable. A Coomassie stained gel containing membrane fractions (corresponding to 1 ml OD₆₀₀ of 0.625 cells) from cells expressing either OmpA-177 or OmpA-177 SA-1 constructs induced with 1 mM (OmpA-177) or 0.3 mM (OmpA-177 SA-1) IPTG, either in LMC500 (OmpA+) or MC1061 Δ OmpA. The samples were either heated in sample buffer for 5 min at 99°C or for 15 min at 50°C. Folded proteins are prefixed with f- and unfolded proteins are prefixed with u-.

smallest degradation band detected with anti-FLAG ran around 27 kDa). Apparently, the periplasmic domain of OmpA was cleaved from the TM domain and the latter was to a large extent degraded.

Taken together, it can be concluded that both the full-length and the OmpA-177 constructs with a FLAG insertion are present in greatly reduced amounts, compared to without insertion or with a SA-1 insertion. Therefore, addition of the periplasmic domain does not improve protein levels of the FLAG insertion. Furthermore, the reduction in protein levels is, at least partly, caused by degradation, as observed on immunoblots.

OM incorporation of truncate and full-length constructs

To study whether the OmpA variants, present in the membrane fraction, have obtained their native form, we examined their heat-modifiability. The native form of the OmpA TM domain is a compact β -barrel that has a particularly tight fold with a half life of 30 min when heated to 72°C in 2% SDS (Koebnik 1999). When heated in SDS at lower temperatures (e.g. 50°C) the β -barrel becomes soluble without unfolding and migrates faster through the gel (30 kDa) relative to its denatured form, which runs at the expected molecular weight (35 kDa). This effect is called heat modifiability (Reithmeier and Bragg 1974) and it is a general property of β -barrels. Various techniques have been used to

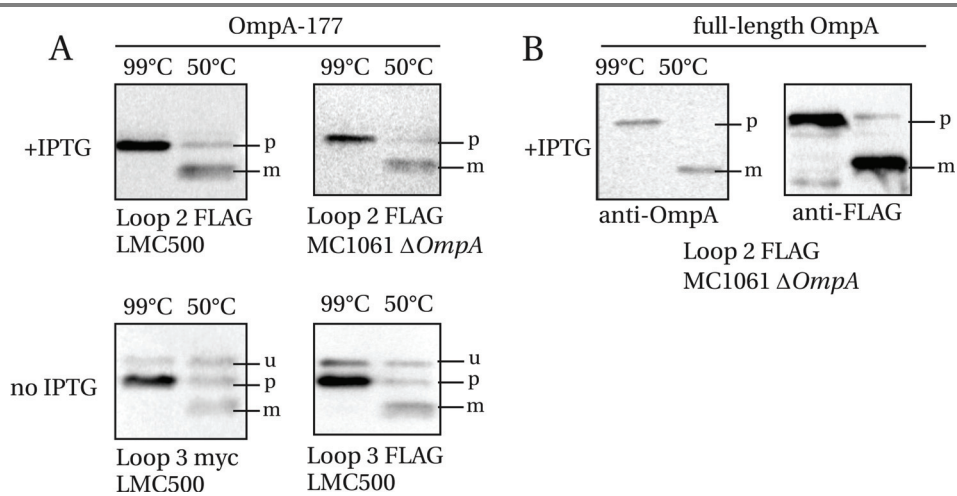


Figure 3.7. OmpA-177 domain variants with FLAG or myc epitopes and a full-length OmpA variant with a FLAG epitope are predominantly heat-modifiable. Cell envelopes of various OmpA-177 TM domain variants (**A**) and the full-length Loop 2 FLAG construct (**B**) were either heated in sample buffer for 5 min at 99°C or for 15 min at 50°C, before being separated on a 15% SDS-PAGE and immunoblotted. Indicated are: (p) processed, unfolded, (m) matured, properly folded and (u) unprocessed, unfolded. In (A) 0.1 μ g/ml anti-FLAG was used for the induced Loop 2 construct, and 1 μ g/ml anti-myc and 0.5 μ g/ml anti-FLAG were used for the uninduced Loop 3 constructs. In (B), 1:10000 anti-OmpA, and 0.1 μ g/ml anti-FLAG was used.

confirm that the 30 kDa form corresponds to the native fold of OmpA (for references consult (Arjara 2007)). It is generally assumed that in vivo, the native form of OmpA is generated only after proper insertion into the outer membrane (Ried, 1994).

Cell membranes containing IPTG-induced OmpA-177 or OmpA-177 SA-1 proteins, expressed in LMC500 or MC1061 Δ OmpA were either heated in sample buffer for 5 min at 99°C or for 15 min at 50°C, then applied on gel, separated by SDS-PAGE and stained with Coomassie (**Figure 3.6**). Note that both OmpC and OmpF do not become soluble at 50°C and are therefore only visible in samples heated at 99°C (Ried et al. 1994). As expected, the endogenous OmpA of LMC500 is fully heat-modifiable. Furthermore, the OmpA-177 protein, but not the OmpA-177 containing the SA-1 insertion, shows the aberrant heat-modifiability already observed in the literature for OmpA-171 (Ried et al. 1994), where the folded protein migrates slower than the unfolded protein (see also discussion). Finally, the OmpA-177 SA-1 protein is also fully heat-modifiable. We conclude that the majority, if not all, of both constructs have reached their native form.

For the FLAG and myc constructs, because of their low levels in the cell, immunoblotting was used to visualize their heat-modifiability (**Figure 3.7**). The OmpATM domain constructs with FLAG or myc are all predominantly heat-modifiable (**Figure 3.7A**, indicated “mature”). As expected, the loop 3 precursor bands (indicated “unprocessed”), present in the membrane fraction, are not at all heat-modifiable. Also a full-length OmpA construct carrying a loop 2 FLAG insertion was found to be fully heat-modifiable (**Figure 3.7B**). We conclude that all FLAG and myc constructs are at least partially heat-modifiable, and thus can be properly incorporated in the outer membrane.

Surface display of loop insertions: fluorescent labeling of cells

To determine the accessibility on the cell surface of the inserted antigenic peptides, both fixed and living cells were labeled. Cells carrying the FLAG and myc in either loop 2 or 3 of OmpA-177 were induced with 0.3 mM IPTG, fixed and stained with monoclonal anti-FLAG or monoclonal anti-myc. As a negative control, the primary antibody was left out, and no fluorescence was observed for any of these samples. All four constructs were detected on the bacterial cell surface (**Figure 3.S5**). Loop 2 insertions show more staining at the poles, whereas loop 3 insertions are more homogeneous.

Living cells were labeled using a biotinylated variant of the anti-FLAG antibody. Labeling of living cells was performed because it was found that fluorescent streptavidin (needed for the SA-1 peptide) penetrated fixed cells to show a nucleoid-like staining (data not shown). The cells could be fixed after labeling to preserve the staining.

Results of labeled, uninduced cells carrying either OmpA-177 FLAG (loop 3) or the full-length OmpA-FLAG (loop 3) showed that both have comparable levels of antibody-accessible FLAG epitope on their surface (**Figure 3.8A, B**). This provides further evidence that adding the periplasmic domain does not result in increased stability of the protein. The limited increase in fluorescence after induction correlates with a modest increase of intact protein, and a larger increase of the 17 kDa degradation band as detected on immunoblot (data not shown).

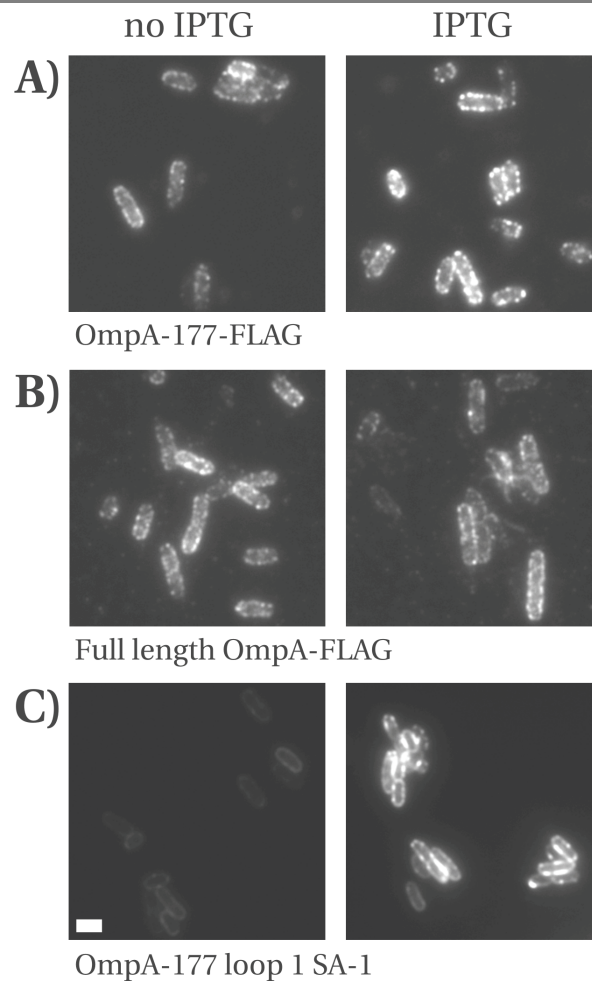


Figure 3.8. Fluorescently labeled cells expressing (A) FLAG in loop 3 of OmpA-177, (B) FLAG in loop 3 of OmpA (full-length), or (C) SA-1 in loop 1 of OmpA-177. Cells were grown in TY medium either without IPTG or with 0.3 mM IPTG added and induced for 2 hours before labeling. Exposure times: (A, B) 1 s, (C) 150 ms. Strain was LMC500. Scale bar dimensions are 1 by 2 μ m.

Finally, living LMC500 cells expressing OmpA-177-SA1 were directly labeled with fluorescent streptavidin, fixed and imaged (**Figure 3.8C**). To be able to compare with and without induction directly, a short exposure time (150 ms) was chosen. Without induction staining was homogeneous along the perimeter of the cells. After induction (and after recovery from the lag phase that occurs in LMC500, see earlier), fluorescence increased markedly, and during labeling, strong streptavidin-mediated cross-linking between cells

occurred, leading to clumps. Overall, we conclude that all the constructs are detected on the cell surface, but for FLAG, and likely also myc, the increase after induction is reduced due to degradation, whereas for SA-1, both efficient labeling and a strong effect of induction on the surface display is observed.

Discussion

Reduced protein levels of FLAG or myc loop insertions in OmpA

In this work we have characterized peptide insertions in the OmpA protein, both in TM domain constructs (OmpA-177) and full-length constructs. As insertions we used the popular FLAG and myc epitopes, and a streptavidin binding peptide SA-1. It has been demonstrated that small (up to 21-residue) peptides could be inserted in loop 2 of OmpA without reduction in protein levels or membrane incorporation (Cole et al. 1983; Freudl 1989). Unexpectedly, introducing a FLAG or myc peptide at this location in the OmpA protein reduced the protein levels with approximately 90% (**Figure 3.3**, **Figure 3.5**). However, the majority of the intact protein was inserted properly in the OM, as judged by its heat-modifiability (**Figure 3.7A**). In contrast, insertion of the SA-1 peptide in loop 1 did not reduce protein levels, similar to the reported insertions in loop 2 (**Table II**).

It could be argued that the observed differences are due to over-expression of the proteins. However, our expression vector (a weakened pTrc99A (Den Blaauwen et al. 2003)) produces less than $5 \cdot 10^3$ proteins in the absence of IPTG (Aarsman et al. 2005), and already at these low expression levels the marked difference in protein level between OmpA with a FLAG insertion and OmpA without insertion is observed (**Figure 3.5**). This suggests that introducing the FLAG epitope leads to an intrinsically reduced protein level, independent of the induction level.

What could be the reason of the observed reduction in protein levels of the FLAG and myc constructs? Since both the FLAG and myc epitopes are effectively negatively charged (**Table II**), they might interact unfavorably with the negatively charged LPS in the OM, or with the Omp85 protein complex responsible for OM insertion (Bos et al. 2007). We speculate that a reduced rate of OM incorporation might cause a buildup of unincorporated (misfolded) OmpA proteins, whose subsequent degradation would explain the reduced cellular levels of the FLAG and myc constructs reported here.

Unexpectedly, in exponentially growing cells without IPTG, about 25% of the loop 3 insertions are not processed. Since OmpA is mostly post-translationally translocated to the periplasm via the Sec system (Eisner et al. 2003), for the loop 3 construct perhaps some

tertiary structure forms in the cytoplasm that delays, or interferes with, its translocation (Mitra et al. 2006). However, induction of constructs with FLAG in loop 2 or loop 3 results in similar amounts of processed OmpA (**Figure 3.S2**), and in similar amounts of FLAG epitope detected on the bacterial surface (**Figure 3.S5**). This suggests that after processing and release into the periplasm, both proteins behave in a similar way.

Overexpression of engineered OmpA variants in LMC500 versus MC1061

Surprisingly, induction of either (FLAG or myc) loop 2 constructs or the OmpA-177-SA1 in LMC500 (MC4100 *lysA*) affects growth rate profoundly. It is difficult to understand that loop 2 FLAG/myc and loop 1 SA-1 constructs cause a similar effect on growth rate in LMC500, since their amounts differ 10-fold. Perhaps the cell regulates the amount of proteins in the OM that are tolerated (little in the case of FLAG/myc, a lot in the case of SA-1). When IPTG induction disturbs this balance, the observed lag period of 30 min might reflect a period in which the cell adapts and restore this balance, after which the cells continue growth.

Accumulation of misfolded OMPs in the cell envelope causes the activation of the σ^E controlled extracytoplasmic stress response (Hasselblatt et al. 2007) that down-regulates OMP expression ((Rhodius et al. 2006)). Indirect evidence for σ^E activation upon IPTG induction of our OmpA loop insertion variants comes from the membrane fractions shown in **Figures 3.3** and **3.4**, where OMP expression (OmpC/F and OmpA) is consistently down-regulated after IPTG induction, but only for loop insertion variants.

In the different genetic background of strain MC1061 and its derivative MC1061 Δ OmpA, expression levels were similar to LMC500, but the growth rate was unaffected upon IPTG induction (data not shown). It has been shown that the σ^E transcription factor is also controlled by intracellular ppGpp levels (Costanzo and Ades 2006). MC1061 has the *spoT1* mutation, that abolishes the ppGppase activity of SpoT and results in increased levels of (p)ppGpp (Cashel, 1996). This could offer an explanation for the observed robustness of MC1061 towards overexpression of the OmpA loop insertion constructs. If MC1061 is better able to cope with folding stress in the periplasm (e.g. by having its stress response genes already expressed, or in higher levels), the balance can be restored immediately, without disturbing the growth rate. Whatever the molecular mechanism may be, our results indicate that MC1061 is a strain of choice when overexpressing engineered

outer membrane proteins such as OmpA.

“Aberrant” heat-modifiability versus normal heat-modifiability

Finally, our results provide insight on the aberrant heat-modifiability observed for 8-stranded β -barrels such as OmpA-171, OmpA-177 and NspA (Vandeputte-Rutten et al. 2003). Heat-modifiability is termed “aberrant” when the unfolded form migrates faster through the gel compared to the folded form. Surprisingly, for the OmpA-177 insertion variants (SA-1, FLAG or myc) heat-modifiability is “normal” again (**Figure 3.6**). Comparing the mobility of OmpA-177 to OmpA-177-SA-1, we find that the folded barrels run at almost similar height, as if the extra residues of SA-1 were absent, whereas after boiling, OmpA-177-SA-1 is retarded with respect to OmpA-177 with an amount corresponding to their difference in molecular mass. These results suggest that as more and more residues are added to the OmpA-171 TM domain, the relative positions between the folded and unfolded domains first decrease until they are equal, before increasing again to appear as “normal” heat-modifiability. This predicts that for some rare OMPs, it would seem as if they would not have any heat-modifiability at all.

Summary

Taken together, these data show that both the FLAG and the myc epitopes are displayed in severely reduced amounts on the cell surface. Apparently, OmpA displays not all small peptides equally efficient. Consequently, for applications in which OmpA should be a carrier of randomly generated peptides a negative bias towards certain peptides that share characteristics of FLAG and/or myc, most likely being strongly (negatively) charged, might occur during screening of these surface display libraries.

Acknowledgements

I like to thank Arnold Driessen and Nico Nouwen (University of Groningen, the Netherlands) for the anti-OmpA antibody, Jeffrey Rice (University of California) for the MC1061 Δ OmpA strain and the plasmid carrying the SA-1 peptide, Svetlana Alexeeva for designing constructs pGV1-4 and creating the SWISS-model loop folding predictions, and Genison Isijk for help with cloning pGI6 and pGI9.

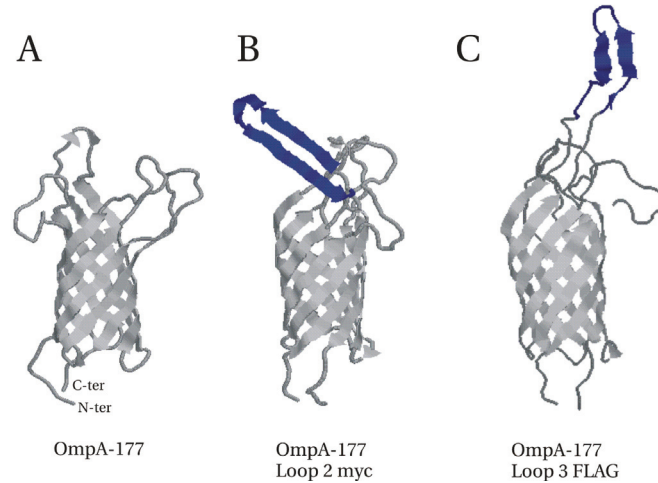


Figure 3.S1. Predicted protein structures by SWISS-MODEL of the OmpA transmembrane domain before and after epitope insertion. PDB entries 1g90.pdb, 1bxw.pdb and 1qjp.pdb were used to build the model. (A) OmpA-177 model. (B) OmpA-177 model with 2xmyc inserted in loop 2 after G70. (C) OmpA-177 model with 3xFLAG inserted in loop 3 after N109.

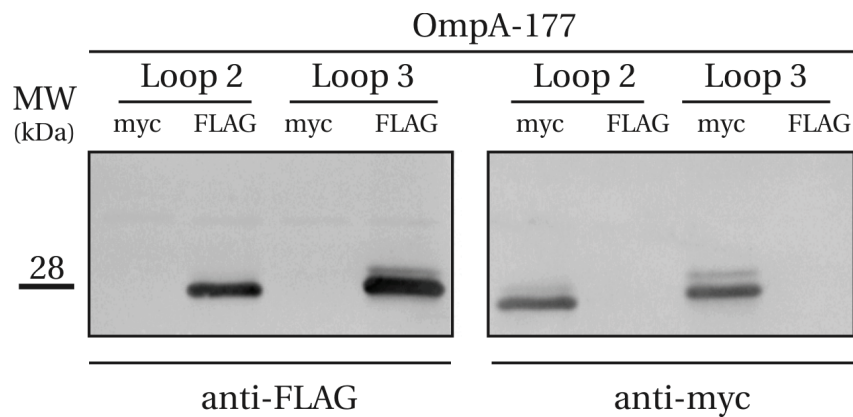


Figure 3.S2. Detection of OmpA-177 TM domain variants with inserted 3xFLAG or 2xmyc peptides on immunoblot. Expression of the variants was induced in LMC500 with 0.3 mM IPTG. From left to right: OmpA-177 loop 2 myc, OmpA-177 loop 2 FLAG, OmpA-177 loop 3 myc and OmpA-177 loop 3 FLAG. For loop 3 variants, unprocessed protein is also present. Left panel: anti-FLAG (3 μ g/ml), right panel: anti-myc (3 μ g/ml). For this blot, a 12% SDS-PAGE gel percentage was used.

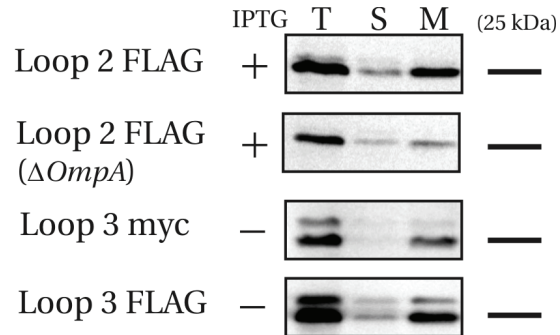


Figure 3.S3. The OmpA TM domain constructs are predominantly present in the membrane fraction. Total cell lysate (T) was fractionated into soluble (S) and membrane (M) fractions. Shown are immunoblots of constructs OmpA-177 loop 2 FLAG (induced), OmpA-177 loop 3 myc (uninduced), and OmpA-177 loop 3 FLAG (uninduced). Strain is LMC500, except for loop 2 FLAG, where results from strain LMC500 and MC1061 $\Delta OmpA$ are shown. Only the relevant portions of the blot are shown. Black line indicates 25 kDa marker band. Antibody concentrations used were 1 μ g/ml (anti-myc), and 0.1 μ g/ml or 0.5 μ g/ml (anti-FLAG) for induced or uninduced FLAG, respectively.

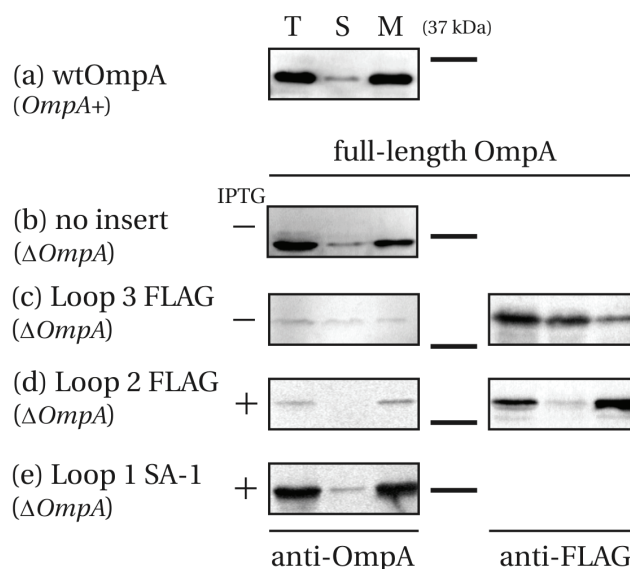


Figure 3.S4. The full-length OmpA constructs (except loop 3 FLAG) fractionate predominantly to the membrane fraction. Total cell lysate (T) was fractionated into soluble (S) and membrane (M) fractions. Shown are immunoblots of full-length OmpA constructs carrying a FLAG insertion in loop 2 (d) or loop 3 (c), and an SA-1 insertion in loop 1 (e). Strain was MC1061 Δ OmpA. As controls, fractions of LMC500 (endogenous OmpA, *OmpA*⁺) (a), and OmpA expressed from plasmid in MC1061 Δ OmpA (b) are shown. Only the relevant portions of the blot are shown. Black line indicates 37 kDa marker band. For the wild type OmpA and induced constructs, a 1:10000 dilution was used for the polyclonal antibody against OmpA. For the uninduced construct, a 1:1000 dilution was used. Anti-FLAG was used for the induced and uninduced FLAG constructs at 0.1 μ g/ml and 1 μ g/ml, respectively. Band intensities in the anti-OmpA blots (b) and (c), and (d) and (e) can be compared directly. Their relative intensities, quantified using densitometry with ImageJ, are shown in **Figure 3.5**.

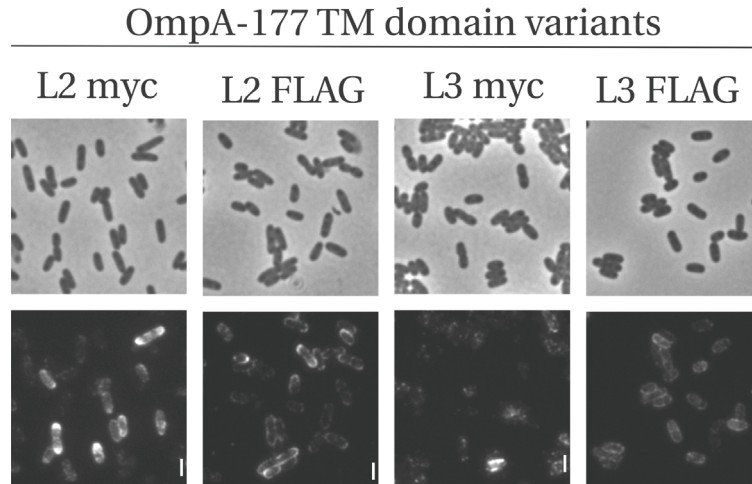


Figure 3.S5. Myc and FLAG epitopes are detected on the surface of cells expressing OmpA-177 TM domain variants. Cells induced with 0.3 mM IPTG for expression of OmpA-177 containing either FLAG in loop 2, myc in loop 2, FLAG in loop 3 or myc in loop 3, were fixed and immuno-labeled with antibodies against FLAG or myc. The scale bar corresponds to 2 μ m. Image exposure time was 470 ms.

Supplementary Materials and Methods

The signal sequence and the first 177 residues of the mature OmpA protein, coding for the transmembrane domain, were cloned in the expression vector pTrc99A (Amann et al. 1988), modified to decrease the basal expression level (i.e. without inducer) to typically a few thousands proteins per cell (pTHV037, (Den Blaauwen et al. 2003)). OmpA-177 was amplified by PCR from the chromosome of LMC500 using primers proOmpANcoIfw and OmpAHindIIIrv, and ligated in the *NcoI* and *HindIII* sites of pTHV037 to create pMD5. The *NcoI* site introduces after the start Met codon an additional alanine codon. The 3xFLAG and 2xmyc epitope loop insertions in loop 2 and 3 (constructs pGV1-4, see table III) were created using overlap PCR. For instance, to create the 3xFLAG insertion in loop 2 of the OmpA TM domain (pGV2), two separate PCRs, containing a region of overlap, were performed on pMD005. The first PCR with primers proOmpANcoIfw and 3xflagOmpAL2RV, and the second PCR with primers 3xflagOmpAL2FW and OmpAHindIIIrv. The two PCR fragments were then mixed, denatured and annealed to form a duplex at the overlap region, and filled in by DNA polymerase (Advantage, Clontech) for 10 cycles. Subsequently, proOmpANcoIfw and OmpAHindIIIrv were added and the fragments were amplified for another 20 cycles, and either cloned into pGEM-T (Promega), sequenced and then transferred to pTHV037, or cloned directly into pTHV037 using *NcoI* and *HindIII* sites. The 3xFLAG insertion in loop 3, and the 2xmyc insertions were created in the same way making use of the following primers: 2xmycOmpAL2RV, 2xmycOmpAL2FW, 2xmycOmpAL3RV, 2xmycOmpAL3FW, 3xflagOmpAL3RV, and 3xflagOmpAL3FW.

pGI9 was created as follows. OmpA-177 was amplified from pMD005 using the primers proOmpANcoIFW and OmpAAgeIHindIIIrv, the PCR product digested by *NcoI* and *HindIII*, and was ligated into *NcoI/HindIII* digested pGV4. This resulted in pGI8 that contains a silent mutation introducing the *AgeI* site in Pro177, for C-terminal addition of the OmpA periplasmic domain DNA fragment. This fragment was obtained by PCR on the LMC500 chromosome, with primers OaperiAgeIFW and OaperiEcoRIHindIIIrv introducing the *AgeI* upstream of the periplasmic domain and adding the linker sequence LEDPPAEF downstream. The PCR product was digested with *AgeI/HindIII* and ligated into *AgeI/HindIII* digested pGI8. pGI6 was created along similar lines: OmpA-177 containing

3xFLAG in loop 3 was amplified from pGV4 using the primers proOmpANcoIFW and OmpAAgeIHindIIIIRV, the PCR product was digested by *NcoI* and *HindIII*, and ligated into *NcoI/HindIII* digested pGV4. This resulted in pGI5. Ligating in the *AgeI/HindIII* periplasmic domain PCR product, used also for pGI9, created pGI6. pGV28 was created by PCR on pB33OA14-SA1 (Bessette et al. 2004) using primers proOmpANcoIFW and OmpAXhoIPstIRV, digestion by *NcoI/XhoI*, and ligated into *NcoI/XhoI* digested pGV14 (unpublished), to get OmpA-177-SS containing SA-1 in loop 1. pGV32 was created by ligation of *SphI* digested, gel-purified fragments of pGV2 and pGI9, introducing the 3xFLAG loop 2 insertion into the full-length OmpA. pGV33 was created by ligation of *SphI* digested, gel-purified fragments of pGV28 and pGI9, introducing the SA-1 loop 1 insertion into the full-length OmpA. A list of primer sequences is available upon request.

IV

Chapter 4: Domain fusions to the C-terminus of cell division protein FtsQ

Abstract

With the aim of sub-localizing the OmpA transmembrane (TM) domain to the site of constriction (mid-cell) in dividing *Escherichia coli*, we explored the possibility of using cell division protein FtsQ as mid-cell localization factor. To establish whether GFP-FtsQ could be used to target a complete protein domain to mid-cell, we constructed fusion proteins between FtsQ and AcrA (a periplasmic efflux pump component) and between FtsQ and ALBP (D-allose binding protein).

A GFP-FtsQ-AcrA protein showed reduced affinity for mid-cell in the presence of wild-type FtsQ, but complemented an FtsQ(Ts) mutant. Further extension with either a HSV or a 3xFLAG epitope to co-localize the C-terminus with the N-terminal GFP *in situ*, caused an “exclusion” from mid-cell. Also, extension with the OmpA TM domain interfered and caused mid-cell exclusion. Surprisingly, when a 3xFLAG epitope was present in the OmpA TM domain, dominant negative effects were reduced and mid-cell localization was somewhat restored in TY medium.

We speculate that for the AcrA extensions, only partially degraded fusion can localize to mid-cell, perhaps because intact AcrA interacts with the efflux pumps present in the lateral cell envelope. If further C-terminal extension with HSV, 3xFLAG or the OmpA TM domain makes the fusions more resistant to degradation, mid-cell localization of degraded fusion would be reduced, explaining the observed mid-cell exclusion.

During the course of this research, it was found that AcrA folds as a coiled-coil with its N- and C-terminus in close proximity. Folded AcrA is therefore not able to function as spacer domain. AcrA was replaced by ALBP, with in between FtsQ and ALBP a myc epitope to act as a spacer and to enable detection. Localization in the presence of wild-type FtsQ was good, and degradation on immunoblot was less pronounced compared to AcrA. This suggests that FtsQ can bring the ALBP domain to mid-cell.

Introduction

Our aim is to construct a fusion protein containing that spatially constrains the OmpA β -barrel to mid-cell during cell division. (see also **Figure 1.4** in **Chapter 1**). In this work, we explore the possibility to use the mid-cell affinity of cell division protein FtsQ to accomplish this. As FtsQ is an inner membrane protein with an extended periplasmic domain (van den Ent et al. 2008), an additional spacer domain is required that bridges the periplasm. During inward growth of the septum, this spacer domain has to connect the FtsQ domain with the OmpA β -barrel domain in the outer membrane. As FtsQ is an essential protein, the fusion either has to be functional, or has to be able to co-localize with functional wild-type FtsQ.

Previous work in our group has shown that the C-terminus of FtsQ could be extended with a small HSV epitope (13 residues) without interfering with mid-cell localization (see Chapter 4, Figure 4 of (Vinkenvleugel 2006)). In this chapter, we have fused complete spacer domains to the C-terminus of FtsQ and characterized their localization and functionality.

As the solute-accessible periplasmic width of *Escherichia coli* is estimated at ~15-21 nm (Matias et al. 2003; Collins et al. 2007), and the C-terminus of FtsQ can extend up to 7 nm into the periplasm (van den Ent et al. 2008), a spacer of ~8-14 nm is needed.

Initially, the efflux pump component AcrA was chosen as spacer domain. At that time, AcrA was described as a elongated protein (~10-20 nm), thought to contain long α -helices and span the periplasm, with its hydrophobic (lipidated) N-terminus anchored in the IM, and its (slightly) hydrophobic C-terminus interacting with the OM (Elkins and Nikaido 2003). Although primary sequence analysis indicated that the N- and C-terminal regions flanking the central α -helical region could come together to form a single lipoyl-like domain (Johnson and Church 1999), the possibility of AcrA folding back on itself was considered unlikely, mostly based on dynamic light scattering experiments that predicted a highly elongated protein (Zgurskaya and Nikaido 1999). Furthermore, as a member of the “membrane fusion” protein (MFP) family (Dinh et al. 1994), AcrA shares homology to a paramyxovirus MFP (Baker et al. 1999). Based on this homology, AcrA’s function was thought similar to that of a viral fusion protein (Baker et al. 1999), and it was speculated that coiled-coil formation could bring together the inner and outer membranes (Johnson and Church 1999). These properties made AcrA a suitable spacer domain to bridge the

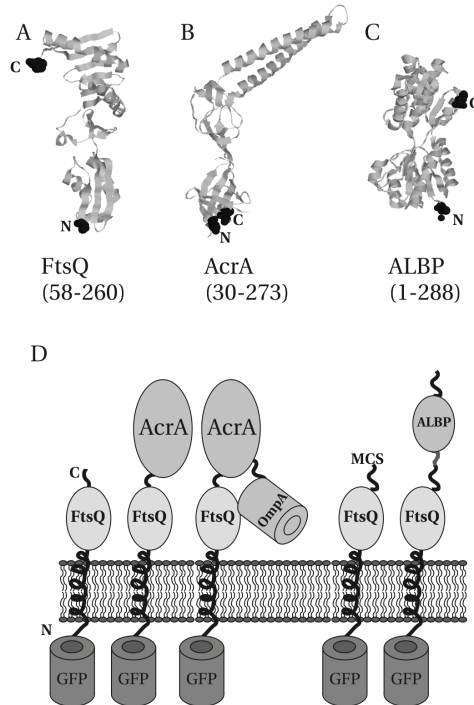


Figure 4.1: (A-C) structures with their N- and C-terminus indicated. For AcrA and ALBP, residue numbering is that of the mature protein. Note that for FtsQ, only the periplasmic domain is shown (with the last 16 residues missing) and for AcrA (397 residues, mature protein 373 residues) the first 29 residues and the last 100 residues of the mature protein are missing. ALBP is complete (311 residues, mature protein 288 residues). Figures were created by Rasmol, PDB files used were 2vh1 (FtsQ) (van den Ent et al. 2008), 2F1M (AcrA) (Mikolosko et al. 2006) and 1gub (ALBP) (Magnusson et al. 2002). (D) Cartoon of the main fusion proteins described in this chapter. From left to right: GFP-FtsQ, GFP-FtsQ-AcrA, GFP-FtsQ-AcrA-(OmpA-177), GFP-FtsQ-MCS and GFP-FtsQ-myc-ALBP.

periplasm.

Later work on AcrA, in particular its crystal structure (first of its homologue MexA (Akama et al. 2004; Higgins et al. 2004), later also for AcrA (Mikolosko et al. 2006)) showed that it folds back on itself to form three separate domains: a β -barrel, a lipoyl domain and a coiled-coil α -helical hairpin (**Figure 4.1B**). It was concluded that it did not span the periplasm and functioned more like an adaptor protein connecting/ regulating/ stabilizing the IM (AcrB) and OM protein (TolC) components of the drug efflux pump (Touze et al.

2004). Thus, AcrA is not suitable to act as a periplasmic bridging domain.

An alternative spacer domain was needed. We subsequently opted for an approach in which the periplasm is bridged through an artificial “string” of folded spacer domains connected with flexible linkers. To prevent proteolysis and/or misfolding it was decided to use native, folded domains instead of unstructured or artificial amino acid sequences. Preferably, the spacer domain should not have any interactions with other cellular components, as these could interfere with mid-cell and/or OM localization. Finally, as already mentioned, its N- and C-terminus should be sufficiently separated to act as spacer domain. With these considerations in mind, the periplasmic D-allose binding protein ALBP (Chaudhuri et al. 1999) was chosen (**Figure 4.1C**). As the D-allose operon is not expressed when its substrate D-allose is absent (Kim et al. 1997), ALBP’s main interaction partners will be expected to be absent when grown in a defined medium without D-allose. Furthermore, its N- and C-terminus are on opposite sides of the protein roughly 5 nm away (**Figure 4.1C**, (Magnusson et al. 2002)). To be able to detect the spacer construct, and to facilitate proper folding of the individual domains, a myc epitope is fused as a linker between two ALBP domains.

In *E. coli*, temperature-sensitive (Ts) mutants are routinely used to check if particular fusions/mutants are functional in the absence of (essential) wild-type protein. E.g. if a particular FtsQ mutant is expressed in a FtsQ(Ts) strain, it is said to complement (i.e. to be functional) if the cells continue to divide normally at the restrictive temperature. This is the temperature at which the Ts strain cannot divide and forms filaments because the endogenous gene product is not functional.

As in this work, a GFP-FtsQ fusion is extended with additional periplasmic domains, this approach is not suitable to establish unequivocally the functionality of a fusion, because extensions can be proteolytically removed without loss of the GFP (localization) or FtsQ (complementation) domains. Therefore, to check if fusion proteins localize to mid-cell intact, *in situ* immunolabeling experiments are performed which are directed against small epitopes attached at the C-terminus of every fusion protein. This allows co-localization of the C-terminus with the N-terminal GFP *in situ*.

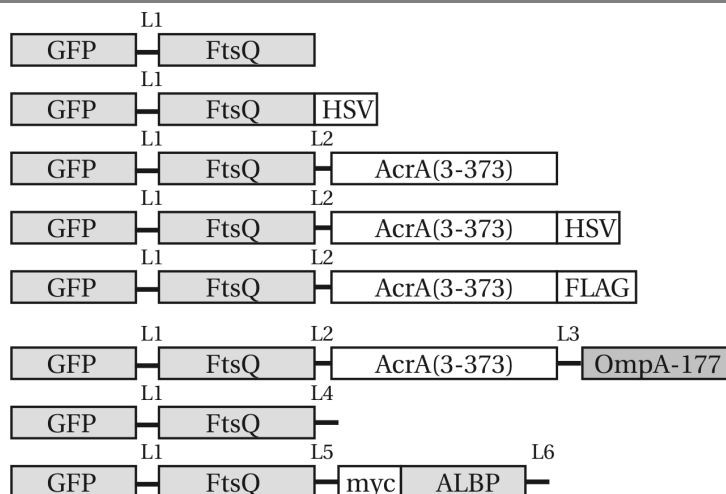


Figure 4.2: Schematic diagram showing all GFP-FtsQ fusion proteins described in this chapter.

Linkers used were L1 (EFNNN, between GFP and FtsQ), L2 (RS, between FtsQ and AcrA), L3 (RAQQ, between AcrA and OmpA) L4 (GSSSSRG, MCS for ALBP fusions), L5 (GSST, L4 after addition of myc-ALBP) and L6 (GSSSSRG, present at the C-terminus of a myc-ALBP building block). Epitopes used are HSV (QPELAPEDPED), 3xFLAG (DYKDHDG-DYKDHDY-DYKDDDDK), and 2xmyc (EQKLISEEDL)₂.

In this chapter, we describe the characterization of a series of C-terminal GFP-FtsQ-based fusion proteins (**Figure 4.1D**, **Figure 4.2**) containing either an AcrA or alternatively, an ABLP spacer domain. Although the fusions based on the AcrA domain are not suitable to bridge the periplasm, they are potentially informative on the tolerance of FtsQ towards C-terminal extension with bulky protein domains, on which the alternative strategy is based.

We found that GFP-FtsQ-AcrA mid-cell localization is less pronounced compared to GFP-FtsQ, but that it complemented the FtsQ(Ts) strain. However, we observed that the fusion is partially degraded to GFP-FtsQ*, and this degradation product alone is sufficient to explain the mid-cell localization and complementation. Further extension of AcrA with epitopes (HSV, 3xFLAG) or with the OmpA TM domain completely abolishes mid-cell localization and causes dominant-negative effects. Surprisingly, introducing a 3xFLAG epitope in the OmpA TM domain partially restored mid-cell localization and reduced the dominant-negative effects. We now know that this epitope makes the OmpA TM domain

susceptible to degradation (see **Chapter 3**). Therefore, this suggests that intact GFP-FtsQ-AcrA-X fusion protein cannot localize, but partially degraded (e.g. GFP-FtsQ*, or GFP-FtsQ-AcrA*) fusion protein can. Whether GFP-FtsQ-AcrA is able to localize remains an open question.

We designed a new series of fusion proteins based on ALBP domains connected with myc spacers. We show that GFP-FtsQ-myc-ALBP localizes to mid-cell. However, at this time, a more promising mid-cell localization candidate was found (see next chapter), and FtsQ was put on hold.

Results

We have used immunoblotting to check for correct expression and possible degradation of the fusions, and used fluorescence microscopy to visualize the (mid-cell) localization of the GFP-fusions. Because it is possible that a fusion will have a reduced affinity for mid-cell compared to wild-type FtsQ, GFP localization was studied in two strains, a common laboratory wild-type strain (LMC500) and an otherwise isogenic FtsQ(Ts) temperature-sensitive strain (LMC531). Functionality or the ability to not interfere with functional wild-type FtsQ is quantified by cell length measurements under various conditions as explained below.

Detection of fusion proteins on immunoblot

In **Figure 4.2**, a schematic overview of the main fusion proteins is shown (C-terminal epitope extensions are not depicted). To simplify the interpretation of results later on, we first discuss the expression and degradation results obtained from immunoblots.

Simultaneously with harvesting cells for microscopy (see below), samples for immunoblotting were taken. The immunoblots (**Figure 4.3**) were probed with a polyclonal anti-GFP antibody that (weakly) cross-reacted with several proteins in *E. coli* whole cell lysates. Open circles indicate full-length proteins at their expected height (GFP-FtsQ: 58.8 kDa, GFP-FtsQ-MCS: 59.4 kDa, GFP-FtsQ-myc-ALBP: 91.2 kDa, GFP-FtsQ-AcrA: 98.7 kDa). Degradation products are marked with asterisks. The first lane of each blot contains cells that do not express GFP.

In our experience, when grown in TY medium without glucose (**Figure 4.3 left panel**), expression levels from the pTrc99A-down plasmid (the expression vector used for all constructs in this chapter) are higher (~2-3 fold) compared to growth in GB1 medium and

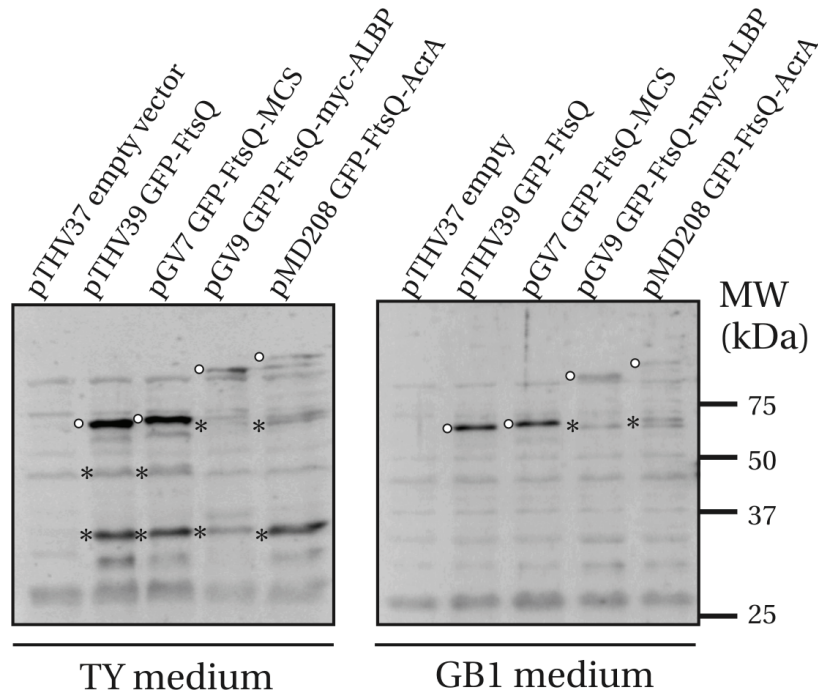


Figure 4.3. Immunoblots of GFP-FtsQ variants probed against the GFP domain. Cells were cultured as described in the caption of Figure 1. Samples were resuspended in sample buffer and boiled. The immunoblot was probed with a polyclonal anti-GFP antibody that (weakly) cross-reacted with several proteins in *E. coli* whole cell lysates. Open circles indicate full-length proteins at their expected height (GFP-FtsQ: 58.8 kDa, GFP-FtsQ-MCS: 59.4 kDa, GFP-FtsQ-myc-ALBP: 91.2 kDa, GFP-FtsQ-AcrA: 98.7 kDa). Degradation products are marked with asterisks. The first lane of each blot contains cells that do not express GFP. When grown in TY medium (left panel), expression levels were higher, and more degradation occurred. When grown in GB1 medium (right panel), both GFP-FtsQ and GFP-FtsQ-MCS have no detectable GFP degradation products. As expected from its 7 extra residues, the GFP-FtsQ-MCS band is slightly retarded with respect to GFP-FtsQ. Both GFP-FtsQ-myc-ALBP and GFP-FtsQ-AcrA are detected at their expected height. In addition, for both GFP-FtsQ-myc-ALBP and GFP-FtsQ-AcrA, a breakdown product GFP-FtsQ* is present. The degradation appears more pronounced for GFP-FtsQ-AcrA.

more degradation occurred. In particular, GFP-FtsQ and GFP-FtsQ-MCS were degraded to what is most likely GFP*.

When grown in GB1 medium (**Figure 4.3 right panel**), both GFP-FtsQ and GFP-FtsQ-MCS have no detectable GFP degradation products. As expected from its 7 extra residues, the GFP-FtsQ-MCS band is slightly retarded with respect to GFP-FtsQ. Both GFP-FtsQ-

myc-ALBP and GFP-FtsQ-AcrA are detected at their expected height. In addition, for both GFP-FtsQ-myc-ALBP and GFP-FtsQ-AcrA, a breakdown product GFP-FtsQ* is present that runs at roughly the same height as GFP-FtsQ, suggesting the proteolytic removal of the C-terminal extension. The degradation appears more pronounced for GFP-FtsQ-AcrA.

Localization and complementation of GFP-FtsQ and GFP-FtsQ-HSV

In this chapter, length measurements of cells containing GFP-FtsQ-based fusion proteins over-expressed from plasmid and grown to steady state are used to make statements about the functionality of the particular fusion. GFP fluorescence at mid-cell, visible as a bright “band” or spot in the middle of a bacterium is a measure for mid-cell affinity. In this thesis, when statements are made about mid-cell localization, this is always judged by visual inspection of fluorescence microscopy images. Furthermore, mid-cell is judged relative to signal elsewhere in the cell. Thus, strong mid-cell localization is when signal is present only at mid-cell and absent from elsewhere in the cell: it is weak when signal is present throughout the cell with only a slight enrichment at mid-cell. For the data presented in e.g. **Table I** (the percentage of “Q-rings” at mid-cell), weak mid-cell localization is scored as mid-cell localization. For the moment, these qualitative judgements are sufficient for our purpose. We use a wild-type strain (LMC500) to study the fusions in the presence of endogenous wild-type FtsQ as well as a (isogenic) temperature-sensitive FtsQ strain (LMC531) to study the fusions in the absence of wild-type FtsQ.

Wild-type FtsQ has a copy number of 25-50 (Carson et al. 1991). Using quantitative immunoblotting, it has been determined that GFP-FtsQ is over-expressed ~70 fold when expressed from the plasmid (pTrc99A-down) used throughout this chapter (Vinkenvleugel 2006). At these expression levels, GFP-FtsQ is present along the complete IM cell perimeter (**Figure 4.5A**), with only a 2-3 fold increase at the division site. However, if expression levels are reduced to ~5 fold over-expression by e.g. integrating GFP-FtsQ in the chromosome, only mid-cell localization remains (Vinkenvleugel 2006).

In the wild-type background, the average cell lengths of the fusions relative to GFP-FtsQ(wt) provide information on how a fusion functions together with wild-type FtsQ. An increase in cell length is interpreted as interference with the functioning of wild-type FtsQ by the GFP-fusion under study (that fusion is then said to be “dominant-negative”). The over-expressed GFP-FtsQ itself is already slightly dominant-negative, as average cell length

is increased compared to cells bearing empty plasmid (3.0 μm compared to 2.4 μm). When GFP-FtsQ is replaced by GFP-FtsQ(E125K), average length is increased further (to 3.7 μm). As no GFP mid-cell localization was observed for this fusion, it can interfere with wild-type FtsQ “from a distance”, possibly by titration of FtsQ binding partners. It is likely that a fusion that interferes with wild-type FtsQ will be non-functional (see below).

As mentioned in the introduction, preliminary experiments showed that the C-terminus of GFP-FtsQ could be extended with a small epitope (HSV, 11 residues, Novagen) without loss of mid-cell localization (Vinkenvleugel 2006). In the wild-type background, cells expressing GFP-FtsQ-HSV were slightly longer compared to cells expressing GFP-FtsQ (3.3 instead of 3.0 μm , **Table I**). This indicates that the GFP-FtsQ-HSV fusion is less functional than GFP-FtsQ.

In the FtsQ(Ts) temperature-sensitive background, the fusions can be studied in the absence of wild-type FtsQ. The FtsQ(Ts) strain used has a chromosomal mutation in the *FtsQ* gene (*FtsQ1*, encoding FtsQ(E125K) (Taschner et al. 1988)) which makes FtsQ temperature-sensitive for mid-cell localization (Aarsman et al. 2005). At the permissive temperature (28°C), it localizes to mid-cell (inferred from the average cell length), but at the restrictive temperature (42°C) it does not (inferred from a GFP-FtsQ(E125K) fusion), and the cells form filaments as length growth continues (Hirota et al. 1968; Ricard and Hirota 1973). It was found that GFP-FtsQ expressed from plasmid localizes to mid-cell and could rescue the FtsQ(Ts) filamentation phenotype (average cell length after two mass doublings at 42°C was 4.7 μm (GFP-FtsQ) instead of 8.8 μm (empty plasmid), LMC500 (empty plasmid) at 42°C is 2.6 μm (Aarsman et al. 2005) and **Table I**). From these average length values, it is clear that complementation (the ability to divide at the restrictive temperature in the Ts background) is not a simple yes or no, but a gradual scale set by the average cell length at 42°C.

Table I Morphological parameters of strains LMC500 and LMC531 expressing FtsQ fusion proteins from plasmid. The cells were grown to steady state at 28°C in GB1 medium and subsequently shifted to 42°C and grown for a further 2 mass doublings. Partly reproduced from (Vinkenvleugel 2006). For FtsQ(Ts) at 42°C, three length classes are indicated with white (functional), light gray (partially functional) and gray (non-functional). For each sample, at least 300 cells were scored. An indication of the width of each length distribution is given by the S.D.

Strain/mutant	wild-type (LMC500) / 28°C			wild-type (LMC500) / 42°C			FtsQ(Ts) (LMC531) / 28°C			FtsQ(Ts) (LMC531) / 42°C		
	length (m)	T(%)	Q(%)	length (m)	T(%)	Q(%)	length (m)	T(%)	Q(%)	length (m)	T(%)	Q(%)
empty plasmid	2.39±0.50	ND	NA	2.59±0.58	ND	NA	4.68±2.40	ND	NA	8.77±3.39	ND	NA
GFP-FtsQ	3.04±0.62	16	23	3.97±1.45	23	31	3.67±0.92	26	28	4.70±1.93	24	46
GFP-FtsQ-HSV	3.34±0.73	39	33	5.09±2.15	D	45	3.26±0.78	33	30	6.28±2.74	D	39
GFP-FtsQ-AcrA	2.98±0.90	26	8	3.43±0.96	38	4	3.20±0.86	38	23	4.28±0.90	47	27
GFP-FtsQ-AcrA-HSV	4.08±1.60	45	4	5.72±3.05	50	2	4.29±1.95	35	8	9.45±4.12	35	5
GFP-FtsQ-AcrA-3xFLAG	4.18±1.44	37	0	5.30±2.83	38	0	4.47±2.10	43	0	7.86±4.31	37/D /B	0
GFP-FtsQ-AcrA-(OmpA-177)	4.45±1.98	ND	0	8.31±4.67	ND	0	7.51±5.59	ND	0	9.18±5.70	ND	0
GFP-FtsQ-AcrA-(OmpA-177)3xFLAG	3.33±1.02	ND	ND	4.88±2.26	ND	ND	4.25±2.04	ND	ND	6.15±2.21	ND	ND

Length indicates average length with standard deviation, T indicates percentage of visually constricting cells, Q indicates percentage of cells with a GFP signal at mid-cell, NA non-applicable, ND not determinable, B blunt filaments, D deeply constricted filaments.

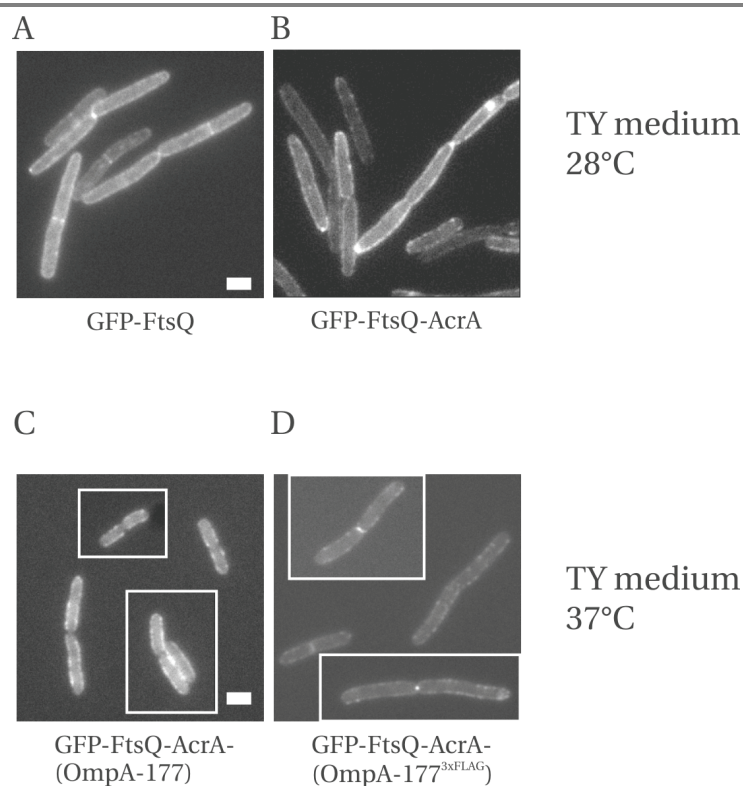


Figure 4.4. Mid-cell localization of FtsQ C-terminal domain fusions grown in TY medium (either at 28°C or, as indicated, at 37°C) in the presence of wild-type FtsQ. **(A, B)** Cells grown in TY medium at 28°C, fixed in growth medium and resuspended in PBS. **(C, D)** Cells grown in TY medium at 37°C, imaged directly, in the presence of growth medium (a collection composed of different raw images is shown). Scale bar has dimensions 1 x 2 μm.

At the restrictive background, GFP-FtsQ-HSV localized to mid-cell, but cell division was partially impaired (6.3 μm filaments). As immunoblotting indicated that the fusion was largely intact (data not shown), we speculate that, as the C-terminus is required for binding downstream division proteins FtsL and FtsB, possibly the presence of the HSV epitope interfered with this process.

For our purpose of localizing C-terminal extensions to mid-cell however, the fact that GFP-FtsQ-HSV not fully functional is not a strict requirement. Since it localizes to mid-cell in the presence of wild-type FtsQ seemingly as good as GFP-FtsQ, it will be expected that the 10-fold reduction in expression levels needed to obtain exclusively mid-cell

localization of GFP-FtsQ will also be possible with GFP-FtsQ-HSV, and thus, we continued the step-by-step assembly of the fusion by addition of the AcrA domain to the C-terminus of FtsQ.

Localization of GFP-FtsQ-AcrA-X fusions in the presence of wild-type FtsQ

First, we compared the localization of all fusions in the presence of wild-type (endogenous) FtsQ (LMC500: MC4100 *LysA*). Initially, the cells were grown in TY medium at 28°C (t_{MD} ~50 minutes, for details see Materials & Methods). As mentioned, the fusions are over-expressed from plasmid about 100 fold, and as overproduction of FtsQ is known to impair division (Carson et al. 1991), it was not surprising that the cells grew as filaments (length ~7-14 μ m, control with empty plasmid 3-6 μ m). However, such extreme conditions can amplify minor differences between the constructs. The cells were fixed in growth medium and imaged.

GFP-FtsQ (**Figure 4.4A**) showed clear mid-cell localization. In contrast, localization of GFP-FtsQ-AcrA (**Figure 4.4B**) was mostly in the membrane, without any clear enrichment at mid-cell in most cells (and some cells had polar spots). Addition of the OmpA β -barrel resulted in exclusion (absence) of GFP from mid-cell (**Figure 4.4C**), but unexpectedly, when the 3xFLAG was present in the β -barrel (**Figure 4.4D**), mid-cell localization was restored in a sizeable number of cells (Note: temperature is 37°C).

Next, the cells were grown in GB1 medium. The cells grow much slower in this medium (t_{MD} ~90-95 minutes). Cells were fixed in growth medium, resuspended in PBS and imaged. Phase-contrast and fluorescence images of the fusions in the presence of wild-type FtsQ are shown in **Figure 4.5**. As expected from a reduction in expression levels due to growth in GB1 medium, we find that cells expressing GFP-FtsQ no longer grow as filaments, although average cell lengths remain higher compared to cells with empty plasmid (Aarsman et al. 2005). Both cells expressing GFP-FtsQ and GFP-FtsQ-MCS show a clear mid-cell localization ("Q-ring"), as well as membrane localization (due to over-expression).

In LMC500 (wild-type background), GFP-FtsQ-AcrA showed reduced affinity for/GFP intensity at mid-cell, (the percentage of cells with Q-rings decreases from 23% to 8% upon addition of AcrA to GFP-FtsQ, **Table I**) and brighter patches along the perimeter of the cell and towards the poles can be observed. Clearly, addition of AcrA to the C-terminus of FtsQ

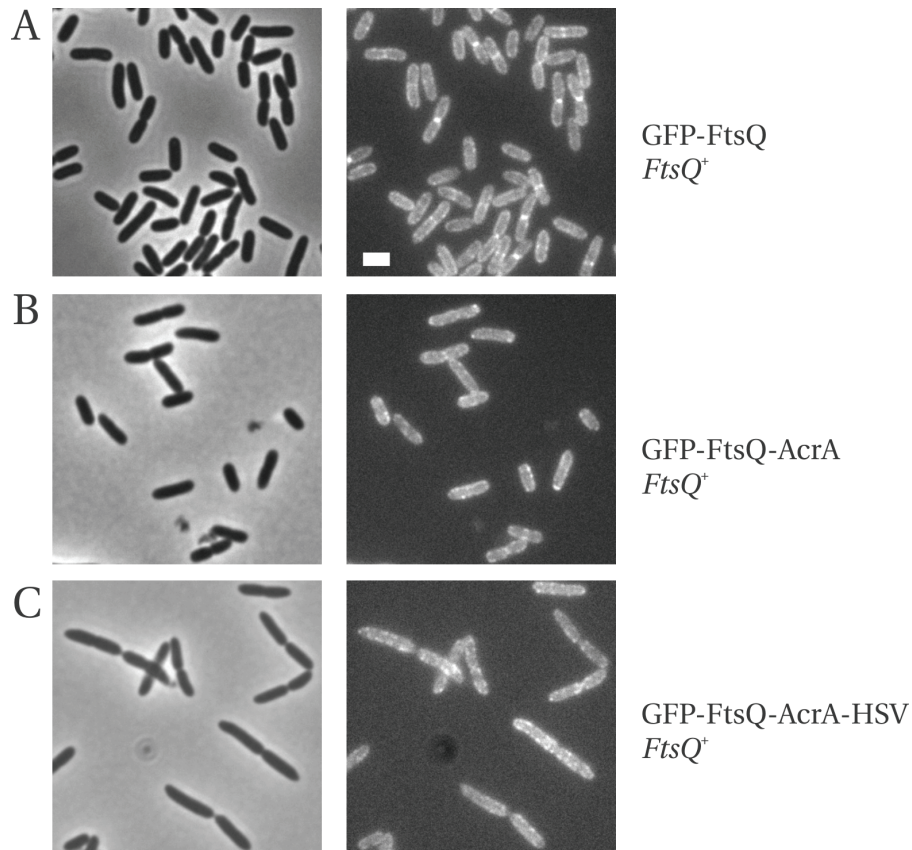


Figure 4.5. Mid-cell localization of FtsQ C-terminal domain fusions in the presence of wild-type FtsQ. Cells grown in GB1 medium were fixed in growth medium, resuspended in PBS and imaged. **(A)** GFP-FtsQ localizes efficiently to mid-cell. **(B)** Cells expressing GFP-FtsQ-AcrA had reduced GFP intensity at mid-cell, and brighter patches along the perimeter of the cell and towards the poles can be observed. **(C)** Further extension of GFP-FtsQ-AcrA with either a HSV (shown) or a 3xFLAG epitope (not shown) abolished mid-cell localization almost completely. For the fluorescent images, exposure times of 1-3 s were used. Scale bar has dimensions 1 x 2 μm .

affects its localization.

Further extension of GFP-FtsQ-AcrA with a HSV (**Figure 4.5C**), a 3xFLAG epitope (not shown) or the OmpA β -barrel (not shown) abolished mid-cell localization almost completely, creating dark bands at mid-cell (mid-cell exclusion), with GFP fluorescence mostly in the cylindrical part of the cell membrane. This suggests that little degradation to

GFP-FtsQ* occurs, since such a truncate would be expected to localize to mid-cell. Also, the fusions exerted dominant-negative effects on cell division, as inferred from the increased cell lengths (**Table I**).

In the previous chapter, it has been shown that insertion of a 3xFLAG epitope into OmpA caused a ~10 fold reduction in expression levels. As already mentioned, when the 3xFLAG epitope is present in the OmpA β -barrel, mid-cell localization is somewhat restored in TY medium (**Figure 4.4D**), although not so much in steady state GB1 medium (data not shown). Nevertheless, in GB1 medium, introduction of 3xFLAG in OmpA caused a dramatic reduction in division impairment, i.e. a reduction of the fusion's dominant-negative effect (**Table I**). (However, no complementation occurred, see below). If we assume that the increased degradation caused by the 3xFLAG insertion also holds true when the barrel is part of an FtsQ fusion protein, then this suggests that degradation of the fusion has a positive effect on the division process.

Localization of GFP-FtsQ-AcrA-X fusions in the presence of FtsQ(E125K)

For the GFP-FtsQ-AcrA based extensions, we also tested their functionality and localization in the absence of wild-type FtsQ, using the temperature-sensitive mutant strain LMC531, as described above. LMC531 cells were grown to steady state at 28°C in GB1 medium. Then, part of the cells was diluted in pre-warmed GB1 medium at 42°C and grown for an additional two mass-doublings. As before, the cells were imaged, their lengths were measured and GFP mid-cell localization was scored. All the relevant parameters can be found in **Table I**. The average length at the restrictive temperature was used to define three complementation classes: (i) Full complementation (Average length similar to GFP-FtsQ: ~5 μ m), (ii) No complementation (Average length similar to empty plasmid: ~9 μ m) and (iii) Partial complementation (Average length in between: ~7 μ m). In **Table I**, the length classes are indicated with different gray scales.

In the presence of FtsQ(E125K), GFP-FtsQ-AcrA localized at mid-cell in 23% of the cells (**Figure 4.6A**). Thus, replacing wild-type FtsQ by FtsQ(E125K) increases the mid-cell localization of GFP-FtsQ-AcrA. For GFP-FtsQ-AcrA-HSV, which did not localize in the presence of wild-type FtsQ, no such improvement was found. Localization patterns with either endogenous FtsQ or FtsQ (E125K) were similar. This is expected when the fusion has lost its capacity for mid-cell localization.

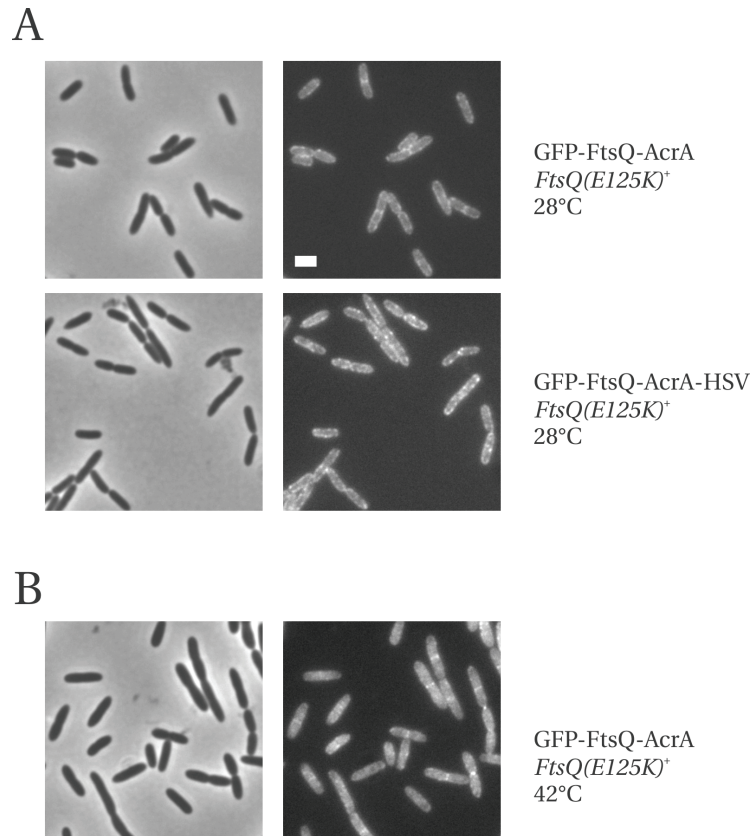


Figure 4.6. Localization of GFP-FtsQ-AcrA and GFP-FtsQ-AcrA^{HSV} in the presence of temperature sensitive FtsQ(E125K) at both **(A)** permissive (28°C) and **(B)** restrictive (42°C) temperatures. LMC531 cells were grown to steady state at 28°C in GB1 medium. Part of the cells was diluted in pre-warmed GB1 medium at 42°C and grown for an additional two mass-doublings. (A) In the presence of FtsQ(E125K), GFP-FtsQ-AcrA is localized at mid-cell in 23% of the cells (Table III). (B) At 42°C, a temperature at which FtsQ(E125K) does not localize to mid-cell, mid-cell localization increased (to 27% of all cells) and cells continue to divide normally. Thus, GFP-FtsQ-AcrA complements the temperature-sensitive LMC531 strain. In contrast, cells expressing GFP-FtsQ-AcrA^{HSV} formed long filaments, and mid-cell localization did not improve (data not shown). Similar results were obtained for cells expressing a GFP-FtsQ-AcrA^{FLAG} fusion (data not shown). Scale bar has dimensions 1 x 2 μm.

At the restrictive temperature (42°C) (**Figure 4.6B**), 27% of the cells showed mid-cell localization and cells continue to divide normally. Thus, GFP-FtsQ-AcrA complements the

temperature-sensitive LMC531 strain. In contrast, cells expressing GFP-FtsQ-AcrA-HSV formed long filaments (~10 μm), and mid-cell localization was not restored (data not shown). Similar results were obtained for cells expressing a GFP-FtsQ-AcrA-3xFLAG fusion and a GFP-FtsQ-AcrA-(OmpA-177) fusion (data not shown). Surprisingly, the GFP-FtsQ-AcrA-(OmpA-177)^{FLAG} fusion not only reduced toxic effects at the permissive temperature, but also exhibited partial complementation. Again, apparently the presence of 3xFLAG inside OmpA-177 improves the functionality of the fusion. We speculate this is due to an increased degradation of the fusion.

Extending GFP-FtsQ with a myc linker and the ALBP domain

Thus AcrA turned out not suitable to act as spacer domain, because of its unfavorable fold as a coiled-coil, and because we found experimentally that further extension destroyed its mid-cell localization capacity. As mentioned in the introduction, AcrA was replaced as spacer domain by ALBP, and myc epitopes were to be used as linkers.

On the DNA level, this required the design of a new multiple cloning site (MCS). The design had to meet several criteria: (i) the complete C-terminal extension downstream FtsQ can be swapped to a different mid-cell localizing factor (e.g. FtsN) via unique restriction sites (this required a unique site upstream of the extension (SacI) and a replacement (PstI) for the downstream HindIII as ALBP contains two HindIII sites), (ii) variable integer numbers of the (–myc-ALBP) spacer building block can be inserted (solved by XhoI/SalI-XmaI compatible ends cloning, see Materials & Methods, and **Figure 4.8** for details) (iii) at the very C-terminus a XmaI site allowed sub-cloning of the HSV/3xFLAG epitopes (iv) GFP could be exchanged easily with other FPs in our lab and (v) linker residues should be preferentially be either {GST} (small) and/or the myc epitope.

When grown in TY medium, GFP-FtsQ-MCS shows weak mid-cell localization but even membrane localization (**Figure 4.7A**). GFP-FtsQ-myc-ALBP had weak membrane localization and lots of bright fluorescent spots (**Figure 4.7B**). When grown in GB1 medium, GFP-FtsQ-MCS showed strong mid-cell localization, similar to GFP-FtsQ(wt) (**Figure 4.7C**). Finally, the GFP-FtsQ-myc-ALBP localized to mid-cell in most dividing cells, but not in all dividing cells, and not as well (i.e. as bright) as the GFP-FtsQ or GFP-FtsQ-MCS (**Figure 4.7D**). As we know from immunoblotting against GFP that the majority of the fusion is intact under these conditions, this suggests that it is possible to fuse a complete protein domain (ALBP) to the C-terminus FtsQ that subsequently localizes it to mid-cell.

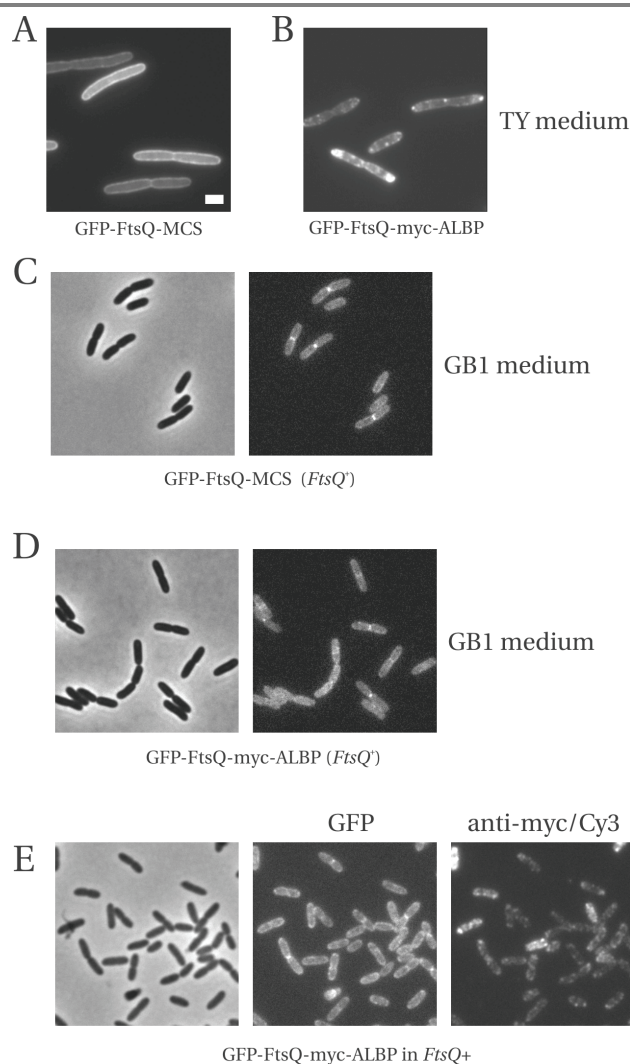


Figure 4.7. GFP-FtsQ-myc-ALBP. (A, B) Cells expressing either GFP-FtsQ-MCS or GFP-FtsQ-myc-ALBP were grown in TY medium at 28°C, fixed and imaged. (C, D) Same strains as in (A,B) now grown in GB1 medium at 28°C. (E) Cells were grown to pseudo-steady state in GB1 medium at 28°C, fixed and permeabilized with Triton X-100, EDTA and lysozyme. Cells were labeled with an anti-myc monoclonal antibody (50 µg/ml). This primary antibody was detected with a Donkey-anti-mouse Cy3-conjugated secondary antibody. Although several cells show a strong GFP mid-cell localization in the green channel, no corresponding myc spot was observed in the red channel (Cy3). Possibly, the signal from a single myc epitope is not sufficient to stand out in the labeling background. Alternatively/additionally, localized in the divisome, in between two presumably folded domains, the myc epitope might not be accessible for antibodies and therefore escape detection. Scale bar has dimensions 1 x 2 µm.

In an attempt to co-localize mid-cell localized GFP with the myc-epitope present at the C-terminus of FtsQ in GFP-FtsQ-myc-ALBP, we permeabilized fixed cells and immunolabeled them with anti-myc antibodies (**Figure 4.7E**). Although this does not prove the presence of ALBP (downstream of the myc epitope) at mid-cell, it can provide information on degradation at mid-cell.

Although several cells show a strong GFP mid-cell localization in the green channel, no corresponding myc spot was observed in the red channel (Cy3). On the whole, no co-localization was apparent, also not for the membrane (cylindrical) localized GFP. Possibly, the signal from a single myc epitope is not sufficient to stand out in the labeling background of the anti-myc antibody. A separate control experiment confirmed that indeed, anti-myc has a high labeling background in permeabilized cells (data not shown).

Alternatively/additionally, localized in the divisome, in between two presumably folded domains, the myc epitope might not be accessible for antibodies and therefore escape detection.

Discussion

First we discuss some implications of the observed mid-cell localization of an FtsQ fusion that is not fully functional (GFP-FtsQ-HSV), yet does not seem to interfere with wild-type FtsQ. Then we try to rationalize the observed behavior of the AcrA fusions, in particular the surprising mid-cell exclusion of the FtsQ-AcrA extensions. We conclude with two strategies to continue work on the GFP-FtsQ-myc-ALBP fusion, which localizes to mid-cell and is not dominant-negative, and therefore suitable for further extension.

FtsQ as part of the divisome appears dynamic

At first sight, it is surprising that GFP-FtsQ-HSV localized to mid-cell as efficiently as GFP-FtsQ(wt) in the presence of a low amount of endogenous FtsQ, but is not fully functional. Why can wild-type FtsQ function normally (the cells are slightly longer) in the presence of a large excess of less-functional FtsQ-HSV at mid-cell? After all, the amounts of wild-type FtsQ (25-50 copies) and plasmid-encoded GFP-FtsQ-HSV protein (2500-5000 copies) differ by two orders of magnitude. And because GFP-FtsQ-HSV localization appears similar to GFP-FtsQ, it is reasonable to expect that both will have equal affinity for the divisome.

If during execution of its (unknown) function FtsQ would be embedded in a static complex that is stable during division, then one expects that during the actual division,

FtsQ-HSV would no longer be able to localize, as all complexes containing FtsQ binding sites would have found their “rare” wild-type FtsQ copy. Since this is not observed, i.e. GFP-FtsQ-HSV stays localized during active division, this suggests that FtsQ localization is dynamic. For a long time, FtsZ was the only divisome component that has experimentally been shown to be highly dynamic (Stricker et al. 2002), but recent FRAP experiments in *Caulobacter* show that also FtsI (PBP3) is dynamic (Costa et al. 2008). Our results indicate that this might hold true also for FtsQ.

Why are GFP-FtsQ-AcrA-X fusions excluded from mid-cell?

The most striking result obtained with the GFP-FtsQ-AcrA fusion series is the mid-cell exclusion and toxicity that occurs after extending GFP-FtsQ-AcrA either with small epitopes or with the OmpA β -barrel. Subsequent insertion of the FLAG epitope into the OmpA barrel then reduces toxicity and partially restores mid-cell localization in TY medium.

Let us try to rationalize these observations. Could the mid-cell exclusion be caused by a reduced affinity for mid-cell (e.g. for binding to FtsK)? This is not likely, because then one would expect a (partial) restoration of mid-cell localization in the absence of endogenous FtsQ (i.e. at the restrictive temperature), which is not observed. Could the mid-cell exclusion be caused by a steric hindrance after extension of AcrA? In this scenario, the extended fusion no longer would fit in the protein complex at mid-cell that FtsQ is part of. However, AcrA contains a N-terminal linker of ~30 residues and a long 90-100 residue flexible C-terminus (Mikolosko et al. 2006). With this in mind, it is not likely that extending FtsQ with a large elongated domain such as AcrA does *not* cause mid-cell exclusion, but a small C-terminal extension to AcrA would suddenly abolish this capacity.

A possible explanation for the observed (weak) mid-cell localization of GFP-FtsQ-AcrA and the subsequent mid-cell exclusion of e.g. GFP-FtsQ-AcrA-HSV could be that addition of e.g. HSV causes stabilization against (occurring) degradation of the GFP-FtsQ-AcrA. In this scenario, the mid-cell localization of GFP-FtsQ-AcrA is then predominantly caused by GFP-FtsQ* that has AcrA proteolytically removed.

Is an increased stability of the GFP-FtsQ-AcrA-X fusions sufficient to explain all the observations? It provides a natural way to explain their toxicity: since they are excluded from mid-cell and more stable, they can titrate away division factors important for cell division (such as FtsL or FtsB, which form a complex with FtsQ (Buddelmeijer and

Beckwith 2004)).

However, to explain the mid-cell exclusion, further assumptions are required. Although, as discussed above, (small) extensions to AcrA are not expected to block mid-cell localization, extension of FtsQ with AcrA itself could already block mid-cell localization. Then it follows that all mid-cell localization observed for GFP-FtsQ-AcrA must be due to GFP-FtsQ*. However, this cannot explain the mid-cell exclusion of the stabilized AcrA extensions. In the absence of diffusion barriers or a dense protein packing in the IM at mid-cell, this is expected to result in a homogeneous distribution of GFP signal over the membrane, and not specifically in the cylindrical part of the cell, as observed. Thus, this scenario is not so likely.

Alternatively, GFP-FtsQ-AcrA is unstable but can in principle localize to mid-cell (i.e. it would do so if it was stable). Then stabilization after extension is not enough to explain the mid-cell exclusion. A further assumption is required; E.g. the existence of AcrA/AcrB/TolC efflux pumps along the cylindrical part of the cell, but not at mid-cell. Based on the relative copy numbers (Tikhonova and Zgurskaya 2004) and a proposed stoichiometry for a single efflux pump (AcrA:AcrB:TolC 9:3:3 (Higgins et al. 2004)), we estimate the presence of a few hundred efflux pumps per cell. Interaction of stabilized AcrA-X with these efflux pumps would explain the observed mid-cell exclusion. This scenario requires that most GFP-FtsQ-AcrA is degraded to GFP-FtsQ*, since otherwise the same mid-cell exclusion would be expected.

Finally, introducing the 3xFLAG epitope in the OmpA barrel four-domain fusion protein reduced toxicity of the construct and partially restored mid-cell localization in TY medium. As such behavior resembles that of GFP-FtsQ-AcrA, this suggests that the stabilization through extension is in part lost. We know that introducing the FLAG epitope into OmpA reduces OmpA expression levels through increased degradation (see previous Chapter). Increased degradation of the fusion GFP-FtsQ-AcrA-(OmpA-177)^{FLAG} and formation of GFP-FtsQ* then explains the observed reduced toxicity and partially restored mid-cell localization.

Thus, the degradation of GFP-FtsQ-AcrA, together with stabilization upon further extension with e.g. HSV or the OmpA barrel, can explain all observations, if it is further assumed that either FtsQ-AcrA is sterically excluded from mid-cell or efflux pumps are present in the cylindrical part of the cell but not at mid-cell.

How to explain our “explanation”? I.e. why would the addition of the HSV or 3xFLAG or the OmpA β -barrel extension make the fusions more resistant to degradation? It has been shown that the flexible C-terminus of AcrA is proteolytically sensitive *in vitro* (Mikolosko et al. 2006). Furthermore, the C-terminus is required for interaction with AcrB, and possibly also with TolC (Elkins and Nikaido 2003; Touze et al. 2004). It is possible that outside of its natural complex, the AcrA C-terminus is susceptible to proteolytic degradation. Addition of an epitope tag could protect the C-terminus from degradation. As popular epitope tags, it is expected for HSV and 3xFLAG that they are resistant to degradation. Likewise, chaperones might protect the β -barrel from degradation.

Finally, results on two GFP-FtsQ-AcrA fusions not discussed here (GFP-FtsQ-AcrA-(PGLSLAVLADERRFSA) and GFP-FtsQ-AcrA-(PGPA), pMD008 and pMD009, see Materials & Methods) provide some additional evidence for the link between degradation and complementation, as GFP-FtsQ-AcrA-(PGLSLAVLADERRFSA) was found to be largely degraded to GFP-FtsQ* at 42°C as determined using immunoblotting with anti-FtsQ (data not shown), and complemented, whereas GFP-FtsQ-AcrA-(PGPA) was found to be largely intact using immunoblotting with anti-FtsQ and did not complement (8.8 μ m filaments) (Vinkenvleugel 2006).

Recommendations for future work on GFP-FtsQ-myc-ALBP

As mentioned before, to check if fusion proteins localize to mid-cell intact, *in situ* immunolabeling experiments must be performed which are directed against small epitopes attached at the C-terminus of every fusion protein. This allows co-localization of the C-terminus with the N-terminal GFP *in situ*. Unfortunately, addition of either a HSV or a 3xFLAG epitope to GFP-FtsQ-AcrA interfered with mid-cell localization.

Because of the proximity of its N- and C-termini and the poor performance of the AcrA fusion proteins, AcrA was deemed unsuitable to function as a spacer domain. Therefore, AcrA was replaced by ALBP, with in between FtsQ and ALBP a myc epitope to act as a linker and to enable detection. Localization in the presence of wild-type FtsQ was good, and degradation on immunoblot was less pronounced compared to AcrA.

To verify that the myc-ALBP fusion is intact, the next step therefore should be the addition of a small epitope tag downstream of ALBP. As the HSV tag has proven itself for the co-localization of GFP and HSV in the GFP-FtsQ-HSV fusion (Vinkenvleugel 2006), this epitope would be first choice to clone downstream the myc-ALBP fusion.

Alternatively, to avoid the laborious immunolabeling procedure and possible problems with aspecific labeling and epitope accessibility, a fluorescent protein (mCherry) could be fused to the very C-terminus of the fusion constructs. mCherry could also be used as a spacer domain itself instead of ALBP, but if multiple copies are placed in series, the presence of mCherry at mid-cell cannot be used as proof for the absence of degradation anymore. A combination of both ABLP and mCherry would be best: With mCherry attached at the very C-terminus of each fusion, more and more ALBP spacer domains can be inserted between FtsQ and mCherry.

Acknowledgements

I like to thank Thessa Vinkenvleugel for all her work on FtsQ, which formed the starting point of this work. In particular I like to thank her for imaging and measuring some of the data points in Table I. In addition, I like to thank Reinier Boon for providing the pMD015 construct, Roland Dries for help with cloning of pGV9 and Svetlana Alexeeva and Frank Poelwijk for useful discussions on cloning strategies. Finally, I like to thank the people at the Plant Pathology/ Plant Physiology departments at the University of Amsterdam (Gert-Jan de Boer, Caroline Michielse, Ringo van Wijk and Eleni Spyropoulou) for their generous help with DNA sequencing.

Materials and Methods

Strains and growth conditions

Strains used are listed in **Table II**. LMC500 (MC4100 *lysA*) and LMC531 were made chemically competent using the calcium chloride method.

For experiments performed in TY medium (1% Bacto trypton, 0.5% Bacto yeast extract, 0.5% NaCl and 3 mM NaOH) at 28°C, overnight cultures were prepared by culturing in TY at 28°C. In the morning, cells were diluted 500x into 10 ml fresh TY and grown in 3.5-4 hours to exponential phase (OD₆₀₀~0.2) before harvesting. Under these conditions t_{MD} ~50 minutes, so we expect ~5 mass doublings, and possible stationary phase accumulations have been diluted a factor 32.

Alternatively, strains were grown at 28°C in glucose minimal medium (GB1 medium, (Taschner et al. 1988). It has the following composition: 6.33 g/l K₂HPO₄·3H₂O, 2.95 g/l KH₂PO₄ (50 mM phosphate buffer pH 7.0) 1.05 g/l (NH₄)₂SO₄ (0.4 mM), 0.10 g/l MgSO₄·7H₂O (8 mM), 0.28 mg/l FeSO₄·7H₂O (1 µM), 7.1 mg/l Ca(NO₃)₂·4H₂O (30 µM), 4 mg/l thiamine (vitamin B1), 4 g/l glucose (20 mM) and 50 g/l lysine (LMC500 is *LysA*) (Monod et al. 1951; Howard-Flanders et al. 1964). For the experiments described in this chapter, overnight cultures were grown in GB1 medium with ampicillin (100 µg/ml) to an OD₄₅₀~1-3. In the morning, the cells were diluted 100x into 10 ml fresh GB1 medium +

Strains	Genotype	Reference
LMC500 (MC4100 <i>lysA</i>)	<i>F⁻, araD139, Δ(argF-lac)U169, deoC1, flbB5301, ptsF25, rbsR, relA1, rpsL150, lysA1</i>	(Taschner et al. 1988)
LMC531 (LMC500 <i>FtsQ</i> (Ts))	LMC500 <i>FtsQ1</i>	(Taschner et al. 1988)
DH5α	<i>F⁻, endA1, hsdR17(r_k⁻ m_k⁺), supE44, thi-1, recA1, gyrA, relA1, Δ(lacZYA-argF)U169, deoR, Φ80 lacZAM15</i>	Lab collection
DH5α-Z1	DH5α <i>LacI_q⁺ TetR⁺</i>	(Lutz and Bujard 1997)

Table II. Strains used in this study.

Amp and grown in 7-8 hours to an OD₄₅₀~0.3-0.6. Under these conditions, t_{MD} ~90 minutes, so we again expect ~5 mass doublings. We compared cells expressing GFP-FtsQ-AcrA not grown to steady state with earlier images that were grown to steady state by continuous growth and dilution in GB1 for 2-3 days, and found that cell morphology and GFP localization are similar. For the results shown in **Table I**, cells were used that were grown to steady state, here defined as the moment when the average cell mass/optical density does not change anymore (Fishov et al. 1995).

DNA Constructs

All DNA manipulation, analysis and bacterial transformations were performed according to standard protocols (Sambrook and Russel 2001). All PCR fragments were sequenced, either at Baseclear (Leiden) or at the AMC DNA sequencing facility (Amsterdam Medical Centre). Primers were ordered from MWG or Biolegio, and Advantage DNA polymerase (Clontech) or *pfuTurbo* DNA polymerase (Stratagene) was used for the PCR reactions. All plasmids relevant to this chapter are listed in **Table III**.

To facilitate sub-cloning of C-terminal peptides/protein domains, a BglII site and a PstI site were introduced at the C-terminus of FtsQ (resulting in 4 extra residues RSLQ) using a PCR on pIB3 (containing GFP-FtsQ) using FtsQEcoRIsense and FtsQBglIIHindIIIRev primers. The fragment was ligated in pTHV022 via EcoRI/HindIII to form pMD001. As pTHV022 (pTrc99A-two-down) contained an in-active promoter, the fragment was subsequently sub-cloned in pTHV039 to form pMD003. pTHV039 is GFPmut2 fluorescent protein (Cormack et al. 1996) fused via linker EFNNN to FtsQ (excluding the start codon) cloned into the empty expression vector pTHV37. pTHV37 is identical to pTrc99A (Pharmacia), except for a “down” mutation in the –35 promoter region, which weakens the promoter, thereby reducing expression (Weiss et al. 1999). All further DNA constructs in this chapter are constructed in this plasmid.

Subsequently, the HSV-tag (FtsQHSVBglIIIFw and FtsQHSVtagHindIIIRev) was ligated in the BglII-HindIII sites of pMD003 to yield pMD007 that expressed GFP-FtsQ-HSV. Residues 27-397 of AcrA (i.e. excluding the signal sequence and the lipidated cysteine) were PCR-ed from the chromosome of LMC500 using the AcrA27BglIIIFw and AcrAXmaIRev primers and ligated via BglII-HindIII in pMD003 to yield pMD008. An additional bp in the XmaI site (CCCCGGGG) caused a frame-shift resulting in an additional 24 c-terminal residues. Then, either a HSV or a 3xFLAG epitope was introduced

at the C-terminus of AcrA via this XmaI site. This was done by annealing partially complementary oligos (AcrAHSVXmaIFw and AcrAHSVHindIIIRev) or (AcrA3xFLAGFw and AcrA3xFLAGRev) and ligating them into pMD008 via XmaI/HindIII to form pMD009 and pMD015, respectively. pMD017 was constructed by ligation of a PCR product on pMD005 (using primers OmpAXmaIFW and OmpAHindIIIRV) and subsequent ligation of the fragment into pMD008 via XmaI/HindIII.

A DNA fragment of the C-terminus of AcrA, obtained by PCR using the BsiWI-AcrAFw and XmaI-AcrARev primers on pMD008, was swapped via BsiWI/HindIII into pMD008 and corrected the XmaI site resulting into pMD208. Subsequently, pMD009, pMD015, and pMD017 were corrected to pMD209, pMD215 and pMD217 via the sub-cloning of an NcoI/XmaI fragment from pMD208. PCR fragments of pGV2 and pGV3 (see **Chapter 3**) using primers OmpAXmaIFW and OmpAHindIIIRV were ligated into pMD208 via XmaI/HindIII to form pGV5 and pGV6 respectively.

The myc-ALBP extension was constructed as follows: A PCR on pMD208 with primers

Plasmid	Protein	Molecular Weight (kDa)	Reference
pTHV039	GFP-(EFNNN)-FtsQ; GFP-FtsQ	58.7	(Vinkenvleugel 2006)
pMD003	GFP-FtsQ-(RSLQ)	59.2	(Vinkenvleugel 2006)
pMD007	GFP-FtsQ-HSV	60.2	(Vinkenvleugel 2006)
pMD208	GFP-FtsQ-AcrA	98.7	(Vinkenvleugel 2006)
pMD209	GFP-FtsQ-AcrA-HSV	100.0	(Vinkenvleugel 2006)
pMD215	GFP-FtsQ-AcrA-3xFLAG	101.7	(Vinkenvleugel 2006)
pMD217	GFP-FtsQ-AcrA-OmpA	118.2	This study
pGV5	GFP-FtsQ-AcrA-OmpA ^{FLAG}	121.0	This study
pGV6	GFP-FtsQ-AcrA-OmpA ^{myc}	120.6	This study
pGV7	GFP-FtsQ-(GSSSSRG); GFP-FtsQ-MCS	59.4	This study
pGV9	GFP-FtsQ-myc-ALBP	91.2	This study

Table III: Plasmids used in this study. All vectors are based on pTHV037 (Den Blaauwen et al. 2003). Predicted molecular weight is indicated in kDa.

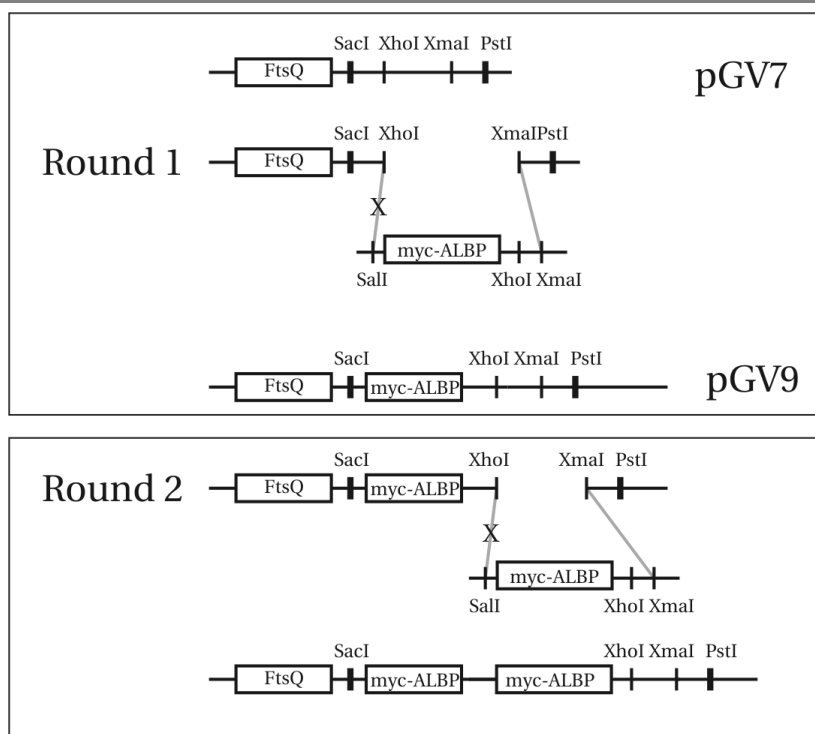


Figure 4.8. Compatible cohesive-ends cloning strategy to clone a series of identical repeats. The insert containing the myc-ALBP spacer fragment contains three restriction sites of which two have compatible cohesive-ends that annihilate each other (SalI/XhoI). Cutting the vector with XhoI/XmaI allows directional cloning of the insert, and after ligation, the existing XhoI site in the vector has disappeared and a new XhoI site (present in the insert) has appeared downstream of the added DNA fragment. “Round 2” shows how repeating the steps in “Round 1” would allow insertion of the next myc-ALBP fragment.

KpnIFtsQFW and FtsQSacIXhoIXmaIPstIHindIIIRV was cloned into pGEM-T, sequenced and subsequently subcloned via KpnI/HindIII into pMD208 resulting in pGV7. The ALBP gene (excluding the signal sequence) was PCR-ed from the LMC500 genome using primers SalImycALBPFW and ALBPXhoIXmaIRV, cloned into pGEM-T and sequenced. Then pGV7 was digested with XhoI/XmaI and ligated with SalI/XmaI digested pGEM-T-(myc-ALBP) to form pGV9. In this process XhoI/SalI annihilate each other and only one XhoI is left behind at the very C-terminus, allowing additional myc-ALBP building blocks to be ligated in (see **Figure 4.8**).

To add additional myc-ALBP fragments, one of two strategies can be followed. Either

by step-by-step addition of single fragments (repeating the procedure that lead to pGV9), or alternatively, as follows:

Adding ligase to purified Sall/XhoI myc-ALBP DNA generates potential inserts containing 1,2,3... myc-ALBP fragments, with each fragment in either a forward or reverse orientation. Only if all fragments are ligated in the proper orientation will XhoI annihilate all internal Sall sites. Therefore, by subsequently digesting with Sall/XhoI, only fragments that are in the correct orientation will remain, and the desired band (e.g. myc-ALBP-myc-ALBP) can be isolated from gel and ligated to XhoI-digested, dephosphorylated pGV9 vector, forming, after screening for the proper orientation, pGV13 (however, after initial attempts to create pGV13, the FtsQ project was put on hold). A list of primer sequences is available on request.

SDS-PAGE and Western blotting

As Protein gel electrophoresis system we used the Bio-Rad mini-gel system protean III. For SDS-PAGE, samples were mixed with sample buffer (end concentration: 62.5 mM Tris pH 6.8, 2% SDS, 10% glycerol, 2% 2-mercaptoethanol) heated to 99°C for 5 min and electrophoresed on 15% polyacrylamide slabs. The bio-rad semi-dry blotting apparatus was used for immunoblotting. Anti-GFP polyclonal antibody (Molecular probes) was used at 1:1000. The bands were detected using the ECL+ chemiluminescence kit (Amersham) and scanning with the STORM 860 fluorescence imager.

Immunolabeling of permeabilized cells

Cells were grown to steady state in GB1 medium at 28°C, fixed in 2.8% formaldehyde and 0.04% glutaraldehyde for 15 min and resuspended in PBS. Membranes were (partially?) dissolved by incubation for 45 min at RT with 0.1% Triton X-100 in PBS. The cells were permeabilized by incubation for 45 min at RT with a fresh solution of lysozyme (100 µg/ml) and EDTA (5 mM e.c.). Next, cells were washed three times by pelleting (7000 rpm for 5 min in a Eppendorf tabletop centrifuge) and resuspension in PBS. Cells were blocked for aspecific binding sites by incubation for 30 min at 37°C in a fresh solution of 5 mg/ml "Blocking reagent for DNA hybridization" (#11096176, Roche) in PBS. Then, primary antibody (mouse monoclonal anti-myc, Roche) was added (end concentration 50 µg/ml) and the cells were incubated for 2 h at 37°C. Then, the cells were washed with PBS/0.05% (v/v) Tween20 and resuspended in blocking reagent. Then, Donkey-anti-mouse Cy3-

conjugated secondary antibody (Jackson ImmunoResearch, USA) was added at 5 µg/ml and the cells were incubated for 30 min at 37°C. Finally, the cells were washed with PBS/0.05% Tween20, resuspended in PBS and stored at 4°C before imaging.

Fluorescence Microscopy

Cells were immobilized on 1% agarose in water slabs-coated object glasses as described by (Koppelman et al. 2004) and photographed with a CoolSnap *fx* (Photometrics) CCD camera mounted on an Olympus BX-60 fluorescence microscope through a UPLANFL 100x/1.3 oil objective (Japan). Images were taken using the public domain program Object-Image2.19 by Norbert Vischer (University of Amsterdam, <http://simon.bio.uva.nl/object-image.html>), which is based on NIH Image by Wayne Rasband. In all experiments the cells were first photographed in the phase contrast mode. Then a fluorescence image was taken using either a blue excitation/green emission filter cube (green channel, EGFP, ex. 450–490 nm, em. 505–555 nm). Images were processed in ImageJ.

V

Chapter 5: Outer membrane assembly of N- and C-terminal fusions to the OmpA transmembrane domain

Abstract

With the aim of sub-localizing the OmpA transmembrane (TM) domain to the site of constriction (mid-cell) in dividing *Escherichia coli*, we studied the outer membrane (OM) assembly of N- or C-terminal fusions to this domain. Various protein domains were genetically fused to the OmpA TM domain. A rare-sugar (D-allose) binding protein (ALBP), and the fluorescent protein mCherry were used that were expected not to interact specifically with other proteins (non-interacting domains). As mid-cell localization domains, the Pal lipoprotein and the septal targeting domain from AmiC (^TamiC), a Tat substrate, were used. As the OmpA TM domain had either a FLAG epitope or a streptavidin binding peptide inserted in a surface-exposed loop, OM assembly could be evaluated using cell surface immunolabeling. Furthermore, the *in vivo* folding state of the OmpA TM domain was determined by a gel-shift assay. In addition, for mCherry fusions, fluorescence microscopy was used to study sub-cellular localization. Our results show that non-interacting fusions to either the N- or the C-terminus of the OmpA TM domain can be assembled in the OM. Interestingly, the localization of the (OmpA-177)-Pal fusion was excluded from mid-cell in the presence of wild type Pal. Finally, we present two specific cases of N-terminal fusions that are not incorporated in the OM, presumably due to specific needs of these fusions.

Introduction

The outer membrane of Gram-negative bacteria contains a variety of proteins (OMPs) that fold as a single protein domain with a compact β -barrel fold. A well-known OMP with an additional C-terminal domain is OmpA, which consists of a N-terminal transmembrane (TM) domain (first 170 residues of the mature protein), connected to a C-terminal periplasmic peptidoglycan (PG)-binding domain. Our goal was to create, in dividing cells, an anchor point in the bacterial outer membrane, such that a micron-sized bead could be attached to a living bacterium and act as both handle and force probe in biophysical experiments. It has been shown that the OmpA TM domain can insert in the OM as efficiently as the full-length protein (Ried et al. 1994), even with an epitope tag inserted into one of its surface-exposed loops (Verhoeven et al. 2008). A possible approach then, is to genetically link the OmpA TM domain to a periplasmic domain that is known to localize to the site of constriction (mid-cell). This requires that the OmpA TM domain (OmpA-177) can insert into the OM with a heterologous domain attached to either its N- or C-terminus.

What would be a suitable mid-cell domain? A high copy number is preferred, preferably $>10^3$, because mid-cell localization and OM insertion at mid-cell of a artificial OMP fusion protein will most likely not be 100% efficient. Assuming only 10% properly inserts and localizes to mid-cell, this would give us $>10^2$ concentrated anchor points, which would allow their detection with conventional fluorescence microscopy. Of course, increasing the number of anchor points at mid-cell also increases the probability of bead attachment.

When this study was initiated, all known periplasmic domains with mid-cell affinity were low copy number ($<10^3$) inner membrane (IM) proteins that extend outwards into the periplasm. Typically, they diffuse around in the IM and dynamically associate with other cell division proteins to form the divisome. One of them, the FtsQ protein, has a copy number of 25-50 (Carson et al. 1991), and consists of an IM α -helix connected to a periplasmic moiety of two sub-domains (van den Ent et al. 2008). For this protein, it has been shown that its C-terminus can be extended with a HSV epitope without interfering with mid-cell localization in the presence of wildtype FtsQ (Vinkenvleugel 2006). Therefore FtsQ was selected as mid-cell localization domain.

As a fusion protein bridging FtsQ and OmpA-177 needs to go through the peptidoglycan layer, we are faced with a potential problem. OM insertion of OmpA-177

when fused to FtsQ should be well timed: it should not occur as long as the FtsQ domain diffuses around, as the fusion might become trapped in the PG mesh. After FtsQ localizes to mid-cell, it should occur as soon as possible, as FtsQ localizes to mid-cell a few minutes before a (phase contrast-) visible constriction appears (Aarsman et al. 2005), at which time the anchor presented by OmpA-177 should be in place for bead tethering.

How to span the periplasm? As the solute-accessible periplasmic width of *Escherichia coli* is estimated at ~15-21 nm (Matias et al. 2003; Collins et al. 2007), and the C-terminus of FtsQ can extend up to 7 nm into the periplasm (van den Ent et al. 2008), a spacer of ~8-14 nm is needed. To prevent proteolysis and/or misfolding it was decided to use native, folded domains instead of unstructured or artificial amino acid sequences. Preferably, the spacer domain should not have any interactions with other cellular components, as these could interfere with mid-cell and/or OM localization. Finally, its N- and C-terminus should be sufficiently separated to act as spacer domain. With these considerations in mind, the periplasmic D-allose binding protein ALBP (Chaudhuri et al. 1999) was chosen. As the D-allose operon is not expressed when its substrate D-allose is absent (Kim et al. 1997), ALBP's main interaction partners will be expected to be absent when grown in a defined medium without D-allose. Furthermore, its N- and C-terminus are on opposite sides of the protein roughly 5 nm away (Chaudhuri et al. 1999). To be able to detect the spacer construct, and to facilitate proper folding of the individual domains, a myc epitope is fused as a linker between two ALBP domains.

During the course of this study, two periplasmic mid-cell domains that bind at the OM side of the PG were discovered (Bernhardt and de Boer 2003; Gerding et al. 2007). Such domains could simplify things enormously, as only a single domain has to be fused to OmpA-177, and the risk of entanglement in the PG would be reduced considerably. One of these domains was Pal, a peptidoglycan-associated lipoprotein (Gerding et al. 2007). It appeared an ideal candidate for fusion to OmpA-177, as it is anchored to the OM, its fold was homologous to the periplasmic domain of OmpA and it has a high copy number of 10^4 (Cascales et al. 2002; Gerding et al. 2007). Also, a Pal-mCherry fusion, expressed at levels expected to be $>10^3$ in a Δ Pal strain, shows almost exclusive localization to mid-cell (Gerding et al. 2007). This suggests that several thousands of potential binding sites at mid-cell are available, indicating a high mid-cell localization potential for a Pal fusion protein. A second periplasmic domain discovered in recent years was the septal targeting domain

	staining	HM
	+	+
	+	+
	+	+
	+	ND
	+	+
	+/-	+
	+/-	+/-
	-	-
	-	ND
	-	ND

Figure 5.1. All domain fusions to the TM domain of OmpA drawn schematically. SS indicates either the signal sequence of OmpA, DsbA, ALBP, Pal or AmiC, depending on the construct. See **Table II** (Materials and methods) for details. The OmpA-177 TM domain contained either a 3xFLAG or a SA-1 peptide insertion in one of its surface exposed loops. OmpA-like indicates the native periplasmic domain of OmpA. Linker sequences are indicated with L1, L2 and L3 and consist of residues LEDPPAEF, SRAQQ and GSS, respectively. Myc represents the residues (GSST)EQKLISEEDL.

of AmiC (Bernhardt and de Boer 2003). Similar arguments as for Pal can be made for it, with a potential caveat that it is a Tat substrate. However, the Tat system can export fusion proteins, as an AmiC-GFP fusion is fully functional in the periplasm (Bernhardt and de Boer 2003).

We constructed a series of fusion proteins to either N- or C-terminus of the OmpA TM domain (see **Figure 5.1** for a schematic overview of all the constructs). To test the efficiency of OM insertion, OmpA-177 was fused to tandem ALBP domains at its N-terminus (designed to be fused behind the FtsQ protein), and mCherry was fused either to its N- or C-terminus. Next, the mid-cell domains Pal and ^TamiC were fused to OmpA-177,

of which Pal to either terminus, and ^TAmiC only to the N-terminus. Fusions were analyzed using immunoblots, combined with a gel-shift assay (also called heat-modifiability) to test the folding state of the OmpA-177 domain. Furthermore, the epitope in the OmpA-177 was detected on the cell surface by fluorescent labeling. Constructs that carried a mCherry fluorescent protein as part of the domain fusion could be imaged directly, and the localization pattern compared with that of fluorescent staining.

It was found that with either the mCherry or the Pal domain fused to its C-terminus, the OmpA TM domain was able to efficiently insert in the OM. Interestingly, the localization of the (OmpA-177)-Pal fusion was excluded from mid-cell in the presence of wild type Pal, but not in Δ Pal background. When a domain was fused to the N-terminus of the OmpA TM domain, non-interacting domains (mCherry, tandem ALBP domains) allowed OM insertion, but with reduced efficiency. However, both for the Pal domain, and the ^TAmiC domain, no OM incorporation of the OmpA TM domain was observed when fused to the N-terminus of OmpA-177. Instead, these fusions behaved as if the OmpA TM domain was absent. For Pal, the N-terminus, which is lipidated and targeted to the OM by the Lol system, could interfere with OM assembly of the OmpA TM domain. For the targeting domain of AmiC, the Tat system could be incompatible with OM assembly of the OmpA TM domain.

Results

As a starting point we used a construct that consists of the TM domain of OmpA (OmpA-177), either with a streptavidin binding peptide (SA-1) (Besette et al. 2004) inserted in surface-exposed loop 1 (OmpA-177^{SA-1}) or with a 3xFLAG epitope inserted in surface-exposed loop 3 (OmpA-177^{FLAG}). Both were shown to insert correctly in the OM, although OmpA-177^{FLAG} had reduced protein levels (**Chapter 3**). All constructs were expressed from a IPTG-inducible weakened-pTrc99A vector (Den Blaauwen et al. 2003). It was found that when cells were grown in MOPS glucose defined rich medium (DRu) (Neidhardt et al. 1974), 50-100 μ M IPTG was needed to get expression levels similar to the basal expression level when grown in TY medium without IPTG (see Materials & Methods).

In the following, experiments with fusions to OmpA-177^{FLAG} were performed in the wild-type strain LMC500 (MC4100 *lysA*) grown in GB1 minimal medium (defined) or TY medium (undefined). Intact cells were fluorescently labeled with anti-FLAG antibody followed by a fluorescent secondary reporter. Experiments with fusions to OmpA-177^{SA-1} were performed in wild-type strain MC1061, grown in DRu medium or TY medium. Cells expressing these constructs were labeled directly with fluorescent streptavidin. Both OmpA-177^{FLAG} as well as OmpA-177^{SA-1}, in both genetic backgrounds (LMC500 and MC1061), became homogeneously fluorescent along the perimeter of the cell after fluorescent labeling (**Figure 5.2A**). No essential differences between fusions to either OmpA-177^{FLAG} or OmpA-177^{SA-1} were observed.

A C-terminal Pal fusion to the OmpA TM domain

An (OmpA-177)-Pal fusion protein was constructed that starts with the signal sequence and TM domain of OmpA, and continues after residue 177 with residues 2-152 of the mature Pal domain (i.e. excluding its signal sequence and the N-terminal lipidated cysteine). At the C-terminus, four residues (LEDP) form part of a linker that allows sub-cloning of the mCherry fluorescent protein (Shaner et al. 2004). Residues 2-39 of Pal are thought to form a unstructured linker region (Cascales and Lloubes 2004). In **Figure 5.1**, all fusions presented in this paper are drawn schematically. Pal Fusions to either OmpA-177^{FLAG} or OmpA-177^{SA-1} were constructed. Correct expression of the construct was verified on immunoblot for the FLAG fusion in LMC500, and a strong band at 41 kDa was detected (calculated at 39 kDa, but 3xFLAG retards proteins a few kDa) (data not

Outer membrane assembly of OmpA fusion proteins

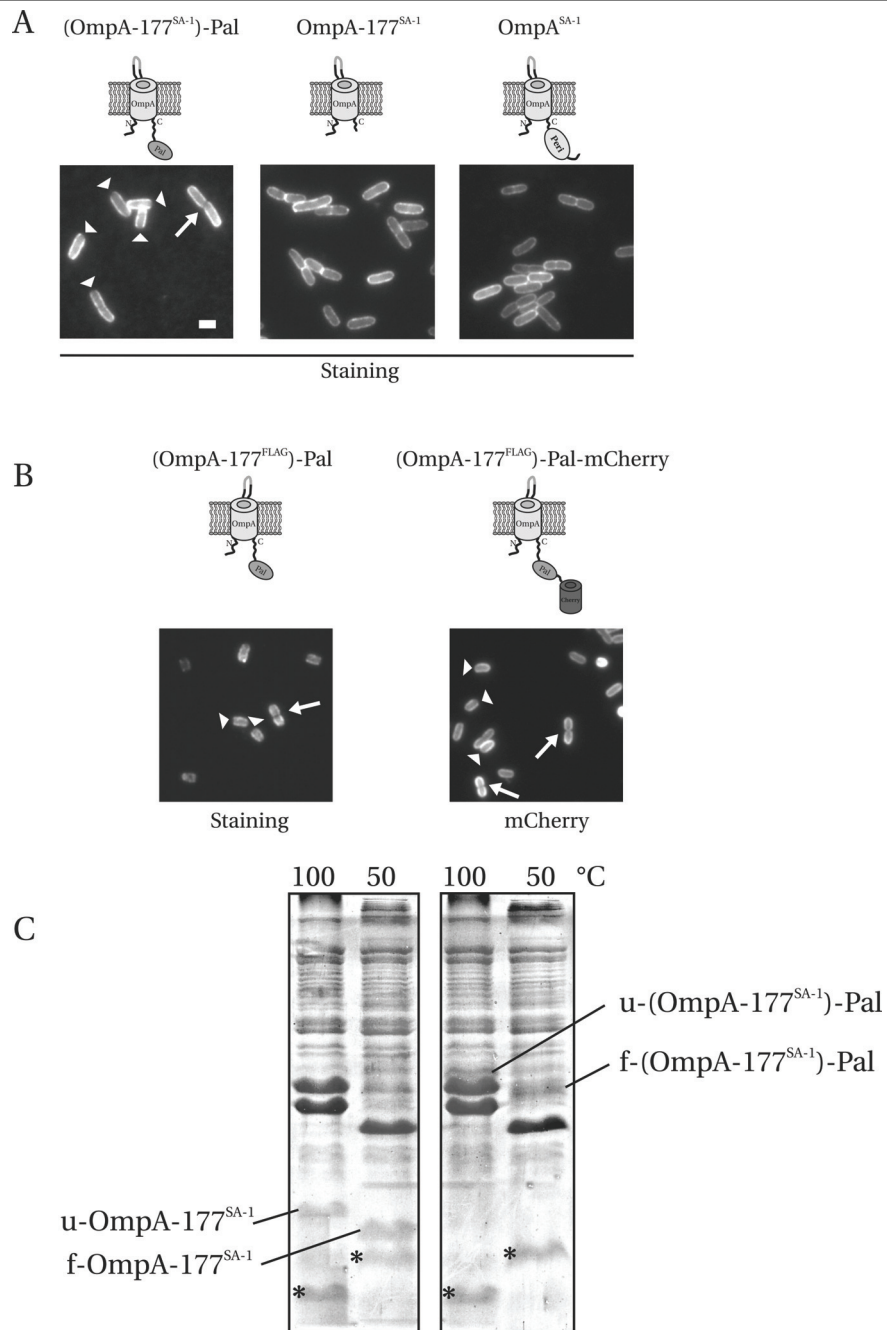


Figure 5.2. OmpA-177-Pal fusion inserts in the OM, but does not localize to mid-cell. (A) MC1061 cells expressing (OmpA-177^{SA-1})-Pal, OmpA-177^{SA-1} or OmpA^{SA-1} (with linker L1 present at its C-terminus, see Figure 1) were grown to exponential phase in DRu medium at 28°C in the presence of 0.1 mM IPTG to an OD600 of 1.0, and labeled on ice with fluorescent streptavidin for 30 min. The cells were then fixed and imaged. The triangles indicate a reduced fluorescence at one pole of non-dividing cells. The arrow indicates a reduced fluorescence at mid-cell in a dividing cell. (B) LMC500 cells expressing (OmpA-177^{FLAG})-Pal were grown to exponential phase in GB1 medium at 28°C in the presence of 0.03 mM IPTG to an OD450 of 0.2 and were labeled with biotinylated anti-FLAG followed by fluorescent streptavidin. The cells were then fixed and imaged. Cells grown under the same conditions expressing (OmpA-177^{FLAG})-Pal-mCherry were fixed and imaged directly. The scale bar is 1 x 2 μ m, and exposure time was 470 ms for all images. The triangles indicate a reduced fluorescence at one pole of non-dividing cells. The arrow indicates a reduced fluorescence at mid-cell in a dividing cell. (C) A Coomassie stained SDS-PAGE gel containing membrane fractions of MC1061 cells expressing either OmpA-177^{SA-1} or (OmpA-177^{SA-1})-Pal grown to exponential phase in DRu medium at 28°C in the presence of 0.1 mM IPTG. Samples were either heated in sample buffer at 99°C for 10 minutes or heated at 50°C for 15 minutes, as indicated. The asterisk indicates an unidentified heat-modifiable band present in both samples. Folded and unfolded β -barrels are indicated with f- and u-, respectively.

shown). Heat modifiability experiments (Verhoeven et al. 2008) of a Coomassie blue stained membrane fraction of cells expressing the OmpA-177^{SA1}-Pal fusion demonstrate that the construct is intact (at 38 kDa, equal to its calculated kDa) and heat-modifiable, and therefore present in the OM, consistent with its detection on the cell surface (**Figure 5.2C**).

(OmpA-177)-Pal in wild-type cells is excluded from mid-cell

The constructs were first studied in a wild-type background (*Pal*⁺). Surprisingly, the addition of the Pal domain leads to the exclusion of the OmpA TM domain from mid-cell, and from (what is most likely) the newly synthesized poles of newborn cells (**Figure 5.2A**). In contrast, labeling of both a strain expressing the OmpA TM domain without Pal, and a strain expressing the full-length OmpA protein, resulted in homogeneous staining patterns with fluorescence along the cell perimeter. In addition, constricting cells even showed a slightly *increased* fluorescence at mid-cell (approximately a factor of 2, as the intensity increase along two cells lying adjacent is similar, thus most likely caused by the close proximity of two OM's during division).

To exclude a possible artifact of the staining procedure (e.g. further cell growth after

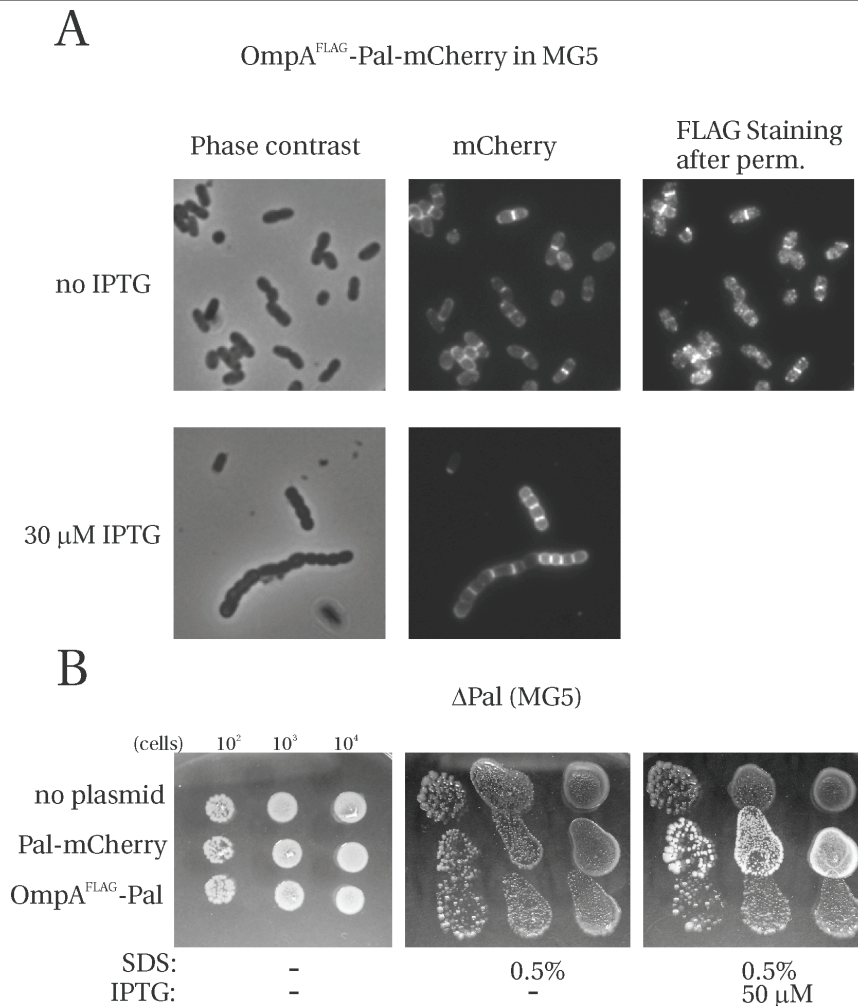


Figure 5.3. OmpA-177^{FLAG}-Pal-mCherry is localized at mid-cell in a ΔPal strain, but not exposed.

Cells were grown to exponential phase in GB1 medium at 28°C, fixed, permeabilized, immunolabeled and imaged (“no IPTG”) or fixed and imaged directly (“30 μM IPTG”). (A) Exposure times were: mCherry 1 s, FLAG staining (Alexa-488-conjugated antibodies) 330 ms (no induction) and mCherry, 150 ms (30 μM IPTG). (B) SDS hypersensitivity assay. The SDS sensitivity of MG5 (ΔPal) is alleviated by expressing proPal-mCherry, but not OmpA-177^{FLAG}-Pal. The difference became clearer after prolonged incubation at room temperature, therefore the SDS plates were imaged after one week at RT.

washing away the fluorescent probe), we constructed a triple fusion by addition of

mCherry to the C-terminus of Pal, which allows direct visualization of the observed sub-localization pattern. Continuous expression with 50 μ M IPTG of the (OmpA-177^{FLAG})-Pal fusion had no effect on growth rate in LMC500. The triple fusion (OmpA-177^{FLAG})-Pal-mCherry was toxic for IPTG concentrations exceeding 30-50 μ M. Induction of this triple fusion gave a similar fluorescent mCherry pattern as observed with labeling against the FLAG tag of a fusion without mCherry (**Figure 5.2B**). As expected, staining of the triple fusion against the FLAG tag gave a pattern that co-localized with mCherry fluorescence (data not shown). Therefore, we conclude that the exclusion of (OmpA-177)-Pal from the division site is not an artifact of the staining procedure.

Localization of (OmpA-177)-Pal in Δ Pal cells

We reasoned that the OmpA-Pal fusion could not compete with wild-type Pal for septal localization, and therefore also expressed the fusion in a Δ Pal strain (MG5). Δ Pal cells have an increased sensitivity to detergents such as SDS (Gerding et al. 2007). These authors showed that IPTG-induced expression of a Pal-mCherry fusion from plasmid was able to rescue this hypersensitivity, allowing growth on plates containing 0.5% SDS. As partial induction of (OmpA-177^{FLAG})-Pal (50 μ M IPTG) in a wild-type background did not interfere with cell growth, we asked whether it was able to complement the Pal deletion in a similar fashion as Pal-mCherry did. OmpA^{FLAG}-Pal did not complement the Δ Pal strain in this assay (**Figure 5.3B**).

Both (OmpA-177^{FLAG})-Pal as well as the triple fusion (OmpA-177^{FLAG})-Pal-mCherry were toxic when grown in the continuous presence of 30 μ M IPTG in GB1 medium, and in the case of (OmpA-177^{FLAG})-Pal-mCherry lead to filaments consisting of cells with multiple stalled constrictions at very short intervals, as if length growth was also affected (**Figure 5.3A**). Apparently, in the absence of wild-type Pal, this fusion inhibits completion of constriction, but allows the formation of new constrictions.

When Δ Pal cells expressing the (OmpA-177^{FLAG})-Pal-mCherry fusion were grown without induction, mCherry was clearly localized to mid-cell in constricting cells (**Figure 5.3A**). As reported before for Δ Pal cells expressing a Tat-exported periplasmic GFP protein (Gerding et al. 2007), fluorescent vesicles accumulated in the medium, and cells had fluorescent blebs (data not shown). Without induction, immunolabeled Δ Pal cells expressing OmpA^{FLAG}-Pal (with or without mCherry) presented only a few FLAG spots on the cell surface (data not shown). However, after fixation and permeabilization, a clear

FLAG signal at mid-cell was detected in constricting cells (**Figure 5.3A**, and data not shown). This signal was absent in fixed and permeabilized Δ Pal cells without plasmid, where only a homogeneous aspecific background was observed after labeling with anti-FLAG (data not shown). This suggests that OmpA-177^{FLAG} is present at mid-cell, but in the periplasm and not in the OM, as permeabilization of the outer membrane was required for the antibodies to reach the FLAG epitope.

Although as mentioned, continuous growth of the triple fusion in the presence of 30 μ M IPTG was toxic, we added 30 μ M IPTG to an exponentially growing culture of cells expressing (OmpA-177^{FLAG})-Pal-mCherry, and after 3 hours of induction, labeled living cells with biotinylated anti-FLAG. Again, constricting cells have a strong mCherry band at mid-cell. Instead of a few FLAG spots, at these higher expression levels, staining has become homogeneous along the perimeter of the cell. In this sample, that had not been permeabilized, lysed cells were present at a low frequency (<1%), and only these cells had in addition to a mCherry band also a co-localized FLAG band at mid-cell. This suggests that next to OmpA-177^{FLAG} detected homogeneously on the cell surface, OmpA-177^{FLAG} is also present at mid-cell, but in the periplasm and not in the OM, as only in (partially) lysed cells the antibody could reach the FLAG epitope.

These observations suggest that in these cells, (at least) two populations of (OmpA-177)-Pal were present: (i) (OmpA-177)-Pal that is incorporated randomly in the OM, without any preference for mid-cell, and (ii) (OmpA-177)-Pal that is localized at mid-cell, but is not incorporated in the OM (perhaps due to OM blebbing). We conclude that the Pal domain cannot specifically target OM incorporated OmpA-177 to the site of constriction, presumably because it can neither compete (in wild-type cells) nor replace (in Δ Pal cells) wild-type Pal.

A C-terminal mCherry fusion to the OmpA TM domain

We decided to explore the possibilities of using mCherry as a fluorescent protein domain to study OM assembly of OmpA-177 with heterologous domains attached. Furthermore, as mCherry is not expected to interact with endogenous proteins, and becomes fluorescent in the periplasm, it is also an attractive candidate to function as a spacer domain in mid-cell localization fusion constructs. As we already knew that the OmpA TM domain could insert when Pal was fused to its C-terminus, we started by replacing Pal with mCherry. Using dual color fluorescence microscopy imaging, we find that the fusion is exported to the

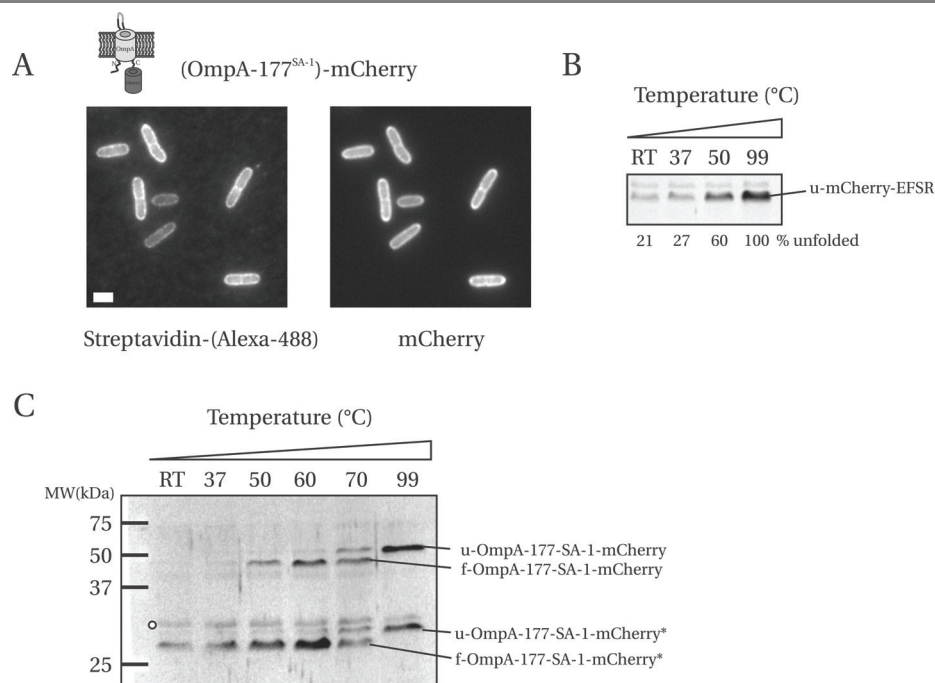


Figure 5.4. Outer membrane assembly of a fusion between the C-terminus of the OmpA TM domain and mCherry. A) Cells grown to exponential phase in DRu medium with 0.1 mM IPTG were labeled with fluorescent streptavidin. Exposure times are as indicated (contrast is enhanced). Scale bar is 1 x 2 μ m. B) Heat-modifiability of mCherry-EFSR. Sonicated cell lysate of LMC500 expressing mCherry-EFSR was resuspended in sample buffer and either; not heated (RT), heated at 37°C for 5 min, heated at 50°C for 15 min, or heated at 99°C for 10 min. Shown is an immunoblot probed with anti-DsRed antibody. The faint band present in each lane is aspecific. The unfolded (denatured) mCherry-EFSR band is indicated. Percentage of unfolded mCherry-EFSR are indicated, assuming that after heating at 99°C all protein is unfolded. C) Heat-modifiability of OmpA-177-SA-1-mCherry. Cells from the same culture used for labeling in A) were sonicated and resuspended in sample buffer. Heat treatment as in B), heating at 60°C and 70°C was for 15 min. The folded and unfolded forms of both the intact fusion and the degradation product are indicated by a preceding f- or u-, respectively.

periplasm, demonstrated by the red mCherry fluorescence along the perimeter of the cell (**Figure 5.4A**). Furthermore, we find that the OmpA TM domain is correctly inserted into the outer membrane, demonstrated by the green fluorescent staining of the SA-1 peptide on the cell surface.

To exclude that in the periplasm, the two-domain fusion was proteolytically degraded

into separate domains, heat-modifiability (gel-shift) experiments were performed. First, we checked for a possible heat-modifiability of mCherry, as it also has a β -barrel fold. To this end, we grew cells expressing a cytoplasmic mCherry, lysed them by sonication, and after varying heat treatment, subjected the samples to SDS-PAGE. We find that after heating at 37°C for 5 min in sample buffer (a condition under which GFP retains its fluorescence in-gel (Drew et al. 2006)), in-gel fluorescence of mCherry could be detected (see M&M), but fluorescence was approximately halved after heating at 50°C for 15 min (data not shown). Furthermore, mCherry could be detected on immunoblot using a monoclonal anti-DsRed antibody (**Figure 5.4B**). A band of the expected height (27 kDa) was present that increased in intensity upon heating (the faint band above it was also present in lysate without mCherry). The inverse relation between in-gel fluorescence and detection on immunoblot indicated that the anti-DsRed antibody only recognizes the denatured conformation of mCherry. We conclude that the mCherry β -barrel fold is less stable than that of the OmpA TM domain, because under conditions where the OmpA TM domain is completely stable (50°C for 15 min), the mCherry β -barrel clearly is not (**Figure 5.4B**). Therefore, the anti-DsRed can be used to determine the folding state of the OmpA TM domain, because only denatured mCherry will be visible, and any gel-shifts observed can then be unequivocally attributed to the OmpA TM domain.

To test the heat-modifiability of the OmpA-177^{SA-1}-mCherry fusion, an immunoblot containing cell lysates heated at different temperatures was probed with anti-DsRed (shown in **Figure 5.4C**). In the following, we assume that already at RT, the (folded) OmpA-177 fusion protein, present in the membrane fraction, is solubilized completely in SDS-PAGE sample buffer. At RT and 37°C, only a degradation band at 26 kDa was detected. At 50°C, mCherry starts to unfold, and the fusion becomes visible on blot. From literature and our own experiments, we know that the folded OmpA TM domain does not unfold at all under these conditions. Increasing the temperature further from 50°C to 99°C, the OmpA TM domain unfolds and the fusion shifts to its expected molecular weight of 49 kDa. These results demonstrate that the OmpA TM domain remains heat-modifiable and therefore is correctly assembled into the OM when mCherry is fused to its C-terminus.

With increasing heat-treatment, the degradation band increased in intensity, suggesting that fluorescent mCherry was present in the lysate. Plasmolysis experiments in which the (periplasmic) plasmolysis bays contain fluorescent mCherry (data not shown)

support this. Surprisingly, this degradation band contained some highly stable secondary structure with a half-life of 15 min at 70°C. After boiling this band shifted to 28 kDa. As denatured cytoplasmic mCherry (with 4 extra linker residues at its C-terminus) migrated at 27 kDa, and if we assume that the N-terminus of mCherry remained intact, then at most some 10-15 additional residues are present. This would be comprised of the LEDPPAEF linker, with only the very last C-terminal residues of OmpA-177. As there is no expected tertiary structure present in these residues, the gel-shift is difficult to explain. However, the very C-terminal end of the OmpA TM domain has recently been found to be covalently modified with oligo-(R)-3-hydroxybutyrate (Xian et al. 2007). A possible explanation could be that this modification is somehow responsible for the gel-shift. Alternatively, the degradation product is degraded on both termini, with the antibody epitope still present, and still able to partially fold to shield the antibody epitope at lower temperatures (needed to explain the increase in band intensity with increasing temperature), but with a larger portion C-terminal OmpA residues present, which tertiary structure (β -strands) unfolds upon heating.

We conclude that cells expressing OmpA-177-SA-1-mCherry contain a mixture of intact fusion assembled in the OM, and proteolytically removed, mostly fluorescent mCherry.

An N-terminal mCherry fusion to the OmpA TM domain

Having established that mCherry was suitable for our purpose, we decided to fuse mCherry to the N-terminus of the OmpA TM domain. This requires that mCherry is sandwiched between OmpA and its signal peptide. As a first step, the OmpA signal sequence was cloned upstream of mCherry and its sub-cellular localization was compared to mCherry without signal sequence. Exponentially growing cells in TY medium were fixed and imaged (**Figure 5.5A**). It is clear that introduction of the OmpA signal sequence causes an increase of mCherry at the perimeter of the cells, something one would expect if only a fraction of mCherry has been exported to the periplasm. Line profiles normal to the cell's long axis confirm this visual impression. We verified that observed cell diameters in phase contrast were equal for both strains ($\sim 1.1 \mu\text{m}$).

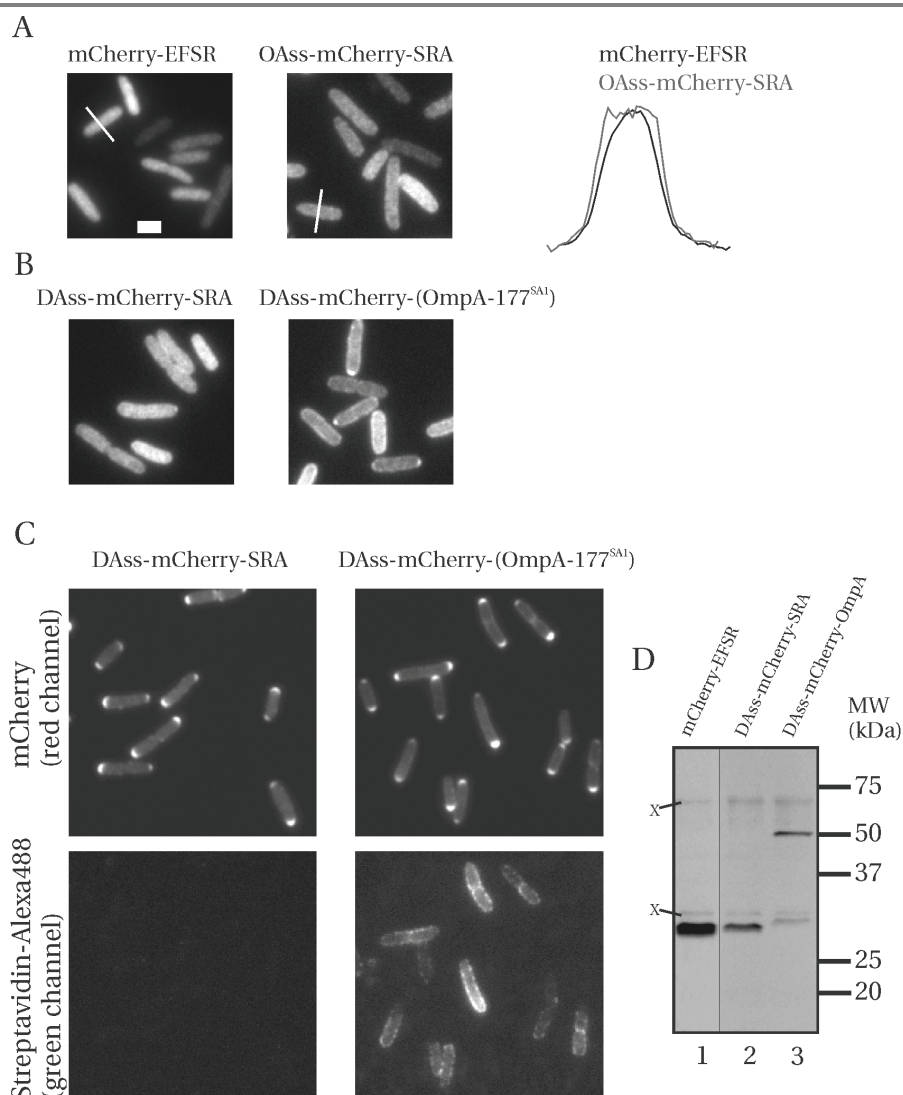


Figure 5.5. Periplasmic export of mCherry and a fusion of mCherry attached to the N-terminus of the OmpA TM domain. (A) Cells grown to exponential phase in TY medium at 28°C expressing either cytoplasmic mCherry (with C-terminal linker residues EFSR) or OmpAss-mCherry-SRA. Exposure time was 470 ms. The scale bar is 1 x 2 μ m. Representative line profiles through cells are depicted, black line: mCherry-EFSR, gray line: OmpAss-mCherry-SRA. (B) Cells expressing either DsbAss-mCherry-SRA or DsbAss-mCherry-(OmpA-177^{SA-1}). Exposure time was 470 ms. (C) Cells grown to exponential phase in DRu medium with 0.1 mM IPTG at 28°C expressing either DsbAss-

mCherry-SRA or DsbAss-mCherry-(OmpA-177^{SA-1}). Exposure times: 100 ms (mCherry), 1.5 s (streptavidin-Alexa-488). Both sets of images received the same contrast enhancements allowing comparison of intensities. **(D)** Immunoblot probed with anti-DsRed (1:500). Two aspecific bands are indicated with X. Lane 1: Sonicated lysate of LMC500 cells expressing mCherry-EFSR were grown in TY at 37°C and induced with 0.1 mM IPTG for 2 hours. Lane 2: MC1061 cells expressing DsbAss-mCherry grown in DRu at 28°C with 0.1 mM IPTG. Cells were resuspended in Sonication buffer, frozen, thawed and solubilized in sample buffer. Lane 3: MC1061 cells expressing DsbAss-mCherry-(OmpA-177^{SA-1}).

A possible explanation for the observed inefficient export could be the rapid folding of mCherry in the cytoplasm, combined with the inability of the Sec translocase to unfold it again, possibly due to (covalent) chromophore formation. If this would be the case, a signal sequence that directs mCherry to the *co*-translational SRP pathway could increase export efficiency, as was found for the cytoplasmic protein thioredoxin 1 fused to the DsbA signal sequence (Schierle et al. 2003). Unexpectedly, after replacing the post-translational OmpA signal sequence by the *co*-translational DsbA signal sequence, export of mCherry to the periplasm did not improve (**Figure 5.5B, left panel**).

Finally, we fused the TM domain of OmpA downstream of DsbAss-mCherry. Surprisingly, this did improve the amount of fluorescent mCherry observed along the perimeter (**Figure 5.5B, right panel**). Maybe the OmpA domain improves translocation, perhaps by reducing the folding rate of mCherry. Less likely, fluorescent mCherry in the cytoplasm becomes associated with the IM via the unfolded SecB-stabilized OmpA peptide moiety.

In TY medium, a mild polar mCherry localization was observed (**Figure 5.5B, right panel**), which increased with increasing expression levels, obtained by growth in DRu medium supplemented with 0.1 mM IPTG (**Figure 5.5C**). To test whether OmpA was able to assemble in the OM, cells were labeled with green fluorescent streptavidin. Dual color fluorescence imaging revealed that the TM domain of OmpA was indeed present in the OM, as a homogeneous staining along the perimeter of the cells was observed. This staining was absent for cells expressing DsbAss-mCherry without the OmpA domain (**Figure 5.5C**). As no increase in staining was observed at the poles, we conclude that apparently, (at least) two distinct populations are present, one that assembles normally in the OM, and one that does not, but accumulates in the cell poles instead.

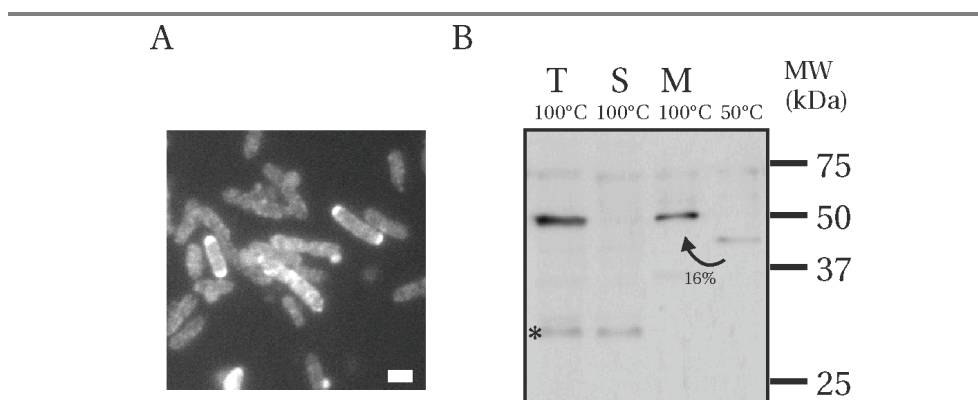


Figure 5.6. DsbAss-mCherry-(OmpA-177^{SA-1}) is heat-modifiable. MC1061 Δ OmpA cells were grown to exponential phase in TY medium and expression was induced with 30 μ M IPTG and induced for 1 hour. When the cells had reached OD600~1.0, **(A)** a sample was fixed in 0.25% formaldehyde and imaged. The scale bar is 1 x 2 μ m. **(B)** The rest of the cells were sonicated on ice, and total lysate (T) was fractionated in soluble (S) and insoluble (membrane, M) fractions (see M&M). Samples were either heated to 99°C for 10 minutes or to 50°C for 15 minutes, subjected to SDS-PAGE and immunoblotted with anti-DsRed antibody (1:500). The asterisk indicates a degradation product at ~28 kDa.

Immunoblots probed with anti-DsRed (**Figure 5.5D**) revealed that under the growth conditions of **Figure 5.5C**, DsbAss-mCherry migrated as a single band, at the exact same height as mCherry-EFSR (27 kDa). This suggests that DsbAss-mCherry is fully processed, and the accumulation in the poles takes place in the periplasm. The DsbAss-mCherry-OmpA fusion was detected predominantly as intact fusion at 48-50 kDa, with a minor degradation band at 28 kDa.

Finally, it was verified that the fusion detected on the cell surface was intact by heat-modifiability experiments. Cells induced for expression of the DsbAss-mCherry-OmpA fusion were fractionated into soluble and insoluble (membrane) fractions. The membrane fraction was either completely denatured (heating at 99°C for 10 minutes) or heated to 50°C for 15 min. It was found that the intact fusion was heat-modifiable (**Figure 5.6**), suggesting that the OmpA TM domain was properly incorporated in the OM. At first sight, this seems strange, as the fluorescent mCherry in the poles was not detected on the cell surface. However, only denatured mCherry can be detected with the antibody used. Quantifying the relative intensities of detected mCherry on blot at 50°C and at 99°C, we

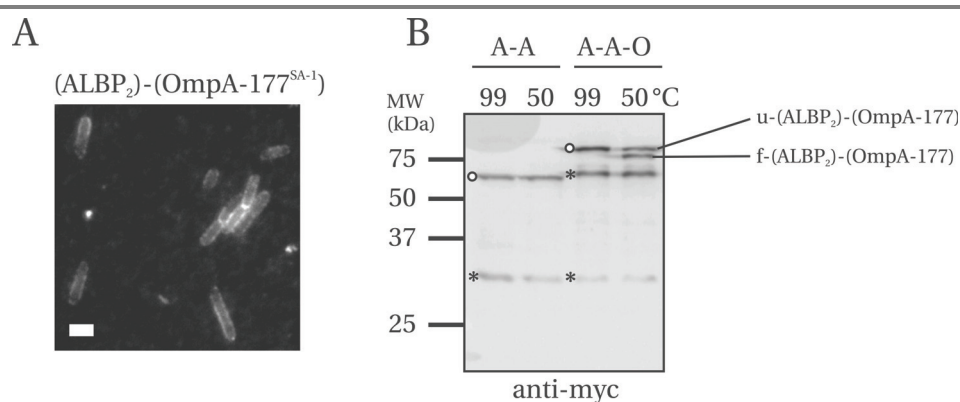


Figure 5.7. A fusion of two ALBP domains to the N-terminus of the OmpA TM domain can insert properly in the OM. (A) Cells grown to exponential phase in DRu medium with 0.1 mM IPTG expressing proALBP-myc-ALBP-(OmpA-177^{SA1}) were labeled with fluorescent streptavidin. Exposure time was 1 s (contrast is enhanced). Scale bar is 1 x 2 μ m. **(B)** Immunoblot probed with anti-myc (1 μ g/ml). A-A: pro-ALBP-myc-ALBP (expected MW: 63 kDa). A-A-O: A-A fused to the N-terminus of (OmpA-177^{SA1}) (expected MW: 87 kDa). Samples were resuspended in sample buffer and either heated at 99°C for 10 min or heated at 50°C for 15 min, as indicated. Intact constructs are indicated with an open circle, degradation products with an asterisk. u- indicates unfolded, f- indicates folded.

find that only 16% of all mCherry in the sample is detected at 50°C (whereas cytoplasmic mCherry is 60% denatured under these conditions). The fluorescent aggregates in the poles might not dissociate and denature at this temperature and escape detection.

Thus, we conclude that a Sec-exported, N-terminal mCherry fusion to the OmpA TM domain can be assembled into the OM. However, in contrast with cells expressing a C-terminal OmpA TM domain - mCherry fusion, mCherry fluorescence can accumulate in the poles, depending on growth and induction conditions.

An N-terminal ALBP₂ fusion to the OmpA TM domain

Before cloning the spacer construct between FtsQ and the OmpA TM domain, we tested also specifically whether a construct consisting of two ALBP spacer domains in tandem, fused to the N-terminus of OmpA-177^{SA1} is able to insert into the OM. To this end we made a proALBP-myc-ALBP-(OmpA-177^{SA1}) triple domain fusion protein (from here on abbreviated to (ALBP)₂-OmpA-177^{SA1}). To determine whether the OmpA TM domain of

this construct was able to insert in the OM, MC1061 cells expressing the (ALBP)₂-OmpA-177^{SA1} construct were labeled with fluorescent streptavidin. A staining along the perimeter of the cells showed that the OmpA TM domain was exported successfully and had inserted into the OM (**Figure 5.7A**). However, the fluorescent signal was significantly weaker than obtained for the unfused OmpA TM domain. This could be due to reduced protein levels of the ALBP tandem itself, as addition of the OmpA TM domain does not influence protein levels significantly, as detected with anti-myc (**Figure 5.7B**).

To determine whether the OmpA TM domain detected in the membrane was intact (i.e. with two ALBP domains attached to its N-terminus), heat-modifiability experiments were performed and the constructs were detected on immunoblot via their myc tag between the two ALBP domains (**Figure 5.7B**). Both intact and partially degraded construct were detected, and approximately half of the intact construct shifted position in the gel, indicative of a properly folded and inserted OmpA TM domain. As a control, it was checked that the Sec exported ALBP-myc-ALBP tandem lacking the OmpA TM domain did not show heat-modifiable behavior under the conditions used. Taken together, these data demonstrate that an artificial two-domain N-terminal fusion to the OmpA TM domain can be assembled in the OM.

An N-terminal Pal-mCherry fusion to the OmpA TM domain

It has been shown that a Pal-mCherry fusion protein localized to mid-cell in both wild type (*Pal*+) background as well as in a Δ Pal strain (MG5) (Gerding et al. 2007). Furthermore, in the Δ Pal strain, induction of Pal-mCherry with 50-100 μ M IPTG from a pMLB1113 based vector (Zagursky and Berman 1984; de Boer et al. 1989), resulted in complementation of all phenotypes of a *Pal* deletion tested: Alleviation of SDS hypersensitivity, a “short-and-round” morphology, and a salt-sensitive cell chaining phenotype (Gerding et al. 2007).

To facilitate C-terminal addition of the OmpA TM domain, we cloned the Pal-mCherry into our weakened pTrc vector with a C-terminal *Xma*I site that introduced three extra amino acids (Pal-mCherry-SRA). Growth in TY medium resulted in the expected envelope and mid-cell localization of this construct in both a wild type (LMC500, *Pal*+) background as well as in a Δ Pal strain (MG5) (**Figure 5.8A**).

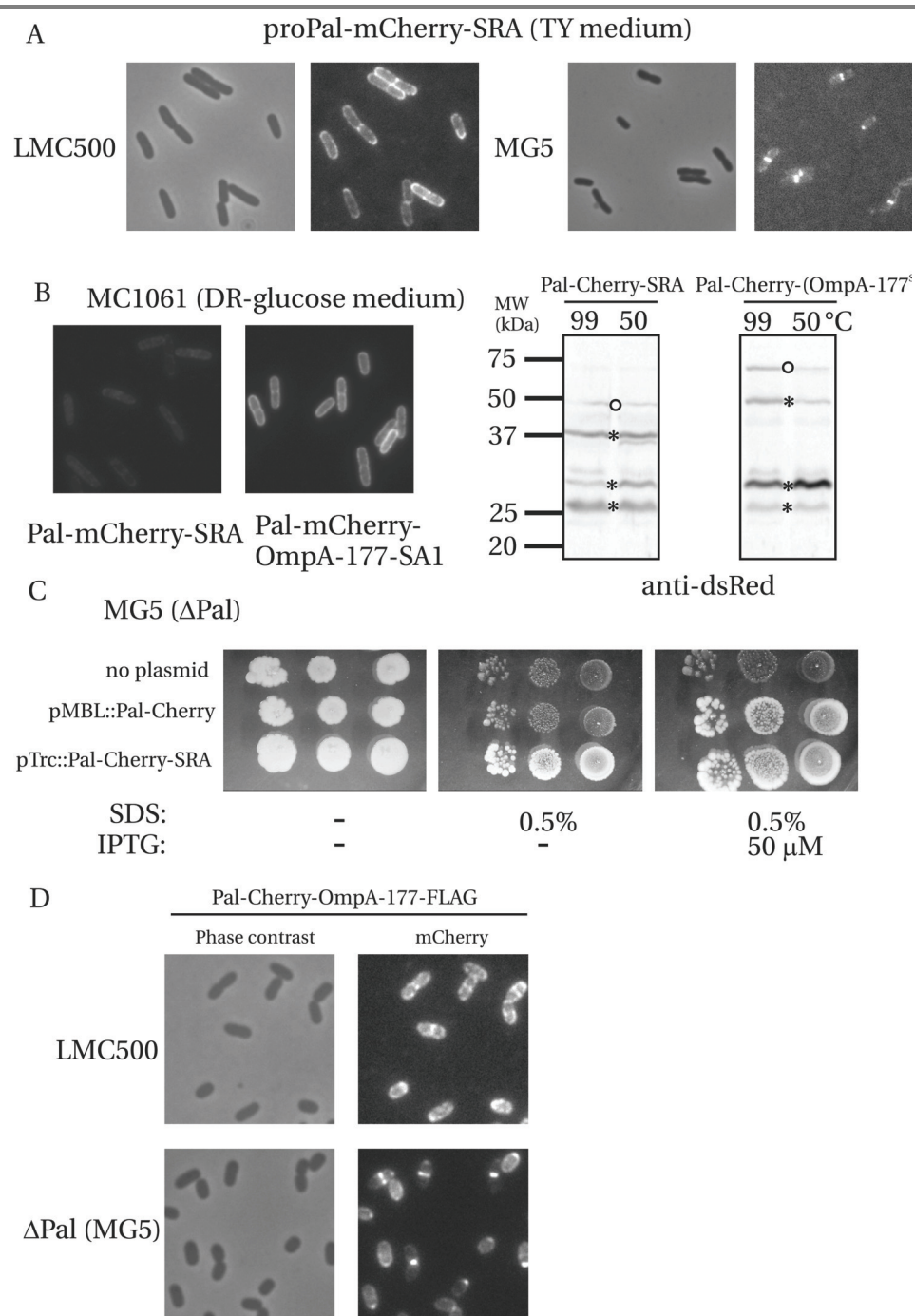


Figure 5.8. proPal-mCherry with the OmpA TM domain fused to its C-terminus. (Pal-) mCherry still localizes to mid-cell, but OmpA is most likely (proteolytically) removed from it. (A) LMC500 cells expressing proPal-mCherry-SRA were diluted from o.n. culture and grown to exponential phase in TY medium at 28°C. (Exposure time was 1.5 s, contrast is maximized). right panel: MG5 cells expressing proPal-mCherry-SRA grown in TY medium. (B) Immunoblot and fluorescence microscopy MC1061 cells expressing Pal-mCherry-SRA and Pal-mCherry-(OmpA-177^{SA-1}). O.n. cultures grown in DRu medium at 28°C were diluted 500x in fresh DRu medium supplemented with 100 μ M IPTG and grown to exponential phase (OD600=1.0). Samples for immunoblotting were taken, before cells were labeled with fluorescent streptavidin (data not shown), fixed and imaged. Exposure time was 2.2 s for both images. Both microscopy images and blots can be compared directly as the same image processing steps were applied to both samples. (C) SDS hypersensitivity assay. The SDS hypersensitivity of MG5 (Δ Pal) is alleviated by expressing either proPal-mCherry from a pMBL1113 vector (needs IPTG), or proPal-mCherry-SRA from a weakened-pTrc99A vector (no need for IPTG). The complementation effect became clearer after prolonged incubation at room temperature, therefore the SDS plates were imaged after four days at RT. (D) Both LMC500 and MG5 cells expressing proPal-mCherry-(OmpA-177^{FLAG}) were grown to pseudo-steady state in GB1 medium at 28°C, fixed and imaged. (Growth details: Cells were diluted 20 000 times from an o.n. GB1 culture grown at 28°C into fresh GB1 supplemented with 10 μ M IPTG and harvested when the OD450~0.3). Exposure times were 1 s and 0.47 s for LMC500 and MG5, respectively. Contrast was maximized for each image.

Surprisingly, fluorescence was strongly reduced when Pal-mCherry-SRA expressing cells were grown in both poor and rich defined media: hardly any fluorescence could be detected both after growth to pseudo-steady state in GB1 minimal medium in the presence of 50 μ M IPTG, as well as after growth in DRu defined rich medium in the presence of 100 μ M IPTG (data not shown). This effect was observed in all three strains used here (MG5, LMC500 and MC1061). An immunoblot probed with anti-DsRed revealed that in MC1061 cells grown in defined rich medium, the Pal-mCherry-SRA protein (expected: 45 kDa, observed 47 kDa) was mostly degraded (main products at 38, 28 and 26 kDa), explaining the low mCherry signal observed with microscopy (**Figure 5.8B**).

In contrast, for the original Pal-mCherry in the pMLB1113 vector (Gerding et al. 2007) in both Δ Pal (MG5) and *Pal*⁺ (LMC500) strains, localization in minimal medium was similar to that observed in TY medium (data not shown). After sub-cloning of the mCherry-SRA fragment into this vector, the “loss of fluorescence” effect was transferred along with it, pinpointing its origin to the three additional C-terminal residues SRA. We are forced to conclude that addition of these additional residues at the C-terminus makes

the fusion susceptible to proteolytic degradation, depending on the differential expression of proteases and/or chaperones under different growth conditions (see below).

As localization in TY medium was unaffected, we tested functionality of the Pal-mCherry-SRA fusion construct for SDS hypersensitivity complementation. Due to a difference in expression levels of the Pal-mCherry fusions by the promoter on the pMBL1113 and weakened-pTrc99A-based plasmids, complementation occurred already without IPTG, as well as in the presence of 50 μ M IPTG (**Figure 5.8C**).

After verifying that our Pal-mCherry-SRA construct was functional, the TM domain of OmpA was fused to the C-terminus of mCherry. mCherry can now be thought of as a linker domain between Pal and the OmpA TM domain. Both fusions with OmpA-177^{FLAG} and OmpA-177^{SA-1} were constructed. Surprisingly, after the addition of the OmpA TM domain, fluorescence in both poor and rich defined media was restored (shown in **Figure 5.8B** for defined rich glucose medium). mCherry localization for the Pal-mCherry-(OmpA-177) fusion was similar to that of Pal-mCherry without the OmpA TM domain (compare **Figure 5.8A** with **5.8D**). Note that in the presence of wild-type Pal (**Figure 5.8B**, also observed for 50 μ M IPTG induction in TY medium (data not shown)), (too) high expression levels of fusion protein apparently can obscure the mid-cell localization.

However, on immunoblots of this fusion, either with a SA-1 or FLAG tag, cells contain, next to intact fusion protein, various degradation products (**Figure 5.8B**). Since some intact fusion was detected on immunoblot, and mCherry showed mid-cell localization, we asked whether the OmpA TM domain was sub-localized to mid-cell too. We failed to convincingly detect either the FLAG epitope or the SA-1 epitope on the cell surface after labeling with anti-FLAG or streptavidin, respectively (data not shown). Even permeabilization of cells followed by anti-FLAG staining did not result in a fluorescent staining pattern that co-localized with the mCherry protein (data not shown), as could be observed for the (OmpA-177)-Pal-mCherry fusion (see above). This suggests that the majority of fluorescent mCherry at mid-cell had its OmpA TM domain proteolytically removed. The immunoblot of the triple fusion with the SA-1 epitope in MC1061 provides some support in this direction, as a prominent band is detected at 48 kDa that could correspond to such a degradation product (**Figure 5.8B**).

Finally, as might be expected, for the fusion with the SA-1 epitope in MC1061, none of the mCherry bands, including the intact fusion, showed heat-modifiable behavior,

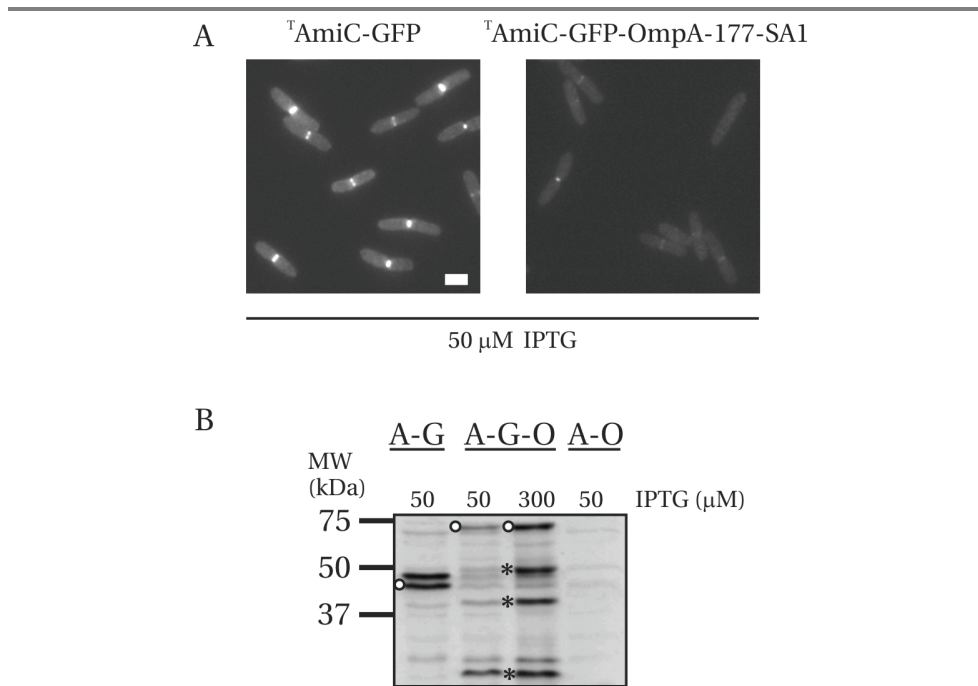


Figure 5.9. Fusions between the septal targeting domain of AmiC and the TM domain of OmpA. (A) Cells grown to exponential phase in DRu medium with 50 μM IPTG expressing either ^TamiC-GFP or ^TamiC-GFP-(OmpA-177^{SA-1}). Exposure time was 1 s. Both images received the same contrast adjustments. Scale bar is 1 x 2 μm. (B) Immunoblot probed with anti-GFP (1:1000). A-G: ^TamiC-GFP. A-G-O: ^TamiC-GFP-(OmpA-177^{SA-1}), A-O: ^TamiC-(OmpA-177^{SA-1}). Intact constructs are indicated with an open circle, (main) degradation products with an asterisk.

suggesting that the OmpA TM domain, at least the fraction that had some portion of mCherry attached, was not properly folded (**Figure 5.8B**). We conclude that the OmpA TM domain, when fused to the C-terminus of a Pal-mCherry fusion, is not able to properly insert into the OM and is (therefore?) very susceptible to degradation.

An N-terminal ^TamiC fusion to the OmpA TM domain

Finally, we took a gamble and fused a Tat-exported substrate to the N-terminus of OmpA-177. It has been shown that preAmiC consists of three domains: a Tat signal sequence, a septal targeting domain (^TamiC) and a catalytic domain (^CamiC) (Bernhardt and de Boer 2003). In this paper, it was shown that removal of the catalytic domain leaves the mid-cell

localization in dividing cells unaffected, demonstrated by a ^TamiC-GFP (GFPmut2) fusion protein. We have re-created this construct in our own expression vector. Indeed, cells expressing this construct show strong fluorescence at mid-cell, when grown in the presence of 50 μ M IPTG in DRu medium (**Figure 5.9A, left panel**). An immunoblot probed with polyclonal anti-GFP (**Figure 5.9B, first lane**) reveals two closely migrating bands also observed by (Bernhardt and de Boer 2003) that were interpreted as processed and unprocessed forms of ^TamiC-GFP. We conclude that approximately half of the construct is processed by the Tat system. Then, the TM domain of OmpA was fused to the C-terminus of ^TamiC-GFP. Introducing the TM domain of OmpA caused a reduction in GFP fluorescence at mid-cell (**Figure 5.9A, right panel**), and the immunoblot shows that not only intact construct but also a lot of degradation bands are present (**Figure 5.9B, second lane**). The mid-cell localization did not improve upon increasing the induction level to 0.3 mM IPTG (data not shown), and the degradation bands became more pronounced (**Figure 5.9B, third lane**).

Finally, we were unable to detect the OmpA domain in the OM with fluorescent streptavidin labeling (data not shown). We also made a fusion of OmpA directly to the C-terminus of ^TamiC, leaving out GFP (used as negative control (fourth lane) in the anti-GFP immunoblot shown in **Figure 5.9B**). For this construct, we could not detect OmpA in the OM with labeling, either. We conclude that the TM domain of OmpA, when exported via the Tat system as a C-terminal fusion to ^TamiC, is not able to properly assemble in the OM.

Discussion

OMP domain organization

Not much is known on to what extent periplasmic domains can be swapped between OMPs, and whether domain order affects OM incorporation. There are several β -barrel outer membrane proteins that contain additional periplasmic domains, attached to either the N- or C-terminus of the TM domain. Examples of TM domains with additional N-terminal domains are the Omp85 protein (5 POTRA domains, involved in OMP biogenesis) (Gentle et al. 2005) and the Imp/LptD protein (contains a single periplasmic domain, involved in LPS biogenesis) (Bos et al. 2004). Also present in the OM are autotransporter proteins, which consist of a N-terminal “passenger domain”, attached to a C-terminal β -barrel TM domain (Bernstein 2007). As the Omp85 protein is required for OM

incorporation of autotransporters (Jain and Goldberg 2007), the OM insertion machinery can insert OMPs that contain an N-terminal domain. A hybrid protein consisting of the signal sequence and two-thirds of the mature portion of periplasmic β -lactamase was fused to the N-terminus of the β -barrel PhoE (Tommasen and Lugtenberg 1984). After proteolytic digestion of membrane fractions, the PhoE moiety was not digested, presumably because it was protected in the outer membrane. Our findings that not only C-terminal, but also N-terminal fusions to the OmpA TM domain are incorporated in the OM further confirm that the Omp85 machinery can incorporate OMPs with N-terminal periplasmic domains. Furthermore, as both fusions to a periplasmic protein (ALBP), and a heterologous protein (mCherry) are assembled in the OM, specific requirements for the N-terminal domain appear to be absent.

Toxicity of fusions

Already in the early 80's, two gene fusions to the OmpA TM domain were constructed (Henning et al. 1983): the first was a fusion between OmpA-228 and 11 of the 12 TM alpha helices of the *TetA* gene (coding for a inner membrane protein). The second was a fusion between OmpA-228 and a viral capsid protein VP1, followed by 77 residues of VP2A (originating from the FMDV enterovirus, where the proteins are post-translationally cleaved) and 30 codons of vector DNA. Cells expressing these constructs at wild-type OmpA levels were not viable. Experiments with radioactive labeling in mini-cells showed that no intact fusion could be detected, only degradation products. Ignoring for a moment the other potential problems with these particular fusions (partial domains, choosing a hydrophobic membrane protein and a protein that assembles into capsids), it seems important to realize the following. Wild-type OmpA is a very abundant protein, with an estimated copy number of $\sim 10^5$ (Henning et al. 1973). As the surface area of the OmpA TM domain is $\sim 10 \text{ nm}^2$ (Pautsch and Schulz 1998) this means that the OmpA TM domain occupies roughly 10% of the surface of *Escherichia coli* (area $\sim 10 \mu\text{m}^2$). As its C-terminal domain binds PG, it might not be possible to swap its PG-binding domain for an unrelated domain while maintaining wild type expression levels. This could cause structural (growth) problems, with the PG layer closely underneath the OM layer (Matias et al. 2003).

For the C-terminal fusions made, which all were incorporated in the OM to a large extent, expression levels in LMC500 of (OmpA-177)-Pal were tolerated up to 50-100 μM IPTG, whereas continuous expression of (OmpA-177)-Pal-mCherry and (OmpA-177)-

mCherry was tolerated only up to 10 μ M IPTG. Maybe Pal can complement the OM tethering of wild-type OmpA, allowing higher expression levels, whereas mCherry obviously cannot. Finally, the increase of toxicity after C-terminal addition of mCherry to (OmpA-177)-Pal might be due to steric hindrance in the crowded space between OM and PG.

Mid-cell exclusion of (OmpA-177)-Pal

Our results show that in a wild type background (both OmpA-177^{FLAG} in LMC500, and OmpA-177^{SA1} in MC1061), (OmpA-177)-Pal is excluded from mid-cell. What could cause this exclusion? If the exclusion is of a physical/space-occupying/steric hindrance type where the presence of wild-type Pal at mid-cell simply does not allow (OmpA-177)-Pal to be present as well, then one would expect the same for the full-length OmpA, as it takes up roughly as much space as (OmpA-177)-Pal. As this is not the case, a difference in properties of the periplasmic OmpA domain and the Pal domain is likely to cause the exclusion. This could, for instance, be a difference in affinity for the peptidoglycan, or an interaction with a (most likely periplasmic) protein, such as TolB. TolB binds Pal with high affinity (Bonsor et al. 2007), and the authors conclude that PG and TolB binding to Pal is mutually exclusive.

How could a Pal interaction cause an exclusion at mid-cell? If wild-type Pal has a higher diffusion rate compared to (OmpA-177)-Pal, then it is expected that when a mid-cell localized Pal binding factor (such as TolB, or a specific high-affinity PG structure) appears during the cell cycle, the faster diffusing wild-type Pal will occupy most of these sites before the slower diffusing (OmpA-177)-Pal has reached them. This reduces the available binding sites for (OmpA-177)-Pal, explaining the reduced presence of this fusion at mid-cell.

This argument requires that Pal binding at mid-cell is not reversible on the timescale of division, i.e. minutes. Furthermore, the diffusion coefficients of (OmpA-177)-Pal and that of lipid-anchored Pal need to differ sufficiently. Reported values for the diffusion coefficient D of lipids in both cell membranes as well as artificial membranes fall in the range 1-10 μ m²/s (Murase et al. 2004). Therefore, the diffusion coefficient of the lipid-anchored Pal in the periplasm might be similar to that of periplasmic GFP (3 μ m²/s, (Mullineaux et al. 2006)). Reported D values for integral (inner) membrane proteins of *Escherichia coli* are in the range 0.01-0.1 μ m²/s ((Deich et al. 2004), (Mullineaux et al.

2006), (Leake et al. 2006)), for an integral OM β -barrel (BtuB) a D value of $0.3 \mu\text{m}^2/\text{s}$ was measured (Spector & Ritchie, Biophysical Society meeting 2007). As the diffusion of (OmpA-177)-Pal is most likely limited by the diffusion of OmpA-177 in the OM, it is not unreasonable to expect a diffusion constant in the range of $0.1\text{-}0.3 \mu\text{m}^2/\text{s}$.

The fact that the localization pattern of OmpA-177-Pal is exactly “inverted” compared to wild type Pal (e.g. wild type stays at the new cell poles in daughter cells for some time, OmpA-177-Pal is absent from new cell poles for some time) provides additional evidence that competition with wild type Pal is involved.

In the Δ Pal background, the homogeneous FLAG staining of (OmpA-177^{FLAG})-Pal is unexpected, as periplasmic (not properly OM incorporated) (OmpA-177^{FLAG})-Pal localizes to mid-cell, suggesting that the mid-cell localization factors are in place. As (OmpA-177)-Pal does not complement, OM blebbing at mid-cell still is expected to occur, and this might prevent the Pal domain from interacting with its mid-cell interaction factors in the periplasm.

We have excluded the possibility of Pal forming a dimer in these considerations, as for Pal, this is based solely on *in vivo* cross-linking (Clavel et al. 1998), which can lead to loss of specificity when high concentrations ($>0.1\%$) formaldehyde are used (Manting et al. 1997). Both TolB and Pal in the TolB-Pal crystal structure were monomeric (Bonsor et al. 2007), and in a NMR structural study of Pal binding to PG precursor, a single Pal was observed (Parsons et al. 2006).

Why the N-terminal Pal and ^TAmiC fusions to the OmpA TM domain are degraded: incompatibility with Lol and Tat systems respectively?

Thus, we find that an (OmpA-177)-Pal fusion is incorporated into the OM, but does not localize to mid-cell. When the domain order is reversed, and OmpA-177 is fused behind a lipoPal-mCherry fusion, lipoPal-mCherry is incorporated in the OM and localizes to mid-cell, but the TM domain of OmpA is not incorporated in the OM and degraded. Perhaps in this case, the TM domain cannot insert autonomously in the OM for some reason, and is subsequently degraded. Alternatively, OM incorporation *in vivo* occurs exclusively via the Omp85 machinery, in which case we could speculate that Omp85 cannot insert the TM domain when it is attached to the lipoPal-mCherry already tethered to the OM.

We found that the OmpA TM domain when exported via the Tat system as a C-

terminal fusion to ^TAmiC was not able to assemble in the OM. This could be due to an incompatibility of the (most likely unfolded with SecB bound) OmpA with the Tat system that exports folded domains. However, for the periplasmic EnvC protein, a Sec substrate, it has been shown that Tat export resulted in a functional protein (Bernhardt and de Boer 2004). Perhaps Tat export is not compatible with OMP insertion, for instance, when OMP insertion requires OMPs to arrive in the periplasm in an unfolded state, normally guaranteed by the Sec translocase (Apparently there is some debate whether Tat can export only folded proteins: Gordon Research Conference 2008)

On export to the periplasm of heterologous proteins

Domain fusions that need to be incorporated in the OM, first need to be properly exported to the periplasm. Thus to create a mCherry fusion to the N-terminus of OmpA, first an exported mCherry construct was needed. A few popular signal sequences are most often used for export (OmpA, PelB, PhoA, pIII) of heterologous proteins (Thie et al. 2008). We initially chose the OmpA signal sequence (OmpAss). However, export of OmpAss-mCherry was not very efficient. We reasoned that after translation of the polypeptide, the mature region of the mCherry preprotein could not be kept unfolded by SecB, and might fold into a translocation-incompetent form, perhaps caused by (covalent) chromophore formation in the cytoplasm. As the SRP pathway allows co-translational export, we replaced the OmpAss by the signal sequence of DsbA. This signal sequence is known to direct proteins into the SRP pathway (Schierle et al. 2003), and it was shown that a rapidly folding cytoplasmic protein (thioredoxin) could be successfully exported when fused to the DsbAss but not when fused to MBPss (MBP is exported via the SecB pathway). However, export did not improve. Surprisingly, fusing mRFP1 (from which mCherry is a derivative) to the C-terminus of either full-length MBP or DsbA, or to a Tat signal sequence (TorAss) resulted in a clear fluorescent halo along the perimeter of the cell (Chen et al. 2005). Furthermore, it has recently been shown that the Sec translocase can actively unfold preproteins (Nouwen et al. 2007). Perhaps the presence of an endogenous preprotein (MBP of DsbA), in combination with a slower (fluorescence) maturation rate of mRFP1 compared to mCherry (Shaner et al. 2004), together allow for more time to start translocation before the fluorophore is covalently formed and the preprotein might become translocation-incompetent. As the Tat system exports folded domains, premature folding (suggested to interfere with export) is expected not reduce Tat export efficiency.

Acknowledgements

I would like to thank Matthew Gerding and Piet de Boer for sharing plasmids, strains and for helpful discussions, Roland Dries for help with cloning of pGV11, pGV12, pRD9, pRD10 and pRD11, Svetlana Alexeeva for providing the pSAV47 construct and Genison Isijk for help with cloning pGI1 and pGI2. Finally, I like to thank Jolanda Verheul for help with the in-gel fluorescence assay.

Materials and methods

Strains and growth conditions

E. coli strains (**Table I**) were grown at 37°C in TY medium containing 1% Bacto trypton, 0.5% Bacto yeast extract, 0.5% NaCl and 3 mM NaOH. Alternatively, strains were grown at 28°C in Defined-rich medium with 0.2% glucose as the carbon source (Teknova M2105 kit) and supplemented with 1 mM thiamine-HCl (Sigma). Expression of the constructs was induced by adding up to 1 mM IPTG or 0.02 % L-arabinose, depending on the plasmid vector (plasmids are listed in **Table II**). Antibiotics were ampicillin (100 µg/ml) or Chloramphenicol (25 µg/ml). LMC500 (MC4100 *lysA*) was made chemically competent using the calcium chloride method. MC1061 and its derivative MC1061 Δ OmpA were transformed using electroporation.

MG5 (Δ Pal) was made competent by first streaking on a high salt (1% NaCl) TY plate supplemented with 20 µg/ml Kanamycin. From this plate, a TY culture with 0.5% NaCl was inoculated and used to make competent cells using the calcium chloride method. It was found that for plasmid transformation, it was important to use TY plates with 1% NaCl at

Strains	Genotype	Reference
LMC500 (MC4100 <i>lysA</i>)	<i>F</i> , <i>araD139</i> , Δ (<i>argF-lac</i>) <i>U169</i> , <i>deoC1</i> , <i>flbB5301</i> , <i>ptsF25</i> , <i>rbsR</i> , <i>relA1</i> , <i>rpsL150</i> , <i>lysA1</i>	(Taschner et al. 1988)
MC1061	<i>F</i> , <i>araD139</i> , Δ (<i>ara-leu</i>)7696, Δ <i>lacX74</i> , <i>galU</i> , <i>galK</i> , <i>hsdR2</i> (<i>r_k-m_{k+}</i>), <i>mcrA0</i> , <i>mcrB1</i> , <i>rpsL</i> , <i>spoT1</i>	(Casadaban and Cohen 1980)
MC1061 Δ OmpA	MC1061 Δ OmpA	(Bessette et al. 2004)
MG5	MG1655 <i>lacIZYA pal</i>	(Gerding et al. 2007)
DH5 α	<i>F</i> , <i>endA1</i> , <i>hsdR17</i> (<i>r_k-m_{k+}</i>), <i>supE44</i> , <i>thi-1</i> , <i>recA1</i> , <i>gyrA</i> , <i>relA1</i> , Δ (<i>lacZYA-argF</i>) <i>U169</i> , <i>deoR</i> , Φ 80 <i>lacZ</i> Δ M15	Lab collection
DH5 α -Z1	DH5 α <i>LacI_q⁺ TetR⁺</i>	(Lutz and Bujard 1997)

Table I. Strains used in this study.

pH 7.0.

In minimal medium (GB1 at 28°C), strain MG5 had a mass doubling rate of ~160-170 min either grown without plasmid in the presence of 20 µg/ml kanamycin or with a plasmid carrying $P_{lac}::Pal$ -mCherry in the presence of 100 µg/ml ampicillin (LMC500 under these conditions grows with a doubling rate of ~85 min).

SDS hypersensitivity complementation assay

This assay was taken from (Gerding et al. 2007). Overnight cultures (grown in TY medium with 1% NaCl) were diluted with TY medium (containing 0.5% NaCl) to an OD₆₀₀ of $2 \cdot 10^{-4}$, $2 \cdot 10^{-5}$ and $2 \cdot 10^{-6}$ (corresponding to approximately 10^4 , 10^3 and 10^2 cells) and 10 µl droplets were pipetted on TY plates with 0.5% NaCl, and optionally SDS (filter sterilized, 0.5%) and/or IPTG (50 µM). Plates were incubated at 28°C (OmpA-177)-Pal) or 30°C (Pal-mCherry-SRA) for 24 hours, followed by a further incubation at RT for one week (OmpA-177)-Pal) or 32 hours (Pal-mCherry-SRA). Plates were imaged with a gel-imager.

Estimation of induction levels

A dense overnight culture grown at 28°C in Defined-rich glucose (DRu) medium of LMC500 cells expressing mCherry was diluted in fresh medium supplemented with increasing amounts of IPTG (between 0 and 1 mM) and grown for 5 hours at 28°C. Cells were fixed and imaged. As a reference, cells grown in TY medium at 28°C were also included. Different regions in the samples (to avoid bleaching) were imaged with increasing exposure times between 22 and 2200 ms, giving a set of images for each induction level. The raw images of DRu-grown cells were then compared to images of TY-grown cells, and for 0.1 mM induction, similar sets of images (fluorescent intensities) were observed.

DNA Constructs

All DNA manipulation, analysis and bacterial transformations were performed according to standard protocols (Sambrook et al., 1989). All PCR fragments were sequenced, either at Baseclear (Leiden) or at the AMC DNA sequencing facility (Amsterdam Medical Centre). Primers were ordered from MWG or Biolegio, and Advantage DNA polymerase (Clontech) or *pfuTurbo* DNA polymerase (Stratagene) was used for the PCR reactions.

Chapter 5

Plasmid	Protein	Precursor/ Processed	Reference
pGV10	proALBP	33.1/30.6	This study
pGV11	proALBP-myc-ALBP	65.3/62.8	This study
pGV12	proALBP-myc-ALBP-OmpA-177-FLAG	87.6/85.1	This study
pGV31	proALBP-myc-ALBP-OmpA-177-SA1	86.5/84.0	This study
pGV4	proOmpA-177-3xFLAG	24.1/22.0	(Verhoeven et al. 2008)
pGV28	proOmpA-177-SA1	23.2/21.1	(Verhoeven et al. 2008)
pGV33	proOmpA-SA-1-LEDPPAEF	39.8/37.7	(Verhoeven et al. 2008)
pSAV47	mCherry-EFSR	27.2	(Alexeeva et al.)
pGI1	OmpAss-mCherry-SRA	29.9/27.8	This study
pGI2	DsbAss-mCherry-SRA	29.2/27.2	This study
pGI4	DsbAss-mCherry-OmpA-SA1	50.2/48.2	This study
pGV15	proOmpA-177-3xFLAG-Pal-LEDP	41.1/39.0	This study
pGV16	proOmpA-177-3xFLAG-Pal-mCherry	68.2/66.1	This study
pGV29	proOmpA-177-SA1-Pal-LEDP	40.0 /37.7	This study
pGV30	proOmpA-177-SA1-LEDPPAEF-mCherry	50.7/48.6	This study
pGV19	proPal-LEDP	19.3/17.1	This study
pMG36	proPal-mCherry	46.4/44.2	(Gerding et al. 2007)
pGV21	proPal-mCherry(SM)-SRA	46.8/44.5	This study
pGV23	proPal-mCherry(SM)-OmpA-177-3xFLAG	69.1/66.8	This study
pGV24	proPal-mCherry(SM)-SRA	46.7/44.5	This study
pGV25	proPal-mCherry(SM)-OmpA-177-3xFLAG	69.0/66.8	This study
pGV26	proPal-mCherry-SRA	46.8/44.5	This study
pGV27	proPal-mCherry-OmpA-177-SA1	68.0/65.7	This study
pRD9	pre ^T AmiC-GFPmut2-SRA	48.6/45.3	This study
pRD10	pre ^T AmiC-OmpA-177-SA1	43.0/39.7	This study
pRD11	pre ^T AmiC-GFPmut2-OmpA-177-SA1	69.8/66.5	This study

Table II: Plasmids used in this study. All vectors are based on pTHV037 (Den Blaauwen et al. 2003), except pMG36, pGV24 and pGV25, which are based on pMBL1113 (Zagursky and Berman 1984). Predicted molecular weight before and after signal sequence processing is indicated in kDa.

We used the expression vector pTrc99A (Amann et al. 1988), modified to decrease the basal expression level (i.e. without inducer) to typically a few thousands proteins per cell (pTHV037, (Den Blaauwen et al. 2003)). All plasmids used in this study are listed in **Table I**.

An XhoI site was introduced at the C-terminus of OmpA-177 3xFLAG by PCR on pGV4 (Verhoeven et al. 2008) using primers proOmpANcoIFW and OmpAXhoIPstIRV. This fragment was cloned into pTHV037 using NcoI and PstI sites, resulting in pGV14. Pal excluding its signal sequence and the Cysteine that becomes acylated, was PCR-ed from the chromosome of LMC500 using primers PalXhoIFW and PalBamHIIHindIIIRV. The PCR fragment was digested with XhoI and HindIII and ligated into XhoI/HindIII digested pGV14 to form pGV15 (proOmpA-177 L3 3xFLAG-Pal-LEDP). mCherry was PCR-ed from pSAV47 (Alexeeva et al.) using primers mCherryFW and mCherryHindIIIRV. This PCR fragment was digested with BamHI and HindIII and ligated into BamHI/HindIII digested pGV15 to form pGV16 (proOmpA-177 L3 FLAG-Pal-LEDPPAEF-mCherry). The LEDPPAEF linker was copied from (Gerding et al. 2007). OmpA-177-SA1 was PCR-ed from pB33OS1 (Bessette et al. 2004) with primers proOmpANcoIFW and OmpAXhoIPstIRV, digested with NcoI/XhoI and ligated into likewise digested pGV15 to form pGV29. mCherry was PCR-ed from pSAV47 using primers mCherryFW and mCherryXmaIHindIIIRV. OmpA-177 L3 FLAG was PCR-ed from pGV4 with primers proOmpANcoIFW and OmpAEcoRIRV, digested with NcoI/EcoRI and cloned into pTHV37 to form pGV17 (proOmpA-177 Loop 3 FLAG followed by 30 residues from the vector). A mCherry fragment from pGV16 was transferred to pGV17 via EcoRI/HindIII (proOmpA-177 L3 FLAG-mCherry) forming pGV18. OmpA-177-SA1 was PCR-ed from pB33OS1 (Bessette et al. 2004) with primers proOmpANcoIFW and OmpAEcoRIRV, digested with NcoI and EcoRI and ligated into likewise digested pGV18 to form pGV30.

proPal (i.e. including its signal sequence) was PCR-ed from the chromosome of LMC500 using primers proPalNcoIFW and PalBamHIIHindIIIRV and ligated to NcoI/HindIII digested pTHV37 to form pGV19 (proPal). OmpA-177 L3 FLAG was PCR-ed from pGV4 with primers OmpAXmaIFW and OmpAHindIIIRV, digested with XmaI/HindIII and ligated into THV37 digested with XmaI/HindIII to form pGV22 (intermediate vector). mCherry was PCR-ed from pSAV47 using primers mCherryFW and mCherryXmaIHindIIIRV. This fragment was digested with BamHI and HindIII and ligated in likewise digested THV037 to form pGV20, containing mCherry-SRA (intermediate

vector). After sequencing, it was found that a silent mutation had been introduced in the mCherry sequence at the last leucine at the C-terminus (...LYKSRA), changing the codon from CTG to CTT (below indicated with (SM)). pGV20 was digested with BamHI and HindIII and the fragment was ligated into likewise digested pGV19 to form pGV21, proPal-mCherry(SM)-SRA. pGV22 was digested with XmaI and HindIII and the fragment was ligated into likewise digested pGV21 to form pGV23. The BamHI/HindIII fragment from pGV20 containing mCherry(SM)-SRA was ligated into likewise digested pMG36 (Gerding et al. 2007) to form pGV24. A BamHI/HindIII fragment from pGV23 containing mCherry(SM)-OmpA177 was ligated into likewise digested pMG36 to form pGV25. To rule out any effect by the silent mutation (SM), a second clone of pGV20 was identified (20.13) that did not contain the SM. A BamHI/HindIII fragment from pGV20.13 was ligated into pGV19 to form pGV26, expressing proPal-mCherry-SRA. OmpA-177-SA1 was PCR-ed from pB33OS1 (Besette et al. 2004) with primers OmpAXmaIFW and OmpAHindIIIRV, digested with XmaI/HindIII and ligated into likewise digested pGV23 to form pGV27.

proALBP was PCR-ed from the LMC500 chromosome with primers proALBPFW and proALBPRV, ligated into pGEM-T and sequenced. A BspHI/PstI fragment was ligated into NcoI/PstI digested pTHV037 to form pGV10. A SacI/PstI fragment containing myc-ALBP was isolated from pGV9 (See **Chapter 4** for details on construction) and ligated into likewise digested pGV10 to form pGV11. OmpA-177 L3 FLAG was PCR-ed from pGV4 with primers OmpAXmaIFW and OmpAPstIRV, ligated into pGEM-T and sequenced. The XmaI/PstI fragment was isolated and ligated into likewise digested pGV11 to form pGV12. OmpA-177 L1 SA-1 was PCR-ed from pB33OS1 (Besette et al. 2004) with primers OmpAXmaIFW and OmpAPstIRV, digested with XmaI/PstI, and ligated into likewise digested pGV12 to form pGV31.

Oligos OmpAssFW and OmpAssRV were annealed to form a dsDNA with overhangs as created by NcoI and EcoRI, and ligated into EcoRI/NcoI digested pGV26 to form pGI1. In this construct, the OmpAss is followed by mature OmpA residues APKD, followed by two restriction sites BglII and EcoRI, that result in residues LEF, before the mCherry sequence (including N-terminal methionine) starts. Oligos DsbAssFW and DsbAssRV were annealed to form a dsDNA with overhangs as created by BspHI and NcoI, and ligated into NcoI digested pSAV47 to form pGI2. This vector allows any protein to become DsbAss exported via the NcoI site right after the signal sequence. A portion of mCherry, fused to OmpA177-

SA1 was isolated from pGV27 via PstI/HindIII and ligated into likewise digested pGI2 to form pGI4.

The septal targeting domain of AmiC was PCR-ed from the LMC500 genome with primers AmiC_FW and AmiC_RV, digested with NcoI and EcoRI and ligated into likewise digested pGV26 to form pRD8 (encoding ^TAmiC-mCherry-SRA). GFPmut2 was PCR-ed from pGV7 (see **Chapter 4** for details on construction) using primers GFP_FW and GFP_RV, digested with EcoRI and HindIII, and ligated into likewise digested pRD8 to form pRD9. OmpA-177-SA1 was PCR-ed from pGI4 with primers prDR_OmpAF_F01 and prDR_OmpAF_R01, digested with EcoRI and HindIII, and ligated into likewise digested pRD9 to form pRD10. The same PCR product of OmpA177-SA1 was also digested with XmaI and HindIII, and ligated into likewise digested pRD9 to form pRD11. A list of primer sequences is available on request.

Preparation of cell lysates

Fresh overnight cultures grown at 37°C were diluted 1000x into 50-100 ml fresh TY medium and cultured at 37°C. Growth was monitored by measurement of the optical density at 600 nm with a spectrophotometer (Perkin-Elmers). IPTG was added at around an OD₆₀₀ of 0.1, and when the cells reached an OD₆₀₀ of 1.0, they were transferred to a 50 ml Falcon tube and put on ice. The cells were then collected by centrifugation for 15 min at 4000 rpm in a tabletop centrifuge at 4°C (Eppendorf). The supernatant was carefully removed, and the cells were resuspended in ice-cold sonication buffer (10 mM Tris-HCl buffer, pH 7.9, supplemented with 1 mM EDTA and 1 tablet of Roche Protease Inhibitor Cocktail), at a concentration corresponding to an OD₆₀₀ of 250. This cell suspension was transferred to a 2 ml Eppendorf tube, and sonicated on ice with a tip sonicator (Branson) in 4-5 10-second bursts with 10 second cooling in between each burst. Debris and intact cells were pelleted in a 4°C cooled centrifuge at 2700 x g for 2 min. The supernatant was transferred to a 1.5 ml Eppendorf tube and frozen at -20°C as total cell lysate.

Fractionation of cell lysates

After thawing, the cell lysate was diluted to 4 ml (corresponding to an OD₆₀₀ of 12.5), and 100 µl of this was saved as “total cell lysate”. The samples were pelleted at 45000 rpm (corresponding to 200.000 x g) for 45 min in an ultracentrifuge (Beckman-Coulter). After centrifugation, 500 µl was saved as “supernatant”. The membrane pellet was resuspended

in 100 µl sonication buffer and frozen at -20°C.

SDS-PAGE, in-gel fluorescence and Western blotting

As Protein gel electrophoresis system we used the Bio-Rad mini-gel system protean III. For SDS-PAGE, samples were mixed with sample buffer (end concentration: 62.5 mM Tris pH 6.8, 2% SDS, 10% glycerol, 2% 2-mercaptoethanol) and either heated to 99°C for 5 min or heated to 50°C for 15 min and electrophoresed on 15% polyacrylamide slabs. In-gel fluorescence of GFPmut2 or mCherry was detected using a STORM 860 molecular imager by scanning the complete SDS-PAGE gel still in between glass plates. (For GFPmut2, quantities of 10-20 ng or more could be detected. mCherry was detected only faintly, because a blue excitation source had to be used). The bio-rad semi-dry blotting apparatus was used for immunoblotting. Anti-FLAG and anti-myc monoclonal antibodies were obtained from Sigma and Roche, respectively. The anti-dsRed monoclonal antibody (#632392, Living colors series) was purchased from Clontech. The polyclonal anti-OmpA antibody was a kind gift from A. Driessen (University of Groningen, Netherlands). The bands were detected using the ECL+ chemiluminescence kit (Amersham) and scanning with the STORM 860 fluorescence imager.

Fluorescent labeling of living cells

Cells were put on ice, and an amount of cells equivalent to 1 ml OD600 of 0.2 (around $2 \cdot 10^8$ cells) was taken for labeling. Cells were collected in all cases by centrifugation at 20.000 x g for 3 min at 4°C. The pellet was resuspended in 100 µl PBS with 0.1% BSA. The cells are incubated on ice for 15 min to block aspecific sites on the cell surface. Then, fluorescent Streptavidin (conjugated to either Alexa-488 or Alexa-546, Molecular Probes) was added (45 µg/ml), and incubated for 30 min on ice. PBS (0.85 ml) was added and the cells were pelleted. After a second wash with 0.5 ml PBS, the cells were fixed in 1 ml PBS with 2.8% formaldehyde and 0.042% glutaraldehyde, washed in 1 volume of PBS and resuspended in 0.1 volume PBS. The cells were either imaged directly or stored at 4°C over night before imaging.

Cells expressing fusions with the FLAG tagged OmpA TM domain were labeled in a similar way: Cells were blocked in GB1 with 3% BSA and incubated for 10 min at RT. Then biotinylated anti-FLAG was added (55 µg/ml) and cells were incubated 10 min at RT. After three washes with GB1 with 3% BSA, fluorescent streptavidin was added (5 µg/ml) and

cells were incubated 10 min at RT. After three washes with GB1, cells were fixed in 1 ml GB1 with 2.8% formaldehyde and 0.042% glutaraldehyde, washed in 1 volume of PBS and resuspended in 0.1 volume PBS.

Fluorescence Microscopy

Cells were immobilized on 1% agarose in water slabs-coated object glasses as described by (Koppelman et al. 2004) and photographed with a CoolSnap *fx* (Photometrics) CCD camera mounted on an Olympus BX-60 fluorescence microscope through a UPLANFL 100x/1.3 oil objective (Japan). Images were taken using the public domain program Object-Image2.19 by Norbert Vischer (University of Amsterdam, <http://simon.bio.uva.nl/object-image.html>), which is based on NIH Image by Wayne Rasband. In all experiments the cells were first photographed in the phase contrast mode. Then a fluorescence image was taken using either a blue excitation/green emission filter cube (green channel, EGFP, ex. 450–490 nm, em. 505–555 nm) or a green excitation/red emission (red channel, U-MNG, ex. 530–550 nm, em. 590 long pass), or both. For dual-color fluorescence imaging, we checked for bleed-through of green fluorophores (GFPmut2, Oregon Green-488 and Alexa-488) on the red channel, and for bleed-through of red fluorophores (Alexa-546 and mCherry) on the green channel. We found that on the green channel, even at long (4.7 s) exposures, no red fluorescence was observed. Cellular auto-fluorescence is present on the green channel, and virtually undetectable on the red channel. Very strong green fluorescence (saturated pixels at 100 ms exposure time on the green channel) could be detected at long (2.2 s) exposure times on the red channel.

ImageJ was used to make line profiles of cells imaged in phase contrast and fluorescence. Cell diameters were measured by estimating the pixel value where the intensity drop at the edge was half the value, and then multiplying by the pixel size (67 nm).

VI

Chapter 6: A counter-propagating optical tweezers setup with independent dual position detection

Abstract

An optical tweezers setup is presented that uses high numerical-aperture (NA) objectives to allow force measurements on beads held in single beam traps, as well as in counter-propagating traps. The temperature of the sample can be set between 23-37°C. Due to the use of a separate low power detection laser, position detection is independent from trapping, and can easily be combined with time-shared multiple traps. Both IR and red lasers are split into two counter-propagating paths. Splitting the detection laser allows position detection to be performed on two trapped particles simultaneously. Using acousto-optical-deflectors (AODs), multiple time-shared traps can be created that can be interactively controlled using in-house developed software. A requirement of the system was to be able to dynamically reposition time-shared trapped beads in close proximity. We demonstrate this by successful DNA tether formation between two trapped beads.

Introduction

In this chapter we describe an optical tweezers setup that uses two high-NA objectives designed to increase the force-range of optical tweezers by trapping high refractive index particles in counter-propagating (CP) trapping mode. It features two QPDs that allow separate position detection on two different particles at the same time. This is achieved by exploiting the counter-propagating design further through the use of counter-propagating detection beams.

Optical tweezers is a technique that allows the generation and measurement of small forces on micron-sized dielectric particles (“beads”), typically in the order of 0.1-100 pN. The particles are held (“trapped”) in a tightly focused laser beam. When a force is exerted on the trapped particle, for small displacements out of the trap, the trap acts as a harmonic spring, with $F=k \cdot x$. By measuring the spatial fluctuations of the trapped particle, one can determine the trap stiffness k , and the particle has become a sensitive force probe.

All optical traps reported in literature so far have been either single beam gradient traps, or low-NA counter propagating traps. Trapping force increases for higher refractive-index difference between particle and medium (Svoboda and Block 1994). However, for single-beam optical traps, when the refractive-index mismatch between particle (e.g. PS, $n=1.59$) and medium (e.g. water, $n=1.33$) becomes too large (e.g. ZnS, $n=2.0$ or TiO_2 , $n=2.4$ (van der Horst 2006)), stable 3D trapping is not possible anymore. Trapping in counter propagating (CP) trapping mode solves this. The scattering forces due to radiation pressure cancel, and the particle is stably trapped in 3D.

Existing CP setups all use low-NA laser beams: Either through the use of low-NA objectives (Ashkin 1970), or through the use of high-NA objectives that are under-filled to capture all the light for calibration (Grange et al. 2002; Smith et al. 2003). However, the high-NA rays contribute most to the gradient force, thus when high forces are desired, high-NA objectives are favored. This motivated our choice for a CP setup with over-filling high-NA objectives. A schematic diagram is shown in **Figure 6.1**: an IR laser is split into two beam paths to create counter-propagating traps. For this setup, successful trapping of high-refractive index particles has been demonstrated (van der Horst 2006; van der Horst et al. 2008). A potential pitfall for using high-refractive index (HRI) particles in biophysical applications could be heating due to absorbance, which was found to be significant for 50 nm gold particles trapped with a single-beam 1064 nm laser (Seol et al. 2006).

Nevertheless, HRI particles also hold great promises for higher trapping forces, with a 6-fold increased trap stiffness compared to similar sized PS particles (Seol et al. 2006), and a >3-fold increase in trap stiffness for 1.1 μm titania ($n=2.4$) particles compared to 1.4 μm sized silica ($n=1.45$) particles (van der Horst et al. 2008).

Several methods exist to calibrate an optical trap. For accurate calibration, the measurement of the position of the trapped particle is required. To do position detection, either the trapping laser itself can be used, or a separate second laser that is super-imposed on the trapping beam. Our setup also incorporates acousto-optical deflectors (AODs) (**Figure 6.1**), which can rapidly scan the trapping beam to create multiple single traps (Visscher et al. 1996), or create traps of extended shape such as line traps or even a “key-hole” trap (Kerssemakers et al. 2003). By using a separate laser, multiple traps can be created that can be calibrated by super-imposing the low power detection laser. The detection laser is coupled into the optical path after the AODs, and is therefore not time-shared. As the setup contains counter propagating beam paths of orthogonal polarization, the setup can be easily extended to double position detection by also splitting the detection laser in orthogonal beams. However, only selecting on polarization can give rise to cross-talk when both beams follow the same optical path (Atakhorrami et al. 2008). One solution is to employ lasers at two different wavelengths, and select with bandpass filters at the detector (Atakhorrami et al. 2008). In our setup, cross talk is expected to be negligible because the orthogonal beams follow counter-propagating directions.

To be able to perform experiments at controlled temperatures up to 40°C, sample heating was incorporated in the setup. Either the sample can be heated directly (Williams et al. 2001), or the sample can be heated via the objective through coupling with the immersion oil. Most high NA objectives are expected to withstand temperatures to up to 40°C without risking damage to the objective (heating should not be too fast) (Bioprotechs, U.S.A). Due to the very small space (~0.5 mm) in between the two objectives, being high NA (and therefore small working distance, 220 μm until the cover slip), we decided to heat the objectives.

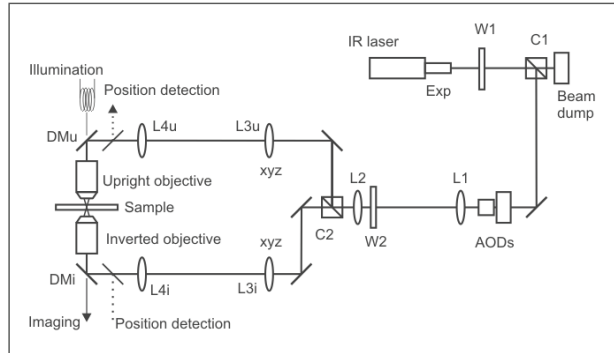
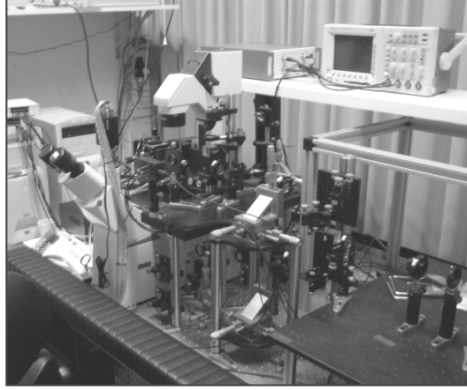


Figure 6.1. An optical trap setup for combined counter-propagating optical trapping and independent quadrant photodiode (QPD) position detection. (Top) Photograph of the Leica inverted microscope, the elevated optical table for the upper beam path and QPD, and the XYZ telescopes for both beam paths. (Bottom) Schematic diagram of the setup. The QPD part is depicted in more detail in **Figure 6.2**. The IR laser can be split at polarizing beam splitter cube C2 to create counter-propagating traps. All experiments described in this chapter have been performed with all laser power directed towards the inverted objective. AODs enable computer-controlled dynamics of the traps and time-shared trapping.

Commercial objective heaters exist that all use Peltier elements that heat a ring, which is clamped around the objective (PeCon GmbH, Germany; Biopetechs, U.S.A). Alternatively, one can build a Peltier based sleeve oneself. Advantages are that heating/cooling is fast, but space is needed for a piece of metal that clamps the object to be heated, as well as a heat sink on the other side (such as water flow). However, although the upright objective could

fit such a heater, the inverted objective surrounded by the piezo stage cannot. An alternative is to use direct heating by water flow. This is slower, as the system needs to equilibrate at the set temperature. Furthermore, a water bath that can cool is needed to control the temperature to below room temperature. The main advantage is that a design based on water flow can be made very compact. Since for our purpose of live-cell trapping, no fast temperature switching was needed, and a few hours time for stabilization of the set temperature was not a problem. Therefore, copper rings were designed that clamp around the objectives and heat the sample by flowing hot water around the objectives.

Detailed Experimental Setup and Calibration method

Optical tweezers setup

A schematic diagram of the setup is shown in **Figure 6.1**. The core of the setup consists of two high-NA (1.2 Leica Plan APO water-immersion, or 1.3 Plan Fluotar oil-immersion) objectives positioned opposite to each other incorporated in a conventional inverted microscope. A continuous wave infra-red (IR) diode-pumped solid-state laser (1064 nm) was used for optical trapping (J201-BL-106C, Nd:YVO₄, Spectra-Physics, Darmstadt, Germany). The beam has a $1/e^2$ diameter of 0.42 mm. The output power of the IR laser is determined by setting the pumping diode electrical current. The laser is stable from 9.5 A (420 mW) to 18.2 A (5.4 W). However, to prevent the optics from being damaged, in practice we did not exceed a current of 13 A (2.2 W). The laser outputs linearly polarized light. Polarizing beam-splitting cubes (C1, C2) and half-lambda wave plates (W1, W2), control the IR beam path. The beam is expanded in two steps to (slightly) overfill the exit pupil (EP) of the objectives (needed for strong trapping): two steps were required since the AODs have a limited aperture. The first expansion occurs immediately after the IR laser (Melles Griot, beam expander, 6x). The second expansion occurs immediately after the AODs by a lens pair L1 and L2 (~3.8x). This results in a total $1/e^2$ beam waist of 9.8 mm (for the 1.2 NA water objectives, the EP diameter is 9.6 mm).

Directly after the AODs, from the resulting 2-d array of AOD diffraction spots, the first-order spot (1,1) is selected using a pinhole. The pair of orthogonal AODs (DTD-276HD6, IntraAction) are aligned (NewFocus, 9071-M aligning mount) such that maximal power is directed into this first-order diffraction spot. In practice, about 60-70% of the power entering the AODs could be directed into the (1,1) spot.

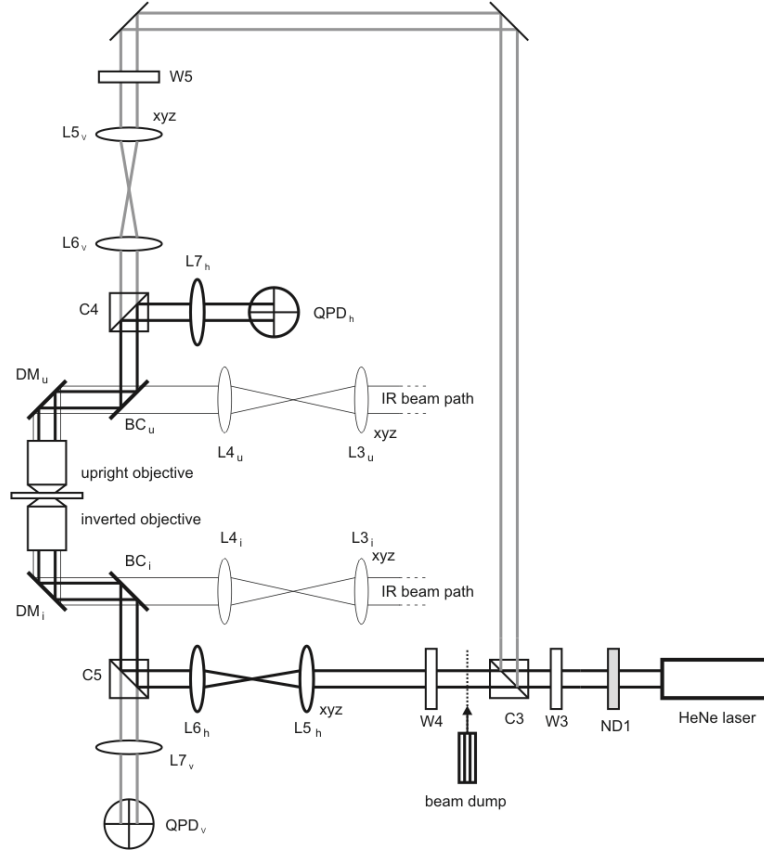


Figure 6.2. Schematic diagram of the independent QPD position detection. A HeNe laser is split into two orthogonally polarized beams that travel in opposing directions through the sample and are imaged onto separate photodiodes. This allows simultaneous, independent position detection of two beads. At polarizing beam splitting cube C3 the detection laser is split in orthogonally polarized beams. The horizontal polarization (thick black beam path) passes the sample traveling from the inverted to the upright objective to be imaged onto QPD_h. The vertical polarization (thick gray beam path) passes the sample in counter-propagating direction, to be imaged onto QPD_v.

Direct Digital Synthesizers (DDSs, Novatech Instruments) generate patterns of sine waves, which are amplified (DPA-502D, IntraAction) and fed to the AODs. This causes the laser beam passing through the AODs to be deflected rapidly such that a single trap is converted into multiple time-shared traps. Part of the DDSs electronics is a Xilinx programmable chip with double buffering that holds the instructions for the DDSes. The

Xilinx chip is controlled by a Labview program (DDScontrol), and loops infinitely to make the DDSs to output a particular pattern. Double buffering allows seamless changing of the patterns. The Labview program allows the traps to be moved interactively, either separately or together.

In both inverted and upright beam paths, a telescope (L3, L4) is present for *xyz*-positioning of the laser foci in the sample. Finally, dichroic mirrors (Chroma Technology Corp.) attached to the inverted microscope direct both IR and red (HeNe) beams onto the objectives into the sample. Two motorized actuators (Newport, 850G-LS) allow coarse positioning of the sample in X and Y over several mm. Fine positioning of the sample is done using a piezo stage (Physik Instrumente (PI), Germany) (range 100 x 100 x 20 μm^3) controlled by an in-house developed program written in C (“confocalpos”). The speed of the piezo can be set (taking into account a calibration factor).

For imaging, an analog Kappa camera (CF 8/4 DX) recording at 25 Hz is attached to a video monitor and a DVD hard disk recorder. Bead positions in recorded movies can be grabbed using a centroid-tracking routine written in IDL. Alternatively, the sample can be recorded on hard disk with a microEnable I framegrabber (Silicon Software, Germany) and a digital camera (UP-600, Uniq, USA) using the “confocalpos” program.

In **Figure 6.2**, a schematic diagram of the CP double position detection is shown. A linearly polarized, low power (5 mW) HeNe 632 nm laser beam (beam waist ~ 1 mm) is attenuated using a neutral density filter ND1 and its polarization is set using half-wave plate W3. This divides the light via polarizing beam splitter cube C3 into the vertically polarized path upwards (to be coupled into the upright objective) and the horizontally polarized path that is coupled into the inverted objective. Note that the (vertically polarized) red beam passing from upright to inverted objective will appear much brighter as now the light falls directly on the CCD camera, whereas for the (horizontally polarized) beam it is the reflection that is imaged (even when using a red filter). The polarization of both beams right after C3 is rotated 90° using half-wave plates W4/W5 to be properly reflected by the beam splitting cubes C4/C5. Two quadrant photo diodes (QPDs, UDT, SPOT-9DMI) are present in the setup to record the positions of two particles separately. Above a certain detection threshold of the QPD, the intensity of the laser spot on the QPD does not affect the power spectrum. The QPD signal is fed to a preamplifier, and sampled by a computer at 30 KHz. A Labview program (QPDcontrol) transforms the raw data to a

power spectrum, and averages the power spectra.

Calibrating the optical trap

A trapped particle can be approximated as a particle undergoing Brownian motion in a harmonic potential well. For such a particle, theory predicts spatial fluctuations with a power spectral density (units: m^2/Hz) that has a Lorentzian shape with a characteristic roll-off (or corner) frequency f_c (Svoboda and Block 1994):

$$S_x(f) = \frac{k_b T}{\gamma \pi^2 (f_c^2 + f^2)}$$

Theoretically, this corner frequency is related to the viscous drag coefficient of the particle γ and the trap stiffness k via ($f_c = \gamma / (2\pi k)$). Stoke's law gives the drag coefficient γ of a perfect sphere with radius r ($\gamma = 6\pi\eta r$) in a medium with viscosity η . Therefore, if the bead diameter and the medium viscosity are known, the drag coefficient can be calculated. Then trap stiffness k follows. For watery fluids such as buffers and growth media, the viscosity can be taken equal to the viscosity of water $1 \cdot 10^{-3} \text{ Pa s}$ at RT. Stoke's law holds only if the bead is sufficiently far away from the surface. In practice, we make sure that the trap stiffness is determined a few μm away from the surface. When the beads used are of a known diameter and sufficiently monodisperse (we use $1.87 \mu\text{m}$ beads with a coefficient of variation ($\text{CV} = \text{SD}/\text{mean}$) of 2.5%), this method is a fast and robust method to calibrate an optical trap.

A well-established method to measure the power spectrum of the spatial fluctuations is to image a laser beam passing through the trapped particle onto a quadrant photodiode (QPD). A QPD can measure the center-of-intensity of the laser spot over time with sufficient bandwidth. A LabVIEW program (QPDControl) has been developed to acquire QPD data, and calculate the average power spectrum. Collected data consists of typically ~50 separate measurements of typically 8192 data points each, sampled at 30 KHz (data sets that are multiples of two are processed much faster by the FFT algorithm). Each data set is converted to the frequency domain by first multiplying it with a window function (rectangular window), followed by a Fast Fourier transform. This results in a frequency domain data set of complex numbers. The power spectrum (power spectral density, PSD) is obtained by squaring the modulus of each complex number ($\text{modulus} = \sqrt{\text{real}^2 + \text{imag}^2}$). The power spectra are then averaged to obtain a smooth

curve, the average power spectrum.

The trap stiffness is determined by fitting a Lorentzian to the averaged power spectrum. A software component (also written in LabView) was added to conveniently estimate the trap stiffness during an experiment. In this module, a frequency window can be defined to select the data used for the fitting algorithm. Requiring input values for the bead diameter and the viscosity of the medium, it then fits a Lorentzian to the selected data and calculates the trap stiffness. Errors are due to the C.V. in bead size (2.5%), due to inaccuracies in determination of the roll-off frequency, and the assumed value of the viscosity (local heating might change this value). Together we estimate them at 10%.

To not only use power spectra to determine the roll-off frequency, but also to determine the detection sensitivity (volts/ μm), it is important to normalize the power spectra in a correct way. The units should be V^2/Hz . A convenient way to check whether a power spectrum has been properly normalized is to calculate the variance of the power spectrum (by integrating from 0 to infinity). This integral should be equal to the variance of the (time-domain) raw data. See page 135 of (Gittes and Schmidt 1998) for useful information pertaining the correct normalization of power spectra.

Results

Optical trapping at controlled temperatures

To perform experiments at elevated temperatures, copper rings were designed and made in-house that clamp around and heat the objectives. The sample is heated through thermal coupling of the objective casing with the sample through the immersion oil. Heat is transformed to the objectives by warm water flowing through the rings. Plastic tubing connected to a pumped, temperature-controlled water bath is split and directed to the two rings. After flowing around the objectives, the water tubing lines are merged again and flow back into the water bath. In **Figure 6.3, left panel**, a schematic diagram is shown indicating the position of the copper rings on the upright (upper) and inverted (lower) objectives. The sample (not drawn to scale) in between the objectives consists of two cover slips separated by grease lines. In **Figure 6.3, right panel**, a photograph of the sample holder containing a simple flow cell made of two cover slips is shown. Immersion-oil between the objectives and the cover slip provides the thermal contact between the heated objective casing and the sample. The temperature of the sample is expected to be a few

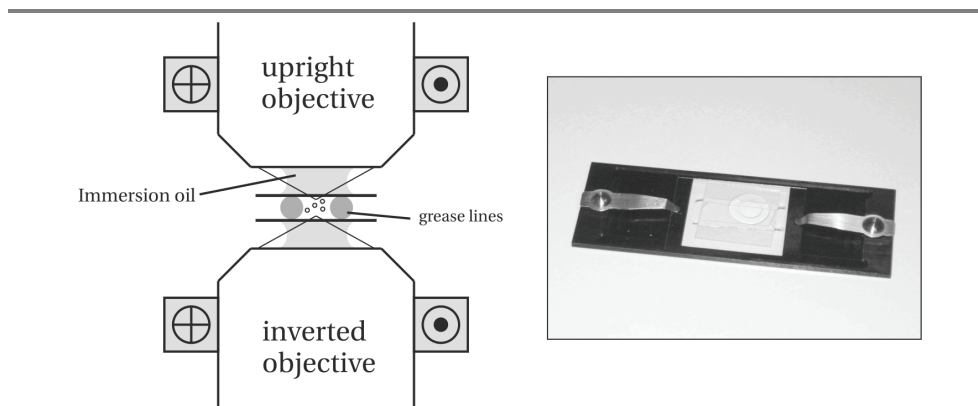


Figure 6.3. Trapping at controlled temperatures. (left) A schematic diagram is shown of a flow cell sample in between the counter-propagating objectives (the sample holder is not drawn). The flow chamber consists of grease lines (dark gray) sandwiched between two thin #1 cover slips (thickness 150-170 μm), and is in thermal contact with the objectives via the immersion oil. The objectives are heated via copper rings connected with flexible tubing through which warm water is pumped by a water bath. The total distance between the two objectives is ~ 0.5 mm. Figure not drawn to scale. (right) a simple flow-cell consisting of two #1 cover slips (18x18 mm and 24x32 mm) and two grease lines (Silicon vacuum grease). The cell is clamped in a sample holder designed and fabricated in-house.

degrees lower than that of the water flowing through the rings due to heat losses.

The temperature in the sample was estimated by using a “dummy” sample consisting of a microscope slide and a cover slip with in between a thermocouple. A single objective bearing a copper ring was placed into contact with the cover slip via a water droplet. We found that a water temperature of 37°C led to a sample temperature of around 30°C . In this asymmetric situation, we under-estimate the temperature compared to a two-cover-slips two-objectives situation. A more accurate determination can be done using a dummy sample made of two cover-slips. However, for our purpose, the actual temperature was not important, as long as it is the same every time, and high enough for bacteria to divide within several minutes.

Water objectives

Water objectives were used for most experiments in this thesis. For oil objectives used with an aqueous sample, the refractive-index mismatch between the immersion oil and that of

the sample introduces spherical aberrations that increase with focus depth, reducing the trap stiffness. Using water-immersion objectives prevents these aberrations, and focusing and imaging (as well as the trap stiffness) should be independent of focus depth.

Evaporation of the water meniscus was found a nuisance when performing experiments at elevated temperatures. This was solved by a special immersion oil (Immersol W, Zeiss) that has the refractive index of water, but is more viscous and evaporates very slowly. This allows prolonged measurements at elevated temperatures using water objectives.

After setting the correction ring on the objective (150 μm was used) to account for the thickness of the cover slip, it was verified up to 30 μm in the sample that indeed the trap stiffness was not reduced. Surprisingly, there was a significant difference (\sim factor 2-3) in measured trap efficiency between the two water objectives available for trapping. As also the reflection of the IR light on the CCD camera differed in intensity but not in appearance, we ascribed the difference to a difference in transmittance at the IR wavelength (1064 nm). For all trapping experiments employing a single beam trap described in the following chapter (**Chapter 7**), the objective with the highest trap efficiency was used (#040).

To compare the performance of the setup with other setups, one needs to know how much laser light ends up in the trap (specimen plane). Typically, 60% of the laser power passes the AODs. Of this, 80% passes the optics between the AODs and the BFP of the inverted objective. Furthermore, we assume that the objective transmittance is 60%, and we estimate that 95% of the laser intensity enters the objective (due to over-filling). Combined, we estimate that 25% of the laser power (when directed fully into one beam path) is present in the specimen plane.

When all laser power is directed into a single beam path to form a single trap using a 1.2 NA water objective, the typical trap stiffness for a 1.87 μm PS particle was around 50 pN/ μm at 420 mW (9.5A) laser output (measured directly after the IR laser source). We can now estimate the (dimension-less) trapping efficiency

$$Q = \frac{cF_{\text{max}}}{n_m P} = 0.05,$$

with F_{max} the lateral escape force of the trapped bead (25 pN), $n_m=1.33$ (refractive index of suspending medium), $P=25\%$ of 420 mW and c the speed of light. As typical trap efficiency values Q of ~ 0.2 - 0.3 are reported for 2 μm PS beads trapped in dual-beam OT, that are

expected to exhibit higher escape forces than single-beam traps because the particle escapes axially (Grange et al. 2002; Smith et al. 2003), our trapping efficiency is in the right order of magnitude expected for a trap created by a single beam.

The trap efficiency of the new setup was compared to an existing trap setup in our lab (Kerssemakers et al. 2003). A single sample was made containing 1.87 μm PS beads. On both setups, a bead was trapped and the trap stiffness was measured. To make a fair comparison, the laser power in both setups was measured just before entering the BFP of the objective. For the new setup presented in this chapter, a trap stiffness was obtained of 150 pN/ $\mu\text{m}/\text{W}$ (NA 1.2, water-immersion). For the existing trap setup, a trap stiffness of 225-250 pN/ $\mu\text{m}/\text{W}$ was obtained (NA 1.3, oil-immersion). We conclude that, when taking into account the difference in NA of the objectives, the performance of both setups is similar, provided that the higher efficiency water objective is used.

The roll-off frequency increases linearly with laser power

Our setup uses a separate red laser with a beam waist $1/e^2 \sim 1$ mm at the BFP of the objective to calibrate optical traps using the power spectral density method. Low-frequency noise in the power spectra, (at least partly) caused by mechanical vibrations of the upper objective with respect to the lower objective (van der Horst 2006), as well as air currents (the setup has not yet been closed off) can sometimes make it difficult to determine high trap stiffness, as the constant PSD plateau is reduced. The detection sensitivity (V/ μm) of the QPD also plays a role: For a higher sensitivity of detection, relative noise contributions due to e.g. air currents or vibrations are reduced.

A 1.87 μm PS bead was trapped in a single-beam trap at three laser powers (0.42, 0.85 and 1.65 W), and for each laser power an average power spectrum was measured. The spectra are shown in **Figure 6.4**. Each spectrum was fitted by a Lorentzian, resulting in roll-off frequencies of 476, 1030 and 1909 Hz, which by using Stoke's law for the drag coefficient result in trap stiffnesses of 50, 100 and 200 pN/ μm . Multiplying with f^2 allows the calculation of the sensitivity, using the plateau value of 0.23 V²/Hz, of 3.1 V/ μm . If we plot the trap stiffness as a function of laser power (**Figure 6.4B**), the trap stiffness increases linearly with the laser power. Not always was the combination noise level/detection sensitivity good enough to accurately determine the trap stiffness at higher laser powers. In these cases, the trap stiffness was determined at low laser power (420 mW /9.5A) and extrapolated to the laser power where the experiment was performed (typically at either

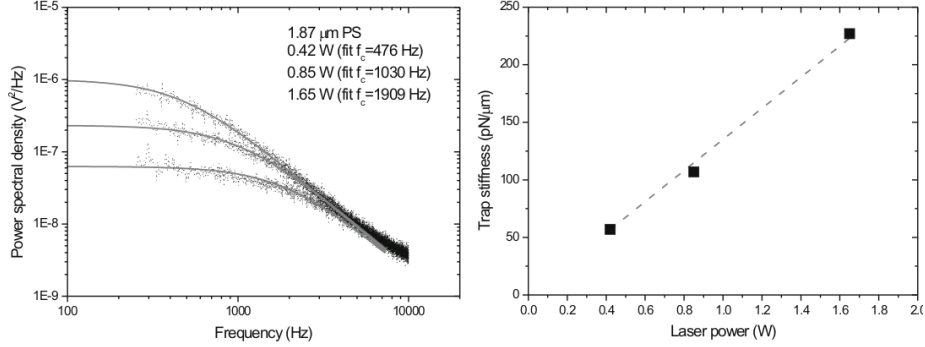


Figure 6.4. Calibration of the optical trap. (left panel) A 1.87 μm PS bead was trapped at three different laser powers. For each laser power, an average power spectrum was measured (rectangular window setting), and fitted with a Lorentzian (gray line curves). Shown are the spectra for the x-direction. Similar spectra were obtained for the y-direction (not shown). Above ~ 5 KHz, anti-aliasing effects are visible, which can optionally be filtered out by low-pass filtering. **(right panel)** From the Lorentzian fit, roll-off frequencies were obtained from which the trap stiffness can be calculated using Stoke's law. A linear fit through the origin shows that the trap stiffness increases linearly with laser power, at least up to 1.65 W at the laser source (this corresponds to 330 mW in the specimen plane assuming that 20% ends up in the trap).

10.4A (840 mW) or 12A (1.65 W)).

DNA tether formation between beads in time-shared traps

To be able to perform force measurements on a bacterium tethered in between two trapped beads, dynamic manipulation of time-shared traps containing beads and bacteria in close proximity is required. The original implementation of the pattern generator that programs the DDSes was such that updating the pattern required a finite time, during which the pattern looping stopped and only single X and Y frequencies were generated. This is not a problem when beads are sufficiently far away from each other. However, for DNA tether formation, we found that beads need to be brought into close contact (~ 100 - 200 nm). We found that when beads became this close, both beads would jump in the single remaining trap that existed temporarily when the pattern was changed. To solve this, a XILINX programmable chip was integrated in the AOD pattern generator (DDS system), which allows the seamless changing of time-shared trap positions.

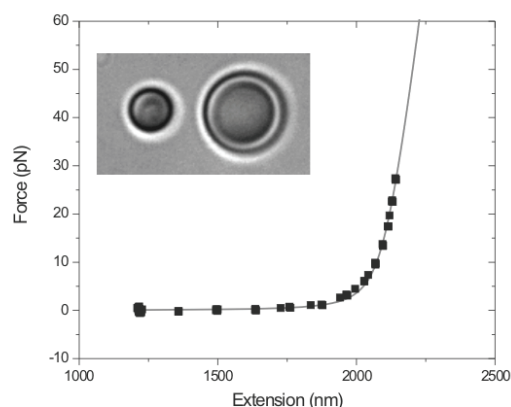


Figure 6.5. Stretching DNA between two trapped beads held in time-shared optical traps.

Shown is a force-extension curve of a DNA molecule tethered in between a biotin bead ($3.27\ \mu\text{m}$, Spherotech) and an anti-Dig bead ($1.87\ \mu\text{m}$, Spherotech). The gray curve is an extensible WLC model with parameters $L=2000\ \text{nm}$, $P=50\ \text{nm}$ and $S=1200\ \text{pN}$ (see text). The trap stiffness of the anti-Dig bead was $80\ \text{pN}/\mu\text{m}$. Laser current was set at $13.0\ \text{A}$ ($2.2\ \text{W}$). Inset shows a bright field video frame of the two tethered beads.

We demonstrate this by successful DNA tether formation between two trapped beads. DNA beads were created by pre-incubating DNA that on one end was functionalized with biotin and on the other end with digoxigenin with an excess of streptavidin, and incubating this with anti-Dig coated antibody beads (for details see **Chapter 7**). DNA Beads were mixed with biotin beads ($3.27\ \mu\text{m}$) and diluted in bacterial growth medium (GB1 minimal medium, see Chapter 3 for composition). This mixture was flowed into a sample cell that was pre-incubated with 3% BSA in GB1 to prevent the beads from aspecific sticking to the surfaces. Two time-shared traps were created using the AODs and a biotin bead and a DNA bead were trapped. Using the “Interactive traps” module within the DDSControl program (written in Labview), the biotin bead was brought in close proximity of the DNA bead by changing the AOD frequency in small discrete steps. After initial tether formation, video recording was started, and the trap containing the biotin bead was moved away from the trapped anti-Dig bead in steps of $\sim 135\ \text{nm}$. After the tether broke, the trap stiffness of the anti-Dig bead was measured at low laser power ($0.42\ \text{W}$) and found to be $15\ \text{pN}/\mu\text{m}$. Assuming a linear dependence of the trap stiffness on the laser

power (shown in the previous section), we infer the trap stiffness during the experiment (laser power 2.2 W) to be 80 pN/ μm . The recorded video was converted to a tiff file using ImageJ, and the positions of both beads were tracked using a centroid-tracking algorithm in IDL (trap_bead). The force on the anti-Dig bead is plotted as a function of the DNA extension (F-x curve) in **Figure 6.5**. An extensible worm-like chain model (with parameters contour length 2000 nm, persistence length 50 nm, and stretch modulus 1000 pN, see next Chapter) provides good agreement with the observed F-x curve.

Effect of laser irradiation on single growing cells

Finally, we demonstrate the possibility of growing bacteria in the optical trap setup. LMC500/pGV4 cells (see **Chapter 3**) were grown to exponential phase in GB1 medium at 28°C, and 3 μl cells were pipetted on top of a GB1 agar slab on a #1 cover slip (24 x 36 mm). The sample was covered with a second #1 cover slip (18 x 18 mm) and sealed with GB1 agar. The water bath was set at 40°C. The sample temperature is expected to be 30-33°C (see earlier). After establishing that indeed all three cells in the field of view were growing at similar rates (**Figure 6.6A,B**), two time-shared traps were created (1 W laser power at the laser source, so we estimate ~125 mW in the sample per trap assuming 25% laser power in the specimen). One trap was kept centered on bacterium #3. The other trap was kept in close proximity of bacterium #2. Bacterium #1 was not exposed to laser light (control) (**Figure 6.6C**). During the experiment, drift in xyz was manually corrected for to keep the bacteria as much as possible at their initial positions relative to the laser traps. Only the bacterium that received continuous radiation displayed a severely reduced growth rate (**Figure 6.6D**).

Single cells growing in a micro-chamber can reach similar growth rates as cells growing in liquid medium (*Adicptaningrum A*, unpublished observations), therefore we used the doubling time to estimate the temperature. At 28°C, LMC500/pGV4 cells growing in GB1 medium with antibiotics have a mass doubling time of ~95 min. Because the control colony grew with a mass doubling time of 80 min, this confirms that the temperature in the sample was around 30°C.

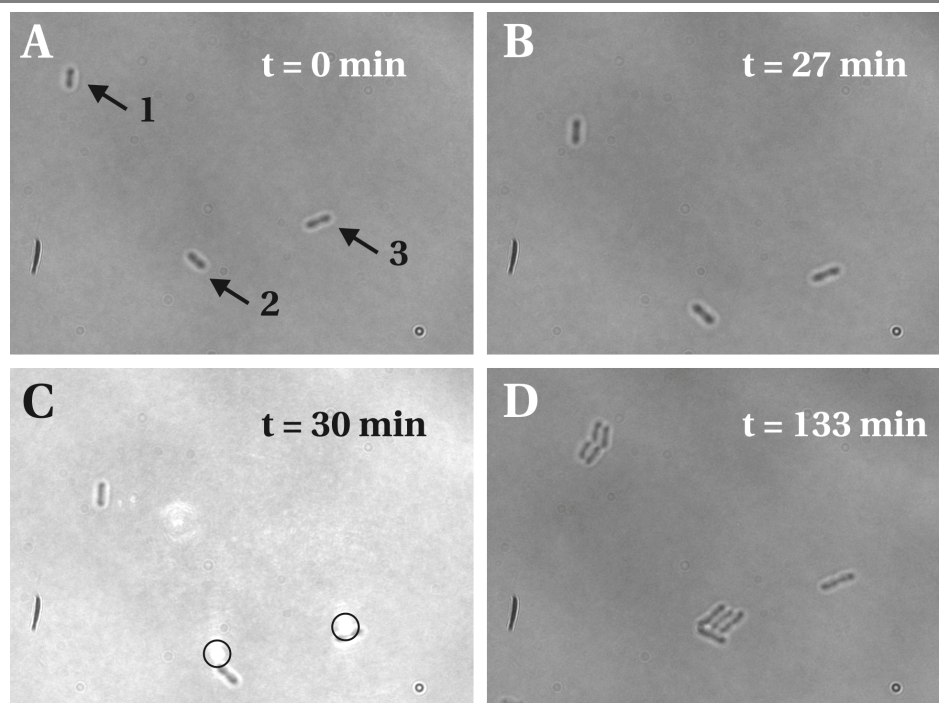


Figure 6.6. Effect of IR laser irradiation on the growth of single cells on agar in the optical tweezers setup. LMC500 cells were grown to exponential phase in GB1 medium at 28°C, and 3 μ l cells were pipetted on top of a GB1 agar slab on a #1 cover slip (24 x 36 mm). The sample was covered with a second #1 cover slip (18 x 18 mm) and sealed with GB1 agar. The water bath was set at 40°C, for this set point the sample temperature was estimated to be 30-33°C (see text). After establishing that indeed all three cells in the field of view were growing at similar rates, two time-shared traps were created. One trap was kept centered on the bacterium #3. The other trap was kept in close proximity of the bacterium #2. Bacterium #1 was not exposed to laser light (control). During the experiment, drift in *xyz* was manually corrected for to keep the bacteria as much as possible at their initial positions relative to the laser traps. Only the bacterium that received continuous radiation displayed a severely reduced growth rate.

(A) First frame. (B) After 27 min. All cells clearly have increased in length. (C) After 30 min. IR laser exposure starts. Circles indicate laser foci. (D) After 133 min. Whereas both bacterium #1 and bacterium #2 have divided twice since (A), the bacterium that received continuous IR irradiation (#3) is still finishing its first division, or has just divided. The control colony (originating from bacterium #1) has a mass doubling rate of ~ 80 min.

Summary

We have presented a versatile optical trap setup that is capable of exerting and measuring high forces due to the use of high-NA objectives in counter-propagating mode, allowing the trapping of high-refractive index particles (van der Horst et al. 2008). This will be useful for biophysical experiments in which high forces can be expected, such as bacterial cell division (this thesis), or the forces generated by bundles of microtubules (Laan et al. 2008). Experiments can be performed at controlled temperature up to 37°C, required to study dynamic cellular processes such as growth and division.

Its versatility is demonstrated by two experiments: (i) the measurement of the force-extension curve of a single DNA molecule tethered in between two beads trapped in time-shared optical traps, (ii) the effect of laser-irradiation on the growth of single bacteria on nutrient agar in the optical trap at physiological temperatures.

Acknowledgements

I would like to thank Astrid van der Horst for help with building the setup, Duncan Verheijde for electronics support, Johan Herscheid for software development, Dirk-jan Spaanderman for design drawings, Wim Brouwer and the workshop for making the sample holder and the objective rings, Henk Dekker for creating the QPD amplifier and filtering circuit and Cees van Doornik for integrating the Xilinx FPGA into the DDS system.

VII

Chapter 7: Force-extension curves of DNA tethers attached to outer membrane protein OmpA in a living bacterium

Abstract

In this work, we characterize a system designed to study force generation during cell division in *Escherichia coli*. We present force-extension (F-x) curves of DNA tethers attached to a bacterial outer membrane protein (OmpA) in a living bacterium. The connection is made via a streptavidin-binding peptide SA-1, genetically inserted in a surface-displayed loop of the OmpA protein.

To separate the DNA compliance from bacterial compliance, the bacterial DNA tethers are compared with “pure” DNA tethers to an immobilized bead. We find that a height difference between the two DNA ends results in under-estimation of the force on the bead, due to what seems a substantial variation of the lateral trap stiffness along the axial direction.

Two variants of the OmpA were compared, one with C-terminal peptidoglycan (PG)-binding domain (*full-length*) and one without (*β -barrel*). For the bacterial DNA tethers, we find that tether lengths and F-x curves are similar to “pure” DNA F-x curves. In addition, for the truncated OmpA *β -barrel*, softer tethers are observed which could correspond to (short) membrane tubes. For the moment we cannot exclude that the observed variations are due to height variations between the tethers. However, for this construct, also two F-x curves were measured for which the tether length is much longer (6-7 μm) than the DNA contour length (2.16 μm). We speculate that these long tethers are membrane tubes, as the tethers displayed (partly) linear force-extension behavior with an effective spring constant of $\sim 3 \text{ pN}/\mu\text{m}$.

Through the measurement of unbinding forces at two different pulling rates, we characterize the weakest bond in the molecular construct. We find unbinding forces that could correspond to the SA-1 peptide/streptavidin bond.

Introduction

Our aim is to tether an optically trapped bead to *Escherichia coli* and measure forces exerted on the outer membrane during growth and division of that bacterium (see also **Chapter 1**). The use of beads as handles to measure forces in biological processes is widespread. Beads can be attached to proteins, e.g. to study force generation by motor proteins such as kinesin (Visscher et al. 1999), or to measure forces of a growing microtubule (Kerssemakers et al. 2006). On the scale of cells, attached beads have been used to deform red blood cells (Mills et al. 2004), or to pull membrane tubes from cells (Dai and Sheetz 1995) or lipid vesicles (Koster et al. 2005). Recently, it was demonstrated that through aspecific adhesion of beads on *E. coli* cells, membrane tubes can be pulled using optical tweezers (Jauffred et al. 2007).

Because we want to measure forces during the invagination of the cell, we cannot directly stick a bead onto a bacterium: the size of the bacterium ($1 \times 3 \mu\text{m}$) and the bead (diameter: $2 \mu\text{m}$) are similar. We need to tether the bead to an attachment point that is smaller than the scale of the invagination ($\sim 100 \text{ nm}$), which requires a spacer. We choose DNA, as it is (relatively) easy to manipulate, and its force-extension behavior is well known. Furthermore, there are many standard ways to attach a DNA molecule to a polystyrene bead.

The surface of an *Escherichia coli* bacterium consists of LPS (lipo-polysaccharide) molecules, and the surface-exposed parts of integral β -barrel proteins (Ruiz et al. 2006). Of these two components, β -barrels will likely withstand the highest forces before extraction. Furthermore, a β -barrel protein has a higher potential for mid-cell localization than an LPS molecule, by e.g. gene fusions in the periplasm (see **Chapters 4 and 5**).

How to tether a DNA molecule to the surface-exposed part of a β -barrel? We want a specific attachment, as only the β -barrel that localizes to mid-cell must be a target for binding. There are two obvious choices: Antibody-antigen and biotin-streptavidin. High-affinity biotinylated antibodies (such as the anti-FLAG M2 antibody) are commercially available. After genetic insertion of the corresponding epitope in one of the surface-exposed parts of the β -barrel, the antibody can bind to the β -barrel. For this approach, conformational restraining of a linear epitope might alter the affinity of the antibody (Giebel et al. 1995; Rice et al. 2006). A biotinylated DNA molecule can be attached to the antibody via streptavidin. Alternatively, the antibody can be covalently linked to the DNA,

however, this is technically more challenging (Cecconi et al. 2008).

It is also possible to biotinylate a β -barrel *in vivo* through genetic insertion of a specific peptide (“acceptor peptide”): an enzyme, biotin ligase, recognizes the acceptor peptide, and covalently adds a biotin molecule to it (Chapman-Smith and Cronan 1999). However, biotinylation in *Escherichia coli* occurs in the cytoplasm, and β -barrels are rapidly exported to the periplasm. Indeed, it was found that the efficiency of biotinylation of the β -barrel LamB was very low (Oddershede et al. 2002), and we want many attachment sites to be present.

A “hybrid” antigen-streptavidin alternative was recently described in a study that screened for peptides binding directly to streptavidin (Bessette et al. 2004). A peptide library was displayed in a surface-exposed loop of the OmpA β -barrel on the surface of *E. coli*, and high affinity binders to (among others) streptavidin were selected. A peptide was isolated (SA-1) that when present in β -barrel OmpA in *E. coli*, showed a thermal off-rate of $\sim 10^{-3} \text{ s}^{-1}$ (Bessette et al. 2004). For the experiments described in this chapter, OmpA containing this SA-1 peptide (cloned in our expression vector) is used (see also below).

Typical literature values for thermal off-rates for antibody-peptide bonds are 10^{-3} - 10^{-4} s^{-1} (Deroo et al. 2008). For the unbinding of a FLAG-tagged protein (not constrained) from anti-FLAG antibody M2 (Sigma) a 10^{-5} s^{-1} thermal off-rate was reported (Nice et al. 1997). Compared to the commonly used biotin-streptavidin (thermal off-rate 10^{-6} s^{-1} (Piran and Riordan 1990)) the lifetime of an antibody-based bond under force will be shorter than that of biotin-streptavidin.

We can use the Bell model to estimate the lifetime of a bond under force. The model assumes that the off-rate depends exponentially on the applied force times a distance x_b (Bell 1978):

$$k_{off}(F) = k_{off}(0) \cdot e^{\frac{Fx_b}{k_b T}} \quad (\text{Equation 7.1})$$

The distance x_b can be interpreted as the distance a ligand has to be displaced “along the reaction coordinate” out of the binding pocket before it unbinds. Assuming a typical value for the barrier width (0.5 nm), antibody-peptide bonds are expected to be strong enough to withstand a force of a few pN for several minutes. Furthermore, by using multiple tethers, the load could be shared and higher forces can be exerted on the cell without breaking the molecular construct.

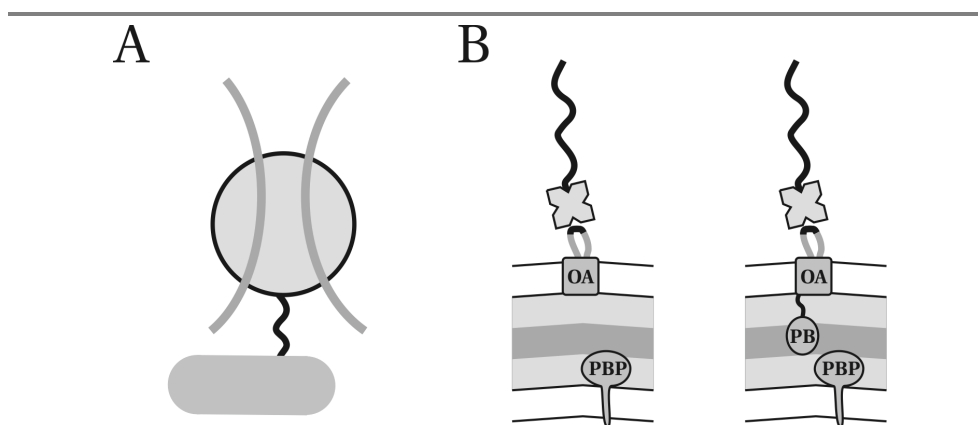


Figure 7.1. Schematic of the experiment: (A) An optically trapped DNA-coated bead is tethered to an immobilized bacterium. (B) Two molecular constructs are compared: the OmpA-177 β -barrel, without periplasmic domain (left), and the full-length OmpA protein, which contains an additional PG (peptidoglycan)-binding (PB) domain. The cell-wall synthesizing complexes are indicated with “PBP”.

The protein fusions used in this chapter are depicted in **Figure 7.1**. Their construction and *in vivo* characterization is described in **Chapter 3**. A strain (MC1061) is used that either expresses OmpA-177^{SA-1} (the β -barrel) or OmpA^{SA-1}. This latter construct consists of the full-length OmpA protein, which includes an additional PG cell wall binding domain (Indicated with “PB” in **Figure 7.1B**). The SA-1 peptide is a cyclic constrained peptide (i.e. it contains two cysteines that form a disulfide bond) that binds streptavidin directly (Bessette et al. 2004).

In single molecule experiments, it is advantageous to pre-form lower affinity bonds and/or bonds that are sterically difficult to reach, in bulk with high concentrations of ligands. In our experiment, the streptavidin-SA-1 bond is less strong than biotin-streptavidin and close to the bacterial cell surface, thus difficult to reach by a DNA-coated bead. Therefore, we pre-form this bond by incubation of cells with streptavidin, and in the single-molecule experiment, create a tether by allowing the biotinylated DNA on the bead bind to streptavidin that is bound on the bacterial surface.

The force-extension relation of a dsDNA molecule is well understood (Bustamante et al. 2000). At low forces, < 5 pN, the DNA molecule behaves like an entropic spring with a persistence length $P \sim 50$ nm, and its force-extension behavior is well-described by the

inextensible Worm-like chain model (I-WLC). However, at higher forces (5-50 pN), the molecule can be extended beyond its contour length L (0.34 nm/bp), thus displaying an intrinsic elasticity where the chemical structure of DNA is altered. In this force range, a simple approximation has been reported in the literature, called the extensible Worm-like-chain model (E-WLC) (Odijk 1995), which gives good agreement with experimentally observed force-extension curves:

$$x = L \left(1 - \frac{1}{2} \left(\frac{k_b T}{FP} \right)^{1/2} + \frac{F}{S} \right) \quad (\text{Equation 7.2})$$

As the contour length L is known for our DNA molecule (2160 nm, see Materials & Methods), the model has two free parameters, the persistence length P and the stretch modulus S . These values depend on buffer and salt conditions; an overview of reported values is given in **Table I**. We chose a persistence length of 50 nm, and a stretch modulus of 1000 pN. Although it is possible to fit the expression to our experimental data and obtain P and S for our conditions (see Materials and Methods), the E-WLC model curve obtained with these parameters was good enough for our purposes and was used throughout this chapter.

In this chapter, we first calibrate the geometry in which the bacterial tethers are formed, using DNA tethers between an immobilized bead and a trapped bead. Then, we analyze force-extension curves of bacterial tethers. Comparison is made with the DNA

Persistence length	Stretch modulus (pN)	Salt concentration	Buffer conditions	Reference
47 nm	1008	10 mM Na+	Phosphate pH 7.0, 0.1 mM EDTA	(Wang et al. 1997)
43 nm	1205	150 mM Na+, 5 mM Mg2+	Phosphate pH 7.0, 0.1 mM EDTA	(Wang et al. 1997)
53 nm	NA (I-WLC)	10 mM Na+	Phosphate pH 7.0	(Smith et al. 1992)
51 nm	1087	150 mM Na+	Tris pH 8.0, 1 mM EDTA	(Smith et al. 1996)

Table I. Experimental values for the Persistence length and Stretch modulus of dsDNA. The persistence length values were obtained from fitting to the I-WLC model (forces < 5pN), whereas the stretch moduli were obtained from fitting to the E-WLC model (2 pN < forces < 50 pN).

tethers between beads and two different strains, which differ only in the presence or absence of an internal anchoring of the OmpA β -barrel to the peptidoglycan cell wall.

Results

DNA tethers to an immobilized bead

The experimental geometry employed is shown in **Figure 7.2A**. Biotin- ($d = 3.28 \mu\text{m}$) or streptavidin- ($d = 6.7 \mu\text{m}$, Spherotech) coated polystyrene (PS) beads were aspecifically adhered on the surface of a flow chamber (see Materials and Methods for details). Then DNA-coated PS beads ($d=1.87 \mu\text{m}$, Spherotech) were flushed in and the sample was transferred to the optical trap. A DNA coated bead was optically trapped, and after recording a power spectrum (giving the trap stiffness k_x and k_y), the bead was brought into close proximity to an immobilized bead by moving the stage. Then, the stage was moved away at a constant speed (either $2.4 \mu\text{m/s}$ or $0.24 \mu\text{m/s}$, termed “fast” and “slow”, respectively).

When a DNA tether has formed, the trapped bead will be pulled away from the trap center. The displacement of the bead from the trap center was determined from recorded video images (25 Hz) by a centroid cross-correlation method (Gelles et al. 1988), and converted into force assuming the linear relationship $F = kx$. Comparing DNA force-extension curves obtained at different trap stiffnesses, we estimate that displacements of the bead are linear with force up to $\sim 300 \text{ nm}$ (see **Figure 7.4B**). It follows that accurate force determination is possible up to a maximum of 30-60 pN depending on the trap stiffness (100-200 pN/ μm). Care was taken to measure the trap stiffness 4-5 μm away from the surface.

If the trapped bead is displaced along the camera X- or Y-axis only, it is sufficient to take only the x or y-values of the tracked stage and trapped bead. We define the tether length as the length of the DNA molecule l_{DNA} plus the DNA-bead radius:

$$x_{tether}(t) = l_{DNA} + r_{bead} = x_{tether}(0) + x_{stage}(t) - x_{bead}(t)$$

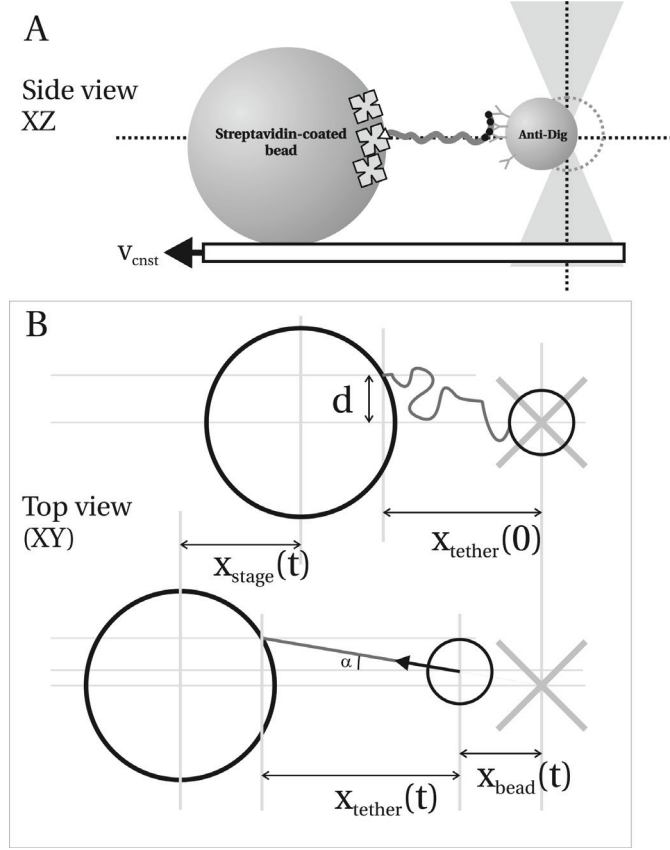


Figure 7.2: DNA force-extension (F-x) curves between an immobilized bead and a trapped bead. (A) Side view of the experimental geometry. (B) Analysis of the video data. The stage displacement in the pulling direction (here along the x-axis) is obtained from video tracking the position of the immobilized bead. The off-axis tethering distance d is indicated. The tether has an unknown length when the recording starts at $t = 0$ ($x_{\text{tether}}(0)$ in upper situation). After stage displacement over distance x_{stage} , the DNA molecule is extended, and force builds up. This force is obtained from video tracking the position of the trapped bead. Due to the force, the trapped bead is pulled out of the trap center by a distance x_{bead} , under an angle α . At forces > 5 pN, this angle can be approximated as a constant (see text). The DNA length is now given by $l_{\text{DNA}} = ((x_{\text{tether}}(0) + x_{\text{stage}} - x_{\text{bead}}) / \cos(\alpha)) - r_{\text{bead}}$. We can choose $x_{\text{tether}}(0)$ such that the experimental F-x curve is super-imposed onto a theoretical F-x curve generated using the extensible Worm-like chain model (E-WLC).

However, if it displaces along both axes, a full analysis in XY is required (Figure 7.2B). Then, the force is given by the magnitude of the force vector

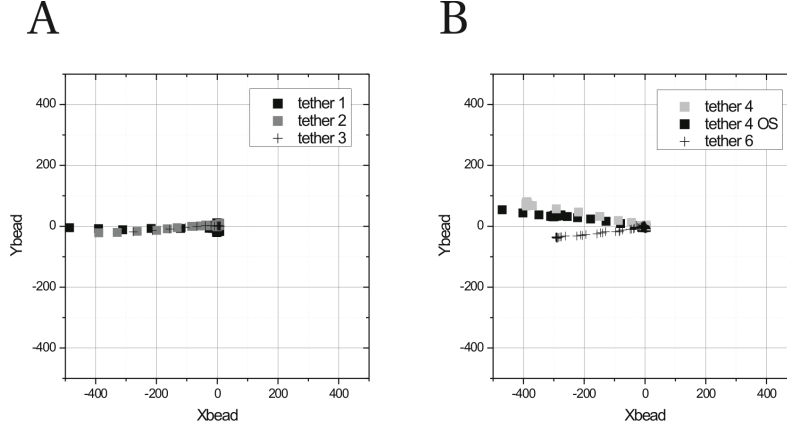


Figure 7.3: The position of the trapped bead determined by video tracking used to construct the DNA F-x curves shown in Figure 7.3. (A) Tethers obtained with immobilized biotin beads, **(B)** Tethers obtained with immobilized streptavidin beads. Although the type of bead does not matter for the shape of the force-extension curve, the distinction is kept here to for visual clarity of the graphs. Angles α were $\sim 0^\circ$ for tethers 1-3 (the left graph), $\sim 11^\circ$ for tether 4, $\sim 7^\circ$ for tether 4 OS (the difference is attributed to drift of the sample, as several minutes had passed between the first and the second curve) and $\sim 7^\circ$ for tether 6. All tracked bead positions for a given tether fall on a straight line. Therefore, as an approximation, the pulling angle α was taken to be constant during the force-extension curve.

$$F_r = |\vec{F}_r| = \sqrt{k_x x_{bead}^2 + k_y y_{bead}^2} = k_r \sqrt{x_{bead}^2 + y_{bead}^2},$$

with $k_x = k_y = k_r$ the lateral trap stiffness. The tether length must be changed in the length along the pulling angle α (defined as the angle of the force vector with either the (camera) X- or Y-axis). For all force values in this chapter, the magnitude of the force vector was taken. For forces above ~ 5 pN, the DNA molecule is almost fully stretched ($> 96\%$ of the contour length) and the pulling angle is measured by $\alpha = \arctan(x_{bead}/y_{bead})$. There are two factors that introduce a non-zero value for the pulling angle α : (i) the pulling direction is not exactly aligned with the camera X-axis. This is a very small effect introducing an angle of $\sim 0.8^\circ$. (ii) the tether attachment point on the immobilized bead can be off pulling-axis. For DNA tethers, this can be neglected also, as the maximum α we obtained was 11° (**Figure 7.3B**, tether 4). This underestimates the tether length with $\cos(11^\circ)$: $\sim 2\%$. For the bacterial tethers, however, a significant pulling angle up to $30\text{--}40^\circ$

($\cos(40^\circ)$ leads to ~25% under-estimation) was sometimes present (see below).

Note that in principle the pulling angle α is a function of the distance between the immobilized bead and the trap center (x_{stage}). If we define the off-axis tethering distance d (normal to the pulling direction), then the pulling angle follows from $\alpha = \arctan(d / (x_{stage} + x_{tether}(0)))$ (**Figure 7.2B**). However, in the region where we consider the pulling angle meaningful (i.e. when the forces are > 5 pN) the stiffness of the DNA molecule increases rapidly, causing small stage displacements to increase the force rapidly. Thus, for small Δx_{stage} we expect small $\Delta \alpha$.

This is shown experimentally in **Figure 7.3**, where the XY trajectories are plotted that trapped beads follow as the force on them increases. Tethers 1-3 were obtained on biotin beads, whereas tethers 4-7 were obtained on streptavidin beads. Indeed, the trajectories are approximately linear, with the pulling angles indicated. To get an impression of the experimental noise, we monitored the force angle for “Tether 4” at a constant DNA extension (force ~ 26 pN) and found that the angle fluctuated around $10.8 \pm 1.5^\circ$. So a meaningful accuracy here is $\sim 1^\circ$. Therefore, for sufficiently stiff tethers, we can treat the pulling angle α constant, and we plot the force vector magnitude as a function of the extension along the x-axis ($x_{stage} - x_{bead}$) divided by $\cos(\alpha)$.

The resulting force-extension (F-x) curves are shown in **Figure 7.4A-C**. The F-x curve expected for a 2160 nm DNA molecule attached to bead of radius 935 nm (expected tether length when the DNA molecule is fully extended: $2160 + 935 = 3095$ nm) given by the extensible worm-like chain model (E-WLC model: $P=50$ nm, $S=1000$ pN) is plotted for comparison. As the absolute length of the tether between the two beads is difficult to measure from the bright field images due to diffraction rings around the beads, the measured F-x curves were manually super-imposed on top of the E-WLC model (i.e. $x_{tether}(0)$ is used as fitting parameter). As can be seen in **Figure 7.4A-C**, all the F-x curves overlap with the E-WLC model and each other for forces below ~ 40 pN (provided the trap stiffness is sufficiently high, see **Figure 7.4B**). F-x curves obtained at both fast ($2.4 \mu\text{m/s}$) and slow ($0.24 \mu\text{m/s}$) pulling rates were found to overlap (**Figure 7.4C**, compare “Tether 4 slow” with “Tether 4 OS” below 40 pN). At forces above 40 pN, the well-known DNA over-stretching transition was observed. During over-stretching, the contour length of the molecule can be increased to $\sim 170\%$ with only little increase in force (Smith et al. 1996). This transition is interpreted as the melting of the two strands (Williams et al. 2001). In

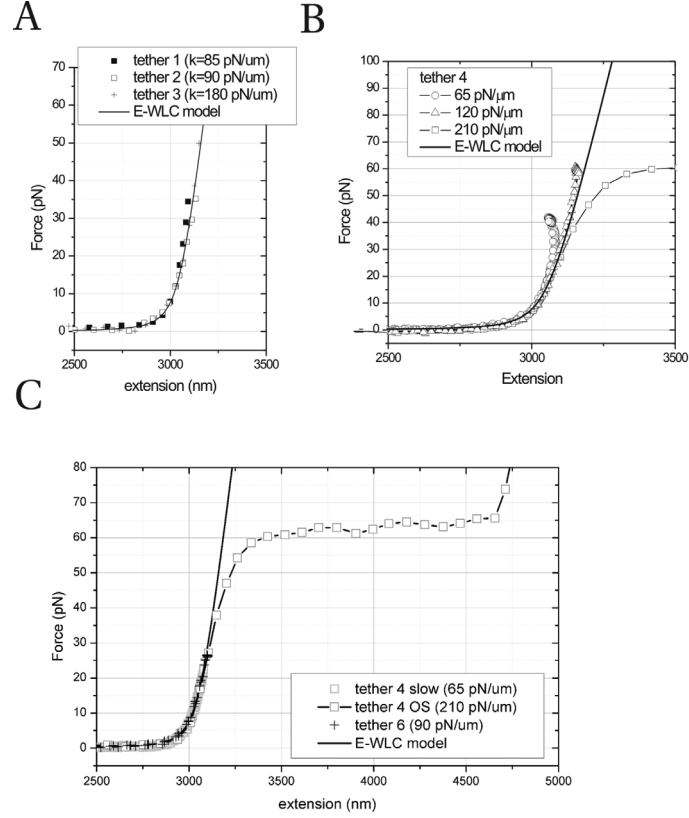


Figure 7.4. F-x curves of DNA tethered between an immobilized bead and a trapped bead. F-x curves of a 2.16 μm DNA molecule tethered between beads via biotin-streptavidin and digoxigenin-anti-digoxenin linkages. In all graphs, the black line curve is an extensible worm-like chain model (E-WLC) for a dsDNA molecule with a contour length of 2160 nm, a persistence length of 50 nm and stretch modulus 1000 pN, shifted with 935 nm to account for the bead radius. The experimental curves were shifted on the x-axis to super-impose them on the DNA model. Trap stiffness values are indicated. **(A):** DNA tethers obtained with biotin beads (3.28 μm PS) and streptavidin-DNA-beads (where the biotinylated DNA was pre-incubated with streptavidin before mixing with anti-dig beads) **(B,C):** DNA tethers obtained with streptavidin beads (6.7 μm , PS) and DNA beads. In **(B)**, the same DNA tether was extended at three different trap stiffness values. By comparing the obtained F-x curves we estimate that the linear regime for our bead/trap combination is ~ 300 nm (see text).

Figure 7.5B two more OS curves are shown. The overstretching plateau force was ~ 62 pN, and after extension to ~ 170 - 175% the force rapidly rises. The force plateau value is similar

to the value reported in literature (65 pN) (Smith et al. 1996).

To estimate the bead displacement range for which the trap is linear, the same DNA tether was extended at three different trap stiffness values (**Figure 7.4B**). We assume that for the highest trap stiffness $k=210$ pN/ μm , the trap is linear up to 42 pN (200 nm). Then, we see that at around 40 pN, for $k=120$ pN/ μm , the F-x curve starts to deviate from the expected F-x curve. The bead displacement is then ~ 300 nm. Furthermore, we see that at around 20 pN, for $k=65$ pN/ μm , the F-x curve starts to deviate from the expected F-x curve. The bead displacement is then ~ 300 nm. This suggests that for a 1.87 μm PS bead in our setup, the trap is linear for bead displacements up to ~ 300 nm. Thus, our original assumption of a linear trap for $k=210$ pN/ μm up to at least 200 nm is valid.

We conclude that the DNA tethers are very reproducible, and that a single E-WLC model can describe all experimentally obtained curves. In these experiments, both ends of the DNA molecule are in a plane roughly parallel to the surface of the flow-cell and through the center of the trapped bead when no force acts on it. As the bacterial tethers will have one end of the DNA molecule below this plane (typically 1-1.5 μm), we first study the effect of this on the F-x curves.

Axial dependence of the trap stiffness and trap center

When a bead is displaced in the axial (z-) direction (normal to the surface of the flow cell), its appearance changes (the diffraction rings change size etc.) After a DNA tether was formed, the immobilized bead was displaced along the axial direction to bring the two ends of the DNA molecule together in one plane normal to the z-axis. This was done in the following way: While continuously displacing the stage back and forward, pulling the tethered bead out of the trap center, the z-position of the immobilized bead was adjusted with the piezo-stage in 0.1 μm steps until visually, the trapped bead's appearance did not change when it was pulled on.

Then the stage was displaced either 0.5 or 1.0 μm down, increasing the distance between the trapped bead and the surface. Next, F-x curves were measured. From the recorded movies, we found that as the lateral force increases, the bead's axial position changes too, in the order of a few 100 nm (by comparing with images of a stuck bead displaced axially). Thus, we find that when one end of the DNA is tethered to a point 1 μm below the trap center, during an F-x curve, bead displacements in the lateral and the axial direction can be of the same order of magnitude! This can be understood if we realize that

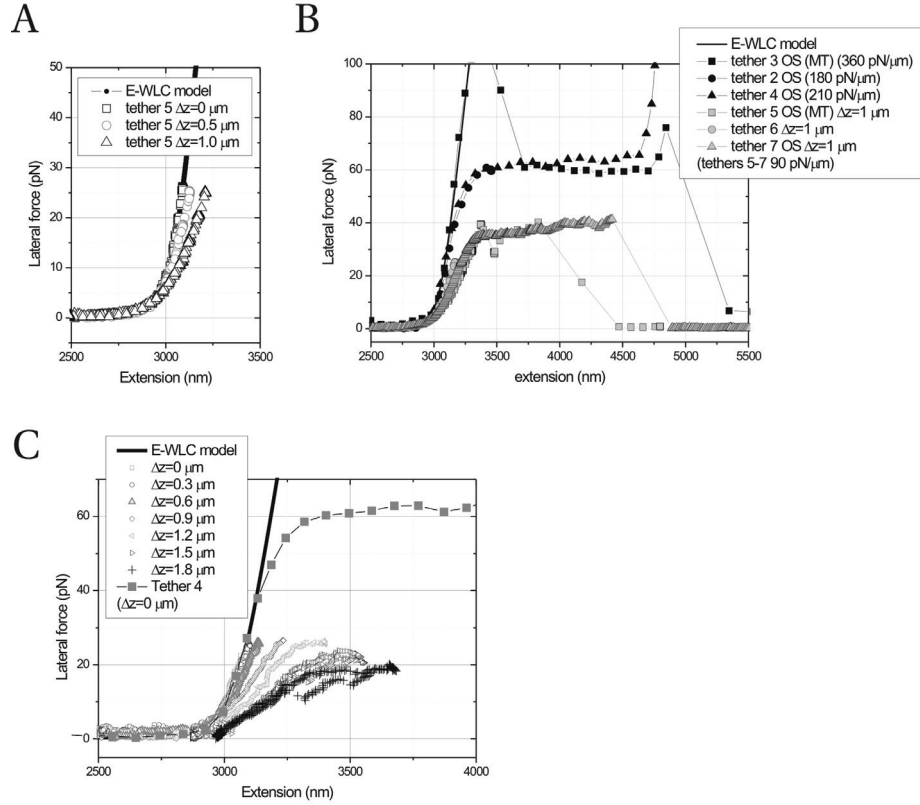


Figure 7.5. Influence of the axial z -position of the anchoring point on the F - x curves of DNA tethers between beads. Black line curve is the same E-WLC as in the previous figures. **(A):** For $\Delta z = 0$, the experimental curve super-imposes well on the theoretical curve. However, already at $\Delta z = 0.5 \mu\text{m}$, for forces above a few pN the force increases less rapidly. This correlates visually with a change in axial position of the trapped bead. For $\Delta z = 1.0$, the distance corresponding to that in the bacterial tethering experiment, these effects are further increased. **(B):** Apparent lowering of the overstretching transition by a factor 1.5-2 due to axial displacement of the trapped bead during the F - x measurement. Black F - x curves are measured at $\Delta z = 0$, gray curves at $\Delta z = 1.0 \mu\text{m}$ **(C):** F - x curves obtained when increasing Δz in steps of 300 nm. Curves were shifted to super-impose on the E-WLC model at low forces. Curves were not corrected for pulling angle (for $\Delta z = 0$, it was 11°). Note the presence of “thermal hysteresis” typically observed when over-stretching dsDNA for $\Delta z = 1.5 \mu\text{m}$ and $1.8 \mu\text{m}$.

the axial trap stiffness is typically several times lower than the lateral trap stiffness (Wang et al. 1997; Rohrbach 2005).

In **Figure 7.5A**, F-x curves of a single tether (Tether 5) at $\Delta z=0, 0.5$ and $1.0 \mu\text{m}$ are shown. The curves were superimposed on the E-WLC model at low forces. As Δz increases, for higher forces, the slope increases progressively less fast than expected from the E-WLC model. This either indicates that the magnitude of the force is under-estimated for a given extension, or that the extension is over-estimated for a given force. As the extension is more likely to be under-estimated since for the extension the projection on the XY plane is used, most likely the force is under-estimated. In **Figure 7.5B**, several overstretching curves are plotted together, either at $\Delta z = 0 \mu\text{m}$ (black curves) or at $\Delta z=1.0 \mu\text{m}$ (gray curves). For the overstretching curves measured at $\Delta z = 0 \mu\text{m}$, as mentioned, the overstretching plateau occurred around 62 pN. Surprisingly, at $\Delta z = 1.0 \mu\text{m}$, the overstretching transition plateau force was reduced to ~35 pN! Apparently, the force is underestimated by almost a factor of 2 when the bead is laterally displaced over ~350 nm. Additional evidence comes from a series of F-x curves where Δz was varied in steps of 300 nm between 0 and $1.8 \mu\text{m}$ that exhibited a progressively reducing overstretching plateau down to 15-20 pN, complete with hysteresis that has been ascribed to re-annealing of locally melted DNA strands (Williams et al. 2001) (**Figure 7.5C**).

In an attempt to take into account the axial displacements, we used geometrical relations deduced in (Wang et al. 1997) to recalculate the force-extension curves for a given axial displacement $\Delta z=0, 0.5$ and $1.0 \mu\text{m}$ of the immobilized bead. Because we also take into account the pulling angle α , and use the magnitude of the force vector in XY, this makes the treatment fully three-dimensional. For a particular pulling angle α in the XY plane, after defining the R-axis as $R = X / \cos(\alpha)$, we can draw the corresponding RZ plane (shown in **Figure 7.6A**). If we assume that the lateral trap stiffness k_r is not a function of z then force balance dictates

$$\frac{F_r}{F_z} = \frac{k_r r_{bead}}{k_z z_{bead}} = \frac{r_{tether}}{z_{tether}} \quad (\text{Equation 7.3})$$

Here, $r_{tether} = x_{tether} / \cos \alpha$, and $z_{tether} = \Delta z - z_{bead}$. As Δz , r_{tether} and r_{bead} are known, we can solve for z_{bead} :

$$z_{bead} = \frac{\Delta z}{\left(\frac{k_z}{k_r} \right) \left(\frac{r_{tether}}{r_{bead}} \right) + 1} \quad (\text{Equation 7.4})$$

Choosing a value of 2.5 for the ratio k_x/k_z , a tether length of 3000 nm, a lateral trap stiffness of 100 pN/μm and $\Delta z = 1.0$ μm, we find that when the force is 25 pN (r_{bead} is then 250 nm), z_{bead} is 172 nm. This confirms that for our experimental geometry, displacements in x and z can be of similar magnitude.

Now we recalculate the tether extension and force, using straightforward geometrical formulas given in (Wang et al. 1997), which can be obtained from the schematic diagram in **Figure 7.6A**:

$$\theta = \arctan\left(\frac{z_{tether}}{r_{tether}}\right), l_{DNA} = \frac{z_{tether}}{\sin \theta} - r, F = \frac{k_r r_{bead}}{\cos \theta} \quad (\text{Equation 7.5, 7.6, 7.7})$$

As can be observed in **Figure 7.6B**, this correction brings the F-x data more in agreement with the expected E-WLC model, but not fully. However, in the Wang study, a feedback system was employed that increased the trap stiffness as the bead was pulled out of the trap. Their displacements were smaller than ours, and their assumption of constant lateral trap stiffness might not hold in our case. It has been shown that the lateral trap stiffness is a function of axial position (C. Tischer, unpublished), and is highest in the beam focus. As the trapped bead is pulled towards this focus in our experiment, it is therefore expected that the trap stiffness increases. If we try to recover the E-WLC model, we can get a reasonable agreement if we assume that $k_r(z)$ increases linearly with bead height, such that $k_r(300 \text{ nm}) = 2k_r(0)$. The calculated force then becomes the apparent force and the real force is given by

$$F_{real} = \left(k_r + \frac{z_{bead}}{300} k_r\right) \frac{r_{bead}}{\cos \theta} = \left(1 + \frac{z_{bead}}{300}\right) F_{app}$$

This can also explain the lowered overstretching plateaus at $\Delta z > 0$. The same 3D model was applied to the overstretching tether 7 that displayed an overstretching plateau force of ~35 pN (**Figure 7.5B**). After correction with the same $k_x(z)$ dependence, a F-x curve with the expected plateau force of ~65 pN is obtained (**Figure 7.6C**). This provides further evidence for an axial dependence of k_x on z , with a doubling of the lateral trap stiffness over a few hundred nm. This appears reasonable, as such distances are also in the order of what is usually reported for the axial bead position relative to the beam focus due to scattering forces. Since Δz is not exactly known for the bacterial tethers (axial positioning of the trap was performed manually in these experiments), in the following, we treat the tethers only in XY, but compare the resulting F-x curves to the F-x curves of “pure DNA”

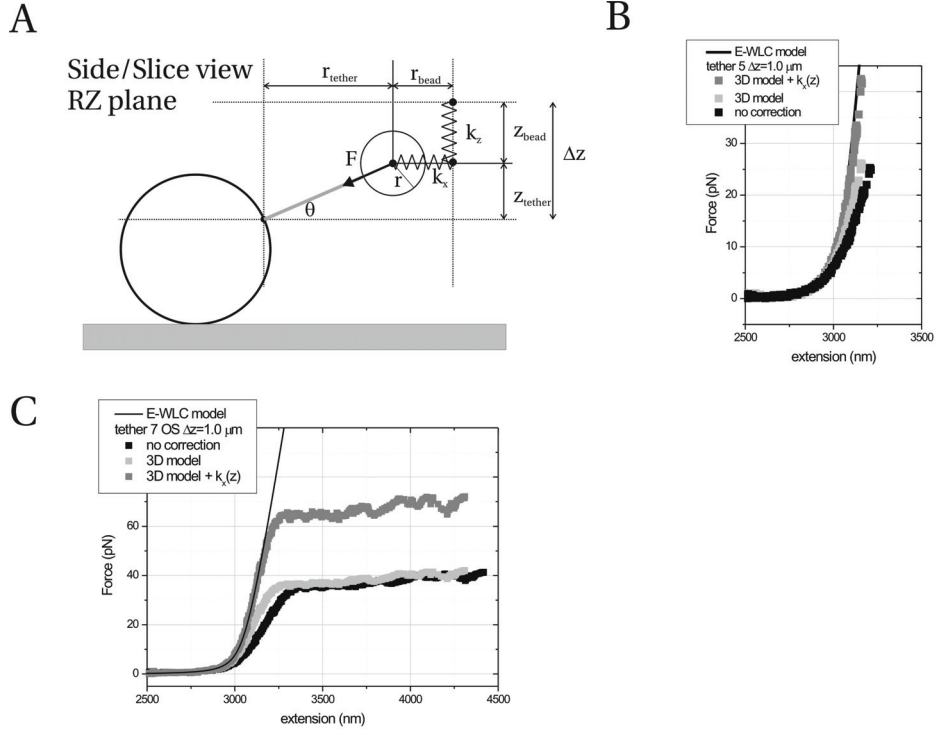


Figure 7.6: Correcting for axial bead displacement. (A): 3D geometrical model used to correct for axial bead displacement (Schematic diagram of the RZ plane). From **Figure 7.2**, it follows that $r_{\text{tether}} = x_{\text{tether}} / \cos(\alpha)$, and $r_{\text{bead}} = \sqrt{x_{\text{bead}}^2 + y_{\text{bead}}^2}$. We assume that $k_z = k_x / 2.5$. r is the bead radius (935 nm). Using the formulas discussed in the text, we calculate z_{bead} and θ , and subsequently F and the true tether length l_{DNA} . (B): Graph that corrects tether 5 at $\Delta z = 1.0 \mu\text{m}$ using the geometrical 3D model. After applying the correction, the match with the expected E-WLC model improves, but there is still a large discrepancy. If we assume that k_x and k_y are a function of the bead's axial position, and (arbitrarily) let them increase linearly from k to $2k$ over an axial distance of 300 nm, we obtain a curve that can be super-imposed on the E-WLC model. (C): the same 3D model applied to the DNA overstretching curve of tether 7 (**Figure 7.5**). The overstretching plateau now lies at ~ 65 pN, the expected value.

tethers for different Δz values.

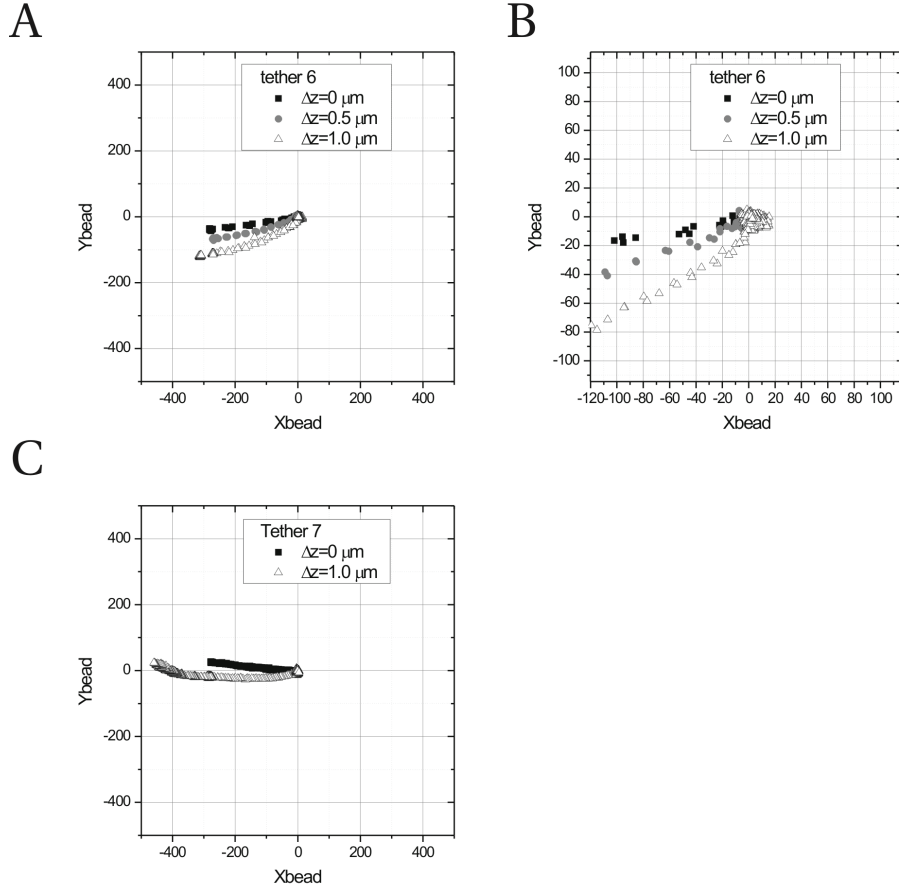


Figure 7.7. The position of the trapped bead determined by video tracking during F-x curves at different Δz . When Δz is non-zero, the bead positions at high forces no longer follow a straight line but a continuously curved trajectory. At low forces, the pulling angle is a function of Δz . **(A):** Tether 6 (a single tether) at three different heights ($\Delta z = 0 \mu\text{m}$, $\Delta z = 0.5 \mu\text{m}$ and $\Delta z = 1.0 \mu\text{m}$). **(B):** Zoom-in on tether 6: the pulling angle α in the low-force regime changes with Δz : from $\sim 10^\circ$ to $\sim 21^\circ$ to $\sim 34^\circ$. **(C):** Tether 7 OS.

Surprisingly, for $\Delta z > 0 \mu\text{m}$, not only the force-increase is reduced, also the bead's XY trajectory no longer is on a straight line, but on a curved trajectory. This is visible from an XY plot of the trapped bead for tether 6 and tether 7 (**Figure 7.7A and 7.7C**) (the F-x curves for tether 6 and 7 were plotted in **Figure 7.5B**). All tethers at non-zero Δz showed increased curving with Δz .

Because the bead appearance changes when it is axially displaced, and the video-

tracking algorithm uses a single reference image of the bead for all frames, we checked whether this could lead to artifacts in detected bead position. Manually, for each subsequent frame, the bead image from the previous frame was used to find the change in bead position. Summing these relative bead changes then yields the position of the bead for each frame. Comparing these with the automated procedure based on a single reference images, similar (curved) XY bead trajectories were found, thus excluding a video-tracking artifact.

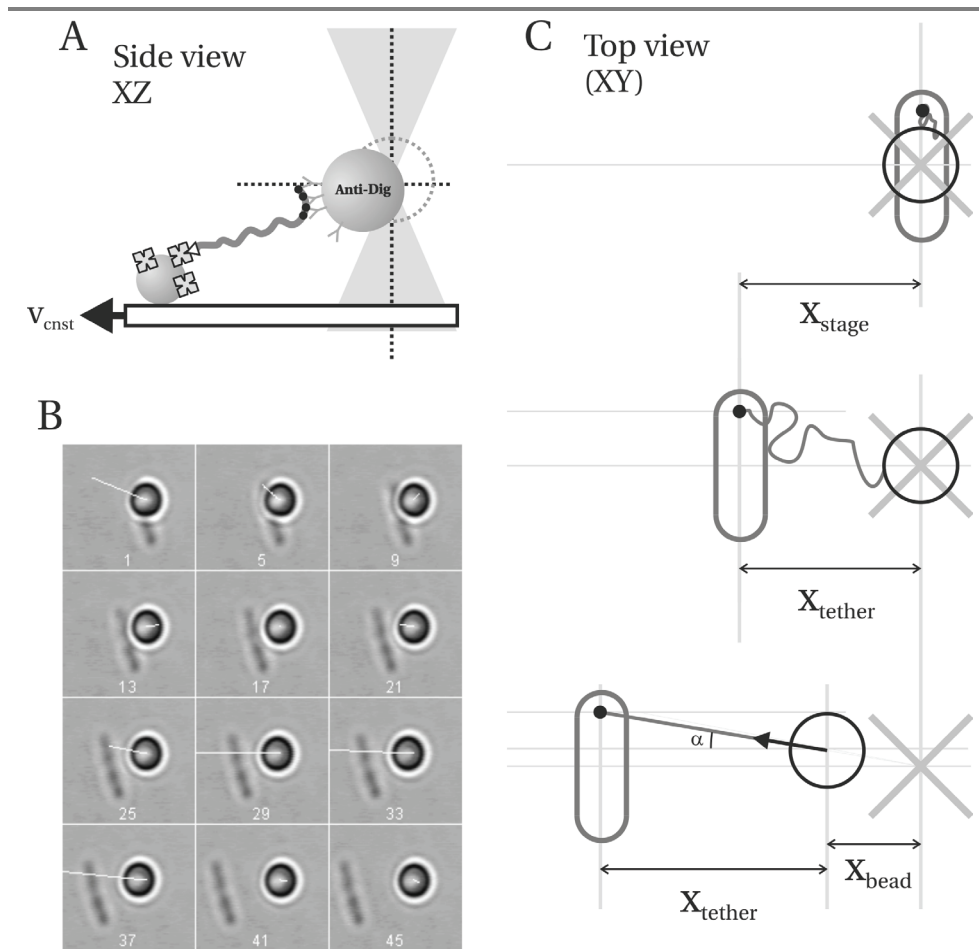
At forces > 5 pN, the curves are approximately linear again, as observed before. However, as can be seen in the zoom-in (**Figure 7.7B**), the pulling angle α is now a function of Δz , as if the anchoring point off-axis (coordinate d) changes with Δz . However, we verified that the center of the immobilized bead only changes a few tens of nm when the stage is displaced over $1\ \mu\text{m}$ in the axial direction. This is expected to have a negligible effect on the pulling angle. We can also exclude drift of the immobilized bead with respect to the trapped bead as the cause, since from video tracking this was found to be ~ 1 nm/s and the experiment was performed within ~ 30 s. Furthermore, the trapped bead's XY trajectories were reversible upon reducing Δz again.

Possibly, the trap center (i.e. zero force position of the trapped bead) changes along the optical axis, due to imperfect alignment of the laser beam or asymmetries in the trap focus. More experiments are needed to test this hypothesis. For example, using the XYZ telescope that controls the position of the laser focus inside the specimen, a trapped particle can be moved through the image plane to visualize the optical axis.

Bacterial tethers to the OmpA β -barrel

A side view of the bacterial tether assay is drawn schematically in **Figure 7.8A**. The bacterium (pre-incubated with streptavidin) is stuck on the surface of the cover slip, and a DNA bead is pressed on top of the bacterium to form a biotin-streptavidin bond between the DNA molecule and the cell, after which the stage is moved away.

How to firmly attach a bacterium to a cover slip? We found that the positively charged biopolymer poly-L-lysine commonly used to immobilize bacteria was not compatible with negatively charged DNA-coated beads. Previously, DNA tethers to bacteria have been used to study DNA import in competent *B. subtilis* ((Maier et al. 2004; Hahn et al. 2005), In these studies, the bacteria were immobilized to silanized cover slips. However, the authors reported slippage events at forces > 4 pN and bacteria detaching from the surface. We tried



a 2% solution of dimethyldichlorosilane dissolved in octamethyl cyclo-octasilane (Amersham Repel-silane), but bacterial sticking did not increase compared to untreated glass. In the end, we chose a procedure in which chromic-sulfuric

acid is used to etch away a layer of glass to create a clean glass surface. We found that when the slides were stored immersed in milliQ, over a few weeks, the adhesion properties of the slides would decrease, and a new batch was prepared.

First, we discuss results from a strain that expresses the OmpA β -barrel that should be free to move in the outer membrane (see also the discussion in **Chapter 8**). From the ~ 120 tether attempts, in most cases the bacterium was pulled off the surface by the trapped

Figure 7.8. Bacterial tethers. (A) The experimental geometry. The bacterium (pre-incubated with streptavidin) is adhered aspecifically to a glass surface. A tether is formed by positioning the trapped DNA-coated bead above the bacterium, bringing them into contact for ~15-20 s to form a biotin-streptavidin bond, and after increasing the axial distance of the trapped bead again, displacing the stage either in X- or Y-direction, depending on the orientation of the bacterium. **(B) Image sequence of a bacterial tether (Tether 5 in Figs. 7.9 and 7.11) that breaks between frames 37-41.** Frame numbers are shown; the movie is recorded at 25 fps. Plotted in each frame is the force vector, calculated from video tracking data of the trapped bead. The length of the vector was made to scale linearly with the magnitude of the force. **(C) Analysis of bacterial force-extension curves.** The calculation of the force-extension data is done in the same way as for DNA tethers between beads, except that now, the stage position and bead center overlap when recording starts. For the analysis, this does not matter. For the last step, super-imposing the F-x curves on the E-WLC model by shifting along the extension axis, this is still allowed, but only to an extent of the diameter of the bacterium, i.e. ~1 μm . This is based on the idea that the pulling angle α provides the anchoring point on the bacterium along its long axis, but that tethering can occur anywhere along the short axis.

bead, sometimes with the bead stuck directly to the bacterium, but also many times clearly via a DNA tether (dragging the bacterium over the surface). In 20 cases, this resulted in tether formation while at the same time the bacterium remained stuck on the surface. A typical tethering event is shown in **Figure 7.8B** (*E. coli* OmpA-177 tether 5). The time between subsequent images in **Figure 7.8B** is 160 ms (not all frames are shown). Plotted also is the force vector on the trapped bead, with the length of the white line proportional with the force.

It was found that ~30 min after addition of the DNA beads to the flow-cell, hardly any tethers could be formed anymore. The thermal off-rate of the SA-1 peptide is 10^{-3} s^{-1} , which means that the average bond lifetime is 17 min. We suspect that streptavidin unbinding from cells in the sample, followed by rebinding onto the biotinylated ends of the DNA causes the observed decrease in tether formation. Due to the high affinity of the biotin-streptavidin interaction and the low amount of biotinylated DNA present on the beads, very low streptavidin background concentrations could already block all tether ends. To circumvent this problem, every 30 minutes, a new dose of DNA beads was flown through the sample. This also prevented the (open) flow-cell from evaporating.

For all 20 tethers, we measured the tether length ($r_{\text{stage}} - r_{\text{bead}}$) when the force had reached 15 pN. From the E-WLC model of our DNA molecule, shifted with 935 nm to account for the bead radius, at 15 pN a tether length of 3048 nm is expected. We found an

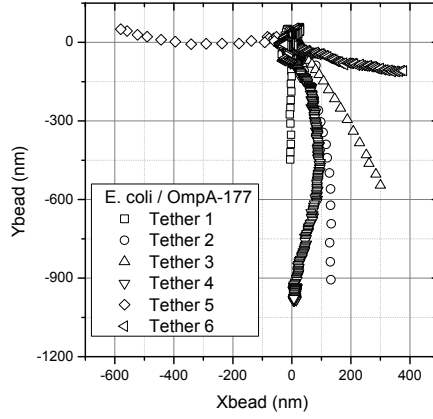


Figure 7.9: The position of the trapped bead determined by video tracking used to construct F-x curves of bacterial tethers to the OmpA-177^{SA-1} β -barrel protein (shown in **Figure 7.11**). Tethers 2-5 show (at high forces) the continuous curving observed previously for “pure” DNA tethers at a $\Delta z \sim 1 \mu\text{m}$. Possibly, along two orthogonal axes the curving is absent, however, experiments that systematically vary the pulling angle are needed to clarify the origin of the curving. For a tilted optical axis, only one symmetry axis is expected.

average bacterial tether length of $2837 \pm 895 \text{ nm}$ (S.D.). Because we under-estimate the tether length (by taking the projection on the XY plane, and ignoring a possible pulling angle α), this indicates that below 15 pN, the bacterial DNA tethers have lengths that are similar to DNA tethers between beads. The large spread is not surprising, since the tether will not be formed *exactly* underneath the trap center, but more likely somewhere on the bacterium within a radius of several hundred nm from the trap center.

For several tethers, a slight reorientation/“jump” ($\sim 100\text{-}300 \text{ nm}$) of the bacterium was visible after the tether broke. This indicates that the bacterium was not completely immobilized and acted as an additional spring as the force increased. Note that it is unlikely that the bacterium actually bends, since higher forces are expected to deform the shape-determining PG cell wall over several hundred nm ($F > 0.5 \text{ nN}$) (Boulbitch 2000; Boulbitch et al. 2000). Instead, compliances in the adhesion sites are likely to be present.

After restricting ourselves to tethers where (i) no sign of multiple tethers was present (i.e. multiple peaks in the F-x curve, and single-step breakage to zero), (ii) the angle between the long axis of the bacterium and the direction of stage displacement (either X-

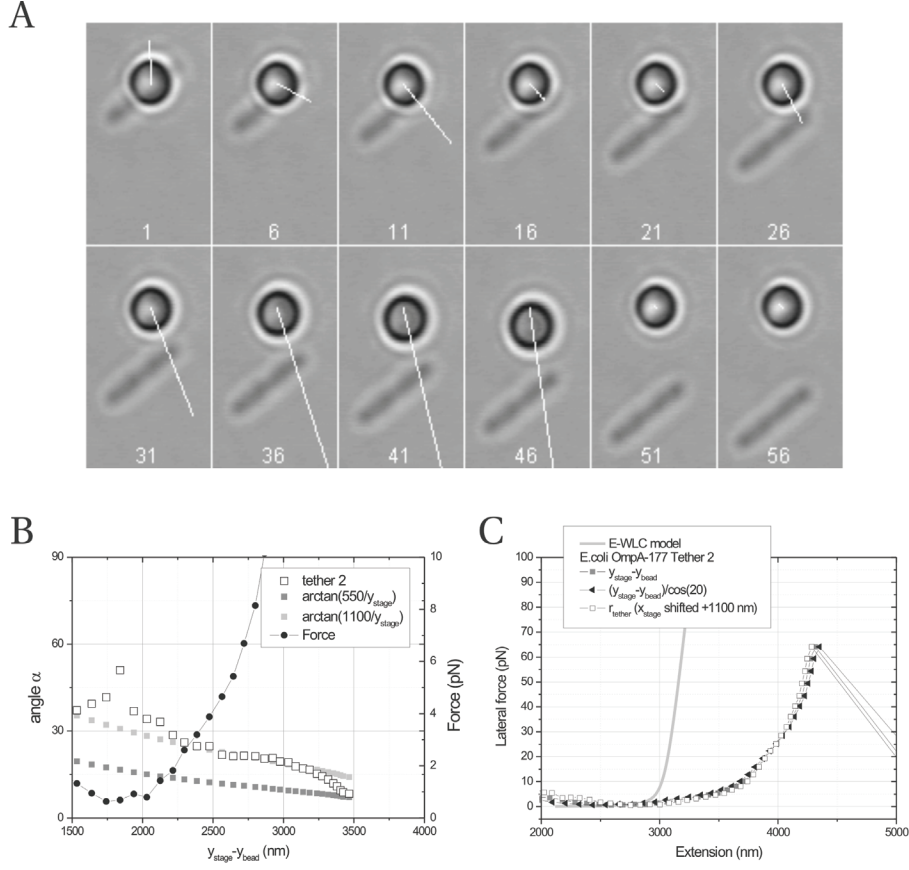


Figure 7.10. Determining the “true” tether extension. (A) Tether 2 image sequence. The force vector is displayed as a white line. Frame numbers are indicated. Movie was recorded at 25 fps. (B) The pulling angle α as a function of tether extension, obtained from the force-angle of Tether 2 (see also **Figure 7.9**), compared with two $\arctan()$ functions expected for either 550 nm or 1100 nm off-axis anchoring. (C) Comparison of three ways to calculate the tether extension (see text), all shifted to overlap the E-WLC model at low force (~ 1 pN). All corrections are minor compared to the overall shape of the curve.

or Y- direction) was greater than 45 degrees (to minimize the risk of creation of additional specific or aspecific tethers as the bead moves over the bacterium) and (iii) no visible displacement of the bacterium was present, 7 tethers remained. Of these seven, one was dropped, as the force vector did not point to the bacterium but to a point on the cover slip, suggesting that it was a surface tether. Note that condition (iii) implies that the bacterium

displaces less than a pixel (say $< \sim 50$ nm) over a force range of ~ 50 pN, and therefore can be considered a (stiff) spring with stiffness $> \sim 1000$ pN/ μ m.

For all bacterial tethers, the visual appearance of the bead indicated that it displaced axially as well as laterally. This is expected, as the attachment point on the bacterium is \sim one bead radius below the trap center. Again, we plot the tracked XY positions of the trapped bead during a F-x curve, shown in **Figure 7.9**. If we restrict ourselves to the linear regime of the trap (~ 300 nm, see **Figure 7.4B**), the trajectories of tethers 1,3,5 and 6 are approximately linear. Tethers 2 and 4 show a curved trajectory already below 300 nm.

A selection of frames for Tether 2 is shown in **Figure 7.10A**, with the force vector indicated by a white line. The force angle of tether 2 is plotted as a function of extension (here simply taken as $y_{\text{stage}} - y_{\text{bead}}$) in **Figure 7.10B**. Possibly, at low forces, the DNA is entropically coiled-up, undergoes a drag force exerted by the fluid and the force vector does not point necessarily in the right direction. When the DNA is straightened out (at forces > 3 pN), the force angle is well-described by the $\arctan(d / y_{\text{stage}})$ function, assuming an anchoring point d 1100 nm off-axis. Around 2750 nm, the force starts to increase rapidly. It is in this regime that we approximate the pulling angle as a constant (here $\sim 20^\circ$). Furthermore, for forces above 30 pN (Above 3250 nm “extension”), the pulling angle starts to deviate from the $\arctan()$.

This could indicate that the anchoring point on the bacterium changes. Note that if it does, it does so in the “wrong” direction (i.e. in the direction opposite to the direction that is expected to decrease the tether length and therefore the force). However, as the bead is no longer in the linear regime, and similar changes in pulling angle have been observed for “pure” DNA tethers anchoring below the trap center, it is as well possible that the trap center changes. For now, we are careful with extrapolating the force vector to make statements about possible relocation of the anchoring point.

What is the proper level of accuracy when analyzing bacterial tethers?

Next, we evaluate three progressively more refined ways to plot the F-x curve for a tether that is anchored “off-axis” at a distance d normal to the axis defined by the pulling direction and the trap center, such as tether 2. The first is the “coarse” approach, by ignoring tether length under-estimations due to the pulling angle, and just plotting $y_{\text{tether}} = y_{\text{stage}} - y_{\text{bead}}$ as a function of the magnitude of the force vector F . A difference with the

F-x curves for DNA in between beads is that here, at $t=0$, the stage position y_{stage} (approximately) coincides with the bead position y_{bead} . Thus, the tether length is now given directly by $y_{stage}-y_{bead}$. Shifting the F-x curve on the x-axis to superimpose on the E-WLC model is now only allowed over a maximum of $\sim\pi/4*d/\cos(\alpha)$ (uncertainty on the bacterium) + $(l_{DNA} + r)(1 - \cos(\alpha))$. (Here, $\alpha\sim 20^\circ$ so maximum shift is ~ 1000 nm, and a bit more since we also underestimate the length due to XY projection) to account for the uncertainty in where on the bacterium the tether is attached. The F-x curve in **Figure 7.10C** was shifted +850 nm to overlap at ~ 1 pN with the E-WLC model.

The second is the approach already used for the DNA tethers: from the bead XY displacements, a pulling angle α is estimated, and the tether length is increased by dividing with $\cos(\alpha)$. For tether 2, this angle was $\sim 20^\circ$ (see above). Now only a +500 nm shift is needed to overlap the E-WLC model at ~ 1 pN, because all tether lengths are increased to 111% (**Figure 7.10C**).

Alternatively, an off-axis tethering point can be estimated (e.g. the $d = 1100$ nm off-axis above), and the length vector between this point and the bead center is used as the tether extension. This was done by shifting the (x_{stage}, y_{stage}) coordinates with $(+1100, +0)$. The pulling angle is now no longer a constant, but a function of (x_{stage}, y_{stage}) . This approach ignores the actual force angle, and therefore ignores possible relocations of the anchoring point. This correction needed a +700 nm shift.

When we compare the three corrections, we find that all corrections are minor effects, and that compared to the spread in the different F-x curves (see below), it suffices to use a “coarse” approach, based on the most simple tether length, i.e. either $x_{stage}-x_{bead}$ or $y_{stage}-y_{bead}$ (depending on the pulling axis).

Bacterial F-x curves

Using the “coarse” approach, the force-extension curves for the 6 tethers are plotted in **Figure 7.11**. For comparison, the (over-stretching) F-x curve of “pure” DNA tether 7 ($\Delta z = 1$ μm) is reproduced from **Figure 7.5**. In **Figure 7.11A**, the F-x curves are plotted up to the end of the linear trap regime ($x_{bead}\sim 300$ nm). From the 6 tethers, (for forces > 5 pN) tethers 5 and 6 appear similar to the “pure” DNA tether, whereas tethers 1-4 appear softer (less stiff). In **Figure 7.11B**, the full F-x curves are plotted. For tether 4 and tether 5, overstretching is observed, although the trapped bead is way outside the linear regime of the trap in both cases ($x_{bead} \sim 600$ nm for tether 5, and $x_{bead} \sim 1000$ nm for tether 6).

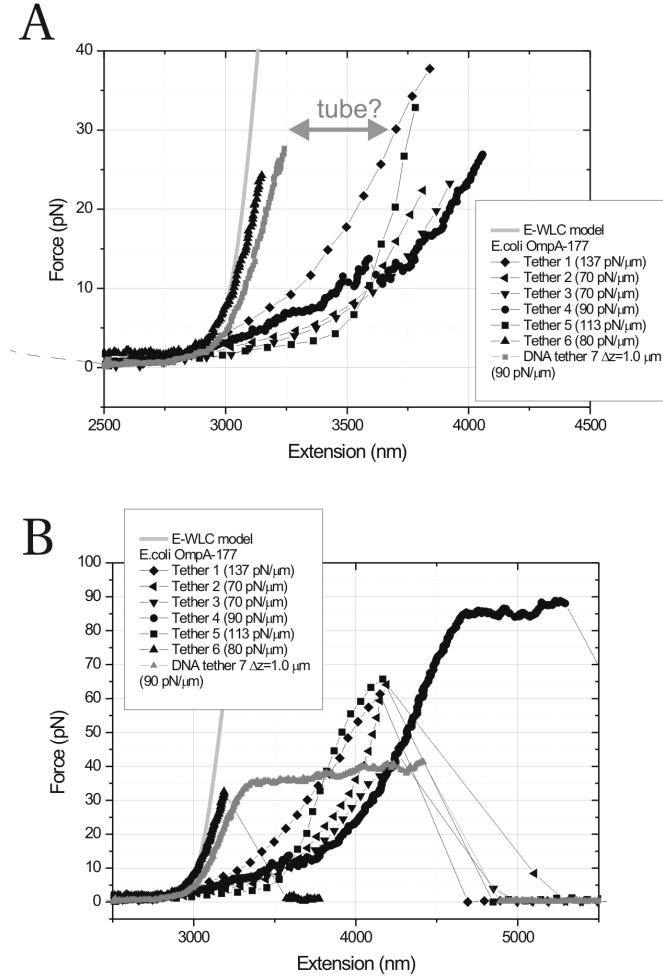


Figure 7.11. Tethers from strain MC1061 expressing OmpA-177^{SA-1}. The force on the bead is plotted as a function of tether extension. For comparison with DNA tethers, both the E-WLC model and DNA tether 6 at $\Delta z=1.0 \mu\text{m}$ are reproduced. The trap stiffness values for each curve are indicated. **(A)** As the trap is no longer harmonic for bead displacements $x_{\text{bead}} > \sim 300 \text{ nm}$, we truncated the curves at this point to allow quantitative comparison between the curves. **(B)** The complete curves for the data shown in **(A)**.

Therefore, the actual OS plateau forces are (much) lower. Possibly, also for tether 1 the onset of overstretching is apparent at high forces.

As the bacterial tethers were created manually by repositioning the sample in the z -axis, it is possible that the softer tethers are “pure” DNA tethers at increased relative height between bead and bacterium (“ Δz ”). As the height increases, the slope of the F - x curve goes down (**Figure 7.5C**). Alternatively, additional compliance is present. As estimated earlier, for these selected tethers, the immobilized bacterium acts as a stiff spring > 1000 pN/ μm . A tether length increase of > 50 nm relative to a “pure” DNA tether is therefore most easily explained by the formation of a membrane tube pulled from the bacterial outer membrane. For example, tether 1 at 30 pN could consist of a DNA tether 1 μm above the bacterium attached to a membrane tube of ~ 400 nm (estimated as the additional extension relative to the “pure” DNA tether at $\Delta z = 1.0$ μm). An alternative explanation would be that no tube is formed and the OM as a whole is displaced, i.e. the distance between PG cell wall and OM is increased without formation of a tube. However, based on our current understanding of the composition of the cell envelope of *Escherichia coli*, a large-scale displacement of the outer membrane away from the PG cell wall over distances more than a few nm would require the rupture of tens to hundreds of molecular bonds, which is unlikely.

What is puzzling for the “softer” tethers (tethers 1-4) is the absence of DNA OS at forces similar to that of the “pure” DNA tether (~ 35 pN). For the bacterial tethers, trap stiffnesses are 70-134 pN/ μm , similar to the trap stiffness for which the “pure” DNA tether was obtained (90 pN/ μm). For the Δz argument, tethers softer than “pure” DNA must be obtained at increased Δz (> 1.0 μm). For tethers 1 and 4 (trap stiffnesses 90 and 134 pN/ μm), one then expects an OS plateau force below ~ 35 pN. However, the observed (onset of) overstretching for these tethers is at ~ 70 and ~ 85 pN, respectively. This argues against Δz being larger than 1.0 μm . Although we cannot rule out that both tethers consist of multiple DNA tethers that break in a single step, we consider this unlikely.

Thus, we must assume that tethers 1 and 4 were obtained at a decreased Δz (< 1.0 μm). Then tube-formation is required to explain the observed “softer” F - x curves. As tethers 2 and 3 are only linear up to ~ 21 pN, possibly the force does not become high enough to observe OS. For these tethers we cannot distinguish between Δz and tube.

Next to the 20 bacterial DNA tethers discussed above, 2 additional tethers (referred to as OmpA-177 tether 7 and 8) were obtained with extension lengths much longer (6-7 μm) than the DNA contour length (2.16 μm). See **Figure 7.12B**. Tether 7 starts with a DNA

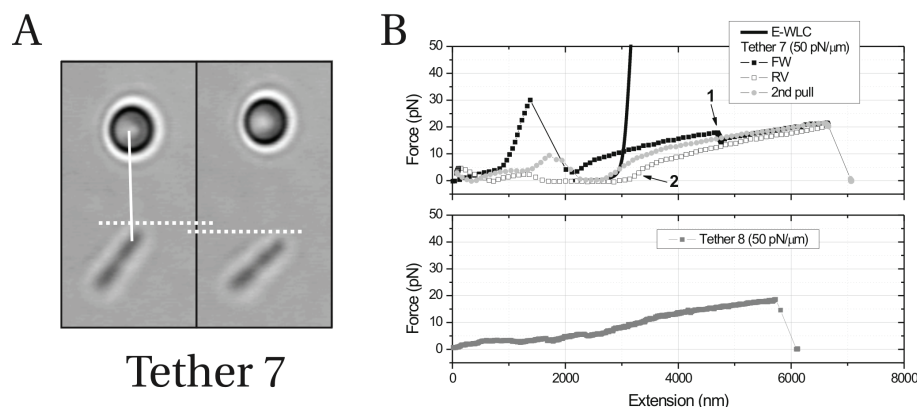


Figure 7.12. Possible membrane tubes pulled from strain MC1061 expressing OmpA-177^{SA-1}. (A) Two frames from a movie in which a bacterial tether is formed that is much longer than the DNA contour length. After the tether breaks, the bacterium “snaps” back ~ 400 nm. The presence of a long tether is indicated by a white line. (B) Force-extension curves of bacterial tethers that were much longer (length $6\text{--}7\text{ }\mu\text{m}$) than the majority of bacterial tethers (length $3\text{ }\mu\text{m}$). Tether 7 was obtained at the “fast” pulling rate, tether 8 at the “slow” pulling rate. For Tether 7, arrow “1” indicates the moment where the stage was halted for 10 s during which the bacterium rotates over ~ 100 nm towards the bead, thus reducing the force. Comparing the forward and reverse curves of the first pull of tether 7, the anchoring point has reoriented over ~ 1000 nm (suggested from the shape near arrow 2), assuming a purely elastic response.

tether as inferred from the rapid force increase around 1000 nm. After this tether breaks, a second tether gradually pulls the end of the bacterium in the direction of the bead. When the force has reached ~ 17 pN, the stage was halted for 10 s (arrow 1 in **Figure 7.12B**). During this time, the bacterium further reorients ~ 100 nm, causing the force to decrease (stage drift was ~ 1 nm/s). However, when stage displacement continues, the tether is extended a further $3000\text{--}4000$ nm up to a final extension up to $7\text{ }\mu\text{m}$, after which the stage motion was reversed. A second pull resulted in a similarly shaped F-x curve above 2600 nm, shifted $+400$ nm. This shift is interpreted as a reorientation of the bacterium. During the F-x curve, the force increase / nm extension (slope of the curve) was remarkably low. At forces > 10 pN (with the bacterium under tension), the tethers displayed approximately linear force-extension behavior with an effective spring constant of ~ 3 pN/ μm . Tether 8 has a similar F-x curve, extends up to $6\text{ }\mu\text{m}$ before it breaks, and has a similar effective spring constant.

Recently, a paper (Jauffred et al. 2007) described membrane tethers extracted from *E. coli* by optical tweezers. The tethers were formed directly between an (aspecifically adhered) PS bead and the bacterium. The tethers described by the authors had lengths several times the bacterial length (up to tens of microns long), a linear F-x curve through the origin, and a spring constant of 10-12 pN/ μ m for first-pull tethers, which was reduced in subsequent pulls.

Based on tether length and the soft linear F-x behavior, it is likely that our long tethers are in fact membrane tubes. Because for tether 7, only around ~3000 nm the bacterium reorients and force builds up in the tether, it is likely that the tether consists of a DNA molecule attached to a membrane tube. As in tether 8, a clear sign of a DNA molecule is missing, it is possible that this tether is a tube that was pulled through a direct bead-cell attachment.

Interestingly, upon reversal of the stage motion, the F-x curve has the same shape. In Jauffred *et al.*, after formation of a membrane tube at speeds similar to our “slow” speed, a viscous relaxation with a relaxation time of ~200 s to a lower “equilibrium” force plateau was observed. Here, however, both “fast” (tether 7) and “slow” (tether 8) pulling rates result in similar F-x curves. This suggests that during tether formation in our system, no viscous contribution is present. However, these data do not exclude that after (elastic) formation, an additional process (one that does not play a role during tether formation) might cause a viscous relaxation in these tethers.

To summarize, although we cannot rule out that the “soft” tethers are simply DNA tethers at increased heights above the bacterium, the fact that no overstretching at forces <35 pN is observed for these tethers despite their single-step breakage, and the fact that 2 of 22 tethers showed characteristics of extended OM membrane tubes, suggests that the “soft” tethers consist of a membrane tube in series with a DNA tether.

Bacterial tethers to full-length OmpA

As wild-type OmpA has a C-terminal periplasmic domain that anchors it to the cell wall, we also pulled tethers on a strain expressing such a construct (see also **Chapter 3**, and **Figure 7.1B**). From the ~150 tether attempts, 22 resulted in tether formation while at the same time the bacterium remained stuck on the surface.

Again, for all 22 tethers, we measured the tether length ($r_{stage}-r_{bead}$) when the force had reached 15 pN. We found an average bacterial tether length of 2712 ± 665 nm (S.D.).

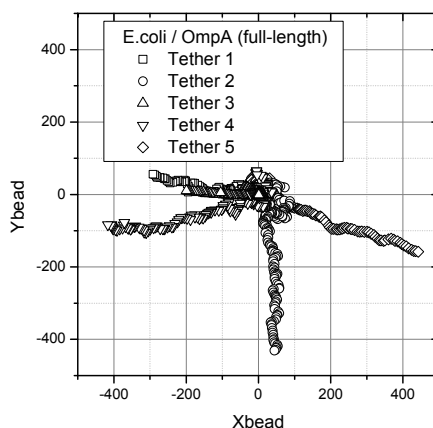


Figure 7.13: The position of the trapped bead determined by video tracking used to construct DNA force-extension curves of bacterial tethers to the full-length OmpA (shown in **Figure 7.14**).

Compared to the average tether length of 2837 ± 895 nm (S.D.) measured for the OmpA-177 β -barrel, this is ~ 100 nm shorter. Thus, both values are similar.

After setting the same constraints as for OmpA-177, 5 tethers remained. Again, we choose the “coarse approach” to plot the F-x curves, with only the x- or y- displacements used to calculate the tether extension. The XY scatter plots of the trapped bead are shown in **Figure 7.13**. The resulting F-x curves for these five tethers are plotted in **Figure 7.14A,B**. For comparison, a F-x curve of “pure” DNA Tether 7 at $\Delta z = 1 \mu\text{m}$ is reproduced from **Figure 7.5**.

Applying the same rationale as with the truncated OmpA tethers, we reason as follows: Tethers 4 and 5 are as stiff as a “pure” DNA tether at $\Delta z = 1 \mu\text{m}$. Tethers 1-3 are less stiff. Examining the tethers for the presence of an OS plateau, we find that tethers 1-4 show (the onset of) OS at forces varying from 20 pN (tether 3) to 35 pN (tether 1 and 4, for tether 4 over-estimated due to beyond linear regime) to 45 pN (tether 2, over-estimated as well). For tether 5, no OS is observed: for this tether the OS plateau is at least > 40 pN (end of linear regime). Thus, tethers 1-4 suggest “stiff” DNA tethers at around $1 \mu\text{m}$ height above the bacterium. Tether 5 completely overlaps with a “pure” DNA tether at $1.0 \mu\text{m}$ height, except that it does not exhibit a reduced OS plateau. There are two explanations possible for a higher OS plateau: either $\Delta z < 1 \mu\text{m}$ or a multiple tether that shows single-step

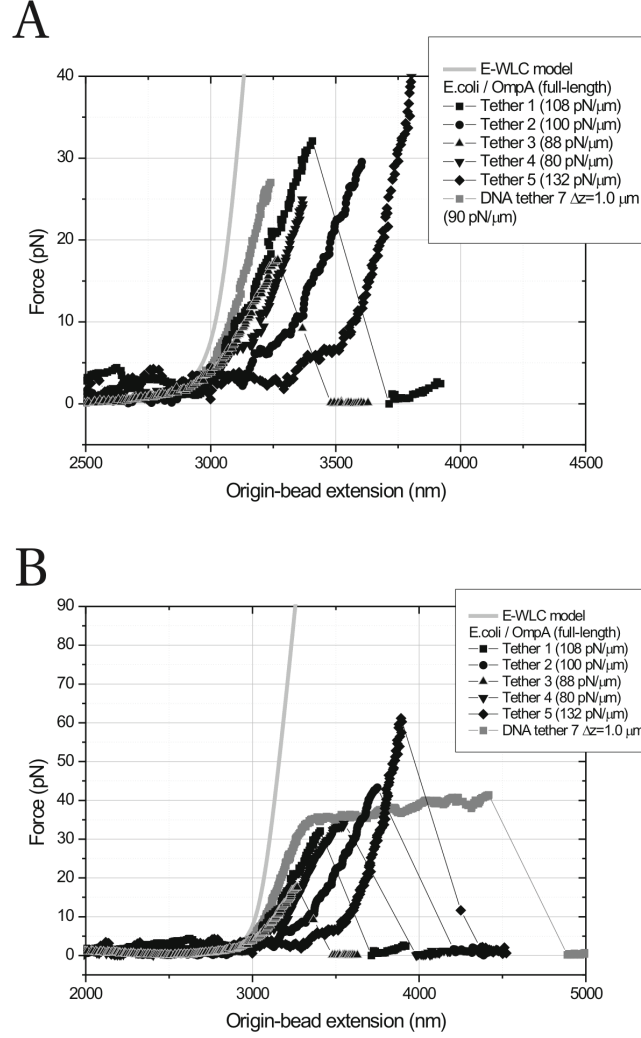


Figure 7.14. Tethers from strain MC1061 expressing full-length OmpA^{SA-1}. The E-WLC model from previous curves is reproduced for comparison. The trap stiffness of the bead varied between 80 and 132 pN/μm. Pulling speed was 0.24 μm/s (“slow”) for all tethers. **(A)** curves are plotted within the harmonic trap regime. **(B)** complete curves.

breaking. If $\Delta z < 1 \mu\text{m}$, then tube formation must occur to explain why it fits exactly the “pure” DNA tether at $\Delta z = 1 \mu\text{m}$ and is not stiffer, as expected for $\Delta z < 1 \mu\text{m}$. For tether 2, similar arguments can be made: it is less stiff than “pure” DNA, it was obtained at a

(slightly) higher trap stiffness, however, onset of OS indicates a plateau force of ~45 pN, which is increased relative to the “pure” DNA curve (**Figure 7.14B**).

Apart from these two tethers, no further indication of membrane tube formation is present in these data. Also, no “long” tubes are ever seen (such as in **Figure 7.12**). Possibly, internal anchoring of the OmpA protein to the rigid PG cell wall prevents membrane tube formation.

Analysis of the measured unbinding forces at two pulling speeds

Dynamic force spectroscopy is the measurement of (single molecule) unbinding forces as a function of force loading rate. At each loading rate a distribution of unbinding forces is found. In practice, one determines the most probable unbinding force at each loading rate by fitting the distribution with a Gaussian. Assuming that unbinding is a random process, which depends on the force through Eq. 2, an expression for the most probable unbinding force $F(r)$ as a function of loading rate r can be obtained (Evans and Ritchie 1997):

$$F = \frac{k_b T}{x_b} \ln \left(\frac{r}{k_{off}(0) \cdot \frac{k_b T}{x_b}} \right) \quad (\text{Equation 7.8})$$

As we know the force at which the tethers break (the unbinding force) at two different pulling rates, we have essentially performed dynamic force spectroscopy (DFS). This allows characterization of the weakest bond within the bacterial DNA tether and thus provides information on its molecular constitution.

There are two caveats: first is that our unbinding forces, especially for the “fast” pulling rate, are most of the time outside the linear regime of the trap. As we have seen, this can either under- or over-estimate the forces. Second, tethers that unbind while in the linear trap regime, will likely underestimate the unbinding force due to additional axial bead displacements as shown earlier. Third, in conventional DFS, the loading rate is constant, whereas here, due to the DNA, the loading rate increases as the DNA molecule is stretched. Furthermore, in the force regime where tethers break (>20 pN), the typical trap stiffness (100-200 pN/μm) is comparable to that of the DNA molecule (100-500 pN/μm). The means that the loading rate (pN/s) also becomes a function of trap stiffness k . This can

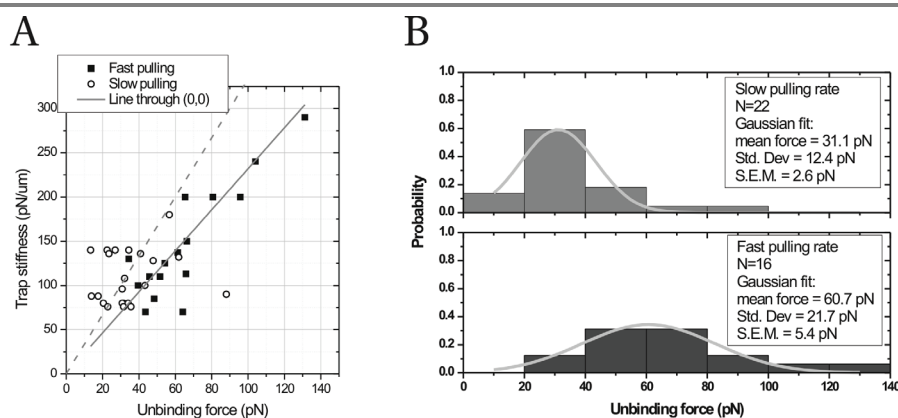


Figure 7.15. Probability distributions of unbinding forces measured at two different pulling speeds. (A) Correlation of the unbinding force with the trap stiffness. The dashed line indicates $x_{\text{bead}}=300$ nm and marks the end of the linear trap regime. **(B)** As both strains gave similar unbinding forces, the unbinding forces of both strains were pooled to obtain better statistics. Each histogram was fitted with a Gaussian function, giving a most probably unbinding force of 31.1 ± 2.6 pN (SEM, $N=22$) and 60.7 ± 5.4 pN (SEM, $N=16$), respectively. The unbinding forces are not corrected for a possible non-linear regime for high bead displacements, and the forces are lower estimates because of axial displacement of the beads, presumably resulting in a higher lateral trap stiffness (see text).

be understood as follows: when two springs are in series, the softer one will extend more than the stiffer one when the end-to-end distance is increased. Thus, for a high trap stiffness value k (stiff spring), mostly the DNA molecule “spring” is extended. If the stage is moving at a constant speed, the DNA molecule will be extended more rapidly, and will, since the force loading rate is higher, on average unbind at a higher force.

With these caveats in mind, we first plot the measured unbinding forces for the two different pulling rates as function of trap stiffness in **Figure 7.15A** (The region left of the dashed line marks the linear trap regime ($x_{\text{bead}} < 300$ nm)). As expected for a higher pulling rate, the unbinding forces are markedly increased. Furthermore, as expected, the measured unbinding force appears a function of trapping stiffness (the gray line is a line fit through the origin for the “fast” pulling rate). This effect should become more pronounced for higher loading rates, as for slow loading rates (low forces), the DNA “entropic” stiffness is the determining factor in the loading rate. This is exactly what we see (Coincidentally, the dashed line can be used as a guide to the eye to describe the dependence of the “slow”

unbinding forces on the trap stiffness).

The pulling rates and trap stiffness values used resulted in force loading rates of ~10-20 pN/s and 100-200 pN/s in the regime of unbinding (high forces). Dividing the unbinding force histograms by the total number of events, we end up with probability distributions to observe a particular unbinding force at the two pulling rates. In doing so, we ignore the trap stiffness spread, as these values varied over a factor two, and the pulling rate varied an order of magnitude. These probability distributions were fitted with a Gaussian function (**Figure 7.15B**). For pulling speeds of 0.24 $\mu\text{m/s}$ and 2.4 $\mu\text{m/s}$, most likely unbinding forces 31.1 pN (S.E.M 2.6 pN, N = 22) and 60.7 pN (S.E.M 5.4 pN, N = 16) were found, respectively.

Discussion

OmpA-177 versus full-length OmpA

In **Figure 7.16**, bacterial tethers to both strains are plotted together, aligned at ~10 pN to compare the slopes at higher forces (> 10 pN). The F-x curves obtained on full-length OmpA are plotted in gray; those obtained on truncated OmpA (OmpA-177, “ β -barrel”) are plotted in black. When comparing tethers, if the F-x curve for tether A is above the F-x curve for tether B in the region $F < 10$ pN, and below it in the region $F > 10$ pN, we say that tether A is “softer” than tether B.

We find that for both strains, tethers are obtained that overlap completely with a “pure” DNA tether at $\Delta z = 1.0 \mu\text{m}$. Additionally, tethers are obtained that are “softer” than the “pure” DNA tether. Comparing the two strains, we find that the tethers obtained from the truncated OmpA strain are “softer” than those obtained from the full-length OmpA. This could indicate the presence of an additional compliance in these tethers, possibly through the formation of membrane tubes, as for this strain two extended tethers have been observed that were much longer than the DNA contour length.

However, there are two factors that complicate the interpretation and comparison of these curves. The first is that all tethers have been created manually, and therefore, it is not expected that Δz is exactly $1.0 \mu\text{m}$ for each curve. As demonstrated in **Figure 7.5C**, variations in Δz in the order of a few hundred nm have significant effects on the observed F-x curve. In principle, the OS plateau force, which is a function of Δz , could be used as a height indicator. However, the trap stiffness at which the curves have been obtained varies

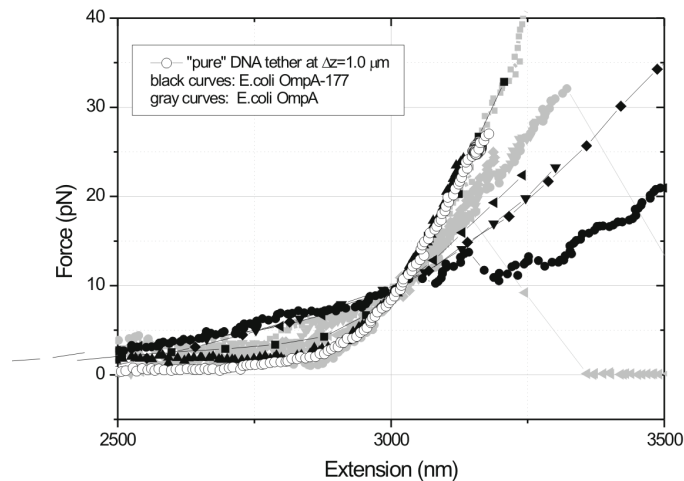


Figure 7.16. Comparison between bacterial tethers of both *E. coli* strains. The tethers were aligned to overlap at ~ 10 pN force. To allow comparison with “pure” DNA tethers to a stiff object, DNA tether 7 at $\Delta z = 1.0 \mu\text{m}$ is reproduced (open circles). Evidently, from both strains can tethers be obtained that are identical to “pure” DNA. However, also “softer” tethers are obtained, for which the stiffness increases much less rapidly as the tethers are extended. For these “softer” tethers, those obtained from the strain with full-length OmpA (gray curves) appear stiffer than those obtained from the strain with truncated OmpA (black curves). A possible explanation for the softer tethers is the formation of membrane tubes, which we expect to be more easily formed from the truncated OmpA strain. At present time, we cannot exclude that the softer tethers, as well as the variation between the two strains, is caused by variations in the relative height between bacterium and trapped bead.

over a factor 2, and for some curves, the OS occurs way outside the linear regime. This is the second complicating factor. For small bead displacements beyond the linear regime, the force appears to increase more than it actually does, however, for larger bead displacements the force will likely go down. This hinders the use of the OS plateau force to rank the tethers in height.

Additional experiments, in which the relative height between bead and bacterium is carefully controlled, e.g. by using the piezo stage to create the tethers, should provide the definitive answer to whether indeed membrane tubes are formed, and if internal PG anchoring by full length OmpA reduces the probability of such tube formation. Also,

increasing the trap stiffness to e.g. 250 pN/ μm will keep the bead within the linear trap regime for forces up to ~ 75 pN, allowing more information to be extracted from the F-x curves at high forces, such as the precise location of the OS force and the unbinding force. This is especially important for tethers obtained at the “fast” pulling rate, as the average unbinding force will be higher.

Correcting for axial displacements

We found that for our experimental geometry, the axial properties of the optical trap are important. As already mentioned, a study was reported that used a similar experimental geometry. There, a DNA molecule was tethered to a cover slip and a trapped bead, with the bead held a few μm above the surface. Force-extension curves were obtained by moving the stage and measuring the (lateral) force on the bead (Wang et al. 1997). The authors applied a geometrical model, with two main assumptions: (i) it was assumed that the lateral trap stiffness k_x did not depend on the bead’s axial position. (ii) It was assumed that the axial trap stiffness k_z was related to the lateral trap stiffness via $k_x/5.9$. They obtained good agreement between the E-WLC model and their measured F-x data. We applied the same geometrical model, and found that although it brought our F-x curves more in agreement with the E-WLC model and with measured F-x curves in which axial contributions could be neglected, but that still a large discrepancy was present. This discrepancy could be resolved by assuming that over a distance of 300 nm, the lateral trap stiffness roughly doubled.

It is possible that assumption (i) does not hold for our system. We use much larger beads, which can “feel” light gradients over greater distances. Furthermore, based on visual appearance and the geometrical model, our beads are axially displaced over several hundred nm. In contrast, (Wang et al. 1997) used 520 nm PS beads, which were trapped ~ 290 nm above the laser focus. A force clamp was used that kept bead displacements below 60 nm from the trap center by increasing the trap stiffness (up to 400 pN/ μm).

As for the second assumption, the ratio between k_x/k_z in (Wang et al. 1997), this value was based on theoretical calculations of the asymmetry of the light distribution near the focus of a focused Gaussian beam. Later experimental values measured in (Rohrbach 2005) found for a 530 nm PS bead a k_x/k_z ratio of 6.1. In the same study, it was found that the stiffness ratio k_x/k_z decreases with increasing bead diameter. The largest PS bead diameter characterized had a diameter of 1.66 μm , for which a k_x/k_z ratio of 2.7 was found.

As we used 1.87 μm PS beads, we chose to use a ratio of 2.5. However, it should be noted that this ratio likely depends on the NA of the objective, as well as the degree of overfilling.

Which unbinding force have we measured?

The molecular construct consists of a dsDNA molecule, on one end attached via multiple digoxigenin-antibody linkages to the bead, and on the other end either via one or two biotin's to one or two streptavidin molecules on the bacterial surface. Each streptavidin molecule can theoretically bind up to three SA-1 peptides, however, sterically it is unlikely that it binds more than one SA-1 peptide. Finally, the SA-1 peptide is part of the OmpA β -barrel embedded in the outer membrane.

We expect that multiple (>5) digoxigenin connections can withstand substantial amounts of force (Neuert et al. 2006). Furthermore, based on the forces required to pull out single Bacteriorhodopsin α -helices from purple membrane (100-200 pN at a force-loading rate of few 100 pN/s (Oesterhelt et al. 2000)), we also expect that pulling the complete OmpA β -barrel from the membrane requires higher forces than observed here. Thus, either the biotin-streptavidin or the (SA-1)-peptide-streptavidin complex is expected to unbind.

In **Figure 7.17**, the (two) measured unbinding forces for the bacterial DNA tethers are plotted as a function of (approximate) loading rate r . The error bars indicate the standard error of the mean, and therefore do not include the possible underestimation of the unbinding forces (due to axial displacement of the bead) for the “slow” pulling speed (estimated to result in a force loading rate r of ~ 20 pN/s), nor the under- or over-estimation (due to axial displacement, or lateral displacement outside the linear regime of the bead) of the unbinding forces for the “fast” pulling speed (~ 200 pN/s). The four gray curves were generated using **Equation 7.8**. For the streptavidin-biotin complex, the curve shown is the best fit through the experimental data reported in (Yuan et al. 2000), which yields a thermal off-rate of $1.67 \cdot 10^{-5} \text{ s}^{-1}$ and a barrier width $x_b = 0.49 \text{ nm}$. For the SA-1 peptide-streptavidin complex, $F(r)$ curves were generated for three different values of x_b (0.1 nm, 0.5 nm and 1 nm) using the thermal off-rate reported in (Bessette et al. 2004).

Ignoring any possible errors in determining the unbinding forces, we find that the theoretical curve for the Streptavidin-(SA-1)-peptide complex with a barrier width of 1 nm best describes our experimental data. However, for the “slow” pulling rate, the unbinding forces are expected to be underestimated approximately a factor two, based on the DNA

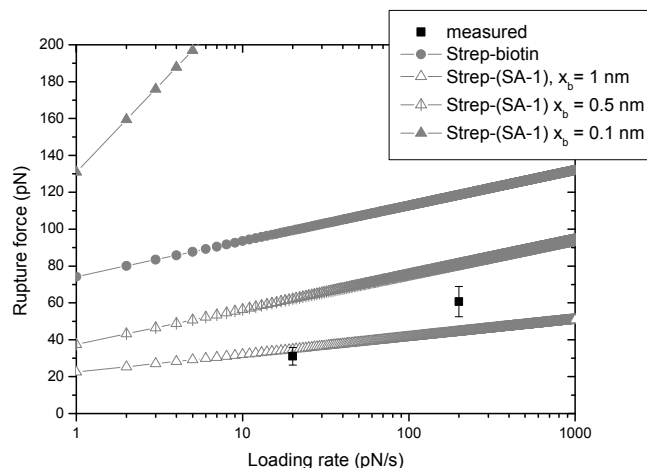


Figure 7.17. Most probable unbinding forces as a function of force loading rate. The measured unbinding forces (see also **Figure 7.15**) are plotted. The error bars indicate the standard error of the mean, and therefore do not include the possible underestimation of the unbinding forces for the “slow” pulling speed (estimated to result in a force loading rate of ~20 pN/s), nor the under- or over-estimation of the unbinding forces for the “fast” pulling speed. The four gray curves were generated using **Equation 7.8**. For the streptavidin-biotin complex, the curve shown is the best fit through the experimental data reported in (Yuan et al. 2000), which yields a thermal off-rate of $1.67 \cdot 10^{-5} \text{ s}^{-1}$ and a barrier width $x_b = 0.49 \text{ nm}$. For the peptide (SA-1)-streptavidin complex, $F(r)$ curves were generated for three different values of x_b (0.1 nm, 0.5 nm and 1 nm) using the thermal off-rate reported in (Besette et al. 2004).

overstretching experiments. Then the “true” unbinding force value will be ~60 pN, which is still almost a factor 2 less than that measured for a biotin-streptavidin bond, but would overlap with the expected value for the Streptavidin-(SA-1)-peptide complex assuming a barrier width of 0.5 nm. Therefore, these data suggest that we have measured the unbinding force of the streptavidin-(SA-1) peptide complex.

Taken together, we conclude that the bacterial tethers most likely consist of a single DNA molecule, attached to a single streptavidin bound to the SA-1 peptide displayed on the cell surface by the OmpA protein. The SA-1 peptide-streptavidin bond appears to be the weakest bond, with a most likely unbinding force of 60 pN at a loading rate of ~20 pN/s.

Acknowledgements

I would like to thank Matthew Tyreman and Thomas Kalkbrenner for providing the end-modified dsDNA and useful discussions and Christian Tischer for help with IGOR programming.

Materials and Methods

Preparation of DNA beads

1.87 μm carboxylated PS beads (Spherotech) were covalently functionalized with polyclonal anti-digoxigenin antibody (sheep, Roche #11333089001) using a commercial kit from Polysciences (Carbodiimide kit for carboxylated microparticles). Successful functionalization was inferred from their ability to form DNA tethers after incubation with dig-functionalized DNA. The DNA was created by PCR-ing a 300-400 bp fragment from pLexLacZ (Invitrogen) with 10% of TTP's replaced by dig-UTPs using primers DigFW and DigRV. This fragment was ligated via BglI to a BglI/AseI DNA fragment (6356 bp) from pDNR-SEAP (Clontech labs). The AseI site (overhang AT) was subsequently Klenow-filled with a nucleotide mix consisting of biotin-C14-dATP, dATP, biotin-C14-dUTP and dTTP. Thus, each DNA molecule has either 0, 1 or 2 biotin's on its end. Assuming that the dig-containing part of the DNA adheres completely to the antibody bead, and assuming a contour length/bp of 0.34 nm, the DNA tethers have an expected contour length of 2.16 μm . The DNA concentration is ~ 30 ng/ μl . The DNA is diluted 100x in PBS, and is mixed with anti-Dig beads (The DNA concentration on the beads was tuned to give mostly single DNA tethers in a bead-bead tethering assay), washed in PBS/1% BSA to get single beads, and incubated together in a small volume (~ 10 -20 μl) on a rotating wheel at 4C for 30 min. Finally, the beads were diluted in growth medium such that typically only a single bead would be present in the microscope's field of view. Primer sequences are available on request.

Bead tethering assay

A flow chamber is constructed by taping a Chromo-Sulfuric Acid/milliQ cleaned 24x32 mm #1 cover-slip on a thick microscope slide, depositing three parallel grease lines with a syringe and pressing a #1 18x18 mm cover-slip on top. This created a flow-cell with lanes of ~ 10 -20 μl volume (dimensions: 18 x 4 mm x 100-200 μm). Either Streptavidin beads

(Spherotech, SVP-60-5, 6.7 μm PS) or biotin beads (Spherotech, 3.28 μm PS) were adhered aspecifically to the glass surface. Sometimes, the immobilized bead would be pulled off the surface during a force-extension experiment. It was found that the bigger the bead, the stronger the aspecific immobilization. Beads were washed three times with PBS, diluted in PBS and flowed into the chamber. Incubation was for 15 minutes at RT, then the chamber was flushed with ~ 5 volumes (100 μl) of PBS, turned upside-down, and further incubated for 15 min. Then the chamber was flushed with ~ 5 volumes (100 μl) of Defined rich glucose medium, and the sample was mounted in a sample holder, put in the setup, and an immobilized bead was searched for in the microscope. Then the sample was removed again, and either biotin-DNA beads (in case of immobilized streptavidin beads) or streptavidin-DNA beads (in case of immobilized biotin beads) were diluted in defined rich glucose medium and flowed in (~ 20 μl). The sample was mounted again, and a freely floating DNA bead was located. Then the microscope diaphragm was fully closed (the little light that leaks through is enough for illumination by the high NA inverted objective). The inverted objective was lowered on top of the sample until just after the diaphragm of the microscope was in focus (i.e. no Kohler illumination). This is required for trap calibration, as the red HeNe laser needs to pass through both objectives to be imaged onto the QPD. Typically, a bead was trapped at low laser power (9.5A current) and an average power spectrum was recorded. At low frequencies, (vibrational) noise obscures the bead motion, and at high frequencies, aliasing of higher frequencies obscures bead motion (the aliasing filter is not yet functional). Therefore, spectra were fit in the range 200-2000 Hz. As roll-off frequencies were typically 200-300 Hz (trap stiffness 20-30 pN/ μm), this region is sufficient to obtain a good fit. Using the viscosity of water ($1\text{E-}3$) and the bead diameter (1.87 μm), the trap stiffness in X and Y is obtained. As the trap stiffness in X and Y direction were always the same within 10%, a single average trap stiffness value in both directions was taken. Trap stiffness values at higher laser powers were scaled linearly (see **Chapter 6**).

Bacterial tethering assay

Strain MC1061 electroporated either with pGV28 (OmpA-177^{SA-1}) or with pGV33 (OmpA^{SA-1}) plasmid (**Chapter 3**) was used. Cells were cultured in defined rich medium at 37°C in the presence of 0.1 mM IPTG to induce expression of OmpA^{SA-1}. After growth to exponential phase (~ 3 hours), cells were resuspended in PBS containing 1 mg/ml BSA and incubated on ice for 10 min (blocking of aspecific sites). Then streptavidin was added (45 $\mu\text{g/ml}$) and

the cells were incubated a further 30 min on ice. Cells were pelleted twice and resuspended in PBS to wash away unbound streptavidin. At these expression levels of the SA-1 tag, pelleting results in an agglutinated clump of cells due to cross-linking by streptavidin. Vigorous pipetting then disperses the cells again. Subsequently, the cell suspension is diluted 10x into PBS and flushed into a flow chamber (volume ~20 μ l, see photograph). Cells were adhered aspecifically to the (chromosulfuric acid cleaned and mQ rinsed) glass cover slip. It was found important for adhesion of cells that fresh cover slips were prepared every 2-3 weeks. After 15 min, the flow chamber is flushed with 5 volumes of PBS (~100 μ l) and turned upside-down. After another 15 min, the flow chamber was flushed again, now with ~5 volumes of defined rich medium. The beads were diluted in growth medium such that typically only a single bead would be present in the microscope's field of view. The trapping laser current supply, and the HeNe position detection laser were turned on 3 hours in advance to stabilize the beams. A tether is formed by reducing the laser power on a trapped DNA bead, positioning the bead above the bacterium and subsequently reducing the z-distance between trap and bacterium (pressing the bead on top of the bacterium), and waiting a few seconds. Then the trap-bacterium distance is increased again manually until the bead has returned to the zero-force z-position, the laser power is increased and the stage is moved away at a constant speed (either 2.4 or 0.24 μ m/s) in either X or Y direction, depending on which direction gives an angle closest to a right angle with the long axis of the cell.

Data analysis

The bacterial tethers were analyzed as follows. The tethering events was recorded at 25 Hz with a DVD recorder and burned on DVD as a collection of 20-30 1-2 minute movies. With an IDL program developed at AMOLF (Track_bead), for each movie, the positions of the bead and stage are tracked with sub-pixel resolution using a cross-correlation algorithm based on a template (portion of an) image. As template used for bead tracking, typically a frame is chosen containing the bead right after the tether broke, as this frame represents the bead position without force acting on it. The stage was tracked either via a bead that was attached (preferred option), or via an additional bacterium attached, or via the bacterium being tethered (least preferred option) depending on what was present in the field of view. Pixel sizes for the camera and objective used (Kappa CF 8/4 DX together with water objective at 1.5X magnification) were determined using the piezo-stage, by moving a

bead stuck on the surface in X and Y steps of 1 μm over the surface and video tracking the positions. We found pixel sizes in X and Y of 93.8 nm and 85.4 nm, respectively. The text files containing the pixel values were subsequently manipulated and plotted in Origin. The stage positions were shifted manually such that the stage position in the frame just before stage translation starts was (0,0). The bead positions were shifted manually such that right after a tether breaks the bead is at (0,0). We defined the tether extension length as $x_{\text{stage}} - x_{\text{bead}}$. Defined in this way, the bead radius is part of the tether extension, and we assume that the tether is attached on the bacterium exactly underneath the center of the bead. The magnitude of the force vector on the bead was obtained by multiplying the length of the bead position vector ($x_{\text{bead}}, y_{\text{bead}}$) with the trap stiffness obtained from an average power spectrum as described above. Plotting the force magnitude as a function of tether extension length yields a force-extension (F-x) curve. The DNA tethers between beads were analyzed in the same way, except that the immobilized bead was tracked for the stage position, and arbitrarily shifted on the X-axis, as the absolute tether extension is not known, only the increase in tether extension since the measurement started.

The force vector was plotted in the video images by the following steps. The DVD movies were re-played and grabbed by an analog video grabber at 40 ms/frame (Silicon Graphics PC, Anaconda) using an IDL program (grabber_program) that writes the grabbed images as a tiff stack. Using a second IDL program (track_bead), the tiff stacks were tracked for the bead position, and care was taken to get the center of the bead template as close to the bead center. The tracked coordinates now indicate the bead position as pixel values. A small routine was written in IGOR that needs as manual input the frame where the force on the bead is zero (usually the last frame), and then writes in each frame the vector between the zero force bead position and the current bead position as a white line that is proportional in length to this distance (and thus can be interpreted as a force vector).

These movies were used to more accurately determine the anchoring point on the bacterium: in ImageJ, the pixel coordinates of the trapped bead at $t=0$ (onset of stage motion) are estimated. Then, the frame right before the tether breaks is used to get the intersection of the force-vector and the bacterium. A straight line crossing this point, and parallel to the pulling direction was drawn, and the frame at $t=0$ is displayed again. The pixel coordinates of the point where this line intersects the bacterium was then estimated,

and the difference in pixel values was used to shift the tracked stage position (starting at 0,0).

To visualize the force vectors in the reference frame where the bacterium does not move, the tracked-stage data from the f-x curves was used. The pixel size calibration constants were determined for the re-played grabbed video data by using a movie in which a bead stuck to the stage was displaced in X and Y in steps of 1 μm .

VIII

Chapter 8: Final Considerations and Recommendations

This chapter will discuss the steps remaining before one can actually exert and measure forces during the division of a single bacterium. We present alternative approaches that we explored, as well as provide recommendations/possibilities for future research. However, we start by summarizing what has been achieved so far:

First, we have engineered a protein (the OmpA β -barrel with the streptavidin-binding peptide) that inserts as efficiently into the outer membrane as wild-type OmpA (**Chapter 3**). Second, we have shown that using this protein, it is possible to attach optically trapped beads to the cell surface of a living bacterium, and we have estimated that a single tether can withstand forces of a few pN for a few minutes (**Chapter 7**).

Major effort has been directed towards the construction of a β -barrel fusion protein that localizes at mid-cell (**Chapter 4 and 5**). A lot has been learned, and as discussed below, we believe that such a fusion protein is technically possible and feasible. To obtain such a fusion protein, two approaches are explored in this thesis: First, the dynamic association of either an endogenous inner membrane protein (e.g. FtsQ) with the “divisome” at mid-cell, followed by OM insertion of its periplasmic “tail” containing the β -barrel protein (**Chapter 4**). Second, the dynamic association of an endogenous periplasmic factor (e.g. Pal) at mid-cell while anchored to a β -barrel present in the OM (**Chapter 5**). The first approach requires the sequential steps of mid-cell association of e.g. FtsQ followed by passage through the septum and OM insertion of the β -barrel. The second approach requires the free diffusion of the β -barrel through the OM as well as that the periplasmic factor must be able to bind to its “septal partner”/molecule/protein at mid-cell when attached to the β -barrel.

Below, we present an overview of the literature on the lateral mobility of β -barrels in the OM of *E. coli*. Although sparse, the current experimental evidence available suggests that free diffusion of β -barrels is indeed possible, especially in *E. coli* strains that produce a truncated LPS, such as K-12. Based on the results obtained in **Chapter 5**, we then provide some suggestions for periplasmic factors on which future fusion proteins could be based.

In parallel with the approach as outlined in the introduction, we have explored

alternative approaches. One approach to avoid the engineering of a mid-cell localized anchoring point in the OM is to make use of a so-called “L-form” *E. coli* strain. This is a mutant strain that has lost irreversibly the capacity to form an OM and PG cell wall. Our (limited) experience with such a strain will be discussed.

In the original experimental concept, the bacterium is attached to optically trapped beads tethered to it on both sides. This fixes the bacterium in space at the point where both forces exerted on it are equal but opposite. Without a specific anchoring point at mid-cell, it is difficult to imagine how two DNA-coated beads can be attached to the division site of a single bacterium on opposite sites. However, it might be possible that after bringing a DNA-coated bead into contact with the bacterium, the bead will be attached roughly at the division site. Then, in the absence of an opposing force by a second tethered bead, an alternative way of holding the growing bacterium in place is required. We have explored two possibilities: the surface approach, and the “dumbbell” approach. The first approach has been the topic of **Chapter 7**, and results that we obtained with the second approach are presented in this chapter.

Finally, we discuss a promising way to improve the strength of the weakest part of the molecular construct, the attachment of the free end of the DNA to the β -barrel. We conclude by discussing two experimental approaches to study the effect of forces on bacterial (wall) growth and shaping in a more general way.

Mobility of β -barrels in the OM

The OmpA-(mid-cell domain) fusion approach relies heavily on the assumption that the OM is a continuous fluid bilayer and that the OmpA β -barrel fusion protein can associate dynamically with periplasmic factors when the cell divides.

Traditionally, the OM is thought of as a tight, gel-like barrier with LPS packed together with cations in a crystalline matrix (Nikaido 2003; Ruiz et al. 2006). Only a hand-full papers exist that study or provide clues on the molecular organization of the bacterial outer membrane and the lateral mobility of its constituents.

Chemically reactive fluorescent dyes exist that are thought to label only surface-exposed cell components. Using such a dye (Texas Red-X-succinimidyl ester), all cell surface components that contain reactive amine-groups can be fluorescently labeled. From pulse-chase and FRAP experiments on labeled *E. coli* cells, it was concluded that there are mobile and non-mobile “elements” in the OM (de Pedro et al. 2004; Ghosh and

Young 2005). However, it remains unclear which components exactly were labeled in these studies. Periplasmic lipoprotein Lpp was also found to become labeled (de Pedro et al. 2004), and reactive agents based on succinimidyl ester have been shown to label also periplasmic and inner membrane components (Bradburne et al. 1993; Sabarth et al. 2002).

Specific diffusion studies have focused on the β -barrel LamB which forms trimers in the OM. LamB in the OM of a living bacterium with a 540 nm streptavidin bead attached was shown to be confined within 25 nm and have a diffusion coefficient of $0.15 \mu\text{m}^2/\text{s}$ (Oddershede et al. 2002). A different study was reported that used either fluorescent phage tails or ~ 20 nm gold beads to track LamB proteins in living cells (Gibbs et al. 2004). Surprisingly, large differences in localization patterns between fixed and living cells were observed for LamB. Tracking 20 nm gold beads attached to LamB in living cells, it was found that two sub-populations existed, termed “mobile” LamB (40% of all trajectories, bead moved over 300 nm in 5 min) and “immobile” LamB (60% of all trajectories, bead moved over 50 nm in 5 min). To explain the immobile LamB, both studies refer to an early observation that LamB interacts with PG (Gabay and Yasunaka 1980). However, from the crystal structure it is not clear how PG binding would be achieved (Schirmer et al. 1995). Possibly, a periplasmic factor could retain LamB.

Indirect evidence for lateral diffusion of β -barrels in the OM comes from studies of the IcsA virulence protein in *Shigella* that forms actin-tails, which propel the bacteria after infection in eukaryotic cells. The IcsA protein is part of the autotransporter family of OM proteins that are large proteins consisting of a cell surface-exposed N-terminal domain anchored in the OM by a C-terminal β -barrel (Bernstein 2007). Autotransporters are sub-localized to old poles already in the cytoplasm by an unknown mechanism (Jain et al. 2006). At the pole, they are exported to the periplasm by the Sec system (which itself is not specifically localized at the pole) and the β -barrels are inserted in the OM mediated by Omp85/BamA (Jain and Goldberg 2007). After polar OM insertion, IcsA laterally diffuses through the OM, forming a concentration gradient, as observed with immunofluorescence (Robbins et al. 2001).

Additionally, there are indications that LPS composition can influence the lateral mobility of β -barrels. Intact LPS molecules are thought not to diffuse, based on a FRAP experiment using fluorescent concanavalin A labeling of *E. coli* with intact LPS (Ghosh and Young 2005). Mutations in LPS synthesis genes affected polar localization of IcsA in the

OM (Sandlin et al. 1995). Based on this, interactions with LPS were proposed to retain the β -barrels at the cell pole (Jain et al. 2006). Consistent with this hypothesis, polar localization of IcsA is reduced in K-12 strains that have truncated LPS, possibly due to increased lateral diffusion (Jain et al. 2006).

Finally, for a different OM β -barrel (the BtuB protein) a diffusion coefficient similar to that of the IM was recently reported (Jeff Spector and Ken Ritchie, Biophysical Society Meeting 2007). Thus, the available evidence suggests that β -barrels *can* diffuse freely in the OM.

It will be important to find out whether this also holds true for the OmpA β -barrel. FRAP experiments on living cells with fluorescent probes attached to the surface-exposed loop might answer this question. Especially the SA-1 peptide is useful for this approach, as this peptide can be directly visualized with fluorescent streptavidin. Although streptavidin is a tetramer, steric hindrance will likely cause it to bind only one OmpA, possibly two. Alternatively, fluorescently labeled anti-FLAG can be used to visualize the FLAG-containing OmpA β -barrel. As a control, full-length OmpA can be used, which we expect to be immobilized or slowed down by its interaction with the PG cell wall.

Restraining a β -barrel to mid-cell

Based on the results with LamB, BtuB and IcsA, it is likely that OmpA also can diffuse in the OM. This would satisfy one of the requirements of the approach followed in **Chapter 5**, which is the fusion of periplasmic factors to the OmpA protein to sub-localize it to the division site. The alternative approach, extending an IM protein, such as FtsQ (see **Chapter 3**), requires that the fusion protein somehow can pass through the PG cell wall without interfering with the dynamic association of the IM protein at mid-cell, for instance, when turnover in the cell wall is so high that it can diffuse laterally while spanning the periplasm. If PG turnover is low, then the timescales of mid-cell association and OM insertion of the periplasmic “tail” should be sufficiently separated, with mid-cell localization occurring first, followed by OM insertion of the tail. In this scenario, an additional worry is what happens after division, i.e. whether the fusion proteins are subsequently “trapped” at the new poles. This would put constraints on synthesis and folding rates of the fusion, as well as create possible problems with titration of “divisome” factors away from mid-cell.

In **Chapter 5**, various OmpA constructs are described that were designed to localize to

mid-cell. Of these, Pal was highly promising due to its homology to the OmpA PG binding domain and its sub-cellular localization (between PG and OM). After fusing Pal to the C-terminus of OmpA, it appears that Pal can no longer compete with wild-type lipoPal. In the absence of wild-type lipoPal, OmpA-Pal was not functional. As only the OM anchoring has changed, possibly the rapid diffusion of Pal in the inner leaflet of the OM is important. After fusing OmpA to the C-terminus of Pal, OmpA can no longer insert into the OM.

Thus, an alternative domain is needed. From the results obtained with the OmpA-Pal fusion, we can conclude that a periplasmic factor is preferred that normally localizes to the space between the PG cell wall and OM at mid-cell and has no strong phenotypic defects when non-functional.

AmiC, a PG hydrolase that localizes at mid-cell and helps to cleave the septum (Heidrich et al. 2001; Bernhardt and de Boer 2003), appears to match these requirements. The catalytic function and its septal localization are separated into two domains, as without catalytic domain the septal domain ^TAmiC localizes to mid-cell. In **Chapter 5**, only a C-terminal fusion is presented, as initially we reasoned that since ^TAmiC localized with a C-terminal GFP, this terminus could accept a fusion without destroying mid-cell localization. However, this domain order prevented OM insertion of OmpA. Possibly, fusing ^TAmiC to the C-terminus of OmpA allows OM insertion and mid-cell localization at the same time. If competition with wild-type AmiC occurs, a Δ AmiC strain can be used. In (Heidrich et al. 2001), it is shown that a Δ AmiC strain growing in LB medium at 37°C forms chains of 3-6 cells in 20-30% of all the cells. Chaining was most obvious in late stationary phase. Thus, in 60-70% of the cells, septum cleavage still occurs, although possibly at a reduced rate.

If AmiC fails to perform, other proteins might take its place. For example, it was recently discovered that the outer lipoprotein RlpA localizes to mid-cell (“rare lipoprotein A”, DS Weiss lab). It has a C-terminal “SPOR” domain that binds PG. Deleting it has apparently no effect on cell division (DS Weiss, Gordon Conference 2008). Another outer lipoprotein is NlpI, which is thought to function during cell division but has not been localized to mid-cell yet (Ohara et al. 1999). This protein is less attractive however, since deleting it renders cells osmotically sensitive (Ohara et al. 1999), which could be indicative of OM problems during division similar to Pal.

Alternative approach: PG cell wall-less *E. coli* (“L-forms”)

As an alternative approach, we have considered *E. coli* mutant cells without PG cell wall and OM (so-called L-Forms) as an alternative. Here we describe what is known, as well as our experience with it.

Treating *E. coli* with lysozyme/EDTA is a standard procedure to destroy its cell wall and permeabilize its OM (Neu and Heppel 1964; Harvey et al. 2004). After such treatment, it has been reported that proteins up to 240 kDa can enter the periplasmic space (Harvey et al. 2004). However, such treatment typically abolishes division, and does not strip the cell entirely of its OM. In the literature, stable PG cell wall-less *E. coli* have been reported. They come in two variants: Spheroplasts are cells that contain IM and OM, but no PG. Protoplasts are cells that contain only IM. One such protoplast strain (as judged from EM pictures (Gumpert et al. 1971)), LW1655F+, was created by continued passages in complex medium in the presence of 6-10% sucrose and penicillin. After some time, this strain lost the ability to grow a cell wall in the absence of penicillin (“revert”), and became a stable “L-form” strain.

Obviously, a strain that contains a Z-ring, but no PG cell wall and OM would be very useful in our proposed optical tweezers experiment, as there is no longer a requirement for an OM fusion protein that artificially localizes to mid-cell. In principle, simply adding an epitope to a (now surface-exposed) periplasmic domain of one of the known cell division proteins (such as FtsQ or FtsN) would be enough.

However, there are several drawbacks: It is osmotically sensitive, requires growth in complex media (e.g. beef-heart-infusion and yeast extract medium) and large inocula (a dense culture is typically diluted 10-100x during a passage to fresh medium) (data not shown, (Siddiqui et al. 2006)). A growing culture is quite heterogeneous: cell size ranges from a few hundred nm to a few μm in diameter (data not shown, (Schuhmann and Taubeneck 1969)). The growth rate is slow, probably partly because division often fails (lysed cells accumulate in the medium). This is probably why a large starting inoculum is needed.

While we were performing preliminary growth experiments with the LW1655F+ strain, a work came out (Joseleau-Petit et al. 2007) that described a method to turn any *E. coli* strain into a “L-form-like” state (envelope structure: both IM and OM in “somewhat disorganized state” (Joseleau-Petit et al. 2007)). Using this method, the authors showed

that their L-form-like cells contained residual PG (~7%), and that PG synthesis was required for their propagation. According to the authors, no published data exists which excludes that in the LW1655F+ L-form, also PG synthesis takes places during division. This might interfere with epitope exposure by periplasmic domains of cell division proteins, as the septal PG covers them during division. However, differences might exist between LW1655F+ and the L-form-like cells. The latter cells appear to have both IM and OM, whereas EM pictures of LW1655F+ showed a single membrane. Furthermore, without a periplasmic space and an OM, it is unclear how septal splitting would occur, as PG hydrolases such as AmiA, AmiB and AmiC are thought to diffuse freely in the periplasm. Without a periplasm, they would be expected to leak into the external medium.

Due to the fact that it was not clearly established that our L-form protoplast indeed did not contain septal PG, L-form division is slow and often fails, and the fragility of the cells (demonstrating epitope exposure specifically at mid-cell requires labeling of living cells) this option was considered too risky and put on hold.

Experimental geometry: assembly of the construct in the trap

In **Figure 8.1**, schematics and preliminary experiments are shown that demonstrate the assembly of a bacterium tethered to one or two DNA-coated beads. In these experiments, the DNA tethers are formed during the experiment in a controlled manner. Alternatively, DNA-beads and cells can be mixed and pre-incubated. However, it is anticipated that after finding a floating bacterium with two DNA-coated beads attached, it will be difficult to make sure that the two beads end up in two separate traps with the bacterium in between.

Note that for these experiments we switched to defined medium, as the commonly used LB/TY medium appeared to interfere with the formation of biotin-streptavidin bonds during DNA tether formation. In retrospect this was not so surprising, since LB/TY medium contains yeast extract, which is a rich source for B vitamins such as biotin (vitamin B7). Presumably, the free biotin binds to streptavidin at the ends of the DNA-coated beads, blocking tether formation to the biotinylated anti-FLAG on the cell surface.

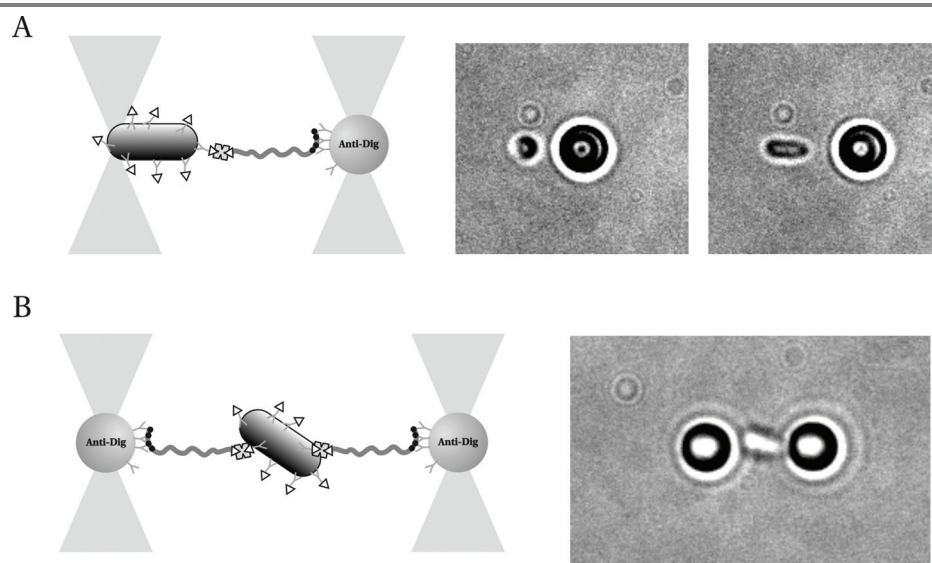


Figure 8.1. Experimental geometries using DNA spacers. (A) A DNA tether is formed by trapping both an antibody-coated bacterium and a DNA-coated bead and forming a biotin-streptavidin bond after bringing both cell and bead in close proximity using two optical traps. (Here the two traps originated from the two opposed objectives and were manipulated manually by XYZ telescopes, i.e. the traps are not time-shared). (B) Using dynamic time-shared traps, first a DNA tether was established as described in (A), after which a second DNA-coated bead was brought into close proximity to the trapped and tethered bacterium. After formation of the second DNA tether, the trap holding the bacterium is turned off and the bacterium is held via two DNA spacers in double optical traps. Here, after a few seconds, the second tether broke and the bacterium was pulled towards the trap holding the bead it remained tethered to.

As the experiment is expected to take several minutes, drift, and unwanted objects jumping into the trap can be a problem. Using rich medium (such as the defined Rich medium used in **Chapter 7**) results in fast growing cells, so that the division occurs as rapidly as possible. Drift of the stage with respect to the optical trap is ~ 1 nm/s at room temperature. By using two time-shared traps directed into the sample via one objective, almost no drift is expected to occur between the two traps, and the residual drift will most likely not be dependent on the sample temperature.

Effect of laser light on bacterial growth

As mentioned, a controlled assembly of the construct is preferred. This requires directly trapping a bacterium using optical tweezers. As the bacterium must divide after assembly, photo-damage to the cell must be minimized.

Soon after the invention of single-beam optical tweezers, it was found that infrared (IR) laser light is much less damaging to cells compared to visible laser light from a green argon laser, which could even “optically execute, shrink” *E. coli* cells (Ashkin et al. 1986). Damage-free trapping of *Escherichia coli* using 80 mW IR laser light for 30 min was reported (Ashkin et al. 1987). However, (Neuman et al. 1999) et al. monitored flagellar rotation rate as a measure of cell viability, and found that using 1064 nm light, within a few minutes rotation rate decreased when trapped with 100 mW in the specimen.

The cells can be briefly trapped without loss of viability: (Ericsson et al. 2000) reported an assay where *E. coli* cells were sorted with optical tweezers, and demonstrated viability by monitoring subsequent growth following the trapping event. Furthermore, (Roos 2000) also showed that an *E. coli* bacterium could grow (slowly) when trapped in weak traps at high-growth speed/rich medium conditions.

In a systematic study of 1064 nm optical trapping damage on trapped *Escherichia coli* (Ayano et al. 2006), the ability to divide was checked after trapping at various times and laser intensities. It was found that the total energy (Power x time) was the determining factor in the loss of division capability. At energy < 0.36 J, division was not affected. For a laser power of 10 mW (measured at the objective), this means 36 s of trapping time before division is affected! Furthermore, division was more easily affected than growth. Recently (Rasmussen et al. 2008), it was shown that continuous IR trapping of *Escherichia coli* at 18 mW in the sample decreases the pH gradient within minutes. Overall it can be concluded that cells can be trapped without loss of viability, but that both trapping time and laser power need to be minimized.

Using time-shared tweezers, we trapped several bacteria at both poles (rod-shaped cells align along the optical axis when trapped) in minimal medium with the water bath temperature at 40°C to monitor length growth. Under these conditions, cells on agar would readily grow into micro-colonies. However, we have never observed growth when directly trapping a bacterium. It is possible that the light intensity in the traps was too high, or that in minimal medium, less light is required to damage the cells (the cells are

also smaller).

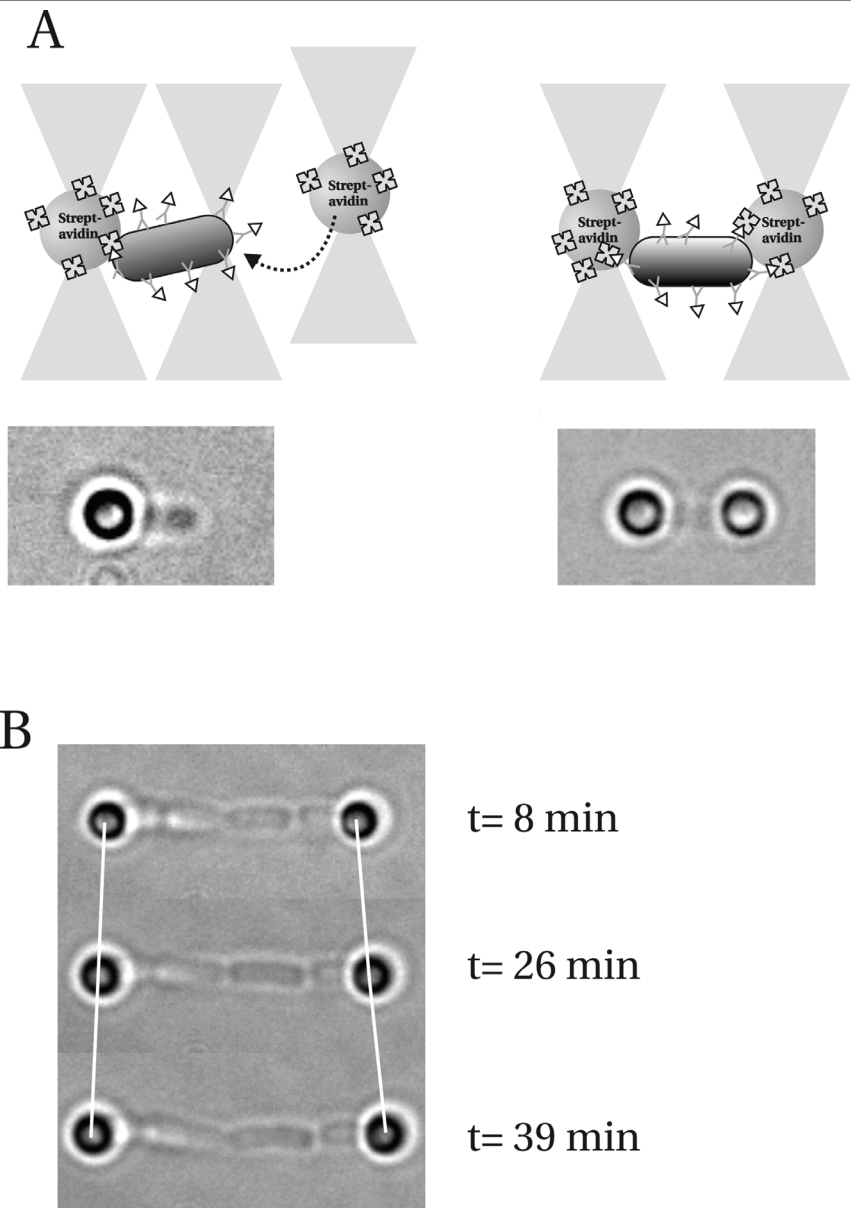
Alternative geometries: surface and dumbbell approach

Thus, we concluded that during the experiment, which takes at least several minutes, direct laser trapping of the cells is not an option. We therefore looked for ways to hold or immobilize a bacterium without directly trapping it, to prevent a block in growth and/or division. We have explored two options: The first (“surface approach”) is described in **Chapter 7**, where tethers are formed on immobilized bacteria on a glass surface (adhered aspecifically). The second (“Dumbbell approach”) is discussed below, and consists of attaching beads as handles directly to the cellular poles.

The disadvantage of the surface approach is that most bacteria are not attached strong enough to withstand forces $> \sim 5$ pN for more than several seconds. A second disadvantage is the three-dimensional geometry of the experiment. Not only lateral, but also axial displacement of the trapped bead has to be taken into account (**Chapter 7**). This can be avoided by sticking bacteria on beads immobilized on a cover slip (Fallman et al. 2004; Jass et al. 2004): this increases the height of the bacterium such that the tether can be made “from the side” in the XY plane. A disadvantage is that refraction of light through the bead (partially) obscures the bacterium. This might not be a problem when measuring e.g. the elasticity of pili or flagella, but it is difficult to see if growth occurs, or if the bacterium displaces (data not shown). In general, the surface approach tries to reconcile two conflicting requirements: to immobilize the bacterium as strongly as possible on the one hand, while on the other hand allowing free unconstrained growth and division.

Therefore, we have experimented with alternative geometries where beads are attached to the bacterial cell poles, and the cell is held by optically trapping the bead handles (**Figure 8.2**). This approach was pioneered in (Roos 2000), where bacteria were mixed with poly-L-lysine coated (core-shell/silica) beads ($d = 675$ nm) and a bacterium with two beads was trapped in two weak traps (5 pN/ μm , 13 mW per trap estimated in the sample) and followed in time. It was found that in rich TY medium at 37°C, the bacterium could continue to grow and divide when held via these handles.

We followed a similar approach. To attach beads we use our specific OmpA-FLAG anchoring (see also **Chapter 3**). The connection between bead and cell is through biotinylated antibodies and streptavidin-coated beads (**Figure 8.2**). Preliminary experiments in bulk indicate that bacteria can grow normally after antibody labeling (after



labeling a lag phase of ~30 min was observed when grown in shakers and following the

Figure 8.2. Growing cells in the dumbbell geometry. (A) Assembling the dumbbell. Three time-shared traps were used to create the dumbbell bacterium trapped in between two beads. First, a bacterium is trapped in two traps (not shown), then with the third trap, a streptavidin bead is pressed to one of its poles and the trap holding that pole is shut off. This is the situation shown in the left panel. Then a second streptavidin bead is attached to the other pole, and then the trap holding that pole is shut off too. The result is shown in the right panel. **(B) Growth within the dumbbell.** After assembling a chain of four bacteria (held together presumably by anti-FLAG antibodies) into dumbbell geometry, the two cells close to the IR laser traps do not grow, whereas the two cells suspended in between grow normally. **Experimental protocol:** LMC500 cells expressing (OmpA-177)-FLAG were grown in GB1 minimal medium at 28°C in the presence of antibiotics and 30 μ M IPTG (continuous induction). In the morning, cells were diluted in fresh medium and grown to OD₄₅₀~0.2. Then, cells were blocked with 0.1% BSA in GB1 medium and labeled with biotinylated anti-FLAG (M2) antibody (e.c. 50 μ g/ml). After washing with medium the cells were mixed with 1.26 μ m diameter streptavidin-coated PS beads (Spherotech, USA) and flown into a sample cell. The sample cell consisted of #1 cover slips (circular, diameter 22 and 15 mm) dipped in melted agarose (0.4%) and dried in a pincer. A flow cell was created by drawing two grease lines on the 22 mm cover slip placed in the sample holder and pressing the 15 mm cover slip on top. The sample was sealed with candle wax. This allows prolonged measurements at elevated temperatures. The water bath was set at 40°C, which results in a sample temperature of ~30°C.

optical density). However, in the trap, after labeling with anti-FLAG, cells grew as chains. Possibly, anti-FLAG binds to FLAG epitopes on both cells, preventing the cells from separating. Chains could be split into individual cells by employing high-powered laser traps (as cells are trapped less efficiently as beads, we estimated forces < 10 pN). Unfortunately, we never observed any growth in any of the dumbbell bacteria. We estimate that the trap stiffness of the polar bead handles was typically a few tens of pN/ μ m. Again, too much irradiation and/or smaller cells and/or more damage-susceptible cells (due to growth in minimal medium) could cause the growth stop. We observed that the bacterium is always attached somewhat underneath the bead, in this way catching more laser light than necessary (**Figure 8.2**). We attribute this to a different height of stable trapping of a bead and a bacterium. Improvements could be sticking the beads more on the ends of a bacterium (this would require traps created by both objectives), as well as using defined rich medium instead of minimal medium.

As mentioned above, a single tether could be made by chance to the region that will constrict. We managed to attach a DNA bead via a DNA tether to a dumbbell bacterium (data not shown). We found that rotation of the bacterium, as well as having to take into

account the positions of three beads (two polar handles and the DNA bead) makes the experiment difficult to analyze.

Without a specific mid-cell anchoring, other potential problems exist. If the OmpA β -barrel can freely diffuse in the OM, it will likely be pulled out of the “saddle point” formed by the constriction. Alternatively, if it is stuck to (existing) PG, such as full-length OmpA, then the invagination cannot be followed since this occurs through new synthesis of PG. Thus an OM protein that dynamically binds to the leading edge of the septum is required to keep the tether at the division site.

Additionally, an under-appreciated fact is that during division of a walled bacterium, the new poles are not shaped perfectly symmetric: often an angle between the long axes of the daughter cells is formed. This angle cannot be straightened out in the OT, and it is likely encoded in the PG cell wall. When attaching beads to such a bacterium, rotation becomes important and the actual invagination becomes more difficult to follow. For example, in an experiment where the “force probe” bead would be held at a constant position and a dividing bacterium must pull the bead out to constrict, the formation of an “septal” angle will (due to the freedom of rotation of the trapped beads) cause a shortening of the distance between bacterium and bead, and from the relaxation of the force in the construct it will appear as if the bacterium expands instead of constricts.

About the strength of the bead handles: as mentioned above, for a prolonged growing bacterium, IR exposure must be minimized. Thus, the polar handle beads must be very weak traps (e.g. 5 pN/ μ m). For a 1 μ m diameter bacterium, assuming spherical caps, full division will typically displace both bead handles ~500 nm each. Thus, during division, their positions require continuous (manual) updating. The weak traps containing the handles limit the allowed force in the DNA tether. This prevents us from exerting forces $> \sim 1$ pN, and only the speed of constriction will likely be measured. A recent approach based on live cell imaging and careful image analysis was able to measure speed of constriction in *E. coli* up to a few hundred nm inwards, so this approach, if it would succeed, would not bring much news (Reshes et al. 2008).

Increasing the strength of the protein-DNA connection

This research is driven by interest in the effect of force on bacterial (cell-wall) growth and division. Assuming that indeed the SA-1 peptide-streptavidin bond can be described with the Bell model for molecular bonds (Chapter 7, Equation 1), with parameters thermal off-

rate $k_{\text{off}} = 10^{-3} \text{ s}^{-1}$ and barrier width $x_b = 0.5 \text{ nm}$, $\sim 5 \text{ pN}$ force is estimated to reduce the bond lifetime to 9 min (17 min at zero force).

Although forces in the order of a few pN are the forces expected for a force-generating Z-ring in the absence of an abundant motor protein, it is possible that higher forces are needed. It will definitely make the experiment easier, as after tether formation, division might not start immediately, whereas tether breakage at $\sim 10 \text{ pN}$ might occur within a minute. Thus, careful timing and control of the force (i.e. exceeding 10 pN will rapidly decrease the bond lifetime) are required for the SA-1 based interaction.

Genetically inserting the 15-amino acid biotin acceptor peptide (Beckett et al. 1999) into OmpA (as was previously done for LamB (Oddershede et al. 2002)) might be good way to increase the strength of the molecular construct. Although the *in vivo* biotinylation, which occurs only in the cytoplasm by endogenous biotin ligase (Chapman-Smith and Cronan 1999), might be too low to have sufficient biotinylated OmpA in the OM to efficiently form a DNA tether during a single molecule experiment, adding biotin and biotin ligase to the external medium can enhance this. That this can work has been shown recently (Howarth et al. 2005; Howarth and Ting 2008).

Effect of forces on a growing bacterium

If we extend the scope of our research question beyond the Z-ring and more general focus on the effect of force on the growth of the bacterial cell wall, then we no longer require a fusion protein that is localized at mid-cell, and different options come in sight.

For instance, directly attaching beads to growing bacterial filaments allows exertion of forces in the range of a few tens of pN at multiple points along the filament. Possibly, such forces are already sufficient to influence the shape of the bacterium as it grows. In preliminary experiments, we have developed a protocol in which biotin beads are attached specifically to a streptavidin-coated bacterial filament. Large diameter biotin beads are used to keep the laser focus sufficiently far away from the bacterium and to prevent growth inhibition. The resulting bead-coated filaments are shown in **Figure 8.3**.

If high forces exceeding a few hundred pN are required to influence cell wall growth, then a technique used to visualize forces during cellular adhesion to its substrate might be used. This technique makes use of surfaces of micro-fabricated transparent PDMS pillars (Tan et al. 2003). After calibration of the pillars, the deflection of such a pillar is a measure of the force exerted on it. In (Tan et al. 2003), the pillars (diameter $3 \mu\text{m}$) had a spring

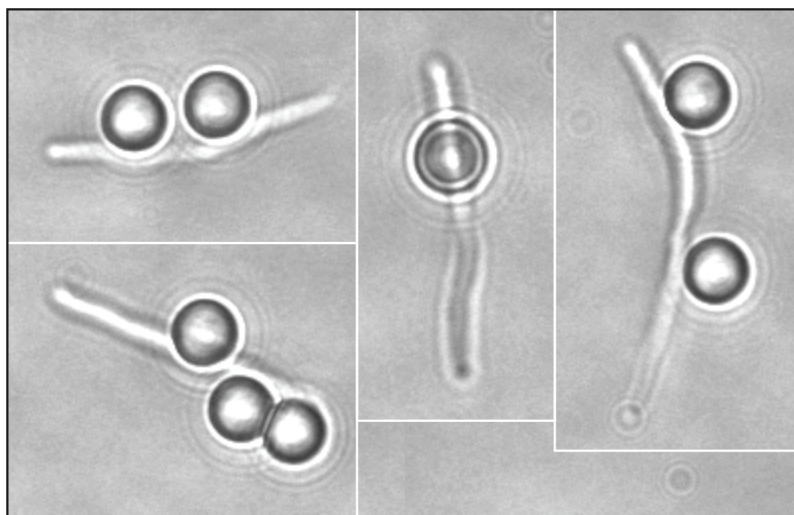


Figure 8.3. Attaching beads as handles to living filamented *E. coli*. Experimental protocol: LMC500 cells expressing OmpA-(SA-1) (on a pBAD plasmid) are grown overnight in Defined rich glycerol (DRy) medium with appropriate antibiotics. In the morning, cells are diluted 500x in fresh DRy. After ~1 hour, expression of OmpA-(SA-1) is induced through growth in the presence of 0.02% arabinose for 2 hours. Then filament formation is induced by addition of cephalixin (e.c. 10 $\mu\text{g}/\text{ml}$) and further growth for 2 hours. Subsequently, cells are labeled with streptavidin: Briefly, 1 ml of cells are concentrated to ~20 μl (~ 10^9 cells) and streptavidin is added (e.c. 50 $\mu\text{g}/\text{ml}$), incubated for 10 min at RT, washed 3 times and resuspended in ~20 μl . ~ 10^9 Biotin beads are also washed and resuspended in ~20 μl . 10 μl of cells is mixed with 10 μl of biotin beads (i.e. bead:cell ratio 1:1) and incubated for 10 min at RT. The mixture is diluted 100x and was imaged in brightfield in the optical tweezers setup.

constant of ~30 nN/ μm , making the technique suitable for forces > ~1 nN. In (Roos et al. 2005) it is shown that such pillars can be coated with poly-L-lysine (PLL) to adhere microtubules. Thus, adhering bacteria on the PLL pillar heads and subsequently inducing filamentation (by blocking division with an antibiotic such as cephalixin) allows measuring the forces that can be generated by a growing bacterium, or alternatively, the forces required to affect shape by growing e.g. a curved filament.

Concluding remarks

We conclude that continuing the search for a mid-cell localized fusion protein in the OM is the direction that holds the greatest promise for the goal of measuring forces in a constricting *E. coli* bacterium. The creation of such a fusion construct will complete the list

of requirements that have to be met before forces can be measured. Using biotin-streptavidin recognition at the bacterial surface, and multiple dig-anti-dig interactions on the bead, a sufficiently strong DNA tethering can be made (**Chapter 7** and this chapter). Using the time-shared optical trapping assembly procedure presented in this chapter, the assembly of a viable dividing bacterium in between two trapped DNA-beads is expected to become a reality. The resulting force measurements will provide a unique way to characterize possible force-generation in a living cell.

Bibliography

- Aarsman, M. E., A. Piette, et al. (2005). "Maturation of the Escherichia coli divisome occurs in two steps." Mol Microbiol **55**(6): 1631-45.
- Addinall, S. G. and J. Lutkenhaus (1996). "FtsZ-spirals and -arcs determine the shape of the invaginating septa in some mutants of Escherichia coli." Mol Microbiol **22**(2): 231-7.
- Akama, H., T. Matsuura, et al. (2004). "Crystal structure of the membrane fusion protein, MexA, of the multidrug transporter in Pseudomonas aeruginosa." J Biol Chem **279**(25): 25939-42.
- Alberts, B. (2002). Molecular Biology of the Cell, Garland Publishing, Incorporated.
- Alexeeva, S. A., G. S. Verhoeven, et al.
- Amann, E., B. Ochs, et al. (1988). "Tightly regulated tac promoter vectors useful for the expression of unfused and fused proteins in Escherichia coli." Gene **69**(2): 301-15.
- Andrews, S. S. and A. P. Arkin (2007). "A mechanical explanation for cytoskeletal rings and helices in bacteria." Biophys J **93**(6): 1872-84.
- Arjara, G. (2007). Refolding a beta-barrel membrane protein. Pasadena, California Institute of Technology.
- Arnoldi, M., M. Fritz, et al. (2000). "Bacterial turgor pressure can be measured by atomic force microscopy." Phys Rev E Stat Phys Plasmas Fluids Relat Interdiscip Topics **62**(1 Pt B): 1034-44.
- Ashkin, A. (1970). "Acceleration and Trapping of Particles by Radiation Pressure." Physical Review Letters **24**(4): 156-159.
- Ashkin, A., J. M. Dziedzic, et al. (1986). "Observation of a single-beam gradient force optical trap for dielectric particles." Optics Letters **11**(5): 288-290.
- Ashkin, A., J. M. Dziedzic, et al. (1987). "Optical trapping and manipulation of single cells using infrared laser beams." Nature **330**(6150): 769-771.
- Atakhorrami, M., K. M. Addas, et al. (2008). "Twin optical traps for two-particle cross-correlation measurements: eliminating cross-talk." Rev Sci Instrum **79**(4): 043103.

Bibliography

- Ayano, S., Y. Wakamoto, et al. (2006). "Quantitative measurement of damage caused by 1064-nm wavelength optical trapping of Escherichia coli cells using on-chip single cell cultivation system." *Biochem Biophys Res Commun* **350**(3): 678-84.
- Baker, K. A., R. E. Dutch, et al. (1999). "Structural basis for paramyxovirus-mediated membrane fusion." *Mol Cell* **3**(3): 309-19.
- Beckett, D., E. Kovaleva, et al. (1999). "A minimal peptide substrate in biotin holoenzyme synthetase-catalyzed biotinylation." *Protein Sci* **8**(4): 921-9.
- Bell, G. I. (1978). "Models for the specific adhesion of cells to cells." *Science* **200**(4342): 618-27.
- Benhar, I. (2001). "Biotechnological applications of phage and cell display." *Biotechnol Adv* **19**(1): 1-33.
- Bernhardt, T. G. and P. A. de Boer (2003). "The Escherichia coli amidase AmiC is a periplasmic septal ring component exported via the twin-arginine transport pathway." *Mol Microbiol* **48**(5): 1171-82.
- Bernhardt, T. G. and P. A. de Boer (2004). "Screening for synthetic lethal mutants in Escherichia coli and identification of EnvC (YibP) as a periplasmic septal ring factor with murein hydrolase activity." *Mol Microbiol* **52**(5): 1255-69.
- Bernstein, H. D. (2007). "Are bacterial 'autotransporters' really transporters?" *Trends Microbiol* **15**(10): 441-7.
- Bessette, P. H., J. J. Rice, et al. (2004). "Rapid isolation of high-affinity protein binding peptides using bacterial display." *Protein Eng Des Sel* **17**(10): 731-9.
- Bi, E. F. and J. Lutkenhaus (1991). "FtsZ ring structure associated with division in Escherichia coli." *Nature* **354**(6349): 161-4.
- Bonsor, D. A., I. Grishkovskaya, et al. (2007). "Molecular mimicry enables competitive recruitment by a natively disordered protein." *J Am Chem Soc* **129**(15): 4800-7.
- Bos, M. P., V. Robert, et al. (2007). "Biogenesis of the gram-negative bacterial outer membrane." *Annu Rev Microbiol* **61**: 191-214.
- Bos, M. P., B. Tefsen, et al. (2004). "Identification of an outer membrane protein required for the transport of lipopolysaccharide to the bacterial cell surface." *Proc Natl*

Bibliography

- Acad Sci U S A **101**(25): 9417-22.
- Boulbitch, A. (2000). "Deformation of the envelope of a spherical gram-negative bacterium during the atomic force microscopic measurements." J Electron Microsc (Tokyo) **49**(3): 459-62.
- Boulbitch, A., B. Quinn, et al. (2000). "Elasticity of the rod-shaped gram-negative eubacteria." Phys Rev Lett **85**(24): 5246-9.
- Bradburne, J. A., P. Godfrey, et al. (1993). "In vivo labeling of Escherichia coli cell envelope proteins with N- hydroxysuccinimide esters of biotin." Applied and Environmental Microbiology **59**(3): 663-668.
- Bramhill, D. (1997). "Bacterial cell division." Annu Rev Cell Dev Biol **13**: 395-424.
- Bramhill, D. and C. M. Thompson (1994). "GTP-dependent polymerization of Escherichia coli FtsZ protein to form tubules." Proc Natl Acad Sci U S A **91**(13): 5813-7.
- Brass, J. M., C. F. Higgins, et al. (1986). "Lateral diffusion of proteins in the periplasm of Escherichia coli." J Bacteriol **165**(3): 787-95.
- Buddelmeijer, N. and J. Beckwith (2004). "A complex of the Escherichia coli cell division proteins FtsL, FtsB and FtsQ forms independently of its localization to the septal region." Mol Microbiol **52**(5): 1315-27.
- Burdett, I. D. and R. G. Murray (1974). "Septum formation in Escherichia coli: characterization of septal structure and the effects of antibiotics on cell division." J Bacteriol **119**(1): 303-24.
- Bustamante, C., S. B. Smith, et al. (2000). "Single-molecule studies of DNA mechanics." Curr Opin Struct Biol **10**(3): 279-85.
- Cabeen, M. T. and C. Jacobs-Wagner (2005). "Bacterial cell shape." Nat Rev Microbiol **3**(8): 601-10.
- Cabeen, M. T. and C. Jacobs-Wagner (2007). "Skin and bones: the bacterial cytoskeleton, cell wall, and cell morphogenesis." J Cell Biol **179**(3): 381-7.
- Carson, M. J., J. Barondess, et al. (1991). "The FtsQ protein of Escherichia coli: membrane topology, abundance, and cell division phenotypes due to overproduction and insertion mutations." J Bacteriol **173**(7): 2187-95.

Bibliography

- Casadaban, M. J. and S. N. Cohen (1980). "Analysis of gene control signals by DNA fusion and cloning in *Escherichia coli*." *J Mol Biol* **138**(2): 179-207.
- Cascales, E., A. Bernadac, et al. (2002). "Pal lipoprotein of *Escherichia coli* plays a major role in outer membrane integrity." *J Bacteriol* **184**(3): 754-9.
- Cascales, E. and R. Lloubes (2004). "Deletion analyses of the peptidoglycan-associated lipoprotein Pal reveals three independent binding sequences including a TolA box." *Mol Microbiol* **51**(3): 873-85.
- Cayley, D. S., H. J. Guttman, et al. (2000). "Biophysical characterization of changes in amounts and activity of *Escherichia coli* cell and compartment water and turgor pressure in response to osmotic stress." *Biophys J* **78**(4): 1748-64.
- Cecconi, C., E. A. Shank, et al. (2008). "Protein-DNA chimeras for single molecule mechanical folding studies with the optical tweezers." *Eur Biophys J* **37**(6): 729-38.
- Chapman-Smith, A. and J. E. Cronan, Jr. (1999). "The enzymatic biotinylation of proteins: a post-translational modification of exceptional specificity." *Trends Biochem Sci* **24**(9): 359-63.
- Chaudhuri, B. N., J. Ko, et al. (1999). "Structure of D-allose binding protein from *Escherichia coli* bound to D-allose at 1.8 Å resolution." *J Mol Biol* **286**(5): 1519-31.
- Chen, J. C., P. H. Viollier, et al. (2005). "A membrane metalloprotease participates in the sequential degradation of a *Caulobacter* polarity determinant." *Mol Microbiol* **55**(4): 1085-103.
- Chen, R., W. Schmidmayr, et al. (1980). "Primary structure of major outer membrane protein II (ompA protein) of *Escherichia coli* K-12." *Proc Natl Acad Sci U S A* **77**(8): 4592-6.
- Clavel, T., P. Germon, et al. (1998). "TolB protein of *Escherichia coli* K-12 interacts with the outer membrane peptidoglycan-associated proteins Pal, Lpp and OmpA." *Mol Microbiol* **29**(1): 359-67.
- Cole, S. T., U. Chen-Schmeisser, et al. (1983). "Apparent bacteriophage-binding region of an *Escherichia coli* K-12 outer membrane protein." *J Bacteriol* **153**(2): 581-7.

Bibliography

- Collins, R. F., K. Beis, et al. (2007). "The 3D structure of a periplasm-spanning platform required for assembly of group 1 capsular polysaccharides in *Escherichia coli*." Proc Natl Acad Sci U S A **104**(7): 2390-5.
- Cormack, B. P., R. H. Valdivia, et al. (1996). "FACS-optimized mutants of the green fluorescent protein (GFP)." Gene **173**(1 Spec No): 33-8.
- Costa, T., R. Priyadarshini, et al. (2008). "Localization of PBP3 in *Caulobacter crescentus* is highly dynamic and largely relies on its functional transpeptidase domain." Mol Microbiol.
- Costanzo, A. and S. E. Ades (2006). "Growth phase-dependent regulation of the extracytoplasmic stress factor, sigmaE, by guanosine 3',5'-bispyrophosphate (ppGpp)." J Bacteriol **188**(13): 4627-34.
- Dai, J. and M. P. Sheetz (1995). "Mechanical properties of neuronal growth cone membranes studied by tether formation with laser optical tweezers." Biophys J **68**(3): 988-96.
- Daniel, R. A., E. J. Harry, et al. (2000). "Role of penicillin-binding protein PBP 2B in assembly and functioning of the division machinery of *Bacillus subtilis*." Mol Microbiol **35**(2): 299-311.
- Davison, M. T. and P. B. Garland (1983). "Immunochemical demonstration of zonal growth of the cell envelope of *Escherichia coli*." European Journal of Biochemistry **130**(3): 589-597.
- de Boer, P. A., R. E. Crossley, et al. (1989). "A division inhibitor and a topological specificity factor coded for by the minicell locus determine proper placement of the division septum in *E. coli*." Cell **56**(4): 641-9.
- de Jonge, B. L., F. B. Wientjes, et al. (1989). "Peptidoglycan synthesis during the cell cycle of *Escherichia coli*: composition and mode of insertion." J Bacteriol **171**(11): 5783-94.
- de Pedro, M. A., C. G. Grunfelder, et al. (2004). "Restricted Mobility of Cell Surface Proteins in the Polar Regions of *Escherichia coli*." J Bacteriol **186**(9): 2594-602.
- de Pedro, M. A., J. C. Quintela, et al. (1997). "Murein segregation in *Escherichia coli*." J

Bibliography

- Bacteriol **179**(9): 2823-34.
- Deich, J., E. M. Judd, et al. (2004). "Visualization of the movement of single histidine kinase molecules in live *Caulobacter* cells." Proc Natl Acad Sci U S A **101**(45): 15921-6.
- Demchick, P. and A. L. Koch (1996). "The permeability of the wall fabric of *Escherichia coli* and *Bacillus subtilis*." J Bacteriol **178**(3): 768-73.
- Den Blaauwen, T., M. E. Aarsman, et al. (2003). "Penicillin-binding protein PBP2 of *Escherichia coli* localizes preferentially in the lateral wall and at mid-cell in comparison with the old cell pole." Mol Microbiol **47**(2): 539-47.
- den Blaauwen, T., M. A. de Pedro, et al. (2008). "Morphogenesis of rod-shaped sacculi." FEMS Microbiol Rev **32**(2): 321-44.
- Denome, S. A., P. K. Elf, et al. (1999). "Escherichia coli mutants lacking all possible combinations of eight penicillin binding proteins: viability, characteristics, and implications for peptidoglycan synthesis." J Bacteriol **181**(13): 3981-93.
- Deroo, S., A. Fischer, et al. (2008). "Non-immunized natural human heavy chain CDR3 repertoires allow the isolation of high affinity peptides mimicking a human influenza hemagglutinin epitope." Molecular Immunology **45**(5): 1366-1373.
- Dijkstra, A. J. and W. Keck (1996). "Peptidoglycan as a barrier to transenvelope transport." J Bacteriol **178**(19): 5555-62.
- Dinh, T., I. T. Paulsen, et al. (1994). "A family of extracytoplasmic proteins that allow transport of large molecules across the outer membranes of gram-negative bacteria." J Bacteriol **176**(13): 3825-31.
- Dogterom, M. and B. Yurke (1997). "Measurement of the force-velocity relation for growing microtubules." Science **278**(5339): 856-60.
- Drew, D., M. Lerch, et al. (2006). "Optimization of membrane protein overexpression and purification using GFP fusions." Nat Methods **3**(4): 303-13.
- Eggert, U. S., T. J. Mitchison, et al. (2006). "Animal cytokinesis: from parts list to mechanisms." Annu Rev Biochem **75**: 543-66.
- Eisner, G., H. G. Koch, et al. (2003). "Ligand crowding at a nascent signal sequence." J Cell Biol **163**(1): 35-44.

Bibliography

- Elkins, C. A. and H. Nikaido (2003). "Chimeric analysis of AcrA function reveals the importance of its C-terminal domain in its interaction with the AcrB multidrug efflux pump." *J Bacteriol* **185**(18): 5349-56.
- Erickson, H. P. (1995). "FtsZ, a prokaryotic homolog of tubulin?" *Cell* **80**(3): 367-70.
- Erickson, H. P. (1997). "FtsZ, a tubulin homologue in prokaryote cell division." *Trends Cell Biol* **7**(9): 362-7.
- Ericsson, M., D. Hanstorp, et al. (2000). "Sorting out bacterial viability with optical tweezers." *J Bacteriol* **182**(19): 5551-5.
- Errington, J., R. A. Daniel, et al. (2003). "Cytokinesis in bacteria." *Microbiol Mol Biol Rev* **67**(1): 52-65, table of contents.
- Evans, E. and K. Ritchie (1997). "Dynamic strength of molecular adhesion bonds." *Biophys J* **72**(4): 1541-55.
- Fallman, E., S. Schedin, et al. (2004). "Optical tweezers based force measurement system for quantitating binding interactions: system design and application for the study of bacterial adhesion." *Biosens Bioelectron* **19**(11): 1429-37.
- Fishov, I., A. Zaritsky, et al. (1995). "On microbial states of growth." *Mol Microbiol* **15**(5): 789-94.
- Freudl, R. (1989). "Insertion of peptides into cell-surface-exposed areas of the Escherichia coli OmpA protein does not interfere with export and membrane assembly." *Gene* **82**(2): 229-36.
- Freudl, R., S. MacIntyre, et al. (1986). "Cell surface exposure of the outer membrane protein OmpA of Escherichia coli K-12." *J Mol Biol* **188**(3): 491-4.
- Fukushima, T., A. Afkham, et al. (2006). "A new D,L-endopeptidase gene product, YojL (renamed CwlS), plays a role in cell separation with LytE and LytF in Bacillus subtilis." *J Bacteriol* **188**(15): 5541-50.
- Gabay, J. and K. Yasunaka (1980). "Interaction of the lamB protein with the peptidoglycan layer in Escherichia coli K12." *Eur J Biochem* **104**(1): 13-8.
- Gelles, J., B. J. Schnapp, et al. (1988). "Tracking kinesin-driven movements with nanometre-scale precision." *Nature* **331**(6155): 450-3.

Bibliography

- Gentle, I. E., L. Burri, et al. (2005). "Molecular architecture and function of the Omp85 family of proteins." Mol Microbiol **58**(5): 1216-25.
- Gerding, M. A., Y. Ogata, et al. (2007). "The trans-envelope Tol-Pal complex is part of the cell division machinery and required for proper outer-membrane invagination during cell constriction in *E. coli*." Mol Microbiol **63**(4): 1008-25.
- Ghosh, A. S. and K. D. Young (2005). "Helical disposition of proteins and lipopolysaccharide in the outer membrane of *Escherichia coli*." J Bacteriol **187**(6): 1913-22.
- Ghosh, B. and A. Sain (2008). "Origin of contractile force during cell division of bacteria." Phys Rev Lett.
- Gibbs, K. A., D. D. Isaac, et al. (2004). "Complex spatial distribution and dynamics of an abundant *Escherichia coli* outer membrane protein, LamB." Mol Microbiol **53**(6): 1771-83.
- Giebel, L. B., R. T. Cass, et al. (1995). "Screening of cyclic peptide phage libraries identifies ligands that bind streptavidin with high affinities." Biochemistry **34**(47): 15430-5.
- Gittes, F. and C. F. Schmidt (1998). "Signals and noise in micromechanical measurements." Methods Cell Biol **55**: 129-56.
- Goehring, N. W. and J. Beckwith (2005). "Diverse paths to midcell: assembly of the bacterial cell division machinery." Curr Biol **15**(13): R514-26.
- Goldstein, R. E. and A. Goriely (2006). "Dynamic buckling of morphoelastic filaments." Phys Rev E Stat Nonlin Soft Matter Phys **74**(1 Pt 1): 010901.
- Grange, W., S. Husale, et al. (2002). "Optical tweezers system measuring the change in light momentum flux." Review of Scientific Instruments **73**(6): 2308.
- Grishchuk, E. L., M. I. Molodtsov, et al. (2005). "Force production by disassembling microtubules." Nature **438**(7066): 384-8.
- Guex, N. and M. C. Peitsch (1997). "SWISS-MODEL and the Swiss-PdbViewer: an environment for comparative protein modeling." Electrophoresis **18**(15): 2714-23.
- Gumpert, J., E. Schuhmann, et al. (1971). "[Ultrastructure of stable L forms of *Escherichia coli* B and W 1655F]." Z Allg Mikrobiol **11**(1): 19-33.

Bibliography

- Hahn, J., B. Maier, et al. (2005). "Transformation proteins and DNA uptake localize to the cell poles in *Bacillus subtilis*." Cell **122**(1): 59-71.
- Harvey, B. R., G. Georgiou, et al. (2004). "Anchored periplasmic expression, a versatile technology for the isolation of high-affinity antibodies from *Escherichia coli*-expressed libraries." Proc Natl Acad Sci U S A **101**(25): 9193-8.
- Hasselblatt, H., R. Kurzbauer, et al. (2007). "Regulation of the sigmaE stress response by DegS: how the PDZ domain keeps the protease inactive in the resting state and allows integration of different OMP-derived stress signals upon folding stress." Genes Dev **21**(20): 2659-70.
- Heidrich, C., M. F. Templin, et al. (2001). "Involvement of N-acetylmuramyl-L-alanine amidases in cell separation and antibiotic-induced autolysis of *Escherichia coli*." Mol Microbiol **41**(1): 167-78.
- Heidrich, C., A. Ursinus, et al. (2002). "Effects of multiple deletions of murein hydrolases on viability, septum cleavage, and sensitivity to large toxic molecules in *Escherichia coli*." J Bacteriol **184**(22): 6093-9.
- Henning, U., S. T. Cole, et al. (1983). "Gene fusions using the ompA gene coding for a major outer-membrane protein of *Escherichia coli* K12." Eur J Biochem **136**(2): 233-40.
- Henning, U., B. Hohn, et al. (1973). "Cell envelope and shape of *Escherichia coli* K12. The ghost membrane." Eur J Biochem **39**(1): 27-36.
- Higgins, M. K., E. Bokma, et al. (2004). "Structure of the periplasmic component of a bacterial drug efflux pump." Proc Natl Acad Sci U S A **101**(27): 9994-9.
- Hirota, Y., A. Ryter, et al. (1968). "Thermosensitive mutants of *E. coli* affected in the processes of DNA synthesis and cellular division." Cold Spring Harb Symp Quant Biol **33**: 677-93.
- Hobot, J. A., E. Carlemalm, et al. (1984). "Periplasmic gel: new concept resulting from the reinvestigation of bacterial cell envelope ultrastructure by new methods." J Bacteriol **160**(1): 143-52.
- Holtje, J. V. and C. Heidrich (2001). "Enzymology of elongation and constriction of the

Bibliography

- murein sacculus of Escherichia coli." *Biochimie* **83**(1): 103-8.
- Horger, I., E. Velasco, et al. (2008). "Langevin computer simulations of bacterial protein filaments and the force-generating mechanism during cell division." *Phys Rev E Stat Nonlin Soft Matter Phys* **77**(1 Pt 1): 011902.
- Howard-Flanders, P., E. Simson, et al. (1964). "A Locus That Controls Filament Formation and Sensitivity to Radiation in Escherichia Coli K-12." *Genetics* **49**: 237-46.
- Howarth, M., K. Takao, et al. (2005). "Targeting quantum dots to surface proteins in living cells with biotin ligase." *Proc Natl Acad Sci U S A* **102**(21): 7583-8.
- Howarth, M. and A. Y. Ting (2008). "Imaging proteins in live mammalian cells with biotin ligase and monovalent streptavidin." *Nat Protoc* **3**(3): 534-45.
- Jain, S. and M. B. Goldberg (2007). "Requirement for YaeT in the outer membrane assembly of autotransporter proteins." *J Bacteriol* **189**(14): 5393-8.
- Jain, S., P. van Ulsen, et al. (2006). "Polar localization of the autotransporter family of large bacterial virulence proteins." *J Bacteriol* **188**(13): 4841-50.
- Janson, M. E. and M. Dogterom (2004). "Scaling of microtubule force-velocity curves obtained at different tubulin concentrations." *Phys Rev Lett* **92**(24): 248101.
- Jass, J., S. Schedin, et al. (2004). "Physical properties of Escherichia coli P pili measured by optical tweezers." *Biophys J* **87**(6): 4271-83.
- Jauffred, L., T. H. Callisen, et al. (2007). "Visco-elastic membrane tethers extracted from Escherichia coli by optical tweezers." *Biophys J* **93**(11): 4068-75.
- Johnson, J. M. and G. M. Church (1999). "Alignment and structure prediction of divergent protein families: periplasmic and outer membrane proteins of bacterial efflux pumps." *J Mol Biol* **287**(3): 695-715.
- Jones, L. J., R. Carballido-Lopez, et al. (2001). "Control of cell shape in bacteria: helical, actin-like filaments in Bacillus subtilis." *Cell* **104**(6): 913-22.
- Joseleau-Petit, D., J. C. Liebart, et al. (2007). "Unstable Escherichia coli L forms revisited: growth requires peptidoglycan synthesis." *J Bacteriol* **189**(18): 6512-20.
- Judd, E. M., L. R. Comolli, et al. (2005). "Distinct constrictive processes, separated in time and space, divide caulobacter inner and outer membranes." *J Bacteriol* **187**(20):

Bibliography

6874-82.

- Kerssemakers, J. W., E. L. Munteanu, et al. (2006). "Assembly dynamics of microtubules at molecular resolution." *Nature* **442**(7103): 709-12.
- Kerssemakers, J. W. J., M. E. Janson, et al. (2003). "Optical trap setup for measuring microtubule pushing forces." *Applied Physics Letters* **83**(21): 4441-4443.
- Kim, C., S. Song, et al. (1997). "The D-allose operon of Escherichia coli K-12." *J Bacteriol* **179**(24): 7631-7.
- Kim, S. Y., Z. Gitai, et al. (2006). "Single molecules of the bacterial actin MreB undergo directed treadmilling motion in Caulobacter crescentus." *Proc Natl Acad Sci U S A* **103**(29): 10929-34.
- Kleinschmidt, J. H. (2006). "Folding kinetics of the outer membrane proteins OmpA and FomA into phospholipid bilayers." *Chem Phys Lipids* **141**(1-2): 30-47.
- Koch, A. L. (1988). "Biophysics of bacterial walls viewed as stress-bearing fabric." *Microbiol Rev* **52**(3): 337-53.
- Koch, A. L. (1998). "The biophysics of the gram-negative periplasmic space." *Crit Rev Microbiol* **24**(1): 23-59.
- Koch, A. L. and M. F. Pinette (1987). "Nephelometric determination of turgor pressure in growing gram-negative bacteria." *J Bacteriol* **169**(8): 3654-63.
- Koch, A. L. and S. Woeste (1992). "Elasticity of the sacculus of Escherichia coli." *J Bacteriol* **174**(14): 4811-9.
- Koebnik, R. (1999). "Structural and functional roles of the surface-exposed loops of the beta-barrel membrane protein OmpA from Escherichia coli." *J Bacteriol* **181**(12): 3688-94.
- Koebnik, R., K. P. Locher, et al. (2000). "Structure and function of bacterial outer membrane proteins: barrels in a nutshell." *Mol Microbiol* **37**(2): 239-53.
- Koppelman, C. M., M. E. Aarsman, et al. (2004). "R174 of Escherichia coli FtsZ is involved in membrane interaction and protofilament bundling, and is essential for cell division." *Mol Microbiol* **51**(3): 645-57.
- Koster, G., A. Cacciuto, et al. (2005). "Force barriers for membrane tube formation." *Phys*

Bibliography

- Rev Lett **94**(6): 068101.
- Koster, G., M. VanDuijn, et al. (2003). "Membrane tube formation from giant vesicles by dynamic association of motor proteins." Proc Natl Acad Sci U S A **100**(26): 15583-8.
- Laan, L., J. Husson, et al. (2008). "Force-generation and dynamic instability of microtubule bundles." Proc Natl Acad Sci U S A **105**(26): 8920-5.
- Lan, G., A. Dajkovic, et al. (2008). "Polymerization and bundling kinetics of FtsZ filaments." Biophys J **95**(8): 4045-56.
- Lan, G., C. W. Wolgemuth, et al. (2007). "Z-ring force and cell shape during division in rod-like bacteria." Proc Natl Acad Sci U S A **104**(41): 16110-5.
- Leake, M. C., J. H. Chandler, et al. (2006). "Stoichiometry and turnover in single, functioning membrane protein complexes." Nature **443**(7109): 355-8.
- Lee, S. Y., J. H. Choi, et al. (2003). "Microbial cell-surface display." Trends Biotechnol **21**(1): 45-52.
- Li, Z., M. J. Trimble, et al. (2007). "The structure of FtsZ filaments in vivo suggests a force-generating role in cell division." Embo J **26**(22): 4694-708.
- Lu, C., M. Reedy, et al. (2000). "Straight and curved conformations of FtsZ are regulated by GTP hydrolysis." J Bacteriol **182**(1): 164-70.
- Lutz, R. and H. Bujard (1997). "Independent and tight regulation of transcriptional units in Escherichia coli via the LacR/O, the TetR/O and AraC/I1-I2 regulatory elements." Nucleic Acids Res **25**(6): 1203-10.
- Ma, X., D. W. Ehrhardt, et al. (1996). "Colocalization of cell division proteins FtsZ and FtsA to cytoskeletal structures in living Escherichia coli cells by using green fluorescent protein." Proc Natl Acad Sci U S A **93**(23): 12998-3003.
- Magnusson, U., B. N. Chaudhuri, et al. (2002). "Hinge-bending motion of D-allose-binding protein from Escherichia coli: three open conformations." J Biol Chem **277**(16): 14077-84.
- Maier, B., I. Chen, et al. (2004). "DNA transport into Bacillus subtilis requires proton motive force to generate large molecular forces." Nat Struct Mol Biol **11**(7): 643-9.

Bibliography

- Malamy, M. H. and B. L. Horecker (1964). "Release of Alkaline Phosphatase from Cells of Escherichia Coli Upon Lysozyme Spheroplast Formation." Biochemistry **3**: 1889-93.
- Manting, E. H., C. van der Does, et al. (1997). "In vivo cross-linking of the SecA and SecY subunits of the Escherichia coli preprotein translocase." J Bacteriol **179**(18): 5699-704.
- Matias, V. R., A. Al-Amoudi, et al. (2003). "Cryo-transmission electron microscopy of frozen-hydrated sections of Escherichia coli and Pseudomonas aeruginosa." J Bacteriol **185**(20): 6112-8.
- Mendelson, N. H., J. E. Sarlls, et al. (2000). "Chiral self-propulsion of growing bacterial macrofibers on a solid surface." Phys Rev Lett **84**(7): 1627-30.
- Mendelson, N. H. and J. J. Thwaites (1989). "Cell wall mechanical properties as measured with bacterial thread made from Bacillus subtilis." J Bacteriol **171**(2): 1055-62.
- Mikolosko, J., K. Bobyk, et al. (2006). "Conformational flexibility in the multidrug efflux system protein AcrA." Structure **14**(3): 577-87.
- Mills, J. P., L. Qie, et al. (2004). "Nonlinear elastic and viscoelastic deformation of the human red blood cell with optical tweezers." Mech Chem Biosyst **1**(3): 169-80.
- Mingorance, J., M. Tadros, et al. (2005). "Visualization of single Escherichia coli FtsZ filament dynamics with atomic force microscopy." J Biol Chem **280**(21): 20909-14.
- Mitra, K., J. Frank, et al. (2006). "Co- and post-translational translocation through the protein-conducting channel: analogous mechanisms at work?" Nat Struct Mol Biol **13**(11): 957-64.
- Moffitt, J. R., Y. R. Chemla, et al. (2008). "Recent advances in optical tweezers." Annu Rev Biochem **77**: 205-28.
- Monod, J., G. Cohen-Bazire, et al. (1951). "Sur la biosynthese de la beta-galactosidase (lactase) chez Escherichia coli; la specificite de l'induction." Biochim Biophys Acta **7**(4): 585-99.
- Mukherjee, A. and J. Lutkenhaus (1994). "Guanine nucleotide-dependent assembly of FtsZ into filaments." J Bacteriol **176**(9): 2754-8.

Bibliography

- Mukherjee, A., C. Saez, et al. (2001). "Assembly of an FtsZ mutant deficient in GTPase activity has implications for FtsZ assembly and the role of the Z ring in cell division." J Bacteriol **183**(24): 7190-7.
- Mullineaux, C. W., A. Nenninger, et al. (2006). "Diffusion of green fluorescent protein in three cell environments in Escherichia coli." J Bacteriol **188**(10): 3442-8.
- Murase, K., T. Fujiwara, et al. (2004). "Ultrafine membrane compartments for molecular diffusion as revealed by single molecule techniques." Biophys J **86**(6): 4075-93.
- Neidhardt, F. C., P. L. Bloch, et al. (1974). "Culture medium for enterobacteria." J Bacteriol **119**(3): 736-47.
- Neu, H. C. and L. A. Heppel (1964). "The Release of Ribonuclease into the Medium When Escherichia Coli Cells Are Converted to Spheroplasts." J Biol Chem **239**: 3893-900.
- Neuert, G., C. Albrecht, et al. (2006). "Dynamic force spectroscopy of the digoxigenin-antibody complex." FEBS Lett **580**(2): 505-9.
- Neuman, K. C., E. H. Chadd, et al. (1999). "Characterization of photodamage to escherichia coli in optical traps." Biophys J **77**(5): 2856-63.
- Nice, E., B. Catimel, et al. (1997). "Strategies for the identification and purification of ligands for orphan biomolecules." International Journal of Peptide Research and Therapeutics **4**(2): 107-120.
- Nikaido, H. (2003). "Molecular basis of bacterial outer membrane permeability revisited." Microbiol Mol Biol Rev **67**(4): 593-656.
- Nouwen, N., G. Berrelkamp, et al. (2007). "Bacterial sec-translocase unfolds and translocates a class of folded protein domains." J Mol Biol **372**(2): 422-33.
- Oddershede, L., J. K. Dreyer, et al. (2002). "The motion of a single molecule, the lambda-receptor, in the bacterial outer membrane." Biophys J **83**(6): 3152-61.
- Odijk, T. (1995). "Stiff chains and filaments under tension." Macromolecules **28**(20): 7016-7018.
- Oesterhelt, F., D. Oesterhelt, et al. (2000). "Unfolding pathways of individual bacteriorhodopsins." Science **288**(5463): 143-6.
- Ohara, M., H. C. Wu, et al. (1999). "Identification and characterization of a new

Bibliography

- lipoprotein, NlpI, in Escherichia coli K-12." *J Bacteriol* **181**(14): 4318-25.
- Osawa, M., D. E. Anderson, et al. (2008). "Reconstitution of contractile FtsZ rings in liposomes." *Science* **320**(5877): 792-4.
- Park, J. T. (1993). "Turnover and recycling of the murein sacculus in oligopeptide permease-negative strains of Escherichia coli: indirect evidence for an alternative permease system and for a monolayered sacculus." *J Bacteriol* **175**(1): 7-11.
- Park, J. T. (1995). "Why does Escherichia coli recycle its cell wall peptides?" *Mol Microbiol* **17**(3): 421-6.
- Parsons, L. M., F. Lin, et al. (2006). "Peptidoglycan recognition by Pal, an outer membrane lipoprotein." *Biochemistry* **45**(7): 2122-8.
- Pautsch, A. and G. E. Schulz (1998). "Structure of the outer membrane protein A transmembrane domain." *Nat Struct Biol* **5**(11): 1013-7.
- Peters, J. E., T. E. Thate, et al. (2003). "Definition of the Escherichia coli MC4100 genome by use of a DNA array." *J Bacteriol* **185**(6): 2017-21.
- Piran, U. and W. J. Riordan (1990). "Dissociation rate constant of the biotin-streptavidin complex." *J Immunol Methods* **133**(1): 141-3.
- Priyadarshini, R., M. A. de Pedro, et al. (2007). "Role of peptidoglycan amidases in the development and morphology of the division septum in Escherichia coli." *J Bacteriol* **189**(14): 5334-47.
- Rasmussen, M. B., L. B. Oddershede, et al. (2008). "Optical tweezers cause physiological damage to Escherichia coli and Listeria bacteria." *Appl Environ Microbiol* **74**(8): 2441-6.
- RayChaudhuri, D. and J. T. Park (1992). "Escherichia coli cell-division gene ftsZ encodes a novel GTP-binding protein." *Nature* **359**(6392): 251-4.
- Reithmeier, R. A. and P. D. Bragg (1974). "Purification and characterization of heat-modifiable protein from the outer membrane of Escherichia coli." *FEBS Lett* **41**(2): 195-8.
- Reshes, G., S. Vanounou, et al. (2008). "Cell shape dynamics in Escherichia coli." *Biophys J* **94**(1): 251-64.

Bibliography

- Rhodium, V. A., W. C. Suh, et al. (2006). "Conserved and variable functions of the sigmaE stress response in related genomes." *PLoS Biol* **4**(1): e2.
- Ricard, M. and Y. Hirota (1973). "Process of cellular division in Escherichia coli: physiological study on thermosensitive mutants defective in cell division." *J Bacteriol* **116**(1): 314-22.
- Rice, J. J., A. Schohn, et al. (2006). "Bacterial display using circularly permuted outer membrane protein OmpX yields high affinity peptide ligands." *Protein Sci* **15**(4): 825-36.
- Ried, G., R. Koebnik, et al. (1994). "Membrane topology and assembly of the outer membrane protein OmpA of Escherichia coli K12." *Mol Gen Genet* **243**(2): 127-35.
- Robbins, J. R., D. Monack, et al. (2001). "The making of a gradient: IcsA (VirG) polarity in Shigella flexneri." *Mol Microbiol* **41**(4): 861-72.
- Rohrbach, A. (2005). "Stiffness of optical traps: quantitative agreement between experiment and electromagnetic theory." *Phys Rev Lett* **95**(16): 168102.
- Romberg, L., M. Simon, et al. (2001). "Polymerization of FtsZ, a bacterial homolog of tubulin. is assembly cooperative?" *J Biol Chem* **276**(15): 11743-53.
- Roos, W. (2000). Optical trapping of core-shell particles and dividing Escherichia coli. Amsterdam, University of Amsterdam.
- Roos, W., J. Ulmer, et al. (2005). "Microtubule gliding and cross-linked microtubule networks on micropillar interfaces." *Nano Lett* **5**(12): 2630-4.
- Ruiz, N. (2008). "Bioinformatics identification of MurJ (MviN) as the peptidoglycan lipid II flippase in Escherichia coli." *Proc Natl Acad Sci U S A* **105**(40): 15553-7.
- Ruiz, N., D. Kahne, et al. (2006). "Advances in understanding bacterial outer-membrane biogenesis." *Nat Rev Microbiol* **4**(1): 57-66.
- Sabarth, N., S. Lamer, et al. (2002). "Identification of surface proteins of Helicobacter pylori by selective biotinylation, affinity purification, and two-dimensional gel electrophoresis." *Journal of Biological Chemistry* **277**(31): 27896-27902.
- Sambrook, J. and D. W. Russel (2001). *Molecular cloning: a laboratory manual*. Cold Spring Harbor, New York, Cold Spring Harbor Laboratory Press.

Bibliography

- Sandlin, R. C., K. A. Lampel, et al. (1995). "Avirulence of rough mutants of *Shigella flexneri*: requirement of O antigen for correct unipolar localization of IcsA in the bacterial outer membrane." *Infect Immun* **63**(1): 229-37.
- Scheffers, D. J., L. J. Jones, et al. (2004). "Several distinct localization patterns for penicillin-binding proteins in *Bacillus subtilis*." *Mol Microbiol* **51**(3): 749-64.
- Scheffers, D. J. and M. G. Pinho (2005). "Bacterial cell wall synthesis: new insights from localization studies." *Microbiol Mol Biol Rev* **69**(4): 585-607.
- Schierle, C. F., M. Berkmen, et al. (2003). "The DsbA signal sequence directs efficient, cotranslational export of passenger proteins to the *Escherichia coli* periplasm via the signal recognition particle pathway." *J Bacteriol* **185**(19): 5706-13.
- Schirmer, T., T. A. Keller, et al. (1995). "Structural basis for sugar translocation through maltoporin channels at 3.1 Å resolution." *Science* **267**(5197): 512-4.
- Schroeder, T. E. (1970). "The contractile ring. I. Fine structure of dividing mammalian (HeLa) cells and the effects of cytochalasin B." *Z Zellforsch Mikrosk Anat* **109**(4): 431-49.
- Schroeder, T. E. (1972). "The contractile ring. II. Determining its brief existence, volumetric changes, and vital role in cleaving *Arbacia* eggs." *J Cell Biol* **53**(2): 419-34.
- Schuhmann, E. and U. Taubeneck (1969). "[Stabil L-forms of several *Escherichia coli* strains]." *Z Allg Mikrobiol* **9**(4): 297-313.
- Schwarz, U. and W. Leutgeb (1971). "Morphogenetic aspects of murein structure and biosynthesis." *J Bacteriol* **106**(2): 588-95.
- Seol, Y., A. E. Carpenter, et al. (2006). "Gold nanoparticles: enhanced optical trapping and sensitivity coupled with significant heating." *Opt Lett* **31**(16): 2429-31.
- Shaner, N. C., R. E. Campbell, et al. (2004). "Improved monomeric red, orange and yellow fluorescent proteins derived from *Discosoma* sp. red fluorescent protein." *Nat Biotechnol* **22**(12): 1567-72.
- Siddiqui, R. A., C. Hoischen, et al. (2006). "The analysis of cell division and cell wall synthesis genes reveals mutationally inactivated *ftsQ* and *mraY* in a protoplast-type L-form of *Escherichia coli*." *FEMS Microbiol Lett* **258**(2): 305-11.

Bibliography

- Smith, A. E., Z. Zhang, et al. (2000). "The mechanical properties of *Saccharomyces cerevisiae*." Proc Natl Acad Sci U S A **97**(18): 9871-4.
- Smith, S. B., Y. Cui, et al. (1996). "Overstretching B-DNA: the elastic response of individual double-stranded and single-stranded DNA molecules." Science **271**(5250): 795-9.
- Smith, S. B., Y. Cui, et al. (2003). "Optical-trap force transducer that operates by direct measurement of light momentum." Methods Enzymol **361**: 134-62.
- Smith, S. B., L. Finzi, et al. (1992). "Direct mechanical measurements of the elasticity of single DNA molecules by using magnetic beads." Science **258**(5085): 1122-6.
- Smith, S. G., V. Mahon, et al. (2007). "A molecular Swiss army knife: OmpA structure, function and expression." FEMS Microbiol Lett **273**(1): 1-11.
- Srinivasan, R., M. Mishra, et al. (2008). "The bacterial cell division protein FtsZ assembles into cytoplasmic rings in fission yeast." Genes Dev **22**(13): 1741-6.
- Stricker, J., P. Maddox, et al. (2002). "Rapid assembly dynamics of the *Escherichia coli* FtsZ-ring demonstrated by fluorescence recovery after photobleaching." Proc Natl Acad Sci U S A **99**(5): 3171-5.
- Svoboda, K. and S. M. Block (1994). "Biological applications of optical forces." Annu Rev Biophys Biomol Struct **23**: 247-85.
- Takeuchi, S., W. R. DiLuzio, et al. (2005). "Controlling the shape of filamentous cells of *Escherichia coli*." Nano Lett **5**(9): 1819-23.
- Tan, J. L., J. Tien, et al. (2003). "Cells lying on a bed of microneedles: an approach to isolate mechanical force." Proc Natl Acad Sci U S A **100**(4): 1484-9.
- Taschner, P. E., P. G. Huls, et al. (1988). "Division behavior and shape changes in isogenic ftsZ, ftsQ, ftsA, pbpB, and ftsE cell division mutants of *Escherichia coli* during temperature shift experiments." J Bacteriol **170**(4): 1533-40.
- Thanedar, S. and W. Margolin (2004). "FtsZ exhibits rapid movement and oscillation waves in helix-like patterns in *Escherichia coli*." Curr Biol **14**(13): 1167-73.
- Thie, H., T. Schirrmann, et al. (2008). "SRP and Sec pathway leader peptides for antibody phage display and antibody fragment production in *E. coli*." N Biotechnol **25**(1): 49-54.

Bibliography

- Thwaites, J. J. and N. H. Mendelson (1985). "Biomechanics of bacterial walls: studies of bacterial thread made from *Bacillus subtilis*." Proc Natl Acad Sci U S A **82**(7): 2163-7.
- Thwaites, J. J. and N. H. Mendelson (1989). "Mechanical properties of peptidoglycan as determined from bacterial thread." Int J Biol Macromol **11**(4): 201-6.
- Tikhonova, E. B. and H. I. Zgurskaya (2004). "AcrA, AcrB, and TolC of *Escherichia coli* Form a Stable Intermembrane Multidrug Efflux Complex." J Biol Chem **279**(31): 32116-24.
- Tommassen, J. and B. Lugtenberg (1984). "Amino terminus of outer membrane PhoE protein: localization by use of a bla-phoE hybrid gene." J Bacteriol **157**(1): 327-9.
- Touze, T., J. Eswaran, et al. (2004). "Interactions underlying assembly of the *Escherichia coli* AcrAB-TolC multidrug efflux system." Mol Microbiol **53**(2): 697-706.
- Uehara, T. and J. T. Park (2008). "Growth of *Escherichia coli*: significance of peptidoglycan degradation during elongation and septation." J Bacteriol **190**(11): 3914-22.
- van den Ent, F., T. M. Vinkenvleugel, et al. (2008). "Structural and mutational analysis of the cell division protein FtsQ." Mol Microbiol **68**(1): 110-23.
- van der Horst, A. (2006). High-refractive index particles in counter-propagating optical tweezers -manipulation and forces -, Utrecht University.
- van der Horst, A., P. D. J. van Oostrum, et al. (2008). "High trapping forces for high-refractive index particles trapped in dynamic arrays of counterpropagating optical tweezers." Applied Optics **47**(17): 3196-3202.
- Vandeputte-Rutten, L., M. P. Bos, et al. (2003). "Crystal structure of Neisserial surface protein A (NspA), a conserved outer membrane protein with vaccine potential." J Biol Chem **278**(27): 24825-30.
- Vazquez-Laslop, N., H. Lee, et al. (2001). "Molecular sieve mechanism of selective release of cytoplasmic proteins by osmotically shocked *Escherichia coli*." J Bacteriol **183**(8): 2399-404.
- Verhoeven, G. S., S. A. Alexeeva, et al. (2008). "Differential surface display of peptides by the transmembrane domain of OmpA." submitted.

Bibliography

- Vicente, M., A. I. Rico, et al. (2006). "Septum enlightenment: assembly of bacterial division proteins." J Bacteriol **188**(1): 19-27.
- Vinkenvleugel, T. M. (2006). Timing of FtsQ midcell localisation and its interaction with other cell division proteins, University of Amsterdam.
- Visscher, K., S. P. Gross, et al. (1996). "Construction of multiple-beam optical traps with nanometer-resolution position sensing." IEEE Journal on Selected Topics in Quantum Electronics **2**(4): 1066-1076.
- Visscher, K., M. J. Schnitzer, et al. (1999). "Single kinesin molecules studied with a molecular force clamp." Nature **400**(6740): 184-9.
- Vjestica, A., X. Z. Tang, et al. (2008). "The actomyosin ring recruits early secretory compartments to the division site in fission yeast." Mol Biol Cell **19**(3): 1125-38.
- Vollmer, W., D. Blanot, et al. (2008). "Peptidoglycan structure and architecture." FEMS Microbiol Rev **32**(2): 149-67.
- Wachi, M. and M. Matsushashi (1989). "Negative control of cell division by mreB, a gene that functions in determining the rod shape of Escherichia coli cells." J Bacteriol **171**(6): 3123-7.
- Wang, M. D., H. Yin, et al. (1997). "Stretching DNA with optical tweezers." Biophys J **72**(3): 1335-46.
- Wang, X. and J. Lutkenhaus (1996). "Characterization of the ftsZ gene from Mycoplasma pulmonis, an organism lacking a cell wall." J Bacteriol **178**(8): 2314-9.
- Weiss, D. S. (2004). "Bacterial cell division and the septal ring." Mol Microbiol **54**(3): 588-97.
- Weiss, D. S., J. C. Chen, et al. (1999). "Localization of FtsI (PBP3) to the septal ring requires its membrane anchor, the Z ring, FtsA, FtsQ, and FtsL." J Bacteriol **181**(2): 508-20.
- Wientjes, F. B. and N. Nanninga (1989). "Rate and topography of peptidoglycan synthesis during cell division in Escherichia coli: concept of a leading edge." J Bacteriol **171**(6): 3412-9.
- Wientjes, F. B., C. L. Woldringh, et al. (1991). "Amount of peptidoglycan in cell walls of gram-negative bacteria." J Bacteriol **173**(23): 7684-91.

Bibliography

- Williams, M. C., J. R. Wenner, et al. (2001). "Effect of pH on the overstretching transition of double-stranded DNA: evidence of force-induced DNA melting." *Biophys J* **80**(2): 874-81.
- Williams, M. C., J. R. Wenner, et al. (2001). "Entropy and heat capacity of DNA melting from temperature dependence of single molecule stretching." *Biophys J* **80**(4): 1932-9.
- Xian, M., M. M. Fuerst, et al. (2007). "Sorting signal of Escherichia coli OmpA is modified by oligo-(R)-3-hydroxybutyrate." *Biochim Biophys Acta* **1768**(11): 2660-6.
- Yao, X., M. Jericho, et al. (1999). "Thickness and elasticity of gram-negative murein sacculi measured by atomic force microscopy." *J Bacteriol* **181**(22): 6865-75.
- Yuan, C., A. Chen, et al. (2000). "Energy landscape of streptavidin-biotin complexes measured by atomic force microscopy." *Biochemistry* **39**(33): 10219-23.
- Zagursky, R. J. and M. L. Berman (1984). "Cloning vectors that yield high levels of single-stranded DNA for rapid DNA sequencing." *Gene* **27**(2): 183-91.
- Zgurskaya, H. I. and H. Nikaido (1999). "AcrA is a highly asymmetric protein capable of spanning the periplasm." *J Mol Biol* **285**(1): 409-20.
- Zinder, N. D. and W. F. Arndt (1956). "Production of Protoplasts of Escherichia Coli by Lysozyme Treatment." *Proc Natl Acad Sci U S A* **42**(9): 586-90.

Summary

This thesis is about cell division in bacteria. What (to me) is fascinating about a bacterium such as *Escherichia coli* is that it can multiply at an incredibly fast pace by growing in length and then simply splitting itself in two. It has been known for decades that our own cells divide by making use of force-generating proteins similar to those present in our muscle cells. However, how a bacterium manages to divide is still a mystery. One of the problems when studying bacteria is their small size (one hundredth of the thickness of a human hair). This was one of the reasons that led scientists to think that bacteria were small “bags of protein”, without an internal cytoskeleton (built from proteins) such as possessed by plant and animal cells. This view has changed in recent years, as it turns out that bacteria have more in common with our own cells than previously thought. For instance, it was found that a protein called FtsZ forms a ring in the middle of a dividing bacterium. There are strong indications that this “Z-ring” generates force to constrict the bacterium. However, this has not yet been proven experimentally. This thesis describes the development of a method to perform force measurements on a single dividing bacterium.

To be able to measure the very small forces that can be produced by single cells, we make use of a technique called “optical tweezers” or “optical trapping”. An optical trap is created by a focused laser beam, and can hold (‘trap’) small beads in liquid. The trapped bead, when calibrated properly, can become an extremely sensitive force sensor. Because it works in a fluid environment, optical tweezers are ideally suited to study cells and proteins. Our optical tweezers set-up consists of a strong laser beam coupled into a commercial microscope. Plastic or glass beads, as well as bacteria (length scale: a thousandth of a millimeter) can be optically trapped. When a force in the order of a millionth of a millionth Newton (one Newton is the force that the earth exerts on a not too heavy book) is exerted on the bead it will slightly displace out of the trap (on a scale of nanometers, a millionth of a millimeter). The strength of the trap can be calibrated by measuring the spatial fluctuations of the trapped bead.

The challenge now is to attach such a bead to a bacterium roughly at the site where the bacterium will divide, because we suspect that at that location, forces are generated. The idea that has been worked out in this thesis is to genetically alter the bacteria in such a way that they produce molecular handles which end up on the bacterial surface, but only

at the division site. We believe this is possible because proteins often consist of multiple domains, which often have their own separate functions. Since protein domains exist that are present on the bacterial surface, as well as protein domains that localize to the division site, it should in principle be possible to create a new fusion protein which is present on the bacterial surface, but only at the division site.

A complicating factor in bacteria is the presence of a rigid cell wall, which is similar in many ways to the cell wall that gives shape to plant cells. When a bacterium divides in two daughter cells, also the new cell poles need to be formed. Or to put it differently: the creation of the new cell poles of the two daughter cells is the process of division. **Chapter 2** summarizes what is known about the processes that shape bacterial cell walls. For these processes, the length scale is that of the single protein molecule (1-10 nm). The focus is on the relatively new hypothesis that forces exerted by cytoskeletal proteins such as FtsZ and MreB play an important role in shaping the cell wall.

The three chapters that follow deal with the creation of the molecular handle. In **Chapter 3** we present experiments in which a surface protein (OmpA, for 'outer membrane protein A') of the bacterium *Escherichia coli* is genetically altered such that a small part of another protein (an epitope) is displayed on the bacterial surface. This is required for bead attachment. Three different epitopes are compared. We show that all three epitopes are displayed on the cell surface, but that the efficiency of protein insertion into the outer membrane differs. The so-called FLAG and myc epitopes are partially degraded by the cell. In contrast, virtually no degradation was observed for the SA-1 epitope. In addition, experiments are described which demonstrate that OmpA with the SA-1 epitope present can insert in the outer membrane with unaltered efficiency when its cell wall binding domain is absent. With this result, we have demonstrated that the OmpA-177 protein domain with SA-1 epitope is a suitable starting point for gene fusions to a second domain with mid-cell affinity.

In **Chapter 4** we study whether the cell division protein FtsQ is able to localize (bring) another unrelated protein domain to mid-cell (the division site). If we would like to localize OmpA to mid-cell using FtsQ, a bridging domain is required to connect the two membranes, since FtsQ is present in the inner membrane, and the OmpA-177 domain in the outer membrane. Initially, the AcrA protein was used as bridging domain. Two issues arose: during the course of our research, the molecular structure of AcrA was published,

and it became clear that it could not function as a bridging protein. Furthermore, fusion proteins between FtsQ and AcrA lost their ability to localize to mid-cell after further extension with extra protein domains (such as OmpA-177). Subsequently, the ALBP protein was chosen as bridging protein. The results are encouraging, as FtsQ-ALBP appears to be present at the division site.

However, after a publication of a study on (yet) another protein, the Pal protein, we decided to change our strategy. Fusions based on FtsQ and ALBP consist of at least five protein domains (GFP, FtsQ, two ALBP bridging domains and the OmpA-177 domain). It is known that as more and more domains are fused in series, the risk that protein domain misfolding and degradation occurs increases rapidly. What makes the Pal protein special is its structural similarity to the cell wall binding domain of OmpA, with the crucial difference that it localizes specifically to the division site. Simply fusing the OmpA-177 domain to the Pal domain could create the desired molecular handle at the division site, with just two protein domains. The experiments in **Chapter 5** however suggest additional complications: *E. coli* can grow without the Pal protein, albeit with a defect in outer membrane attachment to the cell wall. These defects are most severe at the division site. Although we demonstrate that internally, a (OmpA-177)-Pal fusion protein was present at mid-cell in cells lacking native Pal, on the cell surface the fusion protein was not concentrated at the division site. It is tempting to attribute this to the outer membrane attachment problems in these cells. When both the fusion protein and the native Pal protein are present, the native Pal occupies all available spots at the division site, and the opposite of what was aimed at occurs: the molecular handle is now present everywhere on the cell surface, except at the division site. In addition, **Chapter 5** contains results on fusions between various other protein domains and OmpA-177. It seems that when protein domains are fused behind (C-terminal to) OmpA-177 the probability that fusions end up in the outer membrane is greater than when domains are fused in front of (N-terminal to) OmpA-177.

Then the second part of thesis follows, which covers the force measurements. In **Chapter 6** the optical tweezers set-up is described. What makes this optical tweezers set-up special is that the laser light can enter the sample from opposite sides. This allows trapping of particles with a higher refractive index, generating stronger trapping forces on the particle compared to e.g. conventional polystyrene (plastic) particles. In turn, this

allows the measurement of higher forces. Improvements to the set-up, such as the ability to measure at elevated temperatures (required to study bacterial cell division), and the ability to trap and manipulate multiple particles with a single laser beam (so-called ‘time sharing’) are described. The latter can be likened to the circus act ‘plate spinning’, in which multiple plates on sticks are kept rotating by a single person by giving them extra spin from time to time. In the same manner, multiple particles can be kept in place by re-directing a single laser beam rapidly between multiple positions. This technique allows the attachment of two beads to a single bacterium.

Chapter 7 describes experiments in which beads are attached via a DNA molecule to bacteria displaying the SA-1 epitope on their surface. We measure force-extension curves of DNA molecules held between two beads and compare these curves to curves of DNA molecules attached to bacteria. In this way, we obtain information about the properties of the molecular handle on the cell surface. In our experiment, the bead is pulled out of the trap under an angle. Unexpectedly, this has a large effect on the measured forces. However, the results suggest that the molecular handle contained in the outer membrane is pulled off the cell via a membrane tube. Experiments in which the height of the bead with respect to the bacterium is carefully controlled are needed to provide a definitive answer whether tubes are pulled, and if so, whether the presence of the cell-wall binding domain of OmpA can reduce the probability of such an event. These experiments are important, because if the molecular handle can indeed be pulled away from the cell it will have consequences for the experiments aimed at in this thesis.

Finally, in **Chapter 8**, the feasibility of creating a molecular handle at the division site is discussed. An important prerequisite is the ability of the protein domain in the outer membrane to move around to bring the internal domain with mid-cell affinity to the division site. Literature on this topic (although sparse) suggests that this should be possible. In addition, we present alternative approaches explored in this research. These approaches include using a special *E. coli* mutant that has lost its outer membrane and PG cell wall, as well as indirectly trapping a single growing bacterium by attaching beads directly to its poles, and trapping these beads. We recommend a continued search for a fusion protein that localizes to the division site on the cell surface, as the best option to realize the planned experiments on force generation in dividing bacteria.

Samenvatting

Dit proefschrift gaat over celdeling in bacteriën. Voor mij is het fascinerende van een bacterie zoals *Escherichia coli* dat het zich ongelooflijk snel kan vermenigvuldigen door in lengte te groeien en zich 'simpelweg' in tweeën te splitsen. Van de cellen in ons eigen lichaam is al tientallen jaren bekend dat deze zich delen door middel van krachtgenererende eiwitten van hetzelfde type zoals aanwezig in onze spiercellen. Hoe echter een bacterie zich deelt is nog steeds een mysterie. Een van de problemen bij het bestuderen van bacteriën is dat ze zo klein zijn (een honderdste van een enkele mensenhaar dik). Mede hierdoor is lange tijd gedacht dat bacteriën 'zakjes met eiwitten' waren, zonder intern eiwitskelet zoals bijvoorbeeld planten- en dierencellen hebben. In recente jaren is hier verandering in gekomen, en blijkt dat micro-organismes meer op onze eigen cellen lijken dan gedacht. Zo is er ontdekt dat een eiwit genaamd FtsZ een ring vormt in het midden van een delende bacterie cel. Er zijn sterke aanwijzingen dat deze 'Z-ring' kracht genereert om de bacterie te doen splitsen. Dit is echter nog nooit experimenteel aangetoond. In dit proefschrift wordt de ontwikkeling van een methode beschreven om krachtmetingen te doen aan een enkele delende bacterie.

Om de zeer kleine krachten die door enkele cellen geproduceerd worden te kunnen meten maken we gebruik van een 'optisch pincet' (de engelse term is 'optical trap' of 'optical tweezers'). Een optisch pincet is een extreem gevoelige krachtmeter, die werkt met kleine bolletjes in een vloeistof. Omdat krachten in een vloeistof omgeving gemeten kunnen worden is deze techniek zeer geschikt om cellen en eiwitten mee te bestuderen. Ons optisch pincet bestaat uit een microscoop waar een sterke laserbundel in wordt gekoppeld. Door het laserlicht te focuseren tot een diffractiegelimiteerde focus punt (de 'trap') kan een plastic of glazen bolletje van dezelfde orde grootte als van een bacterie hierin gevangen worden. Wanneer een kracht in de orde van een miljoenste van een miljoenste Newton (een Newton is de kracht die de aarde uitoefent op een niet al te zwaar boek) op het bolletje wordt uitgeoefend wordt deze een beetje (op de schaal van nanometers, miljoenste millimeters) uit de trap getrokken. Door de trillingen van het gevangen bolletje precies te meten kan de sterkte van de trap bepaald worden. Daarna kan uit de verplaatsing van het bolletje de kracht worden herleid.

De uitdaging ligt er nu in om zo'n bolletje vast te maken aan een bacterie ongeveer op de plek waar de bacterie zich gaat splitsen, omdat we vermoeden dat daar de krachten

worden gegenereerd. Het idee uitgewerkt in dit proefschrift is om de bacteriën genetisch zo te aan te passen dat ze zelf moleculaire 'handvatten' produceren die op het oppervlak van de bacterie terechtkomen, maar dan enkel en alleen op de delingsplaats. We denken dat dit mogelijk is omdat eiwitten vaak uit meerdere domeinen bestaan, die elk hun eigen functie hebben. Aangezien er eiwitten bekend zijn die zich aan het oppervlak van een bacterie bevinden, en eiwitten die specifiek op de delingsplaats aanwezig zijn, is het in theorie mogelijk om een nieuw samengesteld 'fusie-eiwit' te maken dat aan het oppervlak specifiek op de delingsplaats aanwezig is.

Een complicerende factor in bacteriën is de aanwezigheid van een harde celwand, die in veel opzichten lijkt op de celwand waaraan plantencellen hun vorm ontleen. Wanneer een bacterie zich deelt in twee dochter cellen moet ook deze celwand worden gevormd. Je kan het ook anders zeggen: het vormen van de nieuwe uiteinden van de dochterbacteriën IS het delingsproces. **Hoofdstuk 2** geeft een samenvatting van wat er bekend is over de processen die de celwand vormen. De schaal waarop dit zich afspeelt is op het enkele eiwit niveau (1-100 nanometer). Centraal staat de relatief nieuwe hypothese dat krachten uitgeoefend door celskelet eiwitten zoals FtsZ en MreB hierbij een belangrijke rol spelen.

De drie hoofdstukken die volgen houden zich bezig met het creëren van het moleculaire handvat. In **Hoofdstuk 3** beschrijven we de experimenten waarin een oppervlakte-eiwit (OmpA) van de *Escherichia coli* bacterie genetisch wordt aangepast zodat er een stukje van een ander eiwit (een epitoom) aan het oppervlak wordt gepresenteerd. Dit is nodig om er een bolletje aan vast te kunnen maken. Drie verschillende epitopen worden vergeleken. We laten zien dat alle drie de epitopen inderdaad op het oppervlak aanwezig zijn, maar dat de efficiëntie waarmee dit gebeurt verschilt. De zogenaamde FLAG en myc epitopen blijken gedeeltelijk te worden afgebroken door de cel. De SA-1 epitoom daarentegen wordt vrijwel niet afgebroken. Verder worden experimenten beschreven waarin wordt aangetoond dat het OmpA eiwit met een SA-1 epitoom even goed in het buitenste celmembraan inserteert wanneer het OmpA celwand bindingsdomein afwezig is. Hiermee is aangetoond dat de OmpA-177 eiwit module met SA-1 epitoom een geschikt uitgangspunt vormt om er genetisch een tweede eiwit module met delingsplaats affiniteit aan vast te koppelen.

In **Hoofdstuk 4** worden experimenten beschreven waarin gekeken wordt of het celdelings eiwit FtsQ in staat is een additionele eiwit module naar de delingsplaats te

'lokaliseren' (brengen). Aangezien FtsQ zich in het binnenste celmembraan bevindt en de OmpA-177 eiwit module in het buitenste celmembraan, is er een overbruggende verbindingseiwit module nodig om met behulp van FtsQ OmpA naar de delingsplaats te dirigeren. In eerste instantie is het AcrA eiwit gebruikt als verbindingseiwit. Hier waren echter twee problemen mee: nadat in de loop van ons onderzoek de eiwit structuur werd gepubliceerd werd duidelijk dat het niet als verbindingseiwit kan functioneren, en tevens verloor het fusie eiwit zijn affiniteit voor de delingsplaats wanneer het verder werd uitgebreid met extra eiwit modules. Vervolgens is het ALBP eiwit gekozen als verbindingseiwit. Alhoewel nog niet is aangetoond dat het FtsQ-ALBP fusie-eiwit intact aanwezig is op de delingsplaats zijn de voorlopige resultaten bemoedigend.

Echter, na een publicatie over wederom een nieuw eiwit, het Pal eiwit, werd besloten om van strategie te wisselen. Fusies op basis van FtsQ en ALBP bestaan uit tenminste vijf eiwit domeinen (GFP, FtsQ, twee ALBP verbindingsdomeinen en het OmpA-177 domein). De ervaring leert dat de kans op eiwit vouwingsproblemen en afbraak toeneemt naarmate er meer eiwit domeinen kunstmatig aan elkaar worden geknoopt. Het bijzondere van het Pal eiwit was dat het dezelfde structuur heeft als het celwand bindingsdomein van OmpA zelf, met als grote verschil dat het naar de delingsplaats lokaliseert. Door simpelweg het OmpA-177 domein te fuseren aan het Pal domein zou dan het gewenste 'handvat' op de delingsplaats gecreëerd kunnen worden, en dat met maar twee eiwit domeinen. De experimenten in **Hoofdstuk 5** suggereren een extra complicatie: de functie van het Pal eiwit, en de aanwezigheid van celeigen Pal eiwit. *E. coli* kan zonder Pal eiwit groeien, alleen is er dan een probleem met de aanhechting van het buitenste celmembraan aan de celwand. Alhoewel een (OmpA-177)-Pal fusie intern op de delingsplaats aanwezig is in zulke cellen, is dit niet het geval aan het celoppervlak. Het ligt voor de hand om dit te wijten aan de aanhechtingsproblemen van de cel. Wanneer het celeigen Pal eiwit wel aanwezig is, neemt dit eiwit alle plekken in beslag op de delingsplaats, en vindt er het omgekeerde plaats van wat we wilden: het handvat zit nu overal aan het oppervlak, behalve op de delingsplaats! Verder bevat dit hoofdstuk resultaten van fusies tussen verschillende eiwit domeinen en OmpA-177. Het lijkt erop dat als eiwitdomeinen achter OmpA-177 worden geplakt, de kans dat OmpA-177 in het buitenste celmembraan terechtkomt groter is dan als ze ervoor worden geplakt.

Dan volgt het tweede gedeelte van het proefschrift, waar de krachtmetingen aan bod

komen. In **Hoofdstuk 6** wordt de optisch pincet opstelling beschreven. Het bijzondere aan deze optisch pincet opstelling is dat er laserlicht van beide kanten het preparaat binnenkomt. Hiermee kunnen deeltjes met een hogere brekingsindex worden vastgehouden, wat leidt tot sterkere 'trap' krachten op het deeltje. Hiermee kunnen dus ook hogere krachten gemeten worden. Uitbreidingen aan de opstelling, zoals de mogelijkheid om bij hogere temperaturen te meten (nodig om delende bacteriën te bestuderen), en de mogelijkheid om meerdere bolletjes met een enkele laserbundel tegelijkertijd te manipuleren (het zogenaamde 'time-sharen') worden beschreven. Dit laatste kan vergeleken worden met de circus act 'borden draaien', waarbij meerdere borden op stokken draaiend gehouden worden door ze op gezette tijden een extra slinger te geven. Zo ook kan door maar snel genoeg een laser bundel op verschillende plekken te richten meerdere bolletjes op hun plaats gehouden worden. Op deze manier kunnen twee bolletjes aan een enkele bacterie vastgemaakt worden.

In **Hoofdstuk 7** worden experimenten beschreven waarbij bolletjes via een DNA molecuul vastgemaakt worden aan bacteriën die het eerder genoemde SA-1 epitoom op hun oppervlak presenteren. Door kracht-extensie curves te meten van DNA moleculen tussen twee bolletjes en die te vergelijken met soortgelijke curves van DNA moleculen die aan de SA-1 epitoom vastzitten kunnen we leren over de eigenschappen van het handvat op het celoppervlak. Onverwachts bleek de geometrie van het experiment, waarbij het bolletje onder een hoek uit de 'trap' getrokken wordt, een groot effect te hebben op de gemeten krachten. De resultaten suggereren dat het handvat via een membraanbuis uit het buitenste celmembraan getrokken kan worden. Experimenten waarbij de hoogte van het bolletje ten opzichte van de bacterie nauwkeurig ingesteld wordt moeten uitwijzen of dit inderdaad het geval is, en of het celwand bindingsdomein van OmpA de kans hierop kan verkleinen. Het is belangrijk om dit vast te stellen omdat het niet de bedoeling is dat het handvat uit de cel getrokken wordt tijdens de krachtmeting.

Tenslotte wordt in **Hoofdstuk 8** de mogelijkheid van een fusie-eiwit op de delingsplaats bediscussieerd. Belangrijk hiervoor is dat de eiwit module in het buitenste celmembraan zich moet kunnen verplaatsen om zo de interne module met delingsplaats affiniteit naar het midden te brengen. De (schaarse) literatuur hierover suggereert dat dit mogelijk is. Verder worden alternatieve benaderingen die zijn verkend binnen dit onderzoek in dit hoofdstuk beschreven. Hieronder vallen een speciale *E. coli* mutant die

Samenvatting

geen celwand en buitenmembraan meer heeft, en het vasthouden van een bacterie door kleine bolletjes aan beide celpolen te plakken en deze te 'trappen'. De eindconclusie is dat het voortzetten van de zoektocht naar een eiwit handvat op de delingsplaats zinvol is om zo tot de realisatie van de beoogde experimenten aan krachtgeneratie tijdens celdeling te komen.

Dankwoord

Niet veel mensen op AMOLF weten dat ik al in 1997 als derdejaars natuurkunde student op AMOLF mijn 'Introductie Periode Laboratorium' kwam vervullen, aangetrokken door het magische 'atomen zien' met STM in de groep van Joost Frenken, die in het jaar erop naar Leiden verhuisde. Joost, ik kijk terug op een plezierige en vruchtbare samenwerking tijdens mijn afstuderen in Leiden en daarna als onderzoeker in de Grensvlak fysica groep. Bedankt voor alles!

Verder wil ik graag mijn promotor Marileen en co-promotor Tanneke bedanken voor het in mij gestelde vertrouwen gedurende mijn promotie. Marileen, je was er altijd om rust te creëren, en dingen in het juiste perspectief te plaatsen. Ik heb veel geleerd van jouw pragmatische insteek om al experimenterend alleen die problemen op te lossen die vooruitgang in de weg staan. Tanneke, bedankt voor je enthousiasme, en je geduld met mijn onwetendheid op bio-terrein. Je stond altijd open voor nieuwe ideeën!

Er zijn een aantal mensen die een belangrijke bijdrage geleverd hebben aan dit promotieonderzoek, en die ik hiervoor wil bedanken: Svetlana Alexeeva, Astrid van der Horst, Genison Isijk, Dirk-jan Spaanderman, Wim Brouwer en zijn collega's van de werkplaats, de technici van E&I (en met name Duncan Verheijde, Johan Herscheid, Marco Seynen en Henk Dekker), en niet te vergeten onze groepstechnici Roland Dries, Kim Renders en Henk Bar.

Verder wil ik al mijn collega's bij Moleculaire Cytologie en op AMOLF bedanken voor het creëren en in stand houden van een zeer prettige werksfeer. Ook de piekfijne ondersteuning van de AMOLF bibliotheek, het magazijn, de receptie en de kantine mag niet onvermeld blijven.

Als laatste wil ik mijn vriendin Jansje, vrienden, familie en schoonfamilie bedanken voor alle steun en warmte die ik heb mogen ontvangen tijdens de totstandkoming van dit proefschrift.

Curriculum vitae

Gertjan Verhoeven was born in Leiderdorp, on April 27th, 1977. From 1989 to 1995 he attended the 'Gymnasium' at the Visser 't Hooft Lyceum in Leiden. In 1995 he started a Master's Program in Physics at Leiden University. He obtained a Master's degree in Physics in 2001, after an internship in the group 'Interface Physics' of Prof.dr. Joost Frenken. In this group he worked on the development of the Reactor STM, a scanning tunnelling microscope designed to image catalytic surfaces at ambient conditions. The following two years he remained in the Interface Physics group to work on two projects: the friction between two graphite surfaces, as well as step edge dynamics of a copper single crystal surface. For these projects he developed simulations to model experimental data, both of which resulted in a publication. In Januari 2004, he started his PhD research in the groups of Prof.dr. Marileen Dogterom at the FOM Institute for Atomic and Molecular Physics (AMOLF) in Amsterdam and Dr. Tanneke den Blaauwen at the University of Amsterdam. The results of this work are described in this thesis.